Détermination de la constante de dissociation de l'hybridation ADN / ADN aux interfaces solide/liquide par trois techniques différentes : résonance de plasmon de surface, biopuce par mesure de cartographie de fluorescence et par mesure de fluorescence par champ évanescent

Muchen Li

N°d'ordre NNT : 2018LYSEC028

THESE de DOCTORAT DE L'UNIVERSITE DE LYON opérée au sein de l'Ecole Centrale de Lyon

Ecole Doctorale : Electronique, Electrotechnique et Automatique – ED 160

Spécialité : Ingénierie pour le vivant

Soutenue publiquement le 16/10/2018, par :

Muchen LI

Determination of dissociation constant of DNA/DNA hybridization by three different surface techniques: comparison of surface plasmon resonance, fluorescent microarray and evanescent field fluorescence

---

Thèse préparée à l'Institut des Nanotechnologies de Lyon sous la direction de Yann Chevolot et Thomas Géhin

Devant le jury composé de :

Dr. Yoann Roupioz	Directeur de Recherche CNRS-HDR, SyMMES Grenoble	Président (Rapporteur)
Dr. Anne-Chantal Gouget-Laemmel	Chargée de Recherche CNRS-HDR, LPMC, Palaiseau	Rapporteure
Dr. Yann Chevolot	Directeur de Recherche CNRS-HDR, INL, Ecully	Directeur de thèse
Dr. Thomas Géhin	Ingénieur de Recherche CNRS, INL, Ecully	Co-directeur de thèse

Acknowledgements

It was a great pleasure for me to make a thesis in the team of chemistry and nanobiotechnology in Lyon Institute of Nanotechnology (INL), and I want to thank a lot of people for these three years.

First of all, I would like to thank my supervisors Dr. Yann Chevolot and Dr. Thomas Géhin who give me continuous guidance, support and encouragement during last three years. From Dr. Yann Chevolot, I learned how to conduct a research project logically, from literature review, experiments designing to the finally scientific paper writing. Dr. Thomas Géhin gave me countless lessons on the design and physics of surface plasmon resonance biosensor. I really appreciate your patience. They set a very good example for me, and that will make me benefit all my life.

Secondly, I am so grateful for the PhD fellowship from China Scholarship Council (CSC) which gave me financial aids to conduct my thesis work in France.

Thanks the members of my dissertation committee, Dr. Yoann Roupioz and Dr. Anne-Chantal Gouget-Laemmel who agreed to review the manuscript of the thesis. The thesis would not have been completed without their cooperation and constructive suggestions.

Then I want to thank all the colleagues and friends in my team. Thanks Dr. Lucie Dupin for her help in my work and life at first year in France. Hope your life will be much better than you expected. Thanks Dr. Jean Pierre Cloarec for coaching me how to use the EVA-reader. Thanks for Isabel Nabeth for your excellent coffee and support in the lab. Also, great thanks to Dr. Emmanuelle Laurenceau, Dr. Christelle Yeromonahos, Dr Virginie Monnier, Dr Magali Phaner-Goutorbe, Dr. Salome Ansanay-Alex, Dr. Francesca Zuttion, Dr. Maxime Boksebeld, Dr. Mathieu Caillau, Dr. Feixiong Chen, Jian Zhang, Marie Galvin, Rachael Taitt, Solène Lecot and Olya Sysova for every help and support during last three years. I am extremely lucky to work with these cheerful and friendly colleagues and friends.

Furthermore, I want to thanks all my Chinese PhD friends for the great times we have spent for the past three years: Haohao Ding, Zehua Fu, Xin Guan, Dong Han, He Ding, Fei Zheng, Guang Zhu, Zeyu Liu, Haining Luo, Mingyang Lou, Kaijun Yi, Qingjie Ju, Wenqi Cai, Zihan Shen, Peng Wang, Xingrong Huang, etc.

Finally, I want to thank my family. I could not finish my thesis without your supporting.

Table of Contents

List of figures

List of tables

Acronyms

AFM: Atomic Force Microscopy

BOE: Buffered Oxide Etch

BSA: Bovine Serum Albumin

DCM: DiChloroMethane

DDI: DNA Directed Immobilization

DIC: DiIsopropylCarbodiimide

DNA: DeoxyriboNucleic Acid

dsDNA: Double Stranded DNA

ssDNA: Single Stranded DNA

K_d: Dissociation Constant

k_{on}: On-rate Constant

k_{off}: Off-rate Constant

MCH: MerCaptoHexanol

NHS: N-HydroxySuccinimide

PBS: Phosphate Buffer Saline

PEG: PolyEthylene Glycol

PMIRRAS: Polarization Modulation InfraRed Reflection Adsorption Spectroscopy

RI: Refractive Index

SC: Standard Clean

SDS: Sodium Dodecyl Sulfate

SPR: Surface Plasmon Resonance

SSC: Saline Sodium Citrate

TDSUM: Tert-butyl 11-[dimethylamino-(dimethyl)-silyl]-undecanoate

THF: TetraHydroFuran

XPS: X-ray Photoelectron Spectroscopy

PMMA: Poly(Methyl MethAcrylate)

NN: Nearest-Neighbour

RMS: Root Mean Square

General introduction

Nowadays, there is growing interest regarding the use of biosensors. These micro-devices consist of bio-recognition layer and a transducer. The bio-recognition layer is meant to capture specifically a target (the molecule to be detected). The bio-recognition layer is often composed of immobilized biomolecules (DNA, proteins, carbohydrates) called probes. The transducer transforms the capture event into a measurable signal. The application includes gene chip, food safety, infectious disease diagnostic devices, DNA-driven assembly microarrays and environmental sensors... Such sensors can also be used to measure characteristic kinetic and thermodynamic parameters of biomolecular interactions. For example, Buhot *et al* [1] have demonstrated that ΔG and ΔH could be extracted from Surface Plasmon Resonance (SPR) kinetic curves performed at various temperatures. However, variations from one device to another may be observed due to different grafting chemistry, to the different materials constituting the transducers or to mass transport phenomena. For example, gold is used for SPR while glass is generally preferred for fluorescence. Can this affect the measured K_d? Finally, mass transport can also affect the measurements. Herein, we have focused on DNA/DNA hybridization as a model reaction.

Surface based hybridization may lead to a loss of configurational freedom due to the immobilization of DNA probe, which could result in a decrease in the affinity constant of DNA/DNA hybridization. Therefore, some algorithms derived to quantitatively predict the thermodynamics of hybridization in a homogeneous solution cannot be applied for surface based hybridization. In addition, many factors, such as: surface probe density, DNA secondary structure, ionic strength, DNA recognition interfacial structure, could also influence DNA/DNA hybridization on surface. Therefore, different surface based methods performed under different experimental conditions may give different dissociation constants (K_d) of DNA/DNA duplex formation.

In this context, three different surface based methods (surface plasmon resonance (SPR), evanescent field fluorescence and fluorescent microarray) have been chosen to determine a DNA/DNA hybridization K_d in this dissertation. For these three techniques, three different substrates are required gold, polymer and glass, respectively. SPR biosensor is a powerful tool for *in situ* real-time measurement of DNA/DNA hybridization. It can provide both kinetic (k_{on} and k_{off}) and equilibrium (K_d) data in one simple experiment. No target molecules labeling is required in the measurement. Considering evanescent field fluorescence and fluorescent microarray, they both need the target DNA to be labeled with a fluorescent dye prior to the measurement. The former one is a real-time measurement technique which can provide both

kinetic and equilibrium data of hybridization, the latter one is a steady state method which can only give data near equilibrium.

In our laboratory, a SPR system was built and needed to be validated. The evanescent field fluorescence biosensor is a commercial one (Davos diagnostics) and fluorescent microarray has been successfully applied in measuring the K_d of lectin-glycocluster interactions. Following that, this dissertation addresses four main aims:

1) To validate our homemade SPR biosensor.

2) To optimize gold preconditioning used in the fabrication of SPR biosensor chip.

3) To optimize the experimental conditions for DNA/DNA hybridization on gold surfaces using SPR biosensor.

4) To determine and compare DNA/DNA hybridization K_ds by three surface based methods: SPR biosensor, evanescent field fluorescence biosensor and fluorescent microarray.

Consequently, this dissertation is structured in six chapters as described below:

Chapter 1 reminds the basic notions of thermodynamic and dissociation constants K_d. It gives a non-exhaustive overview on the state of art concerning the determination of biomolecular interactions K_d, especially DNA/DNA hybridization. The current methods used to determine the K_d can be broadly divided into two groups: solution based and surface based methods. In surface based methods, we review the techniques used to immobilize biomolecules on a solid surface and the factors influencing biomolecules interaction on surfaces. Thiolated DNA immobilization on gold and the factors influencing DNA/DNA hybridization are highlighted and described in detail.

Chapter 2 presents the main materials and methods used throughout this dissertation.

Chapter 3 describes the surface plasmon resonance technique. The validation and application of SPR sensing in measuring DNA/DNA hybridization is presented at last.

Chapter 4 is dedicated to the optimization of gold preconditioning for thiolated DNA grafting. Two methods are described: piranha solution and oxygen plasma cleaning. The optimization of piranha cleaning parameters such as the H_2SO_4/H_2O_2 ratio, treatment time and temperature are presented. Then the gold preconditioning by oxygen plasma cleaning and optimized piranha solution cleaning are compared by characterizing gold surface topography, elemental composition and oxidation state. Their effects on subsequent thiolated DNA grafting are compared.

In **chapter 5**, the parameters, such as DNA recognition interfacial structure, ionic strength and secondary structure of DNA sequence were firstly optimized for DNA/DNA hybridization

using SPR biosensor. After, DNA/DNA hybridization K_d was determined by three surface based methods: SPR biosensor, evanescent field fluorescence biosensor and fluorescent microarray. Finally, a comparison between these three methods is given in terms of operability and quality of data obtained.

Chapter 6 completes the dissertation with the main conclusions and outlooks.

Chapter 1

State of the art

1 State of the art

1.1 Theory of thermodynamic

1.1.1 Basic principles

Chemical thermodynamics is a field of chemistry that studies heat and energy flows during chemical reactions. In particular, it can be applied in many fields including biochemistry for biomolecules interactions. The primary aim of chemical thermodynamic is to determine the feasibility and spontaneity of a transformation. To this aim, chemical thermodynamic is not concerned by the path of a transformation but by the initial and final states of the thermodynamic system that are near equilibrium. A thermodynamic system is a physical volume of space that may or may not exchange energy or matter with the rest of the universe: a closed system exchange only energy (no matter) and an isolated system does not exchange matter nor energy.

The thermodynamic states of the system can be described by state variables such as temperature, pressure and state functions. The most common thermodynamic state functions include enthalpy (*H*), entropy (*S*), and Gibbs free energy (*G*). These state functions are independent of the reaction path and depend only on the initial state and final state.

The classical thermodynamic is governed by three fundamental laws:

- The first law states that the energy of an isolated system (no exchange of matter nor energy) is constant. In other word, the energy of the universe is constant.
- The second law states that the entropy *S* of an isolated system can only increase during a transformation. In other words the entropy of the universe can only increase.
- The third principle states that entropy of a perfect crystal at 0 Kelvin is zero.

Most of the state functions arise from the first two principles.

The internal energy *U* of a given system is the sum of microscopic energies (kinetic and potential). According to the first principle, for a chemical reaction occurring in a closed system (no exchange of matter), the energy should be conserved. Therefore, any variation of *U* should give rise to energy exchange with the outside. This energy can be heat or work.

$$\Delta U = Q + W \qquad \text{Equation 1.1}$$

where *U* is the internal energy of the system, *Q* is the heat exchanged and *W* is the work. All three parameters are expressed in Joules.

Most chemical reactions occur at constant pressure (isobar transformation). If the only contribution to the work is the result of pressure, then the work can be written:

$$W_p = -PV_2 + PV_1 = -P(V_2 - V_1) = -P\Delta V \qquad \text{Equation 1.2}$$

where *P* is the pressure in Pascal and *V* the volume in m^3.

Equation 1.1 then becomes:

$$\Delta U_p = Q_p + W_p = Q_p - P\Delta V$$

$$\Delta U_p + P\Delta V = Q_p$$

$$Q_p = (U_2 + PV_2) - (U_1 + PV_1) \qquad \text{Equation 1.3}$$

From Equation 1.3, a new state function can be defined: Enthalpy (*H*).

$$H = U + PV \qquad \text{Equation 1.4}$$

H is expressed in Joule, and it can be defined as the sum of the internal energy and the energy spend by the system to fight against the external pressure.

Entropy (*S*) was proposed by R. Clausius in 1854. It is used to evaluate the degree of disorder of systems. Entropy is also a state function. In chemical reactions, ΔS represents the difference of degrees of disorder of the whole system before and after reactions. *S* is expressed in Joules per Kelvin.

$$\Delta S_{sys} = \frac{Q}{T} \qquad \text{Equation 1.5}$$

where *Q* and *T* are the heat in Joule and the temperature in Kelvin respectively.

The second principle states that the entropy of an isolated system can only increase. However, in the case of a chemical reaction, the system may be closed (energy can be exchanged with the surroundings). A closed system may therefore undergo a transformation that leads to a decrease of potential energy despite a decrease of its entropy.

Consequently, as the entropy of the universe can only increase, the total variation of *S* during a chemical reaction ($\Delta S_{sys} + \Delta S_{surroundings}$) must be positive. In other words, the entropy of the system can decrease providing that it is compensated by an increase of the entropy of the surroundings.

$$\Delta S_{sys} + \Delta S_{surroundings} > 0 \qquad \text{Equation 1.6}$$

If the reaction is isobar and if the work is only related to the pressure forces, the variation of entropy of the surroundings can be expressed as:

$$\Delta S_{surroundings} = -\frac{Q_p}{T} = -\frac{\Delta H_{sys}}{T} \qquad \text{Equation 1.7}$$

Then from Equation 1.6 and 1.7, we get:

$$\Delta S_{sys} - \frac{\Delta H_{sys}}{T} > 0 \qquad \text{Equation 1.8}$$

If the Equation 1.8 is multiplied by *–T*, it gives:

$$\Delta H_{sys} - T * \Delta S_{sys} < 0 \qquad \text{Equation 1.9}$$

As a result, a new state function can be defined: Gibbs free energy (*G*), which is expressed as:

$$G = H - TS \qquad \text{Equation 1.10}$$

where *T* is the temperature in Kelvin, *G*, *H* and *S* are the free Gibbs energy, the enthalpy and the entropy expressed in Joule, Joule and Joule/Kelvin respectively.

Gibbs free energy is one of the most useful state functions in chemistry (including biochemistry) as it allows predicting the direction and the spontaneity of a reaction. A chemical reaction will spontaneously occur if *ΔG* is negative and, when the reaction reaches to equilibrium, *ΔG = 0*. For a chemical reaction,

$$\Delta_r G = (\frac{dG}{d\xi})_{p,T} \qquad \text{Equation 1.11}$$

where *ΔrG* is the slope of *ΔG* and ξ is the extent of the reaction.

$$\mu_i = (\frac{dG_i}{dN_i})_{p,T} \qquad \text{Equation 1.12}$$

where μ_i and N_i are the chemical potential and the number of particle *i* respectively.

Then for a reaction:

$$\gamma_A A + \gamma_B B \leftrightarrow \gamma_C C + \gamma_D D$$

$$dG = (\gamma_C \mu_C + \gamma_D \mu_D - \gamma_A \mu_A - \gamma_B \mu_B) d\xi \qquad \text{Equation 1.13}$$

Equations 1.11 and 1.13 give:

$$\Delta_r G = (\gamma_C \mu_C + \gamma_D \mu_D - \gamma_A \mu_A - \gamma_A \mu_B) \qquad \text{Equation 1.14}$$

μ_i can be expressed as a function of the activity of i:

$$\mu_i = \mu^\circ + RTlna_i \qquad \text{Equation 1.15}$$

where $\mu°$ is the standard chemical potential, R is the gas constant and a_i is the activity of particle i usually expressed as the concentration of particles.

$\Delta_r G$ can then be expressed by replacing μ_i with $\mu° + RT\ lna_i$:

$$\Delta_r G = \Delta G^\circ + RTlnQ \qquad \text{Equation 1.16}$$

where $\Delta G°$ is the standard Gibbs free energy change and Q is the reaction quotient.

When the reaction reaches at equilibrium, $\Delta_r G = 0$. Then equation 1.16 becomes:

$$\ln K_{eq} = -\frac{\Delta G^\circ}{RT} \qquad \text{Equation 1.17}$$

where K_{eq} is the equilibrium constant of the reaction.

In combination with $\Delta G° = \Delta H° - T\Delta S°$, the van't Hoff equation can be derived:

$$\ln K_{eq} = -\frac{\Delta H^\circ}{RT} + \frac{\Delta S^\circ}{R} \qquad \text{Equation 1.18}$$

where $\Delta H°$ and $\Delta S°$ are the standard enthalpy and entropy change respectively. It describes the linear relationship between the natural logarithm of reaction equilibrium constant K_{eq} and the reciprocal of temperature $1/T$, which is widely used to estimate the change of enthalpy $(\Delta H°)$ and entropy $(\Delta S°)$ of a chemical reaction.

For reversible reactions, we can experimentally measure the reaction equilibrium constant at different temperatures. These data can be plotted in a graph with lnK_{eq} on the y-axis and $1/T$ on the x-axis, and linearly fitted by van't Hoff equation. The slope of this linear fitting curve is $\Delta H°/R$ and the intercept is the $\Delta S°/R$.

Therefore, the measurement of the equilibrium constant is an important parameter to assess thermodynamic parameters of biochemical reactions. In the scope of this PhD thesis, we focused on the biochemical reaction occurring at interfaces as the field of research of our group deals with biosensors and microarrays. A biosensor is a device that takes advantage of biochemical reactions in order to titrate a given target. The interaction is then transformed into a measurable signal. Microarrays are the substrates on which biomolecules are immobilized in an array fashion. Hereafter, immobilized molecules are named probes. After interaction of the microarray with a given bio-molecular target, mapping of a measurable signal allows to identify the probes for which the target has the greatest affinity.

In order to deeply understand biomolecules interactions, it is important to have access to the thermodynamic parameters (*ΔG, ΔH and ΔS*) of these interactions. Taking into account the van't Hoff law, reliable measurements of equilibrium constant is a key issue.

Therefore, we have studied three different techniques to measure equilibrium constant (dissociation constant K_d): Surface plasmon resonance, Evanescent field based fluorescence and fluorescent microarray. For these three techniques, three different substrates are required: gold, polymer and glass respectively.

As far as biomolecular interactions are concerned, we have focused on DNA/DNA duplex formation. Therefore, in the following, thermodynamic of DNA/DNA duplex formation is firstly illustrated. Then, we will shortly describe the solution based methods used to characterize the biomolecular interactions and determine the K_d. Finally we will review the methods used to access to K_d on surfaces.

1.1.2 Thermodynamic of DNA/DNA hybridization

DeoxyriboNucleic Acid (DNA) is the molecule that carries the genetic information. It is composed of desoxyribose, phosphate and 4 different nucleobases (cytosine, guanine, adenine, or thymine). The nucleobases are linked at the 2' position of desoxyribose and the resulting conjugates are called nucleoside. The four nucleosides are cytidine (C), guanosine (G), adenosine (A) and thymidine (T). Phosphorylation occurs at the 5' position of the desoxyribose leading to 4 nucleotides. Formation of a phosphodiester bound between the phosphate ester with the free 3' hydroxyl of an adjacent nucleotide allows the formation a single DNA strand. Therefore, DNA is a polymer of the 4 nucleotides linked via phosphodiester bonds between the 3' and 5' positions of two adjacent desoxyribose (as shown in Figure 1.1).

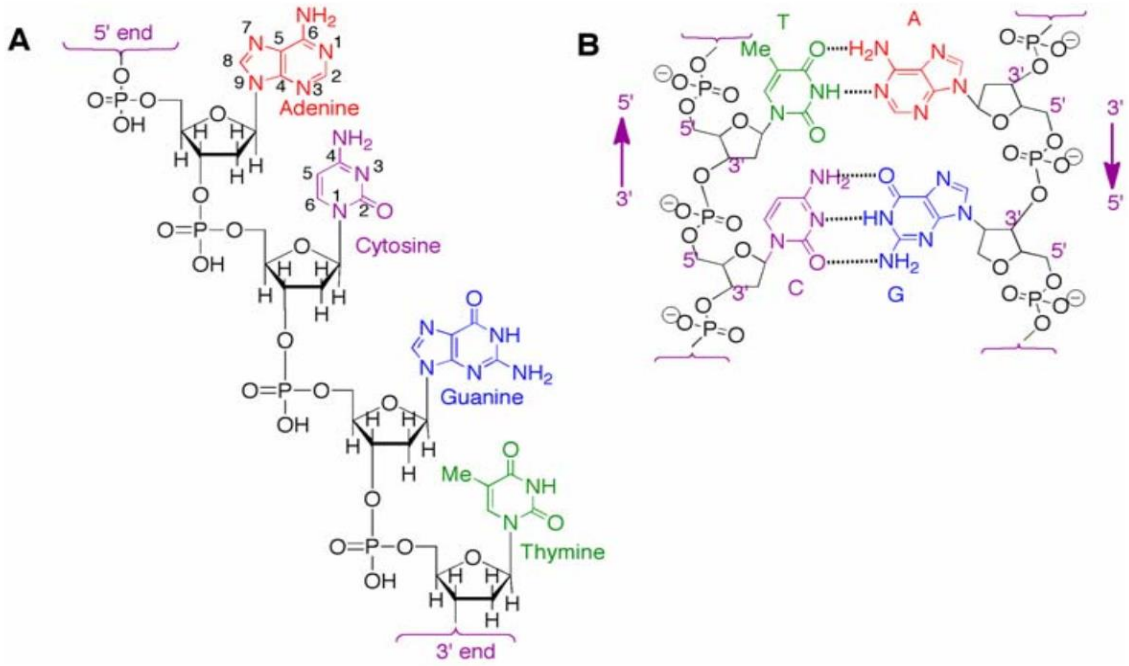

Figure 1.1 A) The structure of single strand DNA, B) Nucleobase pairing in complementary DNA strands, A can pair with T by two hydrogen bonds and C can pair with G by three hydrogen bonds. Adapted from [1].

Two single DNA strands can form a stable non-covalent duplex stabilized by hydrogen bonds and π-stacking (as shown in Figure 1.1B) and destabilized by columbic forces (electrostatic repulsion between the two strands that are polyanions). Electrostatic interactions depend on the Debye length, which is related to the ionic strength of the solution. Since these two base pairs have different numbers of hydrogen bonds, the stability of duplex does not only depend on the chain length but also on the sequence of strands. The sequence of strand is the order of the

nucleotides in the strand. In terms of external environment, the stability of duplex is related to the presence of chaotropic agents, ionic strength, pH and temperature [1]–[3].

Several thermodynamic models used to describe DNA/DNA hybridization have been proposed in the literatures [4], [5]. One of the most accepted ones is the Nearest-Neighbor (NN) model [6]–[8]. In this model, the interaction between two complementary bases is considered to depend also on neighboring bases. 10 different dimer duplexes are possible (as shown in table 1.1).

Sequences	**$\Delta H°$ (kcal/mol)**	**$\Delta S°$ (cal/k*mol)**
AA/TT	-7.9	-22.2
AT/TA	-7.2	-20.4
TA/AT	-7.2	-21.3
CA/GT	-8.5	22.7
GT/CA	-8.4	-22.4
CT/GA	-7.8	-21.0
GA/CT	-8.2	-22.2
CG/GC	-10.6	-27.2
GC/CG	-9.8	-24.4
GG/CC	-8.0	-19.9
Initiation at G·C[a]	0.1	-2.8
Initiation at A·T[b]	2.3	4.1
Symmetry correction[c]	0	-1.4

Table 1.1 Unified NN parameters of enthalpy change and entropy change in 1M NaCl. Adapted from [8]. [a] Initiation parameter for duplex formation starting or ending with complementary base pair (GC). [b] Initiation parameter for duplex formation starting or ending with complementary base pair (AT). [c] Symmetry correction applies only to self-complementary sequences.

The nearest-neighbor model represents the DNA double-stranded sequence as the neighbor base pairs, in which the stability of a complementary base pair depends on the identity and orientation of its neighbor base pairs. The Gibbs free energy change of DNA/DNA hybridization is then the sum of the Gibbs energy for the n dimer duplexes. It also includes an initiation contribution and a symmetry parameter:

$$\Delta G^{\circ}(total) = \sum_i n_i \Delta G^{\circ}(i) + \Delta G^{\circ}(init.\, G \cdot C) + \Delta G^{\circ}(init.\, A \cdot T) + \Delta G^{\circ}(sym.)$$

Equation 1.19

where $\Delta G°(i)$ is the Gibbs free energy change of 10 possible NN dimer duplexes (table 1.1), n_i is the number the occurrences of each NN dimer duplex, $\Delta G°(init.\ G \bullet C)$ and $\Delta G°(init.\ A \bullet T)$ are two additional parameters for the initiation of entire duplex formation depending on the starting

complementary base pair (AT or GC). $\Delta G°(sym)$ is 0.43 kcal/mol at 37 ℃ when the duplex is self-complementary and zero on the contrary.

The unified NN parameters from Table 1.1 are all obtained at 1 mol/L NaCl solution. $\Delta H°$ is assumed to be independent of sodium concentration. For the DNA/DNA hybridization occurring in different salt concentrations, two empirical equations are derived to correct Gibbs free energy and entropy change by salt concentration:

$$\Delta G^{\circ}_{total}([Na^+]) = \Delta G^{\circ}_{total}(1\ M\ Na^+) - 0.114 * N * ln[Na^+] \quad \text{Equation 1.20}$$

$$\Delta S^{\circ}([Na^+]) = \Delta S^{\circ}(1\ M\ Na^+) + 0.368 * N * l\,n[Na^+] \quad \text{Equation 1.21}$$

$\Delta G°_{total}$ *(1M* Na^+*)* and $\Delta S°([Na^+])$ are the Gibbs free energy and entropy change predicted by the NN parameters at 1 mol/L NaCl, *N* is the half of the total number of phosphate in the DNA duplex.

However, the predictions of thermodynamic parameters of DNA/DNA hybridization based on NN parameters also have some limitations. When the chain length of DNA sequences is more than 20, the thermodynamic information obtained by the NN parameters may be greatly different from those measured by the experiment. This is because the DNA/DNA hybridization reaction is not a typical two-state (as many intermediates are produced) and requires a more complex statistical model for accurate calculation. In addition, the prediction by NN parameters neglects the influence of external environments on hybridization, such as the temperature and the pH value of solution, which may cause a great difference between theoretical calculation and experimental results.

Furthermore, the nearest-neighbor model has mainly been developed for duplex formation in solution. Santalucia *et al* have tried to develop a model for hybridization on surfaces. However, along with the common parameters (pH, ionic strength, temperature…), some other parameters may influence duplex formation on solid support: the methods used to immobilize single strand DNA on solid support [9]–[11], the probe density [12], [13], the curvature of solid surface [14], [15] and the distance between the recognition part and the surface [16], which are described in section 1.2.4.

1.2 Methods for the measurements of dissociation constants

The methods employed for the determination of dissociation constant (K_d) can be classified as homogeneous *vs.* heterogeneous phase (solution *vs.* surface based) methods, or steady state *vs.* kinetic based methods. Herein, we have chosen to firstly introduce the methods carried out in solutions. After, we will mainly focus on surface based methods in particular optical methods. In this scope, we will discuss the different methodologies employed to determine the K_d, their advantages, limitations and experimental points that may influence the final results.

1.2.1 Solution based methods

Several different techniques are listed in Table 1.2. The main advantages and shortcomings are summarized. These techniques are either based on the measurements of the free ligands, free receptors and complexes or are based on the analysis of a given signal that can be indirectly related to the formation of the complexes. For example, fluorescence correlation spectroscopy measures the fluctuations of frequency and intensity of a fluorescent signal. The statistical analysis of these fluctuations by autocorrelation of the fluorescence intensity provides essential information about processes governing molecular dynamics. Fluorescence polarization anisotropy measures the rotation speed of molecules which is itself dependent on the gyration radius. Therefore, for example, the free fluorescent ligand will have a different rotation speed than when it combines with the receptor. Some of these techniques require either the ligand or the receptor to be labeled. Similarly to immobilization, the labeling of one of the partners may affect the overall affinity.

Among all the techniques, Isothermal Titration Calorimetry (ITC) is to date the gold standard for thermodynamic parameters measurements of biochemical reactions. In a calorimeter able to measure a sub millionth of a degree, the heat released or adsorbed by a biochemical reaction is measured. More precisely, the calorimeter measures the power needed to maintain the sample cell (where the reaction is performed) at the same temperature as in a reference cell. In the sample cell, increasing amount of one of the partners (in general the ligand) is added to a solution of a known concentration of the other partner until saturation is reached. The areas of heat peaks resulting from each injection are integrated and presented in the Wiseman plot [*Heat(*ΔH*) = f(molar ratio)*]. An appropriate binding model is chosen and the isotherm is fitted to yield the binding enthalpy ΔH, the K_d, and the stoichiometry. As a result, ΔG and ΔS can be calculated from the above data.

Method	Principle	Direct measurement	Separation	Stoichiometry	Rate constant	ΔH and ΔS	Real time	Single molecule resolution	High through-put	Intact cells	purification	Native Ligand	Consumption	Reference
Separation techniques[a]	Ligand and receptor are incubated. At equilibrium, complexes, free ligand and receptor are separated and quantified.	Y	Y	Y	Y	Y	N	N	N	Y	N	Y/ N	H	[17]–[30]
Fluorescence Polarization Anisotropy (FPA)	Fluorescence anisotropy can serve as reporter for ligand binding to protein. If the fluorophore is conjugated to a small ligand, the rate at which it tumbles can decrease dramatically upon bind to a large molecule, which providing the evidence for interaction.	N	N	Y	Y	Y	Y	N	Y	N	N	N	L	[31]–[34]
Fluorescence Correlation Spectroscopy (FCS) FCS in Polarization (FCSP)	Measure the temporal fluctuation of a fluorescent signal intensity in a given volume. These fluctuations can be correlated with the Brownian motion and therefore obtaining the diffusion rate of molecule. FCSP allows measuring the rotational diffusion.	N	N	N	Y	N	Y	Y	N	Y	N	N	L	[34]–[36]
Dynamic Light Scattering (DLS) Static Light Scattering (SLS)	Variation of the scattered light intensity (SLS) and its fluctuation (DLS) are measured. In SLS the scattered light is measured at many angle and variations can be related to the molecular weight. Similarly to FCS, DLS measures the fluctuation of scattered light at a given angle allowing to measure the diffusion rate.	N	N	Y	Y	Y	Y	N	N	Y	N	Y	H	[37]–[39]

Fluorescence Life Time	When a fluorophore is associated with another molecule, this may cause a change in the exited state life time.	N	N	N	Y	N	Y	N	N	Y	N	N	H	[40], [41]
Fluorescence Resonance Energy Transfer (FRET)	In FRET, light energy is absorbed by a first fluorophore (i.e, on the ligand) and transferred to a second dye (i.e.on the receptor). This later radiation is detected. This energy transfer can only occur if the two fluorescent dyes are within a sufficient proximity (Forster radius).	N	N	Y	Y	N	Y	N	Y	Y	N	N	L	[42]–[44]
Scintillation Proximity Assay (SPA)	In the SPA technique, the receptor is immobilized on a scintillation bead. The radio labelled ligand is the detected by scintillation only if it's close enough to the bead, in other words after its interaction with the receptor.	N	N	N	Y	N	Y	N	Y	N	N	N	L	[45]–[47]
Nuclear Magnetic Resonance (NMR)	NMR allows observing quantum mechanical magnetic properties of the atomic nucleus. The chemical shift varies among NMR-active nuclei(^{1}H, ^{13}C, etc), which is also related to its chemical surroundings.	Y	Y	Y	N	N	N	N	N	N	Y	Y/N	H	[48]–[50]
Mass spectroscopy	Thanks to the mass analyzer, the free ligand, free receptor and receptor/ligand complex can be titrated allowing for K_d determination. In general, mass spectrometry is used in conjunction with separation techniques.	Y	Y	Y	Y	Y	N	N	N	N	Y	Y	H	[51]–[53]
Isothermal Titration Calorimetry (ITC)	Measure the heat released from the reactions. Gold standard methods for K_d measurements.	N	N	Y	Y	Y	Y	N	N	N	N	Y	H	[54]–[62]

Table 1.2 Main methods for K_d determination. Adapted from [63]. By direct measurements, it is meant that the K_d is obtained by measuring the concentrations of the free ligand, the free receptor and the complex. On the contrary, indirect methods means that the concentrations are obtained indirectly by measuring, for example, the volume of molecules through complex models based on several assumptions. Separation stands for the fact that it is necessary to separate the complex from the free species. Native ligand or receptor means that they can be used without modifications. Real time, single molecule resolution, stoichiometry, rate constant, ΔH/ΔS, high throughput refer to capabilities measurement of the techniques. Purification concerns whether purified ligand or receptors should be used. Interact cells stands for the ability of the technique to be done in cellulo. ***Y = yes, N= No, L= Low, H= High****.*

[a] Separation techniques include dialysis, centrifugation, electrophoresis, thermophoresis, chromatography and etc.

1.2.2 Surface based methods

In surface based methods, the biochemical reaction is measured at a solid/liquid interface. One of the reactants is immobilized at the surface (probe, P) of a plain or structured substrate (described in 1.2.3 for immobilization techniques), while the other partner is free in solution (target, T). The interaction is then detected by optical means (surface plasmon resonance, fluorescence, interference…), by mechanical means (QCM) or electrical means (electrochemistry, field effect…). From the detected signal, K_d can be determined using either kinetic based methods or steady state methods. In the first case, real time measurements have to be operated. In the second case, measurements are done at equilibrium and real time measurements are not required. Furthermore, some detection techniques require specific labeling (fluorescent dye) or specific materials (i.e. metal for surface plasmon resonance) and consequently require specific surface coupling chemistry for the probe immobilization.

Surface methods have several advantages over solution methods and also some drawbacks. Among the advantages, surface based methods require generally less materials than solution based ones and are high throughput techniques. One of the main drawbacks is related to the fact that the probe is confined at the surface that may lead to kinetic issues [64] (i.e. mass transport issue), may influence the equilibrium state or lead to non-specific adsorption. Additionally, if the probe density is high, one target molecule may interact with several probes at the same time. Then the binding that is measured corresponds to the avidity instead of the affinity. The avidity is sum of affinities between the target and several probes.

In the following, regardless of the detection technique, we firstly described the theoretical basis underlying the kinetic and steady state measurements of K_d. We also discussed the experimental issues that can affect the measurements (mass transport limitation, surface chemistry, non-specific adsorption…) with a special focus on DNA/DNA hybridization. The introduction of our homemade SPR biosensor and commercial evanescent field fluorescence biosensor are given in chapter 3 and annex B, respectively.

1.2.2.1 Kinetic based methods

The kinetic based methods take advantage of real time measurements for determining the on and off rate constant of the biomolecular interactions at a solid/liquid interface. The target is repeatedly injected at concentration ranking from $K_d/10$ up to $10K_d$ and the association signal is recorded as a function of time. During each injection of target, the on-rate is recorded and then, the system is flushed with the buffer allowing for the off-rate determination. The sensor surface is then regenerated (if possible) and the cycle is repeated with a higher target concentration. The simplest model considers a one-step reaction:

$$P + T \leftrightarrow PT$$

Several assumptions are made in this model. Firstly, the only existing species are P (probe), T (target) and PT (probe-target complex). Therefore, any other reaction such as non-specific adsorption of the target is excluded. Also, the target should not interact with any other molecule in the medium and each target should react with only one probe at a time. Symmetrically, the probe should only be involved in the reaction with the target (for example no probe to probe interaction). Furthermore, every probe is considered equal and independent, so steric hindrance, charge repulsion, excluded volume, surface re-organization are neglected. Mass transport limitation should be avoided or kept negligible. Based on these assumptions, the increase of association signal as a function of time can be described by:

$$\frac{ds}{dt} = k_{on}c(s_{max}) - k_{off}\mathrm{s} \qquad \text{Equation 1.22}$$

where s is the signal measured, c is the concentration of the target at a given time, k_{on} and k_{off} are the on and off rate constants respectively. S_{max} is the maximum signal measured at saturation of all the probes. From these rates, the dissociation constant can be derived by:

$$K_d = \frac{k_{off}}{k_{on}} \qquad \text{Equation 1.23}$$

The association reaction can be fitted with a single exponential approach:

$$S_a(c,t) = S_{eq}(c)(1 - e^{-(t-t_0)/\tau}) \qquad \text{Equation 1.24}$$

with

$$\tau^{-1} = k_{on}c + k_{off} \qquad \text{Equation 1.25}$$

where S_a is the measured signal during the association phase, c is the concentration of T at the time t, S_{eq} is the signal predicted at equilibrium, t_0 is the initial starting time of injection and τ is the association timescale. Fitting the association phase data with Equation 1.24, the reciprocal of association timescale τ^{-1} can be obtained at each target concentration. The on rate constant k_{on} and off rate constant k_{off} are then obtained as the slop and intercept of the τ^{-1} *vs.* c plot (Equation 1.25).

For dissociation:

$$s_d\,(c,t) = s_a\,(c,t_c)e^{-k_{off}(t-t_c)} \qquad \text{Equation 1.26}$$

where t_c is the contact time between the target and the probe, S_a the signal at t_c and S_d the predicted signal at t upon dissociation. Therefore, the off rate constant k_{off} can also be estimated by fitting the dissociation phase with Equation 1.26.

According to Zhao *et al* [65], reliable fittings are achieved providing that no truncation of the data are performed due to the target injection or buffer change. However, as already mentioned, the above discussion are based on that all binding sites are equivalent. In case of surface heterogeneity, deviation from the model can be observed. To take this into account, an extended model has been proposed by Svitel *et al* [66], [67], Gorshokova *et al* [68] or Halperin *et al* [69].

The fitting can also be impaired by mass transport limitation; in this case a two-step model should be used. It includes a transport step of target from bulk to the surface and the reaction step:

$$T_0 \overset{k_{tr}}{\leftrightarrow} T + P \leftrightarrow \mathrm{TP}$$

where k_{tr} is a transport coefficient depending on the size and surrounding of the target. As a result, this two-step model can be depicted as:

$$\frac{ds}{dt} = k_{tr}c_0 - k_{tr}c - k_{on}c(s_{max}) + k_{off}s \qquad \text{Equation 1.27}$$

where c_0 is the target concentration in bulk, c the concentration close to surface.

1.2.2.2 Steady state methods

Steady state methods are alternative methods yielding the K_d. According to Zhao *et al* [65], these methods are more robust and reliable than kinetic methods in the sense that they are not affected by kinetic artefacts, such as mass transport limitations.

In steady state experiments, the probe modified surface is incubated with increasing concentration of target until equilibrium is reached. The S_{eq} corresponding to the signal measured at equilibrium is plotted as a function of the initial target concentration allowing constructing an isotherm. The target concentration should span below $K_d/10$ to well above $10K_d$. The equilibrium reaction can be described as previously:

$$P + T \leftrightarrow PT$$

The simplest model describing this reaction is the Langmuir isotherm. Similar assumptions are made as mentionned in section 1.2.2.1. Additionally, the Langmuir isotherm states that a

monolayer is formed at saturation; multilayers are not accepted in this model. Considering that the dissociation constant is described by:

$$K_d = \frac{[P][T]}{[PT]} \quad \text{Equation 1.28}$$

And, considering mass conservation, the target initial concentration can be expressed as:

$$C_T = [T] + [PT] \quad \text{Equation 1.29}$$

when [PT] is small compared with [T], then $C_T \approx [T]$. If X_{eq} is the fraction of probes that have reacted with the target at equilibrium, then:

$$\frac{X_{eq}}{1-X_{eq}} = \frac{C_T}{K_d} \quad \text{Equation 1.30}$$

And $X_{eq} = \frac{S_{eq}}{S_{max}}$, where S_{eq} is the signal measured at equilibrium for a given C_T and S_{max} is the signal observed at saturation. Therefore:

$$\frac{\frac{S_{eq}}{S_{max}}}{1-\frac{S_{eq}}{S_{max}}} = \frac{C_T}{K_d} \quad \text{Equation 1.31}$$

Equation 1.31 can be linearized leading to:

$$\frac{C_T}{S_{eq}} = \frac{1}{S_{max}} C_T + \frac{K_d}{S_{max}} \quad \text{Equation 1.32}$$

From this equation, K_d can be determined as the intercept at the y-axis. There is a detailed review illustrating different equations used to determine equilibrium constant [70], but the Equation 1.32 is the most used one.

In the Langmuir model, as mentioned above, several assumptions are made:

1. No formation of multilayer,
2. Each binding site behaves independently (no interaction between the sites, no steric hindrance…),
3. Measurements are done at equilibrium,
4. No interaction of the target with any other molecules than the probe. Symmetrically, no interaction of the probe with any other molecule than the target,
5. No non-specific adsorption of the target or the probe,

The original Langmuir model was designed for the adsorption of a gas. However, biomolecules in solution behave very differently than in a gas. For instance, the number of conformations that

are available to the target is higher in the solution phase than in the vicinity of the surface that behaves as an impenetrable wall.

1.2.2.3 Experimental factors influencing surface based methods

In practice, deviation from the Langmuir model can occur depending on the experimental conditions:

- The purity of the target solution. Depending on the origin of the sample, the target may be in the presence of several other molecules that can eventually lead to non-specific adsorption and to cross reactions with the target and/or the probe. Consequently, an apparent K_d will be measured [69]. For example, when using extracted dsDNA, after denaturation, two hybridization reactions take place: the target with the probe, and the target with its complementary sequence in solution. To take this into account, control experiment should be performed.
- In the Langmuir model, the target concentration variation is considered to be negligible upon interaction. One has to pay attention when the target to probe affinity is high.
- The surface probe dispersity. Herein, dispersity means that different states of the probe can coexist: probe interacting with the surface, with another probe or in different conformations (hairpin DNA). Similarly to the above point, this will lead to an apparent K_d as different equilibria are involved. Please note that when using small DNA probes, the number of possible configurations is not much influenced by the vicinity of the surface [69], [72].
- The coupling chemistry. The coupling chemistry employed for the immobilization of the probe to the substrate is not always site specific. The result is that sub-populations (dispersity) of immobilized probes may be created because of different orientations or conformations. It can also lead to different surface probe density.
- The surface probe density. The surface probe density is a key parameter as it can influence probe dispersity (orientation or lead to inter-probe interactions), steric hindrance or multivalent interactions. For example, as reviewed by Ravan *et al* [71], DNA probe can experience different regimes as a function of probe density. At low density, the DNA probe can lie flat on the substrate due to non-specific interaction (For example nucleobases interacting with gold). As the DNA probe surface density increases, the inter-probe distance approaches the DNA probe size and the DNA strands tend to stand up on the surface. At higher surface coverage, DNA strands have brush-like conformations. Some researchers [12], [13] have demonstrated that, as the surface density increases, hybridization nucleation sites become less available leading to lower hybridization rate. On the contrary, high surface density of immobilized carbohydrates can enhance their binding

to multivalent lectins through multivalent interactions providing that the in-plane separation between probes is smaller than the distance between binding sites of the lectins [72]–[74]. Similarly, long target DNA may hybridize with more than one probe.

- The surface topography. Surface roughness can influence the probe surface density and probe orientation. Here, we will focus on flat substrates of low roughness or/and porosity.
- The surface vicinity. As mentioned above, the vicinity of the surface as an impenetrable wall does reduce the number of accessible conformations by the target as well as the probe. However, in the case of low molecular weight molecules (oligonucleotide in the 20-mer range) this point can be neglected. Furthermore, due to the anchoring of the probe on the surface, the variation of entropy during the reaction is different than the one happening in solution. However, according to Halperin [69], this contribution can be neglected as far as $C_T >>$ [P]. On the contrary, Schmidt [75] and Hurst [76] claim that the surfaces tend to stabilize DNA/DNA duplex formation. Hybridization at the interface occurs in a specific microenvironment and the consequences of this fact are not clearly understood. For example, the surface will also induce a different ionic strength compared to the solution (diffusion double layer) and it can also influence the target or probe solvatation.
- The non-specific interactions. Non-specific adsorption will lead an apparent K_d. This can be circumvented using anti-fouling molecules such as Poly Ethylene Glycol or capping molecules such as Bovine Serum Albumin or Casein from dried milk. In some cases, the capping molecules can introduce artefacts. BSA, that is glycosylated, may interact with some lectins. Dried milk contains biotin that can interfere with subsequent streptavidin/biotin interactions. However, the cases of non-specific repulsion have also to be considered. For example, Buhot [77] have not only demonstrated that electrostatic repulsion between a target DNA and a probe DNA can false the results, but as the fraction of hybridized target increases, electrostatic repulsion increases also. Probe site are not identical anymore as the reaction progresses and Langmuir isotherm is not valid anymore.
- The experimental conditions under which the biochemical recognition is performed. Biomolecular interactions are very much dependent on the solution environment (temperature, pH, ionic strength of the buffer, surfactant). High ionic strength buffer reduces electrostatic repulsions whether they are specific or not. Similarly, surfactant can reduce van der Waals interactions. In section 1.2.4, we will focus on the parameters influencing DNA duplex formation that are reported in the literature.

These parameters are to be kept in mind when comparing various technologies for K_d measurements in particular when comparing different detection methods. Indeed, as the

substrates may be different, the grafting strategy will also be different. In the following section, we will focus on the coupling reaction of biomolecules on surfaces and how coupling reactions can influence the probe orientation, density and conformation especially for DNA probe on gold substrate.

1.2.3 Immobilization of biomolecules

Coupling reactions aim at the immobilization of the probe on to the substrate. The coupling reactions are traditionally classified into two categories: Non-covalent coupling and covalent coupling. The non-covalent coupling can be further divided into those based on the physisorption of the probe and those based on affinity binding. Physisorption immobilization takes advantage of van der Waals or columbic forces. Affinity coupling uses specific interaction such as avidin/biotin [78]–[80] or histidine/Ni^{2+} [81]–[84], protein G/antibody interactions [85]–[88]. In the following, we will briefly introduce non-covalent coupling including physisorption and affinity coupling. The affinity coupling is mainly based on avidin-biotin interaction. After, a focus on covalent coupling is given.

1.2.3.1 Non-covalent coupling

Two immobilization techniques without covalent bond are discussed in this section. One is based on physisorption. High molecular weight compounds usually provide strong adsorption [89], [90]. It is a convenient immobilization method because the surface usually doesn't need any chemical modification. In some cases, some proteins coverages achieved by physisorption are higher than those obtained by covalent binding, which indicates substantial affinity of proteins toward the surface [91]. Therefore, this technique has been widely applied for antibody adsorption in immunoassay [92], [93]. However, there are some potential drawbacks for physisorption over chemisorption, such as worse reproducibility of the adsorption process and potential protein denaturation upon adsorption [94], [95].

The other technique, affinity coupling, is based on specific biological interactions among which the most popular is probably the biotin-avidin (or streptavidine) interaction. This interaction is one of the strongest non-covalent interactions in the nature. Avidin is a basic tetrameric glycoprotein which consists of four identical subunits, each can bind to biotin with high specificity and affinity (K_d~10^{-15} M) [96], [97]. Therefore, it has been extensively utilized in probe immobilization. For example, biotin-DNA immobilization in chip and sensor-based bioassays, upon preconstruction of streptavidin films on the surface, are performed by this interaction [11], [98]–[100]. This affinity coupling is also reported in the field of carbohydrate microarray [101], [102].

1.2.3.2 Covalent coupling

For covalent coupling, prior to implementing the surface modification, the surface must be cleaned in order to allow the reactive function to come into contact with the material. These cleaning steps aim at removing particulate contamination, chemical contamination and eventually introduce reactive site on the substrate (for example silanols). In surface chemistry, most of the cleaning protocols are based on oxidative reagent, such as Standard Clean (SC) 1 and 2, piranha solution, O_2 plasma or ozonolysis. A review of cleaning procedures for all substrate is beyond the scope of this chapter and complete information can be found in *Handbook of cleaning in microelectronic manufacturing, Scrivener publishing-Wiley 2011*. However, it must be noted that these cleaning steps correspond to highly oxidative and harsh conditions that may lead to the roughening of the substrate, chemical leakage, oxidation of the substrate or eventually its degradation. In chapter 4 we will focus on the effect of cleaning protocol on gold substrates. A literature review about gold cleaning will be presented in this chapter 4.

On a clean substrate, the probe may be directly coupled to the substrate or alternatively, the substrate may need to be first modified with a cross linker. A cross linker is a molecule that possesses two reactive groups allowing it to react with both the substrate and the biological probe.

Let's first consider the reaction with the substrate. In table 1.3, different reactions with different substrates are listed. If the probe immobilized contains one of the chemical functions listed in table 1.3, then the probe can directly react with the substrate after cleaning.

Substrate	Glass/ SiO_x, SiN_x	Silicon	Nitrides (GaN, AlN)	Metals (Au, Cu, Ag, Pt)	GaAs	Metal Oxides (Ag, Au, Al)	Oxides (ITO, TiO_2, ZnO)
Methods	Silane	Hydrosilylation	Silane	Thiols	Thiols	Carboxylic acids	Phosphonic acids
Ref.	[9], [103]–[106]	[107]–[109]	[110]	[111]–[114]	[115]	[116]	[117], [118]

Table 1.3 Non-exhaustive list of reactions reported in the literature for coupling reaction as a function of the substrate material.

Once the substrate are modified with the cross linker, the newly introduced chemical functions are now available for the coupling with the biomolecules (the probe). Figure 1.2 illustrates some possible coupling reaction of biomolecules to surfaces.

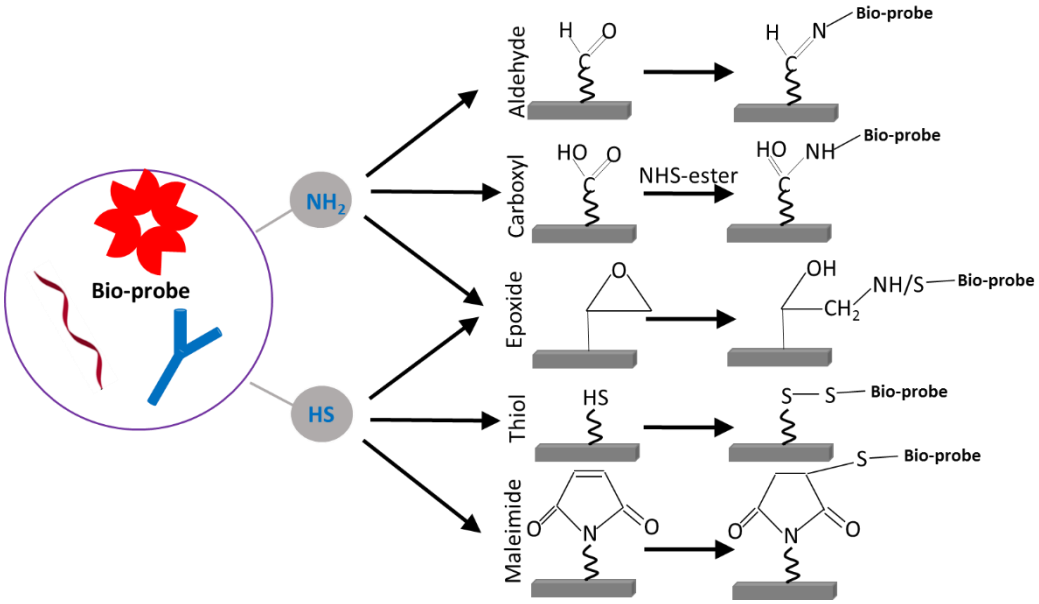

Figure 1.2 Different techniques used to couple the amino or thiol functionalized bio-probe on the solid supports

Reactions depicted in Figure 1.2 take advantage of free thiols or amines within the biomolecules for reactions with aldehyde, epoxyde, maleimide, etc. Before choosing one of the above reactions, one has to ensure that either a free thiol or a free amine is involved in the binding site of the probe.

Among all these reactions, coupling of amine to activated ester is one of the most widely reported ones and particularly the one based on *N*-hydroxysuccinimide esters (NHS esters). For protein, lysine has the highest reactivity among amino acids as the nitrogen doublet of the primary amine of its lateral chain is not involved in a mesomeric delocalisation. This can be advantageously used for an oriented immobilisation of the protein by introducing poly-lysine in the amino-acid sequence. For protein, it is often recommended to carry the coupling reaction with NHS esters under slightly acidic conditions (more precisely 1-2 pH unit below the iso-electric point) in order to favour electrostatic pre-concentration of the protein at the surface of the material (which is quite often negatively charged). Therefore, coupling reactions are mostly accomplished in acetate buffer pH=4.5. However, it must be mentioned that several authors underline the fact that under acidic condition the reaction rate is negligible due to the protonation of the amine [119], [120]. For amino-DNA, an alkyl amine linker has to be synthetically introduced at the 3' or 5' end. Due to the phosphate groups, DNA remains

negatively charged over a wide pH range. Therefore, the coupling reaction with the NHS esters is performed under pH ranging from 7.2 to 8.5 in order to favour amine deprotonation without over increasing the hydrolysis reaction of the NHS ester. Indeed, the half-life of NHS esters is 4 to 5 hours at pH=7.0 and 0°C, and drops to 10 minutes at pH=8.6 and 4°C. High ionic strength buffer can be an option in order to eventually reduce electrostatic repulsion among the immobilized probes allowing for increasing the surface densities [12].

Reactions based on thiol coupling take advantage of the addition reaction of thiol with π bonds. Also, its oxido-reduction properties allow the formation of disulphide bounds. Thiols are naturally present in some proteins via the cysteine amino acid, while they need to be introduced synthetically into DNA oligomer. Thiolated molecules can also form self-assembled monolayers on gold substrate without the need of crosslinker.

In the present PhD work, three kinds of substrates were considered: gold, glass and polystyrene. Therefore, amino-DNA was coupled to glass slides via NHS esters chemistry, while thiolated DNA was directly coupled on gold. For polystyrene, we adopted the physisorption of streptavidin serving as the cross linker. Then, the biotin-DNA was immobilized by streptavidin-biotin interaction. There are some detailed reviews illustrating these three chemical reactions [96], [113], [121]–[123].

1.2.3.3 Parameters influencing thiol chemistry on gold

Different authors have studied the effect of experimental conditions on the grafting of thiolated DNA to gold:

- Thiolated DNA concentration,
- pH of the buffer,
- Ionic strength of the immobilization buffer,
- Thiolated DNA/thiol-alkyl mixed monolayers

All these experimental conditions have been reported to influence the thiol-DNA conformation, orientation, surface organisation and density. Here, we shall also remind that there is an interplay among these parameters. For example, surface density influences DNA conformation (seen in section 1.2.2.3). Therefore, the experimental conditions influencing DNA probe surface density can also influence the probe conformation. A good agreement [12], [124] can be found in the literature on the effect of ionic strength on the thiol-DNA surface coverage. High ionic strength favours higher thiol-DNA coverage by lowering electrostatic repulsion. The effect of pH is less clear as some people claimed that alkaline condition is beneficial to the Au-S bond formation [125], while Peterson [12] claimed that pH had little effect on Au-S bond

formation. NHS-ester chemistry tend to lead to DNA probe surface densities in the 10^{12} probe/cm^2 range, while reaction of thiol-DNA on gold can lead to surface densities ranging from 10^{12} to $5*10^{13}$ probe/cm^2.

Furthermore, in order to limit non-specific absorption, mixed SAMs composed of the thiolated DNA and a thiol-alkyl (or other bio-inert molecules) are used. This can be performed in a one-step reaction using a mixture of thiolated DNA and thiol-alkyl or in a two-step reaction where the DNA is first immobilized on gold followed by an incubation of the resulting surface in a thiol-alkyl solution. In the first case, the DNA relative surface density is controlled by tuning the molar ratio of the two species in solution. It must be noted that the surface ratio may differ from that in solution [126]. In the second case, the DNA relative surface density is controlled by the dilution reaction, i.e. by the thiol-alkyl concentration, the reaction temperature and the reaction time. In general, the thiolated DNA concentrations are in the µmolar range (1-20 µM). Millimolar concentration of thiol-alkyl tend to decrease the DNA surface density by three orders of magnitude at room temperature [12], [127], [128]. There is a good agreement in the literature, that alkyl thiol adlayer backfill times below two hours tend to favour an upright orientation of immobilized DNA probe strand while longer backfill time lead to thiolated DNA removal and consequently to lower the surface density [13], [129]. The reorientation of the thiol DNA at short backfill time (less than 2 hours) is due to the disruption of the nucleobase/Au binding by the alkyl thiol adsorption on gold [13]. Indeed, it has been demonstrated that nucleobases, in particular A and G, tend to interact with gold. Therefore the conformation of DNA not only depends on the backfill time but also on the DNA sequence as poly A or poly G sequence can lead to strong interaction with gold surface [130], [131]. Finally some authors have mentioned that the presence of gold oxide can introduce island like structures and defects in monolayers [132].

In summary, DNA immobilisation experimental condition can affect the surface density, DNA conformation and orientation. We have seen in section 1.2.2.3 that these parameters can influence not only the hybridization kinetic but also the K_d determination. In the next section, we will address these parameters in the scope of DNA/DNA hybridization.

1.2.4 Parameters governing DNA/DNA duplex formation at solid/liquid interface.

In this section, the hybridization occurring between short single stranded DNA oligomers as the target (in large exess) and the probe in a simple buffer (Phosphate Buffer Saline, PBS) is discussed. In the following, we review some parameters influencing DNA/DNA hybridization yield at solid/liquid interface.

- Surface probe density

According to the literatures [11], [12], [15], [16], [127], [133]–[136], surface probe density is one of the most studied but also the most complicated parameter governing DNA hybridization, because its variation could affect other factors, such as probe orientation, conformation and charge density. Figure 1.3 presents the DNA hybridization efficiencies at different probe densities obtained from different research groups. These research groups used different methods to measure the hybridization efficiency (such as SPR, XPS, QCM, or AFM), different immobilization techniques of DNA probe and different experimental conditions for DNA hybridization. Therefore, even for similar surface probe density, the hybridization efficiencies obtained by these different groups vary. However, we can still observe a trend: as the surface probe density increases, DNA hybridization efficiency decreases. When the surface probe density is lower than 10^{13} molecules/cm^2, the hybridization efficiency is generally more than 50%, and can even reach 100%. However, when the surface probe density is higher than 10^{13} molecules/cm^2, the hybridization efficiency significantly drops and is generally lower than 50%. In addition, Peterson [12] and Su [11] used SPR to systematically study the effect of surface probe density on DNA hybridization. Peterson found that when the surface concentration increased from $2*10^{12}$ to $1.2*10^{13}$ molecules/cm^2, the hybridization efficiency decreased from 80% to 10% and the hybridization rate slowed down. The same phenomenon was observed by Su, when the surface density increased from $2*10^{12}$ to $6*10^{12}$ molecules/cm^2, the hybridization efficiency decreased from 100% to 50%. To conclude, a good agreement that a high DNA probe density has a negative influence on the hybridization efficiency is found in literature. This phenomenon could be due to a combination of some factors such as the influence on probe orientation, steric hindrance, decreased number of hybridization nucleation sites or increased surface charge density. In such cases, densely packed probes on the surface limit the insertion of DNA targets into the probe layer.

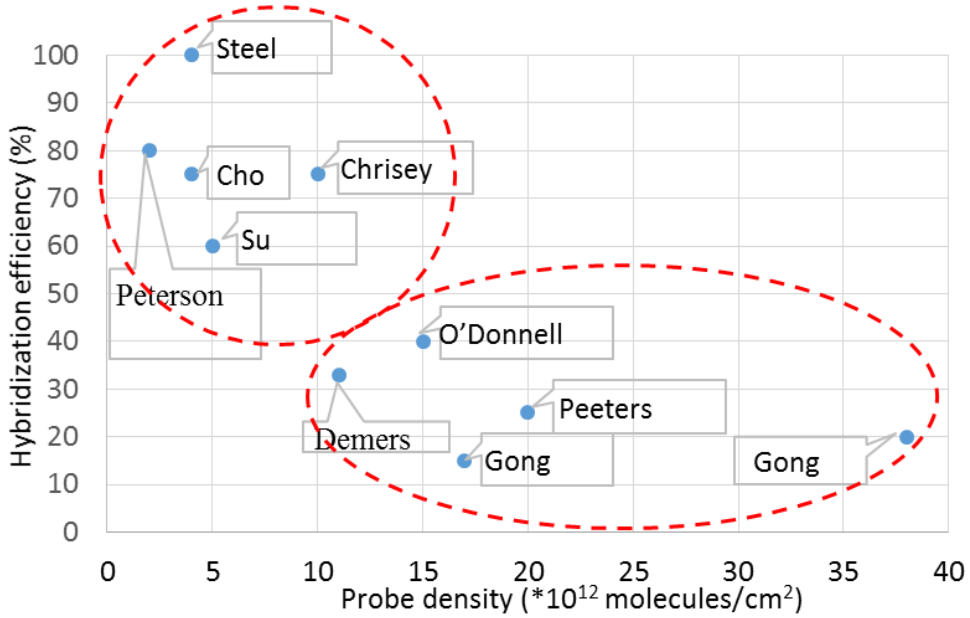

Figure 1.3 A review of the DNA hybridization efficiencies at different probe densities

- Spacer between DNA oligomer and surface (vicinity)

Spacers are usually introduced to reduce steric interference of the substrate on DNA/DNA hybridization behavior on solid/liquid interface. The hybridization yields have been found to increase up to two orders of magnitude by introducing spacers between the surface and the DNA sequence [137], [138]. In a systematic study on the influence of spacers on the hybridization [137], it has been proposed that at least 40 atoms in length is optimal for the hybridization of immobilized DNA. In this case, steric hindrance can be largely decreased. Furthermore, long spacer may provide better orientation of immobilized DNA, thus improves the sensitivity, the detection limit as well as the reproducibility of hybridization [16]. However, as mentioned in section 1.2.2.3, in the case of low molecular weight molecules (oligonucleotide in the 20-mer range), spacer doesn't have a marked effect on hybridization.

- Probe immobilization techniques

Different immobilization techniques can influence the probe orientation and surface density, which could influence the hybridization behavior on solid surfaces. For example, a well-ordered DNA monolayer and a randomly assembled DNA monolayer at similar probe density show a big difference on hybridization efficiency [11]. The well-ordered DNA monolayer shows a higher efficiency in target capturing than the randomly assembled one.

- DNA recognition surface structure

DNA recognition surface structure could influence configurational freedom and accessibility of probe DNA, thus affecting the hybridization behavior. The DNA recognition surface could be tailored by introducing different diluent molecules in mixed SAMs. For example, when diluent molecules are longer than the spacer between probe DNA and surface, it may increase the time taken to form a perfect duplex but have little impact on the initial nucleation [128]. This is attributed to the fact that long diluent molecules decrease the accessibility of probe.

- Probe conformation

Depending on the DNA sequence, self-hybridization may happen in DNA single-strands, resulting in secondary structures such as hairpins. This is more common in long-chain DNA sequences. The secondary structure reduces the number of nucleation sites during DNA hybridization and can greatly affect the rate of hybridization. In addition, complete hybridization requires an additional thermodynamic consumption for the melting of secondary structure, which can remarkably reduce the hybridization efficiency.

- Buffer ionic strength

Because DNA is negatively charged, a high ionic strength that can effectively screen electrostatic repulsion is beneficial to hybridization. It has been shown that, as the buffer ionic strength increases, both the hybridization efficiency and kinetic increase. In addition, applying an external voltage to the hybridization system can also effectively increase the hybridization efficiency and rate [139], [140]. Some researchers [141] experimentally revealed how an applied voltage on the gold surface influences the hybridization efficiency on surface. They found that, even at high probe densities (more than 10^{13} molecules/cm^2), increasing the applied voltage from 0 to +300 mV causes a three fold increase in the hybridization efficiency. On the contrary, with a negative voltage (-300 mV), the DNA hybridization efficiency drops from 10% (zero voltage) to 1%.

- Temperature, pH

High temperatures can destroy the hydrogen bonds formed by DNA hybridization between base pairs. Therefore, high temperatures are often used to denature DNA duplexes. Okahata [2] have investigated the influence of temperature on DNA hybridization on surface by SPR. They show that the association constant decreases with increasing temperature. It was simply explained by the increase of dissociation rate constants (k_{off}) while the association rate (k_{on}) remains constant. A high temperature speeds up the dissociation rate of the DNA duplex. Nevertheless, it should be noticed that, in the case of single-stranded DNA with secondary structure, a high temperature

melts the secondary structure of the DNA so that both hybridization efficiency and rate can increase. The pH value of the solution can influence the amount of negative charge on DNA probes, which may affect the hybridization behavior. For example, Zhang [3] demonstrated that, at high pH 8.5, the space between neighboring probe DNA strands was increased by higher electrostatic repulsive forces, resulting in a higher accessibility of DNA.

1.3 Objectives of the PhD thesis

The main goal of this thesis is to validate and optimize a surface plasmon resonance (SPR) system used to determine the DNA/DNA hybridization K_d on surface, and to compare it with two other surface based techniques: evanescent field fluorescence biosensor and fluorescent microarray. The determination of DNA/DNA hybridization K_d by these three techniques (i.e. endpoint or real time, direct or undirect, fluidic or static) can give us a better understanding of DNA hybridization on surface.

The first part of our work deals with validation and application of our homemade SPR system in the measurement of DNA/DNA hybridization. Then, we describe two cleaning processes for gold surfaces used in SPR biosensor. It has been reported that some oxidative cleaning treatment could produce gold oxides, which may influence the subsequent thiolated DNA immobilization. Therefore, it is important to investigate the properties of gold surface after cleaning and to develop an optimized process to obtain a surface free of gold oxides. For this, we compare two cleaning methods: piranha solution and oxygen plasma in terms of water wettability, roughness, cleanness, oxidation and subsequent thiolated DNA immobilization.

Next, we employed our homemade SPR system to measure DNA/DNA hybridization on surfaces. As illustrated before, the surface based hybridization can be influenced by many factors. Herein, we investigate the influence of interfacial design, ionic strength and secondary structure on the hybridization and try to find optimized SPR assay conditions for DNA/DNA hybridization.

Last, to get a quantitative insight into hybridization, K_ds are determined by SPR, evanescent field fluorescence and fluorescent microarray. These three techniques are compared in terms of operability and the quality of data obtained.

Chapter 2

Materials and methods

2 Materials and methods

This chapter presents main experimental materials and methods employed throughout this dissertation. This includes the materials and methods used for substrate cleaning (gold and glass surfaces), for DNA grafting on the substrate, for DNA/DNA hybridization measurements and for surface characterizations.

2.1 Materials

2.1.1 Chemicals and reagents

The following chemicals were used for DNA chip fabrication. Three different substrates were used: bare glass slides, gold coated glass slides and polystyrene substrates. Short names of DNA sequences are given into bracket.

✧ Probe DNA sequences (from Eurogentec):

- 5'-G**TG AGC CCA GAG GCA G**GG-$(CH_2)_7$-HS (Thiol-P_1)
- 5'-Cy3-**GCT AAT CCA ACG CGG** GCC AAT CCT T-$(CH_2)_7$-NH_2 (Amino-P_2-Cy3)
- 5'-**GCT AAT CCA ACG CGG** GCC AAT CCT T-$(CH_2)_7$-HS (Thiol-P_2)
- 5'-Cy5-**GCT AAT CCA ACG CGG** GCC AAT CCT T-$(CH_2)_7$-biotin (biotin-P_2-Cy5)

✧ DNA sequences used as a diluent molecule on gold surfaces (from Eurogentec):

- 5'-GCC AAT CCT T-$(CH_2)_7$-HS (diluent-P_2)
- 5'-TTT TTT TTT T-$(CH_2)_7$-HS (oligo-T)

✧ Target DNA sequences (from Eurogentec):

- 5'-**CTG CCT CTG GGC TCA** (T_1)
- 5'-**CCG CGT TGG ATT AGC** (T_2)
- 5'-Cy5-**CCG CGT TGG ATT AGC** (T_2-Cy5)

✧ Chemicals:

- Formic acid 99.9%, from Sigma-Aldrich
- Tetrahydrofuran (THF) 99.9%, from Sigma-Aldrich
- Dichloromethane (DCM) 99.5%, from Sigma-Aldrich
- Diisopropylcarbodiimide (DIC) 99%, from Sigma-Aldrich
- N-hydroxysuccinimide (NHS) 98%, from Sigma-Aldrich
- 1-ethyl-3-(3-dimethylaminopropyl)carbodiimide hydrochloride (EDC) 98%, from Sigma-Aldrich
- Phosphate-buffered saline (PBS) powder, from Sigma-Aldrich
- Sodium dodecyl sulfate (SDS), from Sigma-Aldrich
- Polyethylene glycol methyl ether thiol (PEG-SH) MW=2000, from Sigma-Aldrich
- 6-mercapto-1-hexanol 97% (MCH), from Sigma-Aldrich
- Bovine serum albumin (BSA), from Sigma-Aldrich
- Tert-butyl 11-[dimethylamino-(dimethyl)-silyl]-undecanoate (TDSUM) synthesized in our laboratory
- Tween 20, from Sigma-Aldrich
- Saline-sodium citrate (SSC), from Sigma-Aldrich
- Hellmanex III, from Hellma analytics
- Hydrogen peroxide solution in H_2O (35%), from Sigma-Aldrich
- Sulfuric acid (95-97%), from Merck
- Ammonium hydroxide solution (30-32%), from Sigma-Aldrich
- Hydrochloric acid (37%), from Chem-lab
- Buffered oxide etch (BOE): a mixture of 6/7 volume ratio of 40% NH_4F in water and 1/7 volume ratio of 49% HF in water

2.1.2 Substrates

- The glass slides (Nexterion glass D, Schott GMBH) featuring 40 microwells (as shown in Figure 2.1-a) were used as substrate for fluorescent microarrays. The fabrication of microwells on glass slides was achieved by xurography [142], which was done by others. The microwells were 3x3 mm^2 and between 65 and 100 µm deep.
- Nexterion glass D slides were also used as substrates for SPR experiments after gold coating. The glass slides were first cleaned by piranha solution, rinsed in DI water and immediately introduced inside a vacuum deposition chamber (Leybold) with a base pressure of 5.10^{-7} Torr. A 3 nm layer of chromium was first deposited as an adhesion layer (0.5Å/s) followed by a 47 nm film of gold (1-2 Å/s). Three specific areas were drawn on each slide using diamond knife as shown in Figure 2.1-b.
- The chips (Figure 2.1-c), used in evanescent filed fluorescence biosensor are made by injection molding of polystyrene. This polystyrene is similar to that used for ELISA microplates. The chips have two areas; the upper part is composed of eight wells where the reaction takes place. The lower part is an optical prism with a special design for evanescent field fluorescence biosensor.

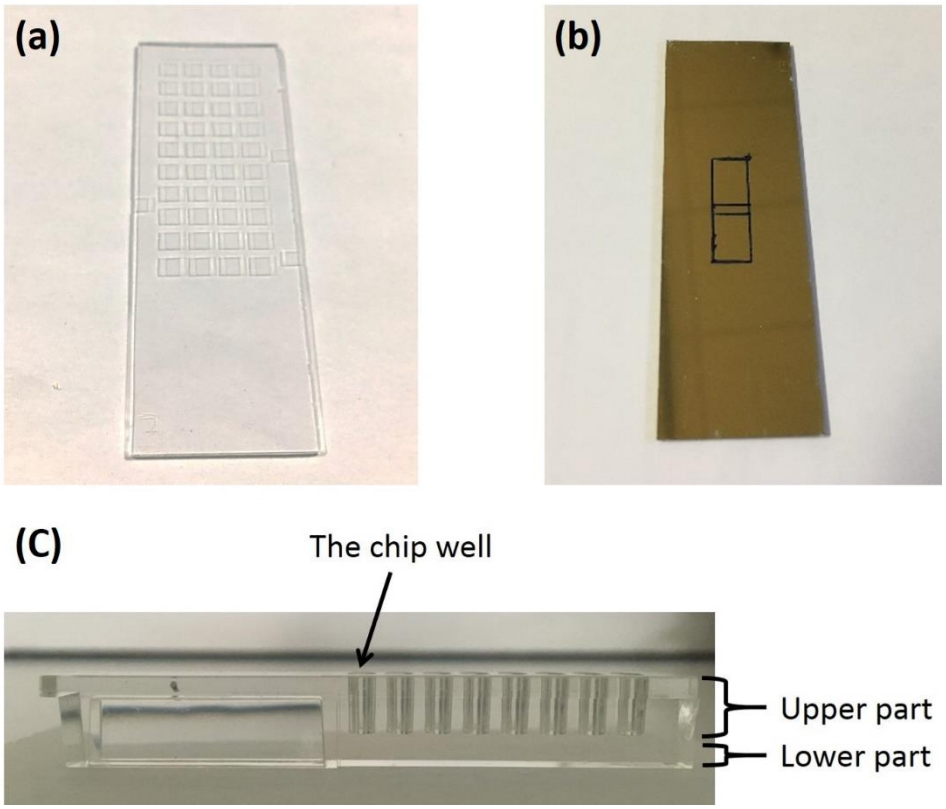

Figure 2.1 (a) Glass slide featuring 40 square wells (4x10), (b) Gold slide with three specified areas, (c) Polystyrene chip featuring 8 wells used in evanescent field fluorescence biosensor

2.2 Protocols

2.2.1 DNA fluorescent microarray fabrication and K_d measurements

The DNA microarray fabrication on glass slides can be divided into four steps:

1) Glass slide cleaning
2) Silanization and activation of carboxylic acid functions
3) Immobilization of probe amino-DNA via amide bond formations
4) DNA/DNA hybridization and K_d determination

The amino-DNA grafting on glass slides were carried out according to Figure 2.2.

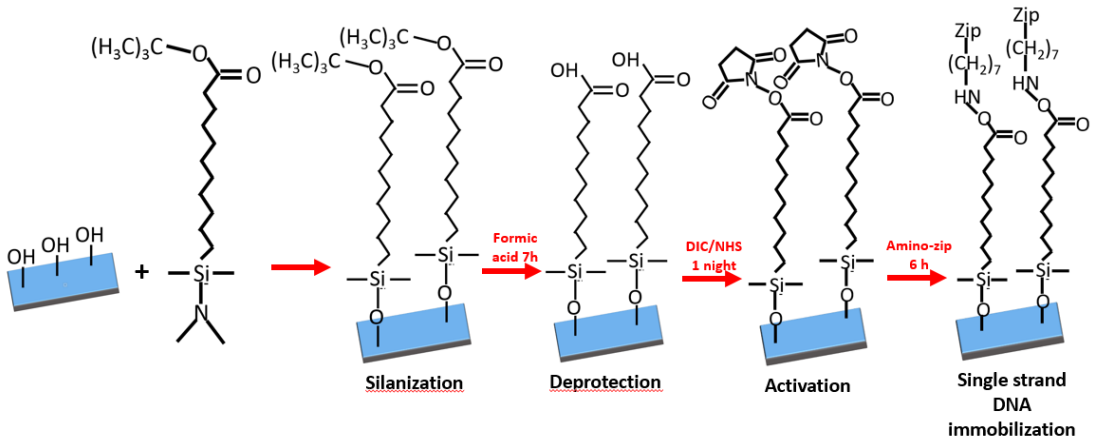

Figure 2.2 The grafting procedure of amino-DNA on glass slide

2.2.1.1 Glass slide cleaning

Freshly prepared glass slides as well as recycled ones were cleaned in an alkaline solution containing surfactants (0.5% solution of Hellmanex) overnight, rinsed with DI water and dried by centrifugation. Then, the slides were treated with piranha solution (1/3 H_2O_2 and 2/3 H_2SO_4) for 30 minutes in order to remove organic contaminants, rinsed with DI water and dried by centrifugation. Then, the slides were cleaned in ammonia hydrogen peroxide mixture (1/9 H_2O_2, 1/9 NH_4OH and 7/9 H_2O) for 1 hour at 80°C under agitation and dip for 3 min in an etching solution (1/7 HCl, 1/7 Buffered Oxide Etch and 5/7 H_2O). Finally, the slides were cleaned again with piranha solution at 180° for 30 minutes, rinsed and silanized.

2.2.1.2 Silanization and NHS activation of glass slide

The microstructured slides were functionalized by silanization with a gas-phase protocol described in a previous report [143]. Before silanization, the glass slide was heated at 150°C for 2 h under dry nitrogen. Then they were functionalized with vaporized TDSUM at 145°C for 12 h at a pressure between 10^{-1} and $4*10^{-1}$ mbar and washed with THF and DI water (10 min, ultrasound).

A de-protection step is required to convert tert-butyl ester into corresponding carboxyl group. The slides were immersed in formic acid for 7 h at room temperature, washed by DCM (10 min, ultrasound) and DI water (10 min, ultrasound).

NHS activation of carboxylic function for the covalent immobilization of amino-DNA was carried out as follow: the glass slides were immersed into the mixture of 3 g NHS (0.1 mol) and 4 ml DIC (0.15 mol) in 250 ml THF and allowed to react overnight under agitation at room temperature. Finally, the slides were rinsed by THF and DCM for 10 min respectively under sonication.

2.2.1.3 Immobilization of amino-DNA on glass slide

Amino-P_2-Cy3 solutions at four different concentrations of 50, 100, 500 and 1000 nM in PBS 10X (pH=8.5) were spotted into the microwells of NHS-activated slides with a *Scienion s3 micro-arrayer*, the spotting map is presented in Figure 2.3. There were 64 spots of corresponding amino-P_2 solution in each microwell, every spot contains 400 pL solution. In the upper twenty microwells, the amino-P_2-Cy3 solutions at 50 (top) and 100 nM (down) were spotted 32 times respectively, resulting in 32 repetitions of the same DNA spot. In the lower twenty microwells, the amino-P_2-Cy3 solution at 500 (top) and 1000 nM (down) were spotted 32 times respectively, resulting in 32 repetition of the same DNA spot.

The immobilization of amino-DNA is conducted by incubating the slide in a water-saturated atmosphere for 3 h, followed by a 3 h incubation in a dry atmosphere. Then, the slides are washed for 30 min at 70°C in a SDS solution (0.1%) and rinsed with DI water.

To avoid nonspecific adsorption of target DNA during hybridization, the slides, after immobilization, are incubated for 2 h with BSA at 4% in PBS 1X (pH=7.4). Then, the slides are washed three times in 0.05% Tween 20 in PBS 1X pH=7.4 (3 min) and three times in PBS 1X pH=7.4 (3 min) and rinsed with DI water.

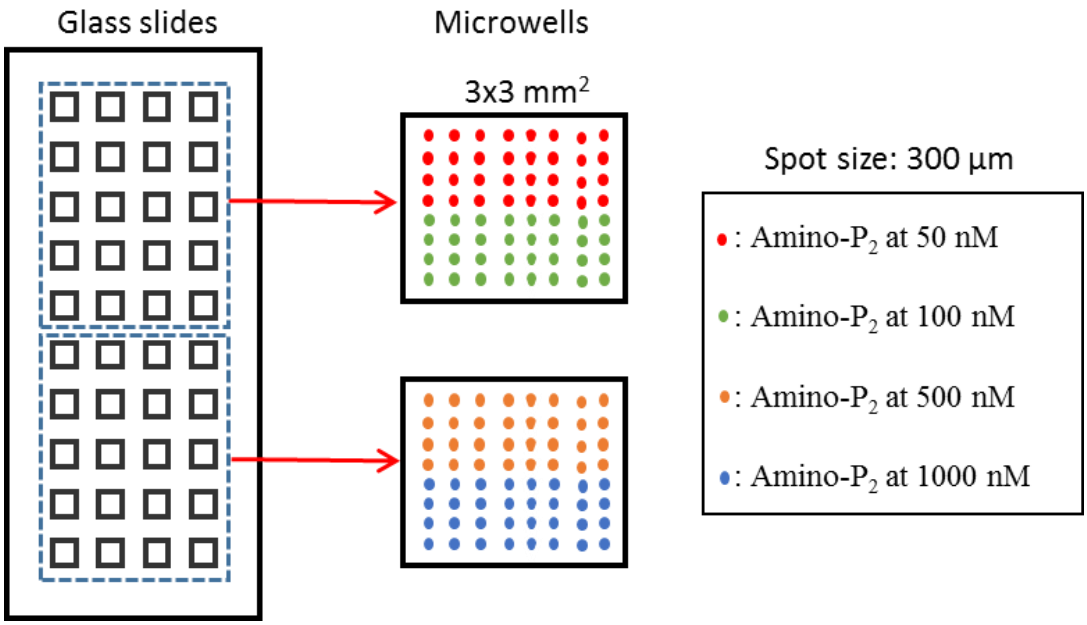

*Figure 2.3 Spotting map: in the upper 20 microwells, 50 and 100 nM amino-P_2-Cy3 solutions in PBS 10X (pH=8.5) were spotted 32 (4*8) times respectively; in the lower 20 microwells, 500 and 1000 nM amino-P_2-Cy3 solutions in PBS 10X (pH=8.5) were spotted 32 (4*8) times respectively. This results in 32 repetitions of the same DNA spot in each microwell.*

2.2.1.4 DNA/DNA hybridization and K_d determination

The T_2-Cy5 sequence, which hybridized specifically with P_2, was used for DNA/DNA hybridization K_d determination. T_2-Cy5 was diluted in PBS 5X (pH=7.2) with a pipetting robot (Tecan EVO100) in order to obtain 20 different final concentrations (see in table 2.1) in a range between 0.01 nM and 2000 nM. Each microwell was filled with 2 µL of one of the diluted solutions and incubated for 3 h at 25°C in a water-saturated atmosphere. Then, the slides were washed with PBS 1X at 50°C for 1 min, then with SSC 2X at room temperature for 5 min and rinsed with DI water for 20 s. Finally, the slides were scanned at 532 nm using a fluorescent scanner (Axon). Image analysis was performed using the Genepix 4100 A software package. The mean fluorescence signal was averaged over the 32 replications spots for each condition.

C-DNA-FI concentration (nM)
0.01, 0.1, 1, 5, 10, 20, 40, 60, 80, 100, 200, 350, 500, 750, 1000, 1200, 1400, 1600, 1800, 2000

Table 2.1 Concentrations of fluorescent labeled complementary-DNA solution

Isotherms were obtained by plotting fluorescence signal at 635 nm as a function of target DNA concentration. The K_d value was determined by linear regression equation (described in section 1.2.2.2):

$$\frac{[Target]}{FI} = \frac{[Target]}{FI_{max}} + \frac{K_d}{FI_{max}} \qquad \text{Equation 2.1}$$

FI represents the fluorescence signal measured at 635 nm due to the DNA/DNA hybridization at a given target DNA concentration (*[target]*) and FI_{max} the maximum fluorescence signal measured when saturation is reached.

2.2.2 Surface plasmon resonance biosensor chip fabrication and K_d measurements

Surface plasmon resonance (SPR) is a real-time technique which can provide kinetic and thermodynamic information on DNA/DNA hybridization. SPR measurements were performed on nexterion glass D coated with 3 nm Cr and 47 nm Au. The whole process can be divided into four steps:

1) Gold slides cleaning
2) DNA chip fabrication
3) Hybridization and regeneration experiments
4) K_d determination

2.2.2.1 Gold slides cleaning

Two different cleaning methods were compared: oxygen plasma cleaning and piranha solution cleaning. The detailed protocols are described in the following.

Oxygen plasma cleaning

The oxygen plasma cleaning was performed in an inductively coupled plasma cleaner (Harrick Plasma). Unless otherwise specified, the working parameters were: forward power = 38 W, oxygen flow = 14 ml/min, pressure = 85 Pa, time = 5 min.

Piranha solution cleaning

Gold coated glass slides were cleaned with a freshly prepared piranha solution (1/3 H_2O_2 and 2/3 H_2SO_4 heaed to approximately 170°C) for 5 min, followed by thorough rinsing with high-purity DI water and then dried by centrifugation.

2.2.2.2 DNA chip fabrication

In order to ensure good experimental repeatability, the gold slides were reused up to 5 times. The clean gold slides were modified with mixed SAMs, including DNA probes and diluent molecules, by two different methods as illustrated in Figure 2.4.

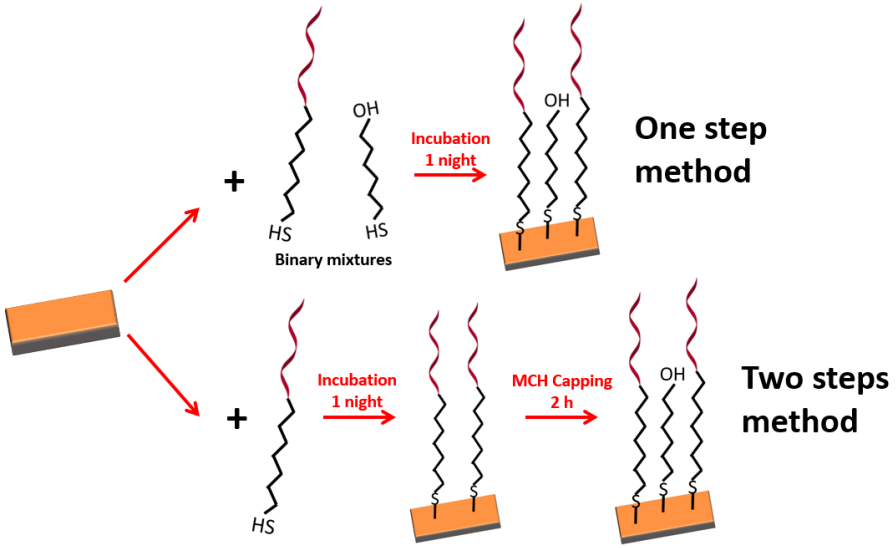

Figure 2.4 Two methods used to form mixed SAMs including thiol-DNA and diluent molecules (MCH) on gold slide

Using the two step method, DNA dilution and capping of the middle area are done in the same step which is very convenient for our SPR experiments. Firstly, 20 µl of 20 µM thiol-P_1 and 20 µM thiol-P_2 in PBS 10X (pH=5.5) are deposited respectively on areas 1 and 3 (as shown in Figure 2.5) of the gold slides and incubated overnight at room temperature in a water-saturated atmosphere. One of the two areas is used as the negative hybridization control. Then, the slides were rinsed successively with PBS 1X (pH=7.4) for 30 min at 70°C and DI water. Finally, 50 µl of 200 µM diluent molecule (MCH, PEG, diluent-P_2 or oligo-T) solution in PBS 10X (pH=5.5) is deposited on the whole reaction area for 2 h at room temperature in water-saturated atmosphere, rinsed with PBS 1X (pH=7.4) for 5 min and DI water for 20 s.

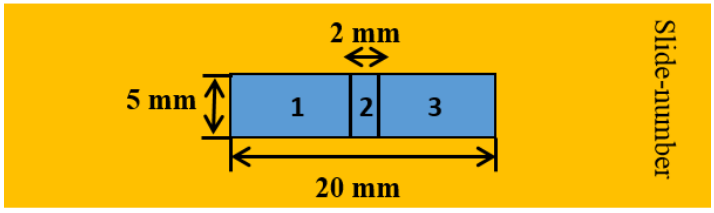

Figure 2.5 Gold slide and reaction areas.

2.2.2.3 Hybridization and regeneration experiments

All the hybridization reactions were done in a home-made SPR system, the configuration of which is described in chapter 3 in more detail. Since the DNA hybridization can be influenced by ionic strength, five different PBS concentrations were tested: PBS 1X, 2X, 5X, 8X or 10X, pH values vary from 7.1 to 7.4. The hybridization is performed by injecting 1 mL of 1 µM complementary-DNA solutions in these buffer solutions onto chips at 25℃. The following injection of the buffer solution without target DNA allows us to observe the dissociation process. The flow rate for experiments was fixed at 65 µL/min. For most experiments, repeated measurements were performed on the same DNA chip which requires a regeneration process. This was achieved using two 1 ml injections of 100 mM NaOH at 1 mL/min.

2.2.2.4 K_d determination

The K_d measurement of DNA/DNA hybridization was carried out by flowing 1 mL of different concentrations of target DNA solutions in PBS 5X (pH=7.2) at 25°C on the same DNA chip. The flow rate was fixed at 65 µL/min. The concentrations of target DNA solutions were 10 nM, 20 nM, 50 nM, 100 nM, 200 nM and 500 nM. The data were fitted with the Langmuir model applied in kinetic and steady-state methods respectively (described in section 1.2.2.1 and 1.2.2.2). All the data fittings are performed with Excel 2010 and Origin 8.0.

2.2.3 Evanescent field fluorescence biosensor chip fabrication and K_d measurements

Evanescent field fluorescence biosensor can monitor the fluorescence intensity emitted by the fluorophores bound on surfaces as a function of time (the principle is illustrated in Annex B). It can provide both kinetic and equilibrium information of DNA/DNA hybridization. The hybridizations were conducted on commercial polystyrene chips from Davos diagnostics (shown in Figure 2.1-c). The whole process of measurement can be divided into two steps:

1) Immobilization of biotin-DNA on polystyrene surface
2) DNA/DNA hybridization and K_d determination

2.2.3.1 Immobilization of biotin-DNA on polystyrene surface

The immobilization of biotin-DNA on polystyrene surface was carried out according to Figure 2.6.

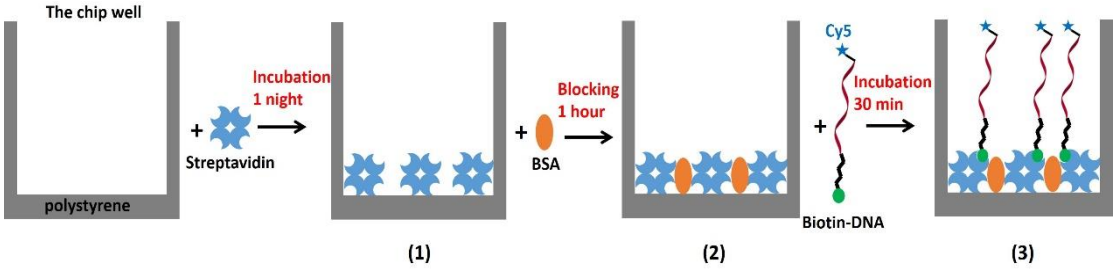

Figure 2.6 The immobilization of biotin-DNA on polystyrene surface

Each well was filled with 50 µL of a 10 mg/mL streptavidin solution in 0.1 M $NaHCO_3$ buffer (pH=9.3) – figure 2.6 step (1). Chips were incubated at room temperature overnight in a water-saturated atmosphere. The wells were then washed four times with PBS 1X solutions, rinsed by DI water and dried. After, 80 µL of blocking buffer (1% BSA and 0.25% Tween20 in PBS 1X) was added in each well and left to incubate for 1 h at room temperature – figure 2.6 step (2). Wells were washed four times with 1X PBS then four times with a sucrose solution (1% of volume ratio in pure water) and dried. Finally, 25 µL of 10 nM or 20 nM biotin-P_2-Cy5 solution in PBS 1X was added in each well and left to incubate at room temperature for 30 min –figure 2.6 step (3). During the incubation, the chip was inserted into the biosensor to monitor the fluorescence intensity emitted by the Cy5 from surface-bound DNA as a function of time. After incubation, non-reacted biotin-DNA solutions were pipetted off. 40 µL of 4% BSA in PBS 1X was added in each well and incubated for 30 min. Wells were washed three times with 40 µL of PBS 1X, then three times with 40 µL of DI water. After this step, chips could be stored for two weeks at -4°C for further DNA/DNA hybridization.

2.2.3.2 DNA/DNA hybridization and K_d determination

All the hybridization reactions measured by evanescent field fluorescence biosensor (Davos diagnostics) were conducted as follow. 50 µL of different concentrations of T_2-Cy5 solutions in PBS 5X (pH=7.2) were added in the different wells. After adding each solution at different concentrations, the chip was immediately inserted into the reader and measured for 15 min. For K_d measurements, the concentrations of T_2-Cy5 solutions used were 10 nM, 20 nM, 50 nM, 100 nM, 200 nM and 500 nM. The real-time monitoring data were fitted with a Langmuir model applied in kinetic and steady-state methods respectively (described in section 1.2.2.1 and 1.2.2.2). All the data fittings are performed with Excel 2010 and Origin 8.0.

2.2.4 Surface characterization

Contact Angle (CA) measurement, AFM, XPS and PM-IRRAS were mainly used to determine the gold surface wettability, topography, oxidation state and modifications. The principles of these surface characterization techniques can be found in Annex A.

2.2.4.1 Contact angle measurement

A 1 µL water droplet was used in all measurements. The contact angles were measured right after deposition using WinDrop software from GBX. At least three different areas were measured and averaged to get a reliable value for each sample.

2.2.4.2 AFM

The Atomic Force Microscope (AFM) used is a Di CP-II Veeco Instruments SPM Scanner. The tip generally used is a Brucker model RTESPA-300 Si-doped antimony tip. It is based on a cantilever 3.4 µm in height, 125 µm in length, the tip diameter is less than or equal to 10 nm. Topography and phase images were taken in air, at room temperature, using tapping mode. The data analysis was performed with Proscan software.

2.2.4.3 XPS

All X-ray Photoelectron Spectroscopy (XPS) spectra were recorded in a Vacuum Science Workshop (VSW) chamber equipped with a monochromatized X-ray source (AlK_a = 1486.6eV). Take-off angle was set to 90 °. The spectral resolution for all the scans was 0.1 eV and the spectra was the result of several scans (usually 3 to 10). XPS spectra was baseline corrected using a Shirley background subtraction and the peaks were fitted using Gaussian-Lorentzian peak shape (30%). Spectra analysis was carried out with CasaXPS and origin 8.0. Full widths at half maximum (fwhm) for Au 4f peak was constrained to be 0.9 eV.

2.2.4.4 PM-IRRAS

The substrates used in Polarization-Modulation Infrared Reflection Adsorption Spectroscopy (PM-IRRAS) are glass slides coated with 3 nm Cr and 200 nm Au. The PM-IRRAS spectra were recorded with a Nicolet 6700 Fourier-Transform Infrared (FTIR) spectrometer coupled to a tabletop optical module (TOM box). Polarization modulation is done using a photoelastic modulator (ZnSe cristal, Hinds Instruments) operated at 50 kHz and a synchronous sampling demodulator (GWC Instruments). The optical signal is measured using a MCT-A detector (ThermoElectron Scientific). All spectra were acquired at ambient temperature at resolution of 4 cm^{-1} and were the result of 512 scans with a full spectral range of 4000-800 cm^{-1}. In order to obtain optimum signal and sensitivity on gold, the angle of incidence is 82.5º. Further analysis on the spectra were performed with TQ analyst and Origin 8.0 software.

Chapter 3

Introduction to our homemade SPR biosensor

3 Introduction to our homemade SPR biosensor

3.1 Introduction

SPR method is now one of the leading analysis technologies for characterizing and quantifying molecular interactions; it is widely used in biology, medicine, chemistry and other fields. Owing to its unique advantages, it has become a conventional method for the detection of receptor/ligand interactions, antibody/antigen interactions or drug screening... It can measure the dynamic adsorption process of biological molecules on surfaces in-situ and in real-time. It has a quite high sensitivity, and does not need to label the sample.

The first documented observation of Surface Plasmons (SP) dated back to 1902, when Wood noticed a narrow black band in the spectrum of the white light diffracted by a metallic grating [144]. Later, in the year 1968, Kretschmann [145] and Otto [146] proposed simple methods for the optical excitation of SP using the Attenuated Total Reflectance (ATR) method, which are still used in most current SPR analysis instrument. Biomolecular interactions measurement by SPR started in the year of 1982 when Nylander and Liedberg first applied it for gas detection [147] and biosensing [148]. Today, the application of SPR biosensors has expanded a lot and several commercial instruments are available. Pharmacia Biosensor AB company (became BIAcore AB in 1996) developed the world's first commercial SPR device during 1989-90 and have dominated the market since then. It is still the ''golden standard'' for measuring real-time biomolecular interactions.

3.2 Physics of SPR sensor

3.2.1 Plasmons

Plasmons can be defined as a quantum for the collective oscillation of free electrons (the term refers to their plasma-like behavior). Different types of plasmons can be excited in metallic objects: volume plasmons in bulk metals, surface plasmon polaritons at the interface between metals and dielectrics, localized surface plasmons in nanoparticles...

- Volume plasmon

For volume plasmons, the resonant oscillation of the charge density occurs at the plasma frequency of the metal ω_p. Above ω_p, electric fields can penetrate into the matter which becomes transparent to radiation. Volume plasmons are longitudinal waves (the wavevector is parallel

to the electric field) and therefore can not be excited by light but by particle impact. For example, they can induce energy losses of $\hbar\omega_p$ (~10 eV) in electron-energy-loss spectra [149]. The plasma frequency ω_p depends mainly on the electron density and is given by:

$$\omega_p = \left(\frac{ne^2}{m\varepsilon_0}\right)^{1/2} \qquad \text{Equation 3.1}$$

where n is the free electron density, e and m their charge and effective mass, and ε_0 the vacuum permittivity. For gold, the plasma frequency is $1.37*10^{16}$ rad.s^{-1} and corresponds to a wavelength of ~140 nm. Considering only free electrons (Drude's model), the relative permittivity of a lossless metal is real and can be written:

$$\varepsilon_m = 1 - \left(\frac{\omega_p}{\omega}\right)^2 \qquad \text{Equation 3.2}$$

where ω is the angular frequency of the incident radiation. Lossless Drude's metals have negative permittivities for $\omega < \omega_p$ and their absolute values increase with the wavelength exceeding the values found in dielectrics.

- Surface plasmon

The surface plasmons are a collective excitation of free electrons that can exist at the interface between two materials. It is similar to the volume plasmon, but the coherent oscillation of free electrons is confined at the metallic surface. This electron plasma oscillation creates an electromagnetic field (as depicted in Figure 3.1) that decays exponentially into both media with typical decay lengths of a few tens of nanometers in the metal and up to several hundreds of nanometers in the dielectric.

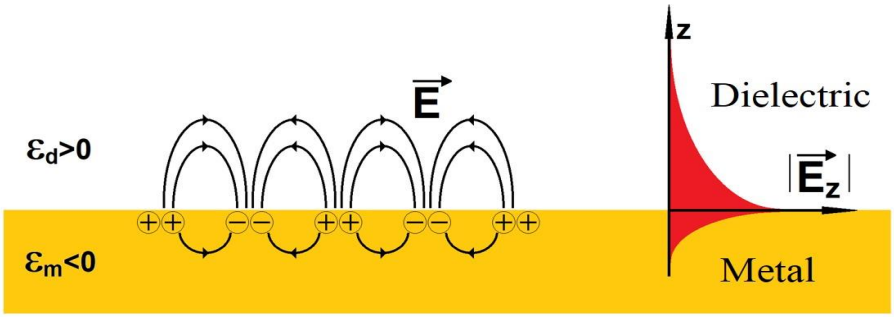

Figure 3.1 Collective oscillation of electrons at the boundary of two media (surface plasmon waves)

Using Maxwell's equations with the proper boundary conditions give us some conditions for the existence of a surface wave at a planar metal/dielectric interface: i) there is no solution for transverse electric (TE) surface modes, ii) for transverse magnetic (TM) modes, the conditions for SP existence are:

$$\varepsilon_d \varepsilon_m < 0 \text{ (existence)} \qquad \text{Equation 3.3}$$

$$\varepsilon_d + \varepsilon_m < 0 \text{ (propagation)} \qquad \text{Equation 3.4}$$

which imply that one of the dielectric functions must be negative with an absolute value exceeding that of the other. Noble metals (ex. gold and silver) have a large negative real part of the dielectric constant and a small imaginary part. Therefore, surface plasmon can exist at their interface with a dielectric such as glass or air. This analysis also gives the dispersion relation for surface plasmon:

$$k_{sp} = \omega/c \, [\varepsilon_m \varepsilon_d/(\varepsilon_m + \varepsilon_d)]^{1/2} \qquad \text{Equation 3.5}$$

where ε_m and ε_d are the dielectric constants of the metal and the dielectric medium outside the metal respectively, c is the light propagation velocity in vacuum. Using the relative permittivity ε_m of Equation 3.2 for a metal, the Equation 3.5 becomes:

$$k_{sp} = \omega/c[\frac{\varepsilon_d(\omega^2-\omega_p^2)}{\omega^2(1+\varepsilon_d)-\omega_p^2}]^{1/2} \qquad \text{Equation 3.6}$$

We can compare this dispersion relation with the one for light incident to a surface with an angle θ, for which the wave vector parallel to the surface is:

$$k_x = \frac{\omega}{c} \varepsilon_d^{1/2} \sin\theta \qquad \text{Equation 3.7}$$

We can see that k_x is always less than k_{sp} if the absolute value of ε_m is not superior to ε_d, so surface plasmon cannot be excited by simply illuminating the surface.

3.2.2 Excitation of surface plasmon

The wave-number of a surface plasmon is higher than the wave-number in the dielectric so the light incident at an insulator/metal interface cannot excite them as illustrated in Figure 3.2. It would be necessary to increase the wave-number of the light so that the wave-vectors in both materials could be matched.

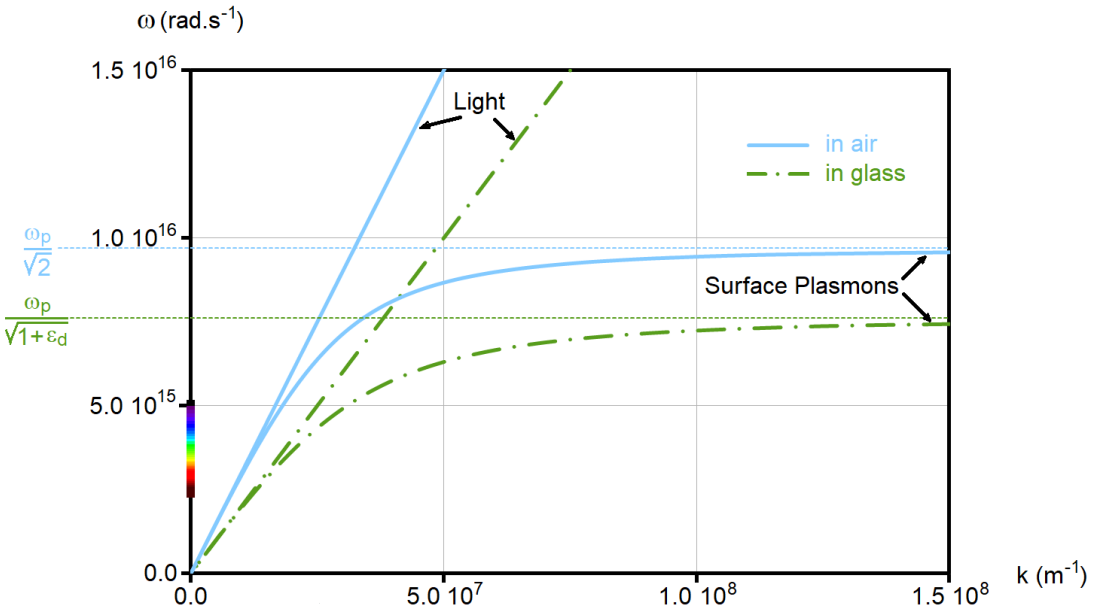

*Figure 3.2 Dispersion relation of surface plasmon (Equation 3.6) and light (Equation 3.7) at the interface of gold and air or glass, calculated with ε_{air}=1.0, ε_{glass}=2.25 (BK7) and ε_{gold} according to Equation 3.2 with ω_p=1.37*10^{16} rad.s^{-1}.*

It can be seen on Figure 3.2 that light incident on the glass/metal interface can coupled to the surface plasmon at the air/metal interface. This leads to two common approaches to excite surface plasmons using two configurations introduced by Kretschmann [145] and Otto [146]. They are illustrated in Figure 3.3.

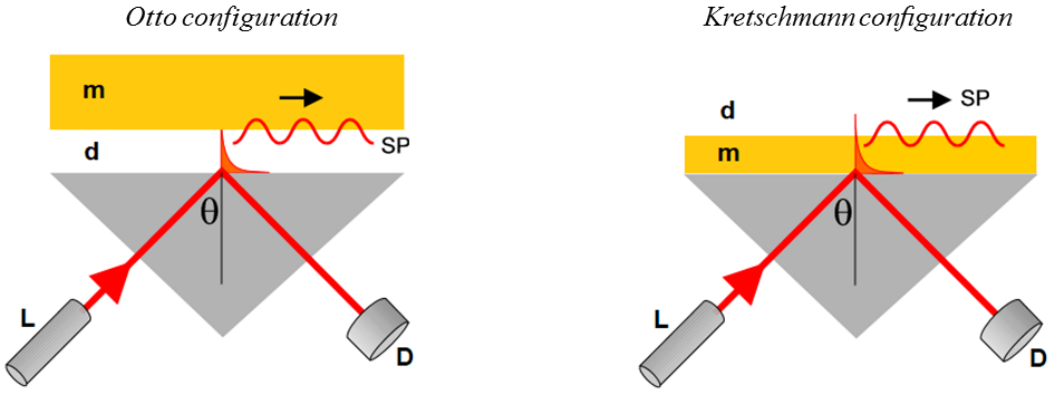

Figure 3.3 Excitation of surface plasmons (SP) in the Otto (left) and Kretschmann (right) configuration; L: light source, D: detector, m: metal layer, d: dielectric.

In Otto geometry, the light wave is incident on a high refractive index prism/dielectric film (air, water...) interface at an angle of incidence larger than the critical angle. It produces an evanescent wave that propagates along the prism/dielectric interface and can be coupled to

surface plasmon if its propagation constant is equal to that of the surface plasmon. In the Otto configuration, the metal thickness can be semi-infinite but the dielectric layer thickness must be controlled precisely (typically to a few micrometers).

The Kretschmann configuration is more convenient to use. A high refractive index prism is coated with a thin metal film and interfaced with a dielectric medium which thickness can be semi-infinite. The light wave propagates inside the prism and is incident on the metal film where it is reflected back into the prism. A part of the light wave propagates in the metal in the form of an evanescent wave that decays exponentially in the direction perpendicular to the prism/metal interface. If the metal film thickness is thin enough (about 50 nm), the evanescent wave can couple with a surface plasmon at the metal/dielectric interface.

Most SPR systems reported in the literature use prism couplers, while there still other methods of excitation, like grating or waveguide couplers, that are often used in miniaturized systems. The prism coupling in the Kretschmann configuration is very convenient and only needs simple optical elements and is therefore the method we have chosen for our experimental setup.

3.2.3 Surface plasmon resonance as a sensor

As mentioned before, surface plasmons are excited at the interface between a metal layer and a dielectric medium which is the sensing medium. Any change in the refractive index of this medium induces a modification of the propagation constant of the surface plasmon and therefore modifies the coupling condition between the light wave and the surface plasmon. If it occurs close enough to the gold surface (in the field of the surface plasmon), it can be detected by measuring the conditions of resonant excitation. Depending on which characteristic of the reflected light is measured, we can distinguish several types of SPR sensors that are based on 1) angular modulation, 2) wavelength modulation, 3) intensity modulation, 4) phase modulation and 5) polarization modulation. The first three types are the most common and illustrated in Figure 3.4.

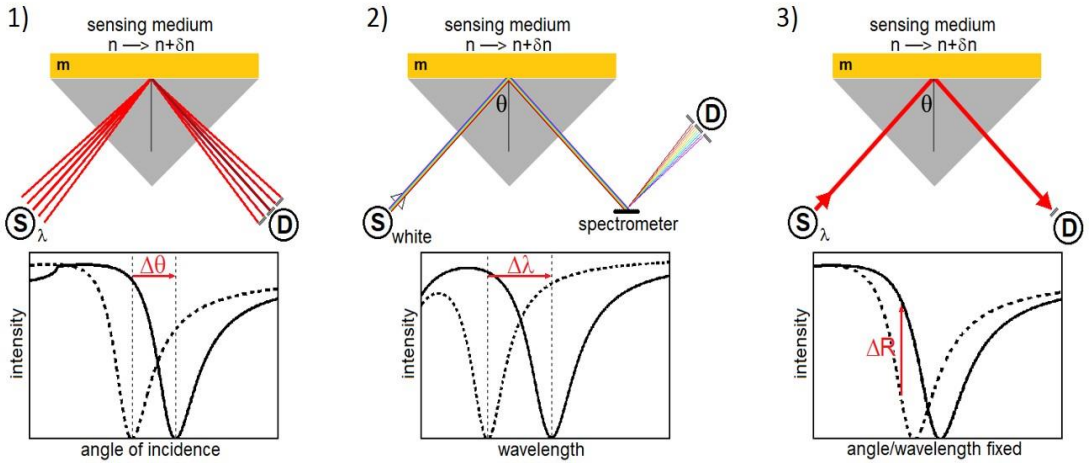

Figure 3.4 Illustration of SPR sensors based on (from left to right) angular (1), wavelength (2) and intensity modulation (3).

Measuring the variation of the reflected monochromatic light at fixed angle (Figure 3.4-3) seems an attractive solution to build a SPR biosensor and is often used in 2D imaging systems. However, as no angular or wavelength scan is done, the signal is quite sensitive to the source and detector noise and the dynamic range is limited to the linear part of the SPR curve. Angular (Figure 3.4-1) and wavelength (Figure 3.4-2) scanning systems are also convenient and the former does not need any spectrometer but only a goniometric stage. Since a light emitting diode, a rotation stage and a photo-diode are enough to perform angular scanning SPR experiment, a more elegant way to do is to use wedge-shaped beam of light and a photodiode array, getting rid of any moving part. Since the first report on SPR sensor using a coupling prism and angular modulation by Matsubara [150], this type of sensor has been improved and commercialized by several manufacturers (including Biacore AB). The homemade SPR device we built and used is a wedge-shaped beam system based on angular modulation.

3.3 Instrumentation of our homemade SPR system

There are four essential units composing our SPR device: optics, temperature control, liquid handling unit and sensor chip. It is depicted schematically in Figure 3.5 a. An intensity dip in the reflected light due to SPR can be detected by CCD camera. The angular position of this dip depends on the refractive index of the medium in the immediate vicinity of the sensor chip surface. During the adsorption of molecules on the sensor surface, the refractive index at the sensor chip surface changes, resulting in a shift of dip position. This shift is observed in real time, as shown in the sensorgram in the Figure 3.5 b.

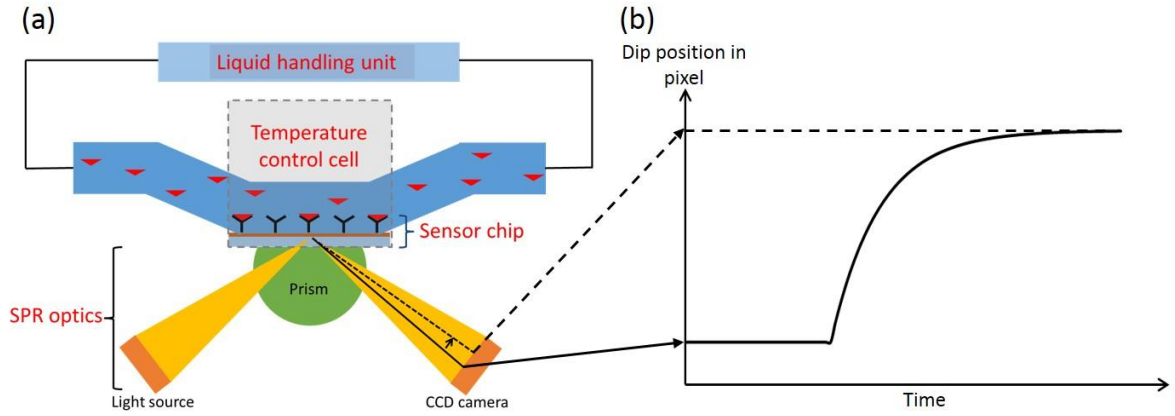

Figure 3.5 (a) Schematic view of the four main units of our SPR instrument: 1, SPR optics; 2, liquid handling unit; 3, temperature control cell; 4, sensor chip. The biomolecular interaction takes place in the temperature control cell on the sensor chip. (b) The sensorgram by plotting the position of the SPR dip vs. time.

3.3.1 SPR optics

A wedge-shaped beam system based on angular modulation was chosen in the SPR optics. The schematic view of that is illustrated in Figure 3.6. A far-red Light Emitting Diode (LED) with a nominal wavelength of 740 nm and 22 nm spectral half width is coupled to a multimode fiber (Ø=400 µm, 0.39 NA). This light source is collimated using a spherical lens (75 mm focal length) into a 1 inch diameter beam. The beam passes through a bandpass filter (740 nm, 10 nm FWHM) followed by a film polarizer. A plano-convex round cylindrical lens (75 mm focal length) focalizes the beam into a line through a hemi-cylindrical coupling prism (BK7 glass, n=1.512). The internally reflected beam is collimated again using a spherical lens (75 mm focal length) and followed by a second plano-convex round cylindrical lens, then directed to the CCD camera.

Both optical arms (illumination arm and detection arm) are mounted on linear translation stages fixed on rotation stages and the prism holder height can also be adjusted. The reflected beam is captured on a CCD camera (Stingray F-201B from Allied Optic) which resolution is 1624x1234 pixels (cell size: 4.4 µm). The signal is digitized with a 14 Bit ADC at a frame rate of 14 fps. A software developed with LabVIEW (National Instruments) is used to analyze and log the data. The CCD camera images can be defined up to five areas, each of them yields an angular reflectivity pattern. An analysis algorithm extracts these defined areas and averages the ranges of rows. This yields the plots of reflected intensities versus (angular) CCD pixels before analyzing their distributions. The pixel of minimum (i.e. the dip position) can be calculated from the angular distribution of each area using different algorithms. We have used the common

centroid method with basic threshold value (typically about half of the dip height) and the polynomial fitting method limited to a portion determined by the inflexion points of the curve. Both methods have shown similar performances in our system but the algorithms were sensitive to the shape of the curve. Due to noise and imperfections in the SPR device, the portion of the curve determined according to a threshold value or to the inflexion positions may change. This leads to intermittent baseline shifts that are prejudicial to a proper sensorgram analysis. In the end we have decided to stick with the solution of using a low reflectivity threshold (1/10 of the dip height) then fitting a polynomial (order 3) to this portion and subsequently calculating the minimum of the polynomial.

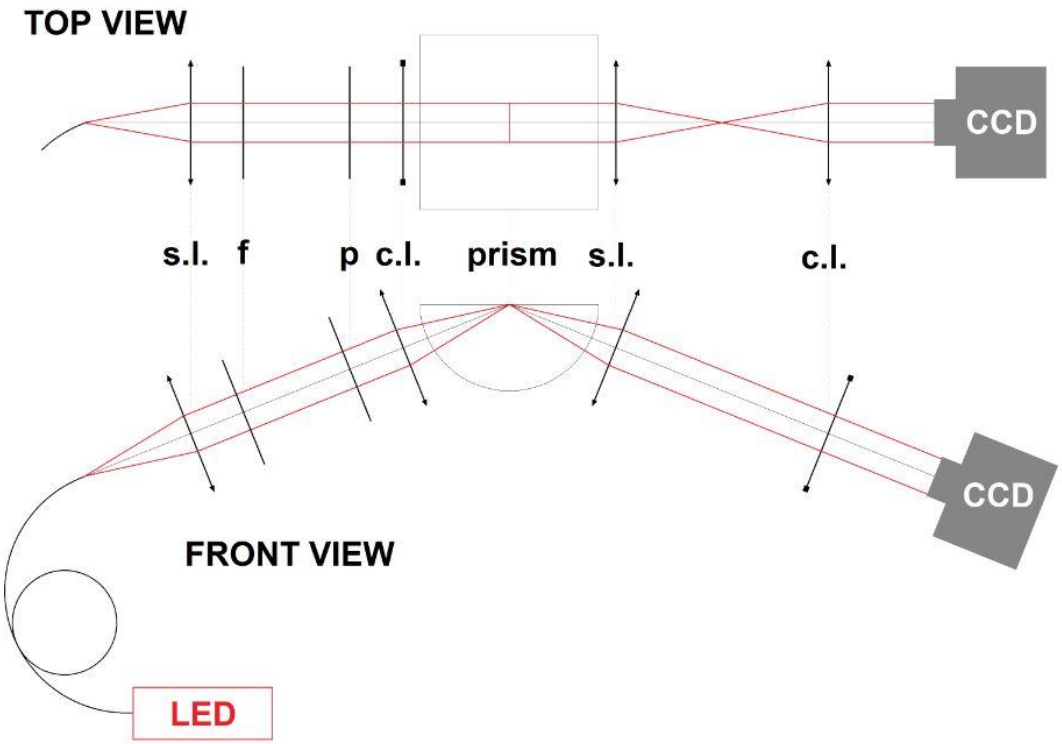

Figure 3.6 Schematic view of SPR optics. s.l.: spherical lens; c.l.: cylindrical lens; f: bandpass filter; p: polarizer.

3.3.2 Temperature control and liquid handling system

The configuration of the temperature control system is illustrated in Figure 3.7. Gold coated glass slides (sensor chips) are stuck into the prism using a refractive index matching liquid (Cargille Labs, n=1.515). The cell for biomolecular reactions is defined by a 1 mm thick sheet of fluoroelastomer (the height can be changed) that was milled to form a 10 mm long and 1.5 mm wide hollow channel in the middle. This sealing sheet is simply deposited on the gold coated slides and covered by a flat teflon piece (cell upper cap) that contains the fluid inlet and outlet channels. The cell volume is 15 µl and can be lowered using a thinner sealing sheet. The

system is fully enclosed into a copper box that is itself thermally insulated from the outside space by a PMMA box. A recirculating chiller is used to control the temperature of the system (between 5 and 90 °C with a stability of ± 0.1 °C) by flowing water between the copper and PMMA compartment.

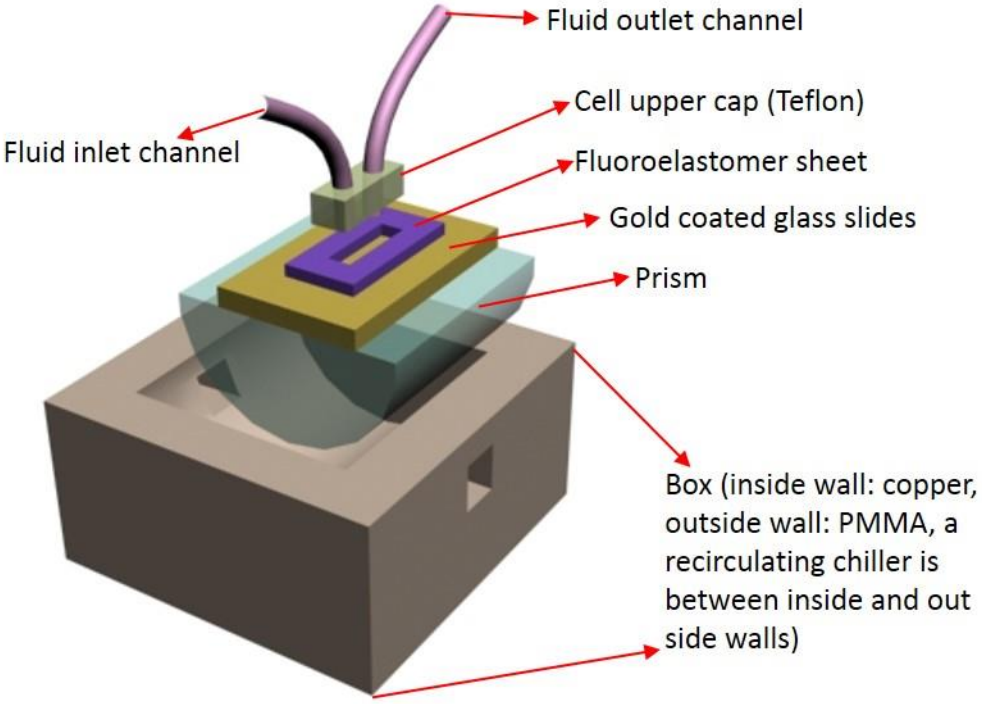

Figure 3.7 Schematic view of the temperature control system.

The fluidic system used in this work comprises a serial dual-piston pump (HPLC isocratic pump) which volumetric flow rate between 1 and 10 ml/min that is connected to an adjustable micro-splitter valve. This flow divider system allows using low flows around 10 to 100 µl/min. The buffer solution is sent to the reactor cell through a low pressure manual sample injection valve. This valve, usually equipped with a 1 ml injection loop, is used to inject the analyte solution in the reactor cell.

3.3.3 SPR sensor chip

Sensor chip has an important influence on performance of the SPR device, since it is where biomolecule interactions take place. As Figure 3.8 shows, four elements: glass substrate, adhesion layer, gold layer and mixed monolayers, make up the chip applied in our SPR device.

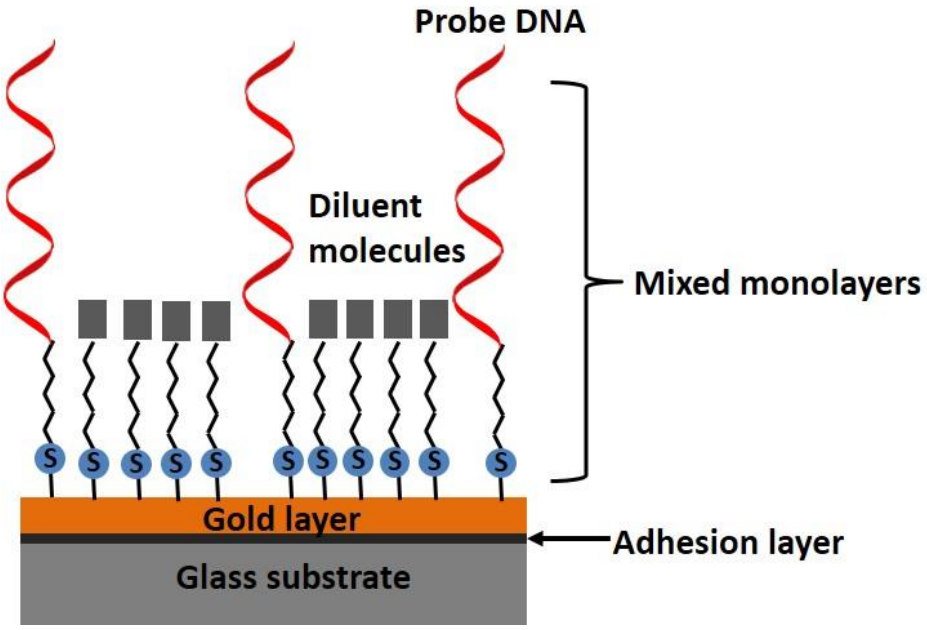

Figure 3.8 Architecture of a SPR sensor chip: the gold-coated glass substrate is covered by mixed self-assembled monolayers including probe DNA and diluent molecules. The adhesion layer is for sticking gold and glass together.

The glass substrate is covered with a thin gold layer (47nm, see chapter 2 section 2.1.2 for experimental details), which enables surface plasmons to be excited. The material and geometry of glass substrate is compatible with the prism used in the instrument optics. Chromium presenting good adhesion to silicon oxide (or glass) is used as an adhesion promoter for gold (that has a poor adhesion on glass). In order to reduce the influence of chromium on the film optical properties, the layer should be as thin as possible (~3 nm, see chapter 2 section 2.1.2 for experimental details). The mixed monolayers including probe DNA and diluent molecules are formed by self-assembling through Au-S bond. There are three purposes for using the mixed SAMs. One is that diluent molecules inserted into the gap between probes show great advantage in resisting the non-specific adsorption. Secondly, for DNA hybridization, diluent molecules can decrease the surface density of DNA probes, thus reducing the effect of steric hindrance on DNA hybridization. Thirdly, diluent molecules are able to change the molecular orientation of DNA probes on gold, providing increased accessibility towards target DNA. In section 5.1, we

discussed four diluent molecules that were used to fabricate the mixed monolayers for DNA hybridization and compare the results with pure DNA monolayer.

3.4 SPR assay

3.4.1 SPR validation

As mentioned above, SPR is measuring the Refractive Index (RI) in the near vicinity of sensor chips. In principle, the measured SPR signal should be linearly related to RI changes (in a limited range). Therefore, our SPR sensor needs to be validated by monitoring the dip position toward known refractive index increments. This can be done using some standard solutions in a series of concentrations, such as sucrose solutions [151]–[153], sodium chloride solutions [154], [155], glycerol solutions [156]–[158], ethanol solutions [151] or Phosphate Buffered Saline (PBS) solutions [155], [159]. All these standard solutions present a good linear relationship between their concentration and their RI.

In our case, the validation of our SPR device was performed using PBS solution, a widely adopted buffer in biosensing applications. PBS solutions of different concentrations were prepared using commercial pouches containing 8 g of NaCl, 0.2 g of KCl, 1.42 g of Na_2HPO_4 and 0.24 g KH_2PO_4. They are dissolved in a serie of volumes of water ranging from 100 to 1000 ml to obtain the concentrations at 10X to 1X respectively.

The dip position shift was recorded during the injection of PBS solution at different concentrations (shown in Figure 3.9 (a)). All the dip position shifts expressed in pixels were evaluated from the position difference between each concentration tested and a reference value considered as the blank sample (pure water in Figure 3.9). As reported before [159], the RI of PBS solutions is linearly related with its concentration and it can be seen in Figure 3.9 that our SPR signal (dip position shift) is also linearly related to the PBS solution concentrations. The sensitivity is extracted from the slope of calibration curve and a 1X difference of PBS concentration corresponds to 64.6 pixels shift. As the sensitivity of our system can be adjusted (position of optial lenses) or can vary with samples, it is measured before each experiment and y-axis of sensorgrams is converted from pixel shift to PBS concentration ‘jump’ units (a unit of 1 corresponds to the shift observed when the PBS buffer concentration rises from xX to ($x+1$)X), which is shown in Figure 3.10.

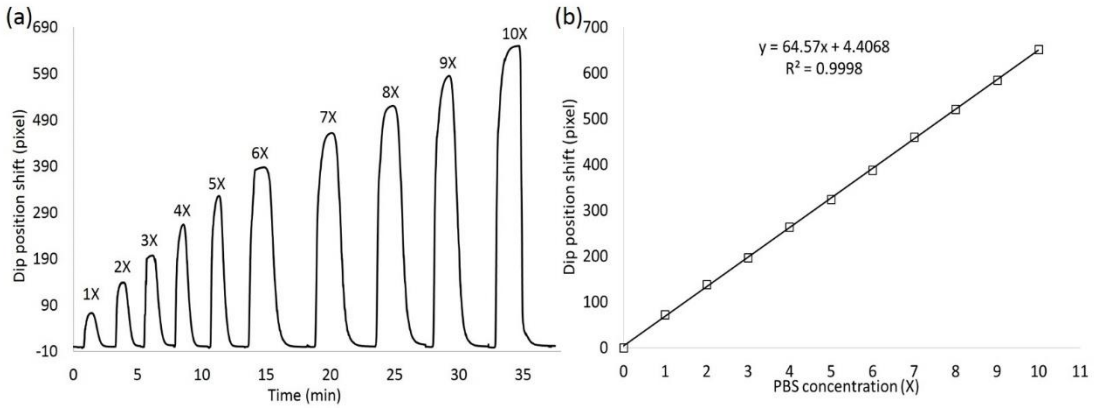

Figure 3.9 (a) Dip position shift over time for different concentrations of PBS buffer at fixed temperature (25°C). (b) Calibration curve of dip position shifts versus different concentrations of PBS buffer.

In order to compare these values with those reported in the literature and mainly with those obtained with 'Biacore' instruments which are given in 'Response Unit', we used the fact that 'Biacore' reports that a 1% DMSO solution gives a signal of roughly 1200 Response Unit. We monitored the dip position shifts during the injection of DMSO solutions in water at volume concentrations ranging from 0.5% to 2%. The sensitivity extracted from this experiment (in the same conditions as used in figure 3.9) is 55 pixels shift by 1% of DMSO. Therefore, the y-axis units used in our experiments can be approximatively converted in 'Biacore Response Unit' by multiplying the values by ~1400.

3.4.2 The steps of an assay

In my work, the SPR device was used to measure DNA hybridization. The DNA probe was immobilized on the sensor chip previous to the measurement. After, the target DNA was flowed on the chips and captured by the probes. Figure 3.10 shows the SPR signal step-by-step in one measurement cycle. Thiol-P_1 was used as the probe immobilized on gold surface, T_1 complementary to P_1 was the target. Unless stated, all the experiments are run at a flow rate of 65 µl/min and are temperature controlled at 25°C.

Each measurement started with flowing the sensor surface with a PBS 5X buffer solution. It is very important to have a stable baseline before hybridization starts - Figure 3.10 step (1). At this point, the sensor chips containing the active probe DNA were stable and ready to capture the target DNA. Next, a calibration was performed by injecting the PBS 4X buffer solution to obtain the dip position shift corresponding to 1X difference of concentration of PBS buffer - Figure 3.10 step (2). This calibration step is performed prior to each measurement. Dividing the hybridization signal by the calibration signal can make the data measured under different

sensitivity conditions comparable. After that, the 1 μM target DNA (T_1) solution in PBS 5X is injected and the targets are captured on the chips by specific hybridization - Figure 3.10 step (3). At this step, both association and dissociation kinetic information on DNA hybridization are obtained from the real-time measurements. Next, PBS 5X buffer solution is re-injected, which causes dissociation of the target DNA from chip - Figure 3.10 step (4). Thus, the dissociation kinetics can also be derived from this process. Finally, a regeneration solution (100 mM NaOH) is injected, which breaks the specific binding between target and probe DNA - Figure 3.10 step (5). If properly anchored to the sensor surface, the probe DNA should remain on the chips, while all of target DNA are removed. Since the DNA hybridization measurements require carrying out the experiment for several times, it is necessary to conduct multiple tests with the same sensor chip, so to use a regeneration solution which leaves the DNA probes intact. If the regeneration is incomplete, remaining target DNA leads to a shifted baseline level.

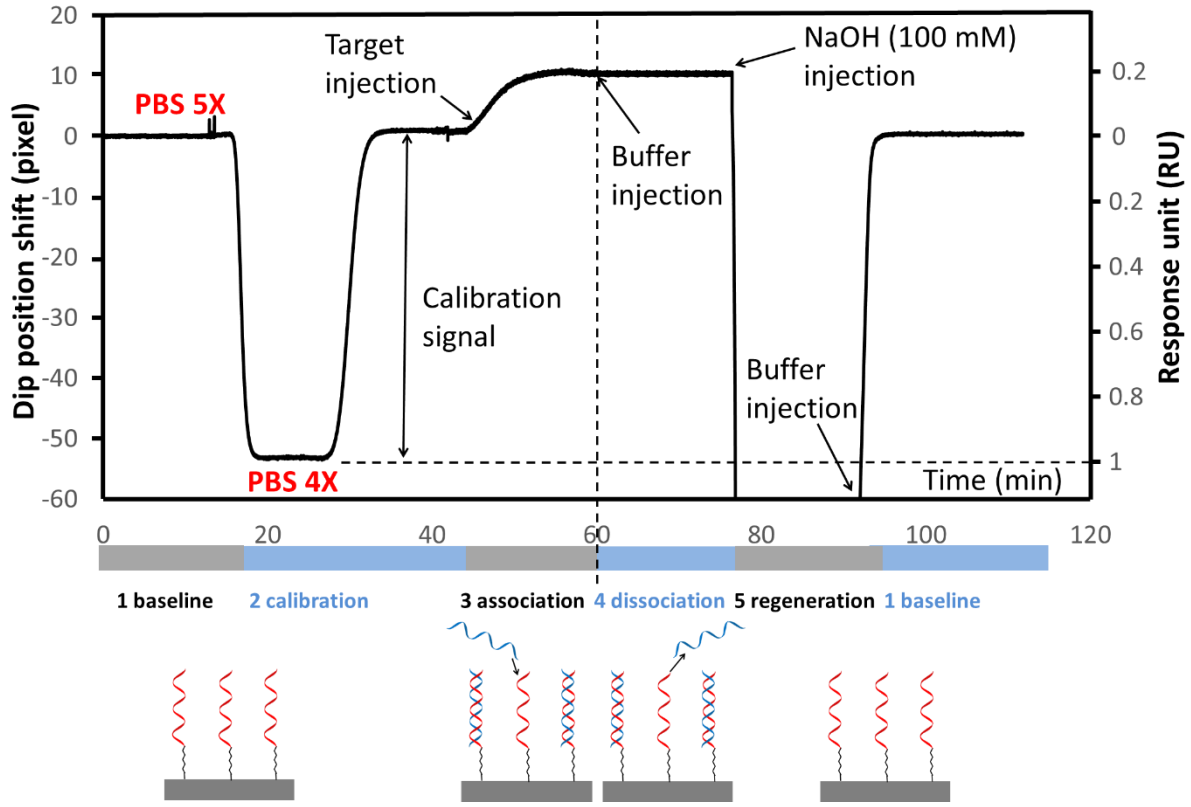

Figure 3.10 Sensorgram presenting the steps of a measurement cycle of DNA hybridization: 1, PBS 5X buffer was injected on the chip (baseline step); 2, PBS 4X buffer was injected to get the calibration signal which indicating the SPR sensor response corresponding to 1X difference of concentration of PBS buffer (calibration step); 3, Injection of 1 μM target solution (association step); 4 Re-injection of PBS 5X buffer (dissociation step); 5, Removal target DNA from surfaces by injecting 100 mM NaOH (regeneration) followed by a new measurement cycle.

3.5 Conclusion

In this chapter, we have introduced our homemade SPR system. It consists of a Kretschmann configuration optics, a temperature control cell, a liquid handling system and a sensor chip. Regarding the optical set-up, a fan-shaped beam allows to send a 740 nm-monochromatic light at different angles simultaneously. The temperature of the reaction cell can be controlled from 5 to 95 ºC. The fluidic system used contains a serial-piston pump, an adjustable micro-splitter valve and a 15 µL-reaction cell. The flow rate can be varied from 10 to 10000 µl/min. Glass slides coated with a 50 nm gold layer and a 3 nm chromium adhesion layer are used as sensor chips.

The SPR system has been calibrated by monitoring the SPR signal (dip position) as a function of PBS buffer concentration. Results showed a good linearity between the response and the refractive index of the buffer.

Chapter 4

Gold preconditioning

4 Gold preconditioning

4.1 Introduction and context

Gold is one of the most commonly-used materials in biochip for a variety of applications such as: QCM, SPR [11], [100], [127]. We used 50 nm or 200 nm thin films of gold deposited on borosilicate glass slides (pre-coated with a 3 nm chromium adhesion layer) as substrates for Surface Plasmon Resonance (SPR) or surface characterization techniques, such as Phase Modulation Infrared Reflection Absorption Spectroscopy (PM-IRRAS), Atomic Force Microscopy (AFM) and X-ray Photoelectron Spectroscopy (XPS) respectively. The surfaces of these substrates were then modified by DNA grafting in order to perform kinetic studies of DNA/DNA hybridization. The grafting reaction is possible if the reactant can have access to a clean gold surface.

Gold surface energy has been reported to be 1.5 J/m^2 [160]. It is decreased by adsorption of surrounding entities (organic molecules, particles…) in particular volatile organic compound. Furthermore, micro/nanotechnological processes may also lead to surface contamination. The thiol grafting on gold cannot cope with highly contaminated surface. Furthermore, reproducible surface reaction requires having reproducible starting surfaces. Therefore, the surface needs to be prepared in particular the contamination is to be removed.

Therefore, a number of different techniques have been developed for gold cleaning and most of them are based on the implementation of oxidative treatment such as oxygen plasma, ultraviolet/ozone or piranha (hydrogen peroxide/sulfuric acid mixtures). The gold/water contact angle is often used for the characterization of cleaning treatment efficiency. However, the wettability of water on a clean metallic gold has been a subject of debate over the last decades. On one hand, several researchers have found that metallic gold was hydrophilic. In 1980, Tennyson Smith [161] reported that the metallic gold surface has a water contact angle of 0°. This angle increased rapidly to 30-60° because of the carbon contaminations absorbed on the surface. Following the Smith's work, Gaines [162] and Schrader [163] also found that clean oxygen-free gold was super hydrophilic (water contact angle below 10° [164]), and became less hydrophilic after short exposure to air. On the other hand, other researchers claimed that the super hydrophilic behavior of gold surface can only be obtained if an oxide layer is formed. These authors demonstrated that clean metallic gold surface exhibited less hydrophilic property with a contact angle ranging from 50° to 70° [165]–[167].

Indeed, gold has been reported to be oxidized into Au_2O_3 under UV ozone [168] or oxygen plasma [165]. However, gold surface property after piranha solution cleaning is less clear. Some authors have reported that gold surfaces are oxidized by piranha solution. Their finding was sustained by the fact that the measured water contact angle after cleaning was below 20° [169] and surface oxygen composition was increased [170]. In addition, Yurui Xue *et al* [125] attributed the shift towards higher binding energy of Au 4f doublets in XPS spectra to gold oxides formation. On the other hand, other authors found that gold remained metallic after piranha solution cleaning leading to a contact angle with water contact angle of more than 50° [171], [172].

Additionally, the gold oxide is unstable. Therefore it may disappear before its characterization. This stability seems to depend on experimental conditions. Indeed, it may persist for longer time in ultra-high vacuum and its life time is shorter under ambient atmosphere [173] [174]. Also, the oxide can be reduced by ethanol (10 min immersion [175]) or decomposed by a thermal treatment of several minutes at 360 K under ultrahigh vacuum [176].

In fact, the presence of this oxide is an important issue as it may influence the thiol grafting on gold [177]. For example, John T. Woodward *et al* [132] have reported that gold oxide can introduce defects or "island" structure during the self-assembled monolayer formation through Au-S bond. This is the reason why some authors have proposed to reduce it by exposure to ethanol, by thermal treatments or by a 24 h waiting time under ambient atmosphere prior to performing the reaction with thiol. Nevertheless, all of them bear the risks of re-contamination from air or reagents used during the reduction reaction.

The purposes of this chapter are to report on the optimizations of gold preconditioning. Two preconditioning methods were evaluated: piranha solution cleaning and oxygen plasma cleaning.

4.2 Results and discussions

As a starting point, we have measured the water contact angle on a 200 nm freshly deposited gold layer obtained by e-beam evaporation (see section 2.1.2). The base pressure inside the deposition system was below $5*10^{-7}$ mbar. Figure 4.1 shows the water contact angle (θ_{H2O}) as a function of ambient atmosphere storage time (t). t=0 corresponds to the opening of the deposition system. Just after opening of the system, water was able to completely wet the gold layer. Within 1 h of exposure in air, the θ_{H2O} increase quickly to around 65°, which can be explained by the atmospheric carbonaceous contaminants absorbing on the clean gold surface

[161]. Then, it increases slower until reaching a plateau region corresponding to a contact angle of 80° probably due to the full coverage of the surface by carbonaceous contaminants. Since the gold deposition is carried out in a high vacuum chamber free of oxygen, the gold just after deposition can be regarded to be in metallic state. In addition, Tennyson Smith [161] investigated the property of deposited gold in ultrahigh vacuum with auger electron spectroscopy and demonstrated that the freshly deposited gold is free of oxygen. Therefore, we may hypothesize that under our condition of fabrication, the freshly deposited metallic gold is super hydrophilic and the water contact angle on the gold surface increases from 0 to 80° as the hydrocarbon contamination adsorbs on the surface.

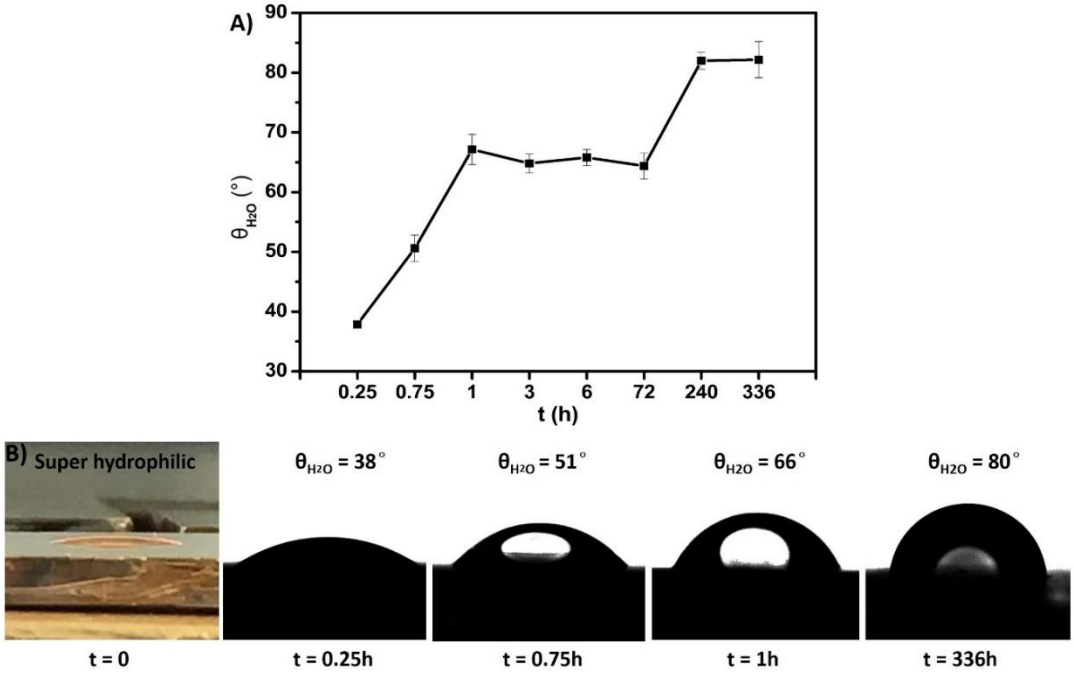

Figure 4.1 A) Graphique illustrating contact angle of water on gold as a function of time for gold sample stored in ambient air. B) Images of water drops on gold samples freshly deposited (0 h) and stored in ambient air for 0.25 h, 0.75 h, 1 h, 336 h.

In the following, we have compared piranha solution cleaning of gold substrate with oxygen plasma cleaning. First, piranha solution cleaning was optimized. Then, oxygen plasma and optimized piranha solution cleaning were compared using contact angle measurements, atomic force microscopy and x-ray photoelectron spectroscopy.

4.2.1 Piranha solution cleaning

The effects of three parameters of the piranha solution were investigated: H_2SO_4/H_2O_2 volume ratio, temperature and time. Optimization of these three parameters was performed using only water contact angle measurements. Before cleaning, freshly deposited gold samples (200 nm thickness) were stored in lab for more than 240 h leading to an initial contact angle ranging from 80° to 85° prior to piranha solution cleaning.

4.2.1.1 H_2SO_4/H_2O_2 volume ratio

Table 4.1 lists the water contact angles measured on the gold slides cleaned by piranha solutions. Five different H_2SO_4/H_2O_2 volume ratios were used. Cleaning time was set to 20 min. The water contact angle was measured three times at different places of the same sample and averaged.

H_2SO_4/H_2O_2 volume Ratio	**θ_{H_2O} (°)**
1:1	56 ± 12
2:1	52 ± 19
3:1	32 ± 4
4:1	33 ± 3
5:1	43 ± 11

Table 4.1 Contact angles of water on gold cleaned by piranha solution at different H_2SO_4/H_2O_2 volume ratios. The contact angle was averaged from 4 measurements on the 2 different samples.

As the concentration of sulfuric acid was increased, the water wettability of treated gold increased from 56° using the 1:1 ratio to 33° with the 4:1 ratio. At a ratio of 5:1 a higher standard deviation of the measured water contact angle was observed. Piranha solution cleaning process consists of two steps. First, the contaminants are dissolved by the sulfuric acid, followed by an oxidation reaction due to the presence of H_2O_2 or H_2SO_5 [178]. Therefore, increasing the sulfuric acid concentration may allow a better dissolution of the contaminants from the surface. However, H_2O_2 mixing with sulfuric acid generates H_2SO_5 intermediates and this mixing reaction is exothermic. Therefore, as the concentration of H_2O_2 decreases, the temperature of the solution decreases which may negatively influence the cleaning efficiency. Therefore, if water contact angle is considered as a measure of hydrocarbon contamination removal, it seems that the best ratio is 3:1. However, we have observed that freshly deposited gold had water contact angle of 0°. It is probably due to that, under these conditions, piranha was not able to

fully remove the carbon contamination. Therefore, we have tested whether heating could promote further removal of the contamination.

4.2.1.2 Temperature

To vary the cleaning temperature, the sulfuric acid temperature was set to 4, 25 and 90°C before the addition of hydrogen peroxide. The H_2SO_4/H_2O_2 volume ratio was 3:1. After mixing, the temperature was recorded: a plot of the solution temperature *vs.* the time after the addition of hydrogen peroxide is given in left part of Figure 4.2 a. The sample was immersed in the mixture right after the mixing of sulfuric acid with hydrogen peroxide and was left 5 min in the mixture. The water contact angle measurements were performed after 5 min cleaning and pictures are presented in Figure 4.2 b.

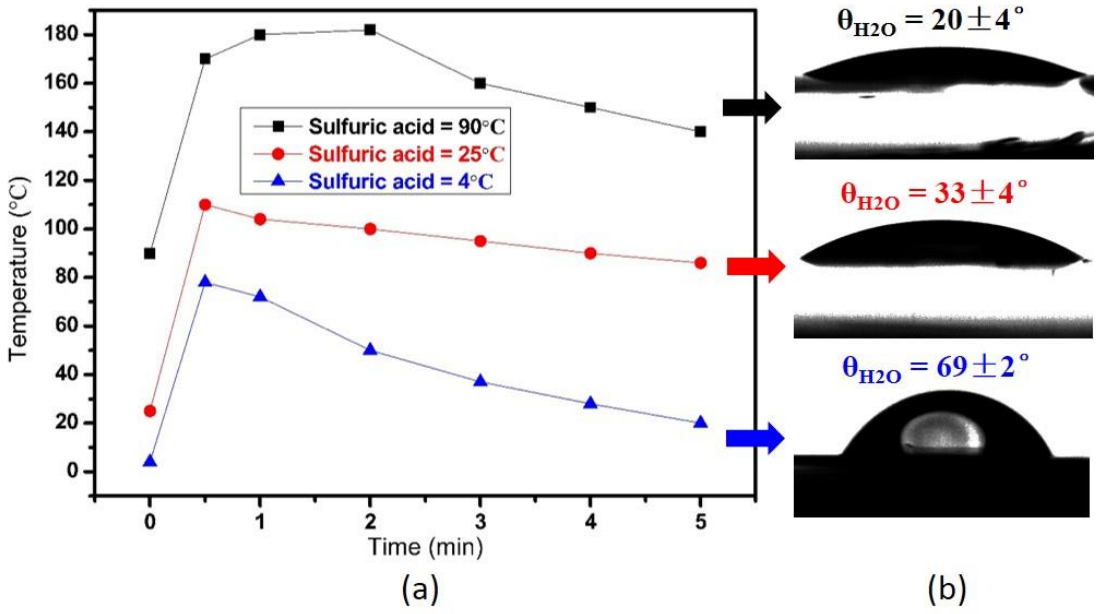

Figure 4.2 Effect of temperature of piranha solution on water wettability of gold. The blue, red and black lines in the left graph (a) represent the temperature of piranha solution as a function of time after addition of H_2O_2 into 4, 25 and 90 °C sulfuric acid, respectively. The right graph (b) represents the water contact angles on gold samples after 5 min piranha solution cleaning. The water contact angle was measured three times at different places of the same sample and averaged.

Results show that the water contact angle decreases from 69° to 33° and to 20° with increasing treatment temperature. Therefore, preheating of the sulfuric acid allows reaching lower water contact angles but does not permit to reach the wettability below 20° observed with freshly deposited gold.

4.2.1.3 Time

For a better understanding of the interplay between time and temperature on the cleaning efficiency of piranha, the water contact angles as the function of cleaning time for gold substrates treated with preheated and unheated sulfuric acid are presented in Figure 4.3. The 90°C preheated sulfuric acid piranha mixture leads to a gold surface having water contact angle of 22° after 5 min. Then, the angle decreases slowly, reaching 20° at 22 min. It remains steady for longer incubation times. A similar behavior was observed when using 25°C sulfuric acid for the fabrication of the piranha solution but the water contact angles remains above 30°.

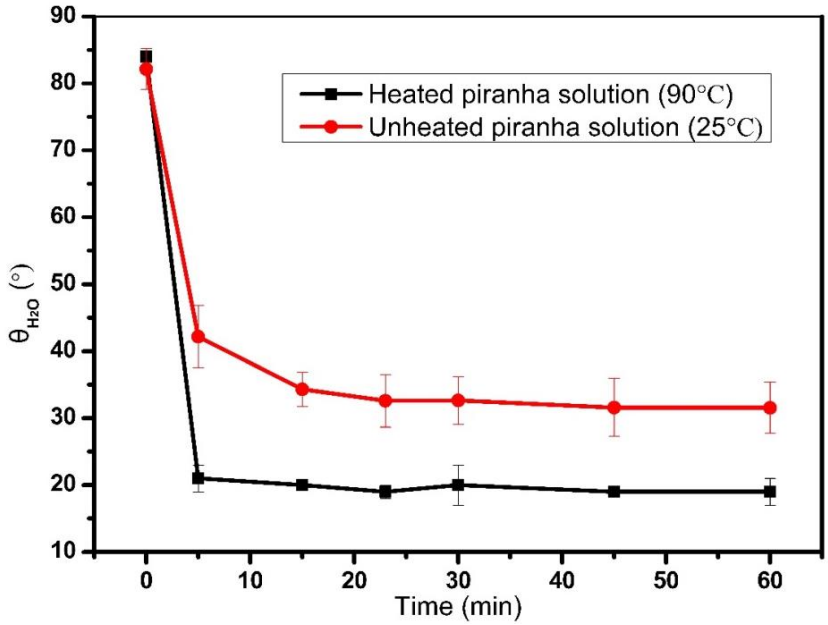

Figure 4.3 Water contact angles on gold cleaned by heated piranha solution (sulfuric acid heated to 90 °C) and unheated piranha solution (sulfuric acid is at room temperature 25°C) as a function of cleaning time. The water contact angle was measured three times at different places of the same sample and averaged.

In conclusion, it was found that heating the piranha solution was compulsory to reach θ_{H_2O} around 20° but we could not reach complete wetting (θ_{H_2O} close to 0°) as reported by some authors and as observed for just deposited gold. The optimized piranha treatment in our case is performed with the following parameters: H_2SO_4/H_2O_2 volume ratio at 3:1, preheating the sulfuric acid to 90°C and cleaning for 5 min.

However as mentioned in the introduction, several authors claimed that only gold oxide Au_2O_3 could lead to complete wetting and that this oxide layer may affect the self-assembled monolayer formation.

Therefore, in the following, XPS is employed to check the oxidation state of the gold layer following an optimized piranha treatment. In parallel, gold substrates saturated with carbonaceous contaminants from ambient air are submitted to oxygen plasma treatment. The two resulting surfaces are compared.

4.2.2 Comparison of oxygen plasma cleaning versus piranha cleaning

The gold samples were cleaned by oxygen plasma for different times from 20 s to 300 s. In all cases, the water contact angles were 0°. To our knowledge, the water wettability of gold surface is not only determined by the surface energy but also the surface roughness. Therefore, before checking the cleanness and oxidation state of gold surface, we firstly studied if the preconditioning treatment can alter the gold surface topography using AFM.

4.2.2.1 Roughness of gold surface

We investigated the roughness of gold surfaces after optimized piranha treatment or oxygen plasma cleaning and compared them with untreated surface. The gold layers are 200 nm thick with an adhesion layer of chromium of 3 nm. The oxygen plasma was performed with the following parameters: forward power = 38 W, oxygen flow = 14 ml/min, time = 5 min. AFM characterization (see in Figure 4.4) shows that the surface topography of untreated gold surface was formed by islands having a width of around 200 nm and didn’t change after optimized piranha treatment or oxygen plasma cleaning. The Root Mean Square (RMS) roughness for them are 1.9-2.3 nm. Therefore, the change in water wettability of gold surface after the cleaning can only be due to the change of surface energy.

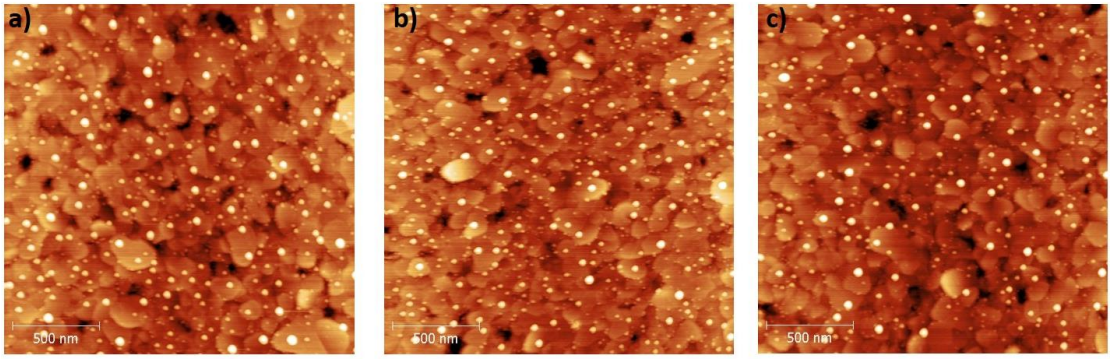

*Figure 4.4 AFM topography image over a randomly-selected 4 μm^2 (2*2) area on the untreated gold surface (a), oxygen plasma cleaned gold surface (b) and piranha cleaned gold surface (c). RMS roughness was measured three times at different places of the same sample and averaged.*

4.2.2.2 Cleanness and oxidation of gold surface

The cleanness and oxidation of gold surface after optimized piranha treatment or oxygen plasma cleaning were assessed using XPS. The treatment conditions were the same as previously described. Figure 4.5 shows typical survey spectra of ambient air stored gold (240 h), after subsequent treatment by oxygen plasma (5 min) or piranha solution (5 min). For the ambient air stored gold sample (Figure 4.5 spectra A), characteristic peaks are observed at 58 eV, 84-88 eV, 330-350 eV, and 550 eV corresponding to the Au5p, Au4f, Au4d and Au4p respectively. An additional peak at 285 eV is observed and correspond to the C1s contribution. This contribution corresponds roughly to 20 % of a monolayer. Following oxygen plasma cleaning for 5 min or piranha cleaning for 5 min, the contribution at 285 eV is not observed anymore, which indicates the removal of the C1s contribution.

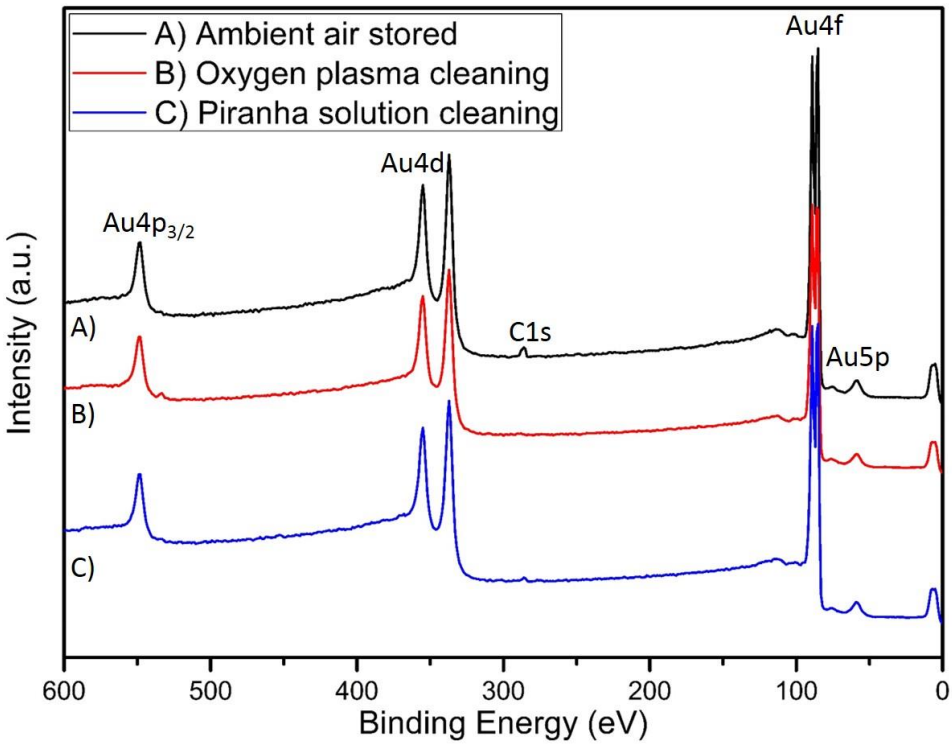

Figure 4.5 XPS survey spectra of ambient air stored gold (A) and after subsequent cleaning with oxygen plasma (B) and piranha solution (C).

For the identification of the chemical state of gold, high resolution narrow scan spectra of Au 4f doublet lines were recorded (see in Figure 4.6) for ambient air stored gold, piranha cleaned gold and oxygen plasma cleaned gold. For all samples, the measured chemical peaks for the Au $4f_{7/2}$ and Au $4f_{5/2}$ were 84.2 eV and 88 eV, respectively. Such chemical peaks can be attributed to metallic gold and not to an oxide or sub oxides which are expected to be recorded at 86 eV and 89 eV for the Au $4f_{7/2}$ and Au $4f_{5/2}$, respectively.

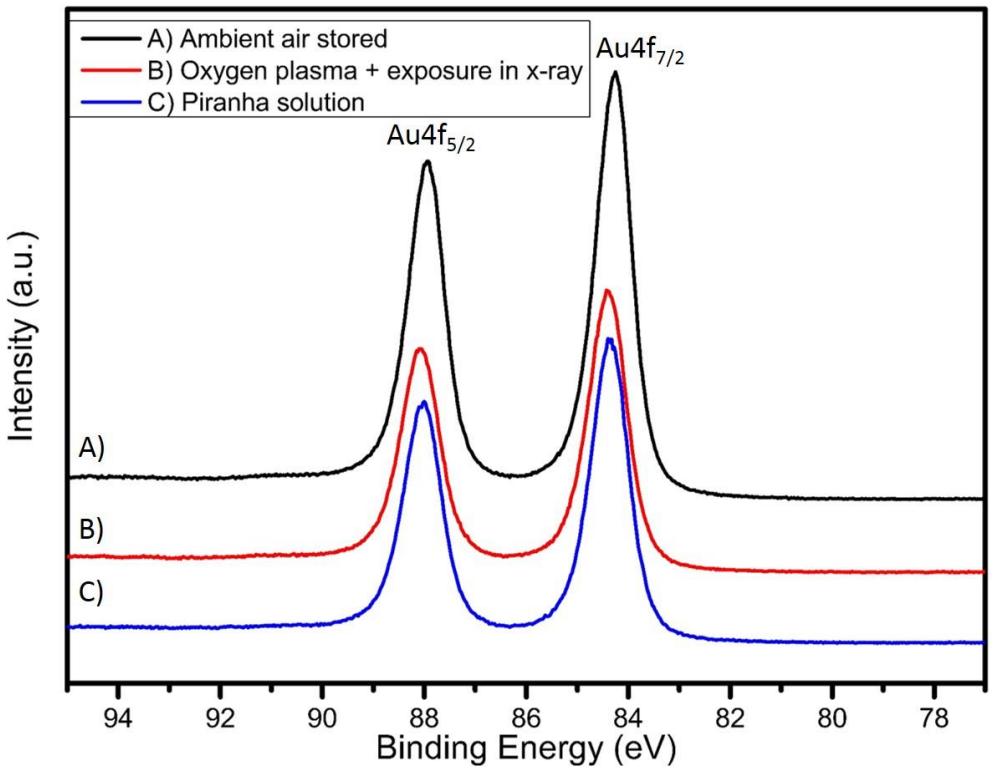

Figure 4.6 XPS spectra of 4f doublet lines of gold samples stored in ambient air (A), after oxygen plasma cleaning (B) and piranha solution cleaning (C).

It should be noticed that two additional chemically shifted peaks appeared on the first scan on Au energy window at higher binding energy for the gold sample just after oxygen plasma cleaning. However these two peaks were stable only for the duration of the first scan and could not be recorded. They may be related to a very thin gold oxide layer and their disappearance may be due to its fast decomposition induced upon X-ray exposure. However, Palazon *et al* [174] found that gold oxide created by oxygen plasma was stable over 12 h under ultra-high vacuum. XPS spectra was recorded using the same XPS system. In the case of Palazon *et al*, the plasma system was operated for 5 min with a forward power of 350W (reflected power 100W), 400 ml/min of O_2 and the pressure was 90 Pa. In our case, the plasma system was operated for 5 min, with a forward power of 38 W, a flow of oxygen of 14 ml/min and the pressure was 86 Pa. Furthermore, our plasma system probably generates milder conditions as compared to that used by Palazon *et al* (inductively versus capacitively coupled plasma) and leads to a thinner oxide layer.

In addition, some other studies of the stability of gold oxide under exposure of x-ray flux reported that:

- 1 to 5 min oxygen plasma cleaning under a power of 300 W and 600 W in an oxygen atmosphere (O_2 pressure ~25Pa) produce gold oxide layers with thicknesses of about 5-7 nm and 6-10 nm, respectively. Both are stable during an XPS analysis of several scans [179], [180].
- Gold oxide generated by oxygen DC (direct current) reactive sputtering (O_2 pressure ~13 Pa) for 15 min was reduced very slowly under X-ray exposure in 12 h, which is consistent with the observation of Palazon [176].
- Gold oxide generated with oxygen plasma becomes negligible after a 4 h exposure to X-ray and is completely reduced after a continuous exposure of 9 h [181].
- 1-2 nm thick gold oxide layers generated by UV ozone are reduced during data acquisition with XPS, which is similar with our observation [168].

Given the above-mentioned reported works, the higher power and longer time for the same plasma cleaning instrument can produce thicker gold oxides resulting in higher stabilities under X-ray exposure. Considering the low power and short time applied in our oxygen plasma cleaning, we propose that only a very thin layer of gold oxide is produced and decomposes very quickly under X-ray.

Finally, it is difficult to conclude whether piranha treatment leads or not to the formation of a gold oxide. Indeed, following immersion of the sample in the piranha mixture, it is compulsory to rinse the sample with water prior to perform XPS analysis. However some authors have reported that the gold oxides generated by UV ozone in ultrahigh vacuum decomposed substantially after 1 min water rinse with XPS spectra [182]. Since the piranha solution cleaning is in water environment and at high temperature, both of these two factors could result in the fast decomposition of gold oxides.

As a conclusion, using our cleaning protocols, we were not able to show the formation of an oxide gold layer or at least a layer stable over a few minutes. The water contact angle was below 25º after piranha cleaning and 0° after plasma cleaning. Therefore, it seems that the 0° contact angle obtained after plasma cleaning cannot be attributed to the formation of an oxide layer, but rather to a higher cleaning efficiency than piranha.

4.2.2.3 Immobilization of thiolated DNA

At last, we immobilized thiolated DNA on optimized piranha and oxygen plasma cleaned gold surfaces respectively and recorded the resulting PM-IRRAS spectra (see in Figure 4.7). The parameters for oxygen plasma cleaning were the same as that in previous section. The immobilization was performed by the deposition of 20 μM DNA solution in PBS 10X on the gold surfaces overnight, at 25ºC. The upper two spectra in Figure 4.7 were collected with the gold sample cleaned by oxygen plasma and after subsequent thiolated DNA grafting, while the lower two spectra were collected with the gold sample cleaned by piranha solution and after thiolated DNA grafting.

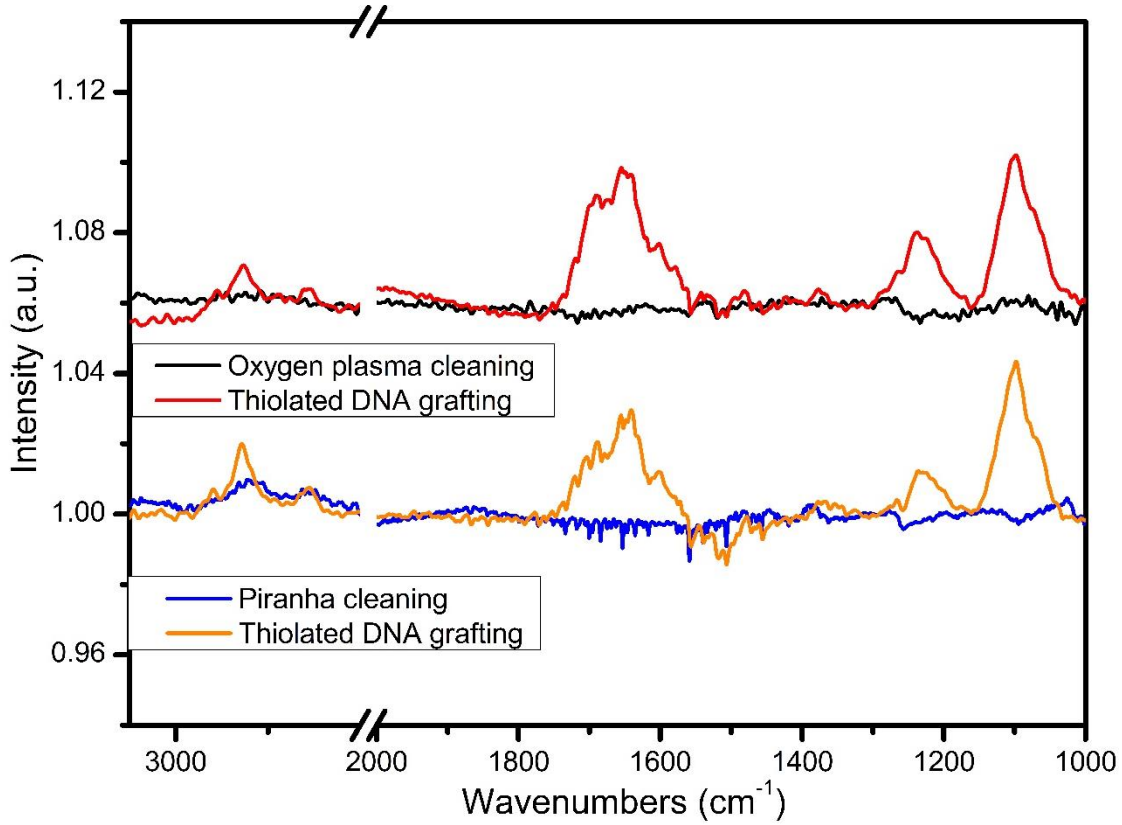

Figure 4.7 Upper two: PM-IRRAS spectra of oxygen plasma cleaned gold surface (black) and after thiolated DNA grafting (red). Lower two: PM-IRRAS spectra of optimized piranha cleaned gold surface (blue) and after thiolated DNA grafting (orange). The thiolated DNA grafting was conducted with 20 μM DNA solution in PBS 10X (ph=5.5).

After thiolated DNA grafting, the gold samples cleaned by oxygen plasma (red) and piranha solution (orange) exhibit the same features, indicating the presence of DNA strands. For instance, the two infrared signatures recorded at 1095 cm^{-1} and 1240 cm^{-1} correspond to the symmetric and asymmetric stretching vibration of PO_4^{3-} group of the DNA phosphodiester backbone [183] and the region from 1550 to 1750 cm^{-1} was attributed to carbonyl (C=O), C=N

stretching, and exocyclic-NH_2 bending vibration in nucleobases [184], [185]. In addition, the bands at 2925 cm^{-1} and 2855 cm^{-1} can be attributed to vibration modes of the alkyl chain from DNA and of the spacer $(CH_2)_6$ between thiol group and DNA. There is not a significant difference of intensity between these peaks obtained from these two cleaned gold surfaces. It indicates that these methods can be used as alternatives to each other for preconditioning gold surfaces applied in thiolated DNA grafting.

4.3 Conclusions

In this chapter, we aimed at optimizing preconditioning condition to obtain a clean gold surface without oxidation. Two cleaning methods are compared: piranha solution and oxygen plasma. Firstly, the water wettability of gold surface after cleaning was studied. The results showed that the best water wettability of gold surface after piranha cleaning is the water contact angle of around 20º, and heating is a compulsory factor to reach that. For oxygen plasma treatment, even a very short time (20s) can make the gold surface super hydrophilic (0º).

Next, the gold surface topography and roughness after cleaning were characterized using AFM. It showed that surface roughness is altered marginally after piranha solution or oxygen plasma cleaning which confirms that changes of wettability are only due to changes of surface energy. Then, the gold surface cleanness and oxidation were investigated using XPS. It was found that both cleaning methods can efficiently remove the carbonaceous contaminants on gold surfaces. For gold oxidation, we observed it only during the first scan of oxygen plasma cleaned gold but was not stable enough to be recorded. Therefore, using our cleaning protocol, we were not able to evidence the formation of an oxide gold layer or at least a layer stable over a few minutes. The super hydrophilic property obtained after oxygen plasma is probably due to a higher cleaning efficiency than piranha solution.

Finally, the layers of thiolated DNA on cleaned gold surfaces were characterized using PM-IRRAS. There was no significant difference upon cleaning methods and both piranha solution and oxygen plasma cleaning can be adopted in our case. They can be used as alternatives to each other for preconditioning gold surfaces applied in thiolated DNA grafting. In our case, the optimized piranha solution is used for cleaning gold surfaces applied in thiolated DNA grafting.

Chapter 5

Determination and comparison of DNA hybridization K_d by three surface based methods: surface plasmon resonance, evanescent field fluorescence biosensor and fluorescent microarray

5 Determination and comparison of DNA hybridization K_d by three surface based methods: surface plasmon resonance, evanescent field fluorescence biosensor and fluorescent microarray

5.1 Introduction

A single strand DNA can hybridize specifically to its complementary sequence according to Watson-Crick rules. This property makes them a useful tool in biotechnology and nanotechnology applications [186]–[188]. DNA hybridization can be performed in solution and on solid surfaces. Solution-phase hybridization has been investigated extensively by UV absorbance and isothermal titration micro-calorimetry [59], [189], [190]. Some algorithms [5]–[8] have been derived to quantitatively predict the thermodynamics of hybridization for short oligonucleotides. However, it has been difficult to apply these results in the case of surface based hybridization [69]. It has been reported that interfacial architecture [11], [13], [127], [128], secondary structure [64], [191], [192], ionic strength [2], [140], [193], and surface probe density [12], [133], [138], [194] strongly influence the kinetic and efficiency of hybridization. Therefore, different surface based methods performed under different experimental conditions could result in different quantitative data such as hybridization dissociation constant K_d.

The quantitative analysis of DNA hybridization on surface can be performed by two different ways: kinetic methods and steady state methods. Fluorescent microarray is a widely applied method in the determination of K_d of biomolecules interaction based on steady state analysis [195], [196]. It allows to simultaneously characterize the various interactions in a high-throughput and high-sensitivity way with very few amount of materials. In addition, it can be applied for the measurements of biomolecular interactions with very high affinity ($K_d \approx 10^{-12}$ M) [197]. The combination of microarray with traditional fluorescence scanning technology can provide end-point data of biomolecular interactions, while the kinetic information (on-rate and off-rate constants) cannot be obtained. Therefore, two real-time biosensors with sufficient sensitivity and selectivity have been chosen for obtaining both kinetic and equilibrium information of DNA hybridization. One is evanescent field fluorescence biosensor (the principle is illustrated in Annex B). Similarly to fluorescent microarray, it requires to label target molecules with fluorescent dyes. This technique uses an evanescent wave as the

excitation light source instead of the light directly from laser in conventional fluorescence excitation configuration. Due to the small penetration depth (~200 nm) of the evanescent field, only fluorophores bound to the substrate can be excited, while the majority of free labeled target DNA is outside of the range of the evanescent field. Therefore, washing step to remove free labeled DNA in solution can be avoided. With this technique, real-time detection of target molecules can be achieved by monitoring the fluorescent intensity with time. However, the introduction of fluorophores may influence the biomolecules interactions [198]–[202]. As reported by Moreira [203], in the case of hybridization between two DNA strands with different length, the fluorophores on DNA target can stabilize the formed DNA duplex. Indeed, fluorophores attached on the DNA target termini may interact with unpaired bases of probe. In order to avoid the influence of fluorescent dyes, another real-time detection based on SPR was developed (the principle is illustrated in chapter 3). SPR biosensor doesn't require the labeling of target molecule, so that the effect of the fluorescent dyes on DNA hybridization can be completely eliminated. Therefore, these three different detection approaches i.e. real-time or steady state, with or without fluorescent dyes, were all used to determine the DNA hybridization K_d and compared in terms of operability and quality of obtained data.

In this chapter, we firstly investigate the optimization of experimental conditions for DNA hybridization using SPR biosensor. After, a detailed determination and comparison of DNA hybridization K_d by SPR biosensor, evanescent field fluorescence biosensor and fluorescent microarray is given.

5.2 Optimization of experimental condition for DNA hybridization

In this section, all DNA hybridizations were measured using SPR biosensor and the substrates used are gold films with a thickness of 50 nm. For surface characterization using PM-IRRAS, the substrates used are gold films with a thickness of 200 nm. The thiolated DNA probe is directly coupled via Au-S bond formation on gold surface cleaned using optimal piranha solution.

Before studying the optimal experimental conditions for DNA hybridization, we firstly explored how to efficiently immobilize DNA on gold surfaces via thiol chemistry. As mentioned in section 1.2.3.2, high ionic strength is beneficial for thiolated DNA immobilization because it can screen the electrostatic repulsion between negatively charged DNA. However, the influence of pH is still in debate. Some people claimed that alkaline condition is beneficial to the Au-S bond formation [125], while Peterson [12] claimed that pH has little effect on Au-S bond formation. Therefore, we grafted thiolated DNA on 200 nm gold film under different pH environments and recorded the resulting PM-IRRAS spectra. The grafting was conducted in PBS 10X and at room temperature.

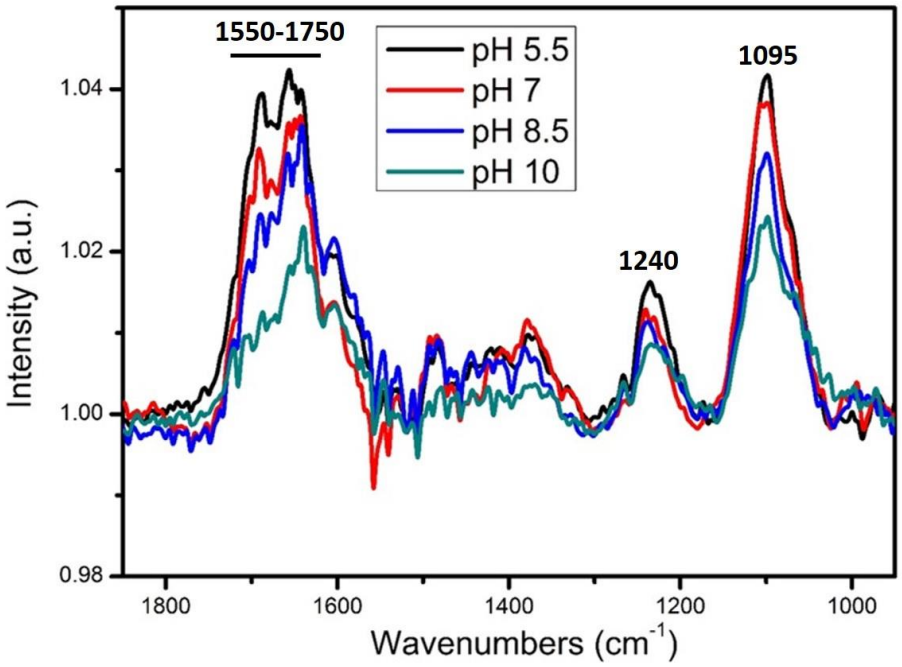

Figure 5.1 PM-IRRAS spectra of a layer of thiol-DNA formed on the 200 nm thick gold films under different pH environments. All the immobilizations of thiol-DNA on gold were conducted by incubation with 20 μM thiol-DNA in PBS 10X overnight, at 25 ºC.

Figure 5.1 shows the PM-IRRAS spectra corresponding to the layer of thiol-DNA formed under different pH environments. The infrared signatures at 1095 and 1240 cm^{-1} were attributed to the symmetric and asymmetric stretching vibration of PO_4^{3-} group of the DNA phosphodiester backbone and the region from 1550 to 1750 cm^{-1} was attributed to carbonyl (C=O), C=N stretching and exocyclic-NH_2 bending vibration in nucleobases. The intensities of these peaks corresponding to the DNA increased as the pH value decreased. This indicates that the acidic environment is beneficial for thiolated DNA grafting on gold surface. From the literature [3], [204]–[206], the isoelectric point of DNA is reported to be around 5. Therefore, acidic

environment pH = 5.5 (close to the isoelectric point) may cause partially protonation of phosphate backbone of DNA, which reduce electrostatic repulsion between DNA probes and favors the DNA adsorption process [207]. In addition, Zhang [3] has demonstrated that, as the pH decreased from 9.5 to 4.5, the electrostatic repulsion between DNA strands decreases, which was attributed to the increase in the degree of protonation of DNA. As a result, the effect of pH on thiolated DNA immobilization may be related to the electrostatic repulsion of between DNA strands instead of the formation of Au-S bonds. On the basis of these observations, we decided to conduct all the thiolated DNA immobilization on gold at pH=5.5.

5.2.1 Influence of diluent molecules on DNA hybridization

Mixed self-assembly of thiolated DNA and diluent molecules forming two-component DNA recognition surface on gold has served as an important model system for the study of DNA hybridization on surfaces, because it can effectively improve hybridization efficiency and inhibit non-specific adsorption between target DNA and bare gold. P_2 (probe 2) and T_2 (target 2), which are a pair of complementary DNA sequences, were used in our study of the influence of diluent molecules on DNA hybridization. P_1, which is completely uncomplementary to T_2, was used as a negative control. Four different molecules: MCH, PEG, diluent-P_2 and oligo-T, were chosen to be used as the diluent molecules in two-component DNA recognition surfaces. The sequences and molecular structures of these molecules are described in Table 5.1 and Figure 5.2.

Probe:	**P_1**: 5'-GTG AGC CCA GAG GCA GGG-$(CH_2)_6$-HS
	P_2: 5'-GCT AAT CCA ACG CGG GCC AAT CCT T-$(CH_2)_6$-HS
Target:	**T_1:** 5'-CTG CCT CTG GGC TCA
	T_2: 5'-CCG CGT TGG ATT AGC
Diluent molecules:	**MCH (6-mercapto-1-hexanol)**: HS-$(CH_2)_6$-OH (MW = 134 g/mol)
	PEG-thiol (Polyethylene glycol methyl ether thiol): HS-CH_2CH_2-$(OCH_2CH_2)_n$-OCH_3 (MW = 2000 g/mol, n≈43)
	Oligo-T: 5'-TTT TTT TTT T-$(CH_2)_6$-HS (MW = 2872 g/mol)
	Diluent-P_2: 5'-GCC AAT CCT T-$(CH_2)_6$-HS (MW = 3159 g/mol)

Table 5.1 Sequences and formula of molecules used for SPR measurement. The complementary parts are colored

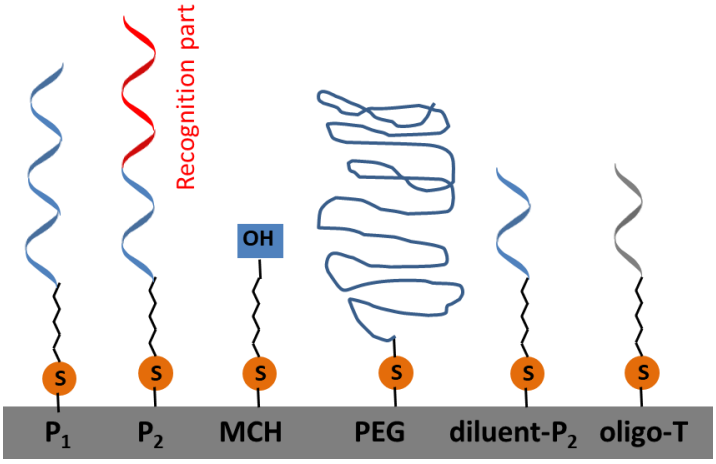

Figure 5.2 Sketch map of molecular structure of molecules used for SPR measurement.

- MCH is a short alkyl chain with hydroxyl in the top which has the same length as the spacer between P_2 sequence and thiol group.
- PEG is long chain molecule with high flexibility which shows good resistance toward nonspecific DNA or protein absorption [81], [208]–[212].
- Diluent-P_2 is equivalent to the P_2 sequence without recognition part.
- Oligo-T is a short DNA sequence including 10 thymine bases with $(CH_2)_6$ as the spacer, which also has the similar length as the P_2 without the recognition part.

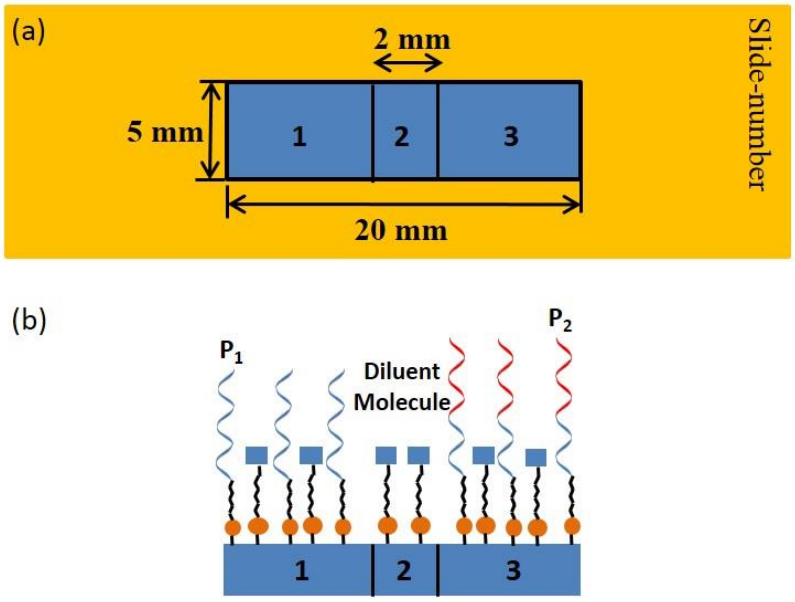

Figure 5.3 (a) Gold slide and reaction areas, (b) A schematic of SPR sensor chip.

The fabrication of four different two-component DNA recognition surfaces was done using a two-step method: firstly, 20 μM P_1 and P_2 in PBS 10X (pH=5.5) were deposited respectively on areas 1 and 3 (as shown in figure 5.3 a) of the 50 nm thick gold slide and incubated overnight at room temperature in a water-saturated atmosphere. Secondly, 200 μM diluent molecule (MCH, PEG-thiol, Oligo-T or diluent-P_2) solution in PBS 10X (pH=5.5) was deposited on whole reaction area (1+2+3) for 2 h at room temperature in a water-saturated atmosphere. Thus, DNA probe dilution and capping the middle area can both be done in this second step. The resulting SPR sensor chip surface is presented in Figure 5.3 b. Area 3 is the P_2T_2 hybridization area while area 1 is used as negative control.

Our homemade SPR biosensor was used to monitor the P_2T_2 hybridization on pure P_2 recognition surface and on four different two-component surfaces of P_2 diluted with MCH, PEG, diluent-P_2 or oligo-T. The corresponding sensorgrams are presented in Figure 5.4 and the sensor response is expressed as described in section 3.4.1. All the hybridizations were performed at 1 μM of T_2 in PBS 5X and 25°C. Comparing Figure 5.4 a and 5.4 b, the addition of 200 μM MCH in dilution process efficiently increases the signal of P_2T_2 hybridization from 0.08 (pure P_2 surface) to 0.17 (P_2 + 200 μM MCH), by a factor of 2. This could be due to two factors: one is that the thiolated DNA absorbed on gold surface through the nitrogen-containing nucleotide bases (thus laying on the surface) "stands up" and extends further into the solvent phase after the addition of MCH [124], [213], [214]. The other one is that the addition of MCH decreases the P_2 surface density, which reduces steric hindrance and improves hybridization efficiency [12], [129]. In addition, exchanging with 400 μM MCH causes a significant decrease in hybridization signal from 0.17 (P_2 + 200 μM MCH) to 0.06 (P_2 + 400 μM MCH). This was attributed to the fact that such a high concentration of MCH removes a large amount of DNA probes and therefore reduces the hybridization signal. To sustain this hypothesis, PM-IRRAS spectra of pure P_2 surfaces treated with 200 μM or 400 μM MCH were recorded (shown in Figure 5.5). As with the previously presented PM-IRRAS spectrum of the DNA molecule layer on gold, the peaks at 1095 and 1240 cm^{-1} are attributed to the symmetric and asymmetric stretching vibrations of PO_4^{3-} group of the DNA phosphodiester backbone, and the region from 1550 to 1750 cm^{-1} is assigned to carbonyl (C=O), C=N stretching, and exocyclic-NH_2 bending vibration in nucleobases. These bands corresponding to DNA were observed for pure P_2 surface diluted with 200 μM MCH but no more detected after the treatment with 400 μM MCH.

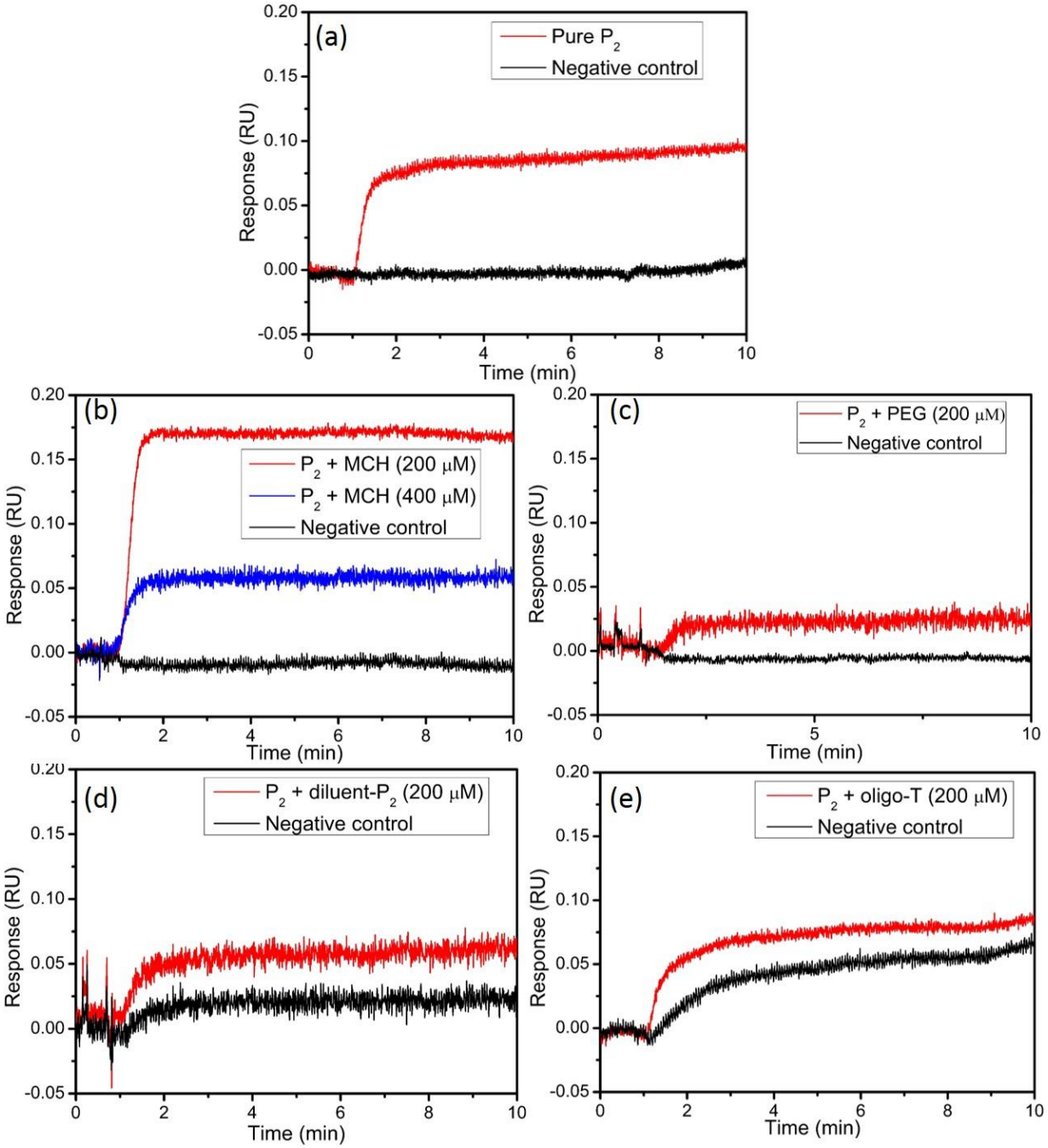

Figure 5.4 Sensorgrams of P_2T_2 hybridization on pure P_2 surface (a) and four different two-component surfaces of P_2 with MCH (b), PEG (c), diluent-P_2 (d) or oligo-T (e). All the hybridizations were performed at 1 μM of T_2 in PBS 5X flowing at 65 μl/min at 25°C. The Y-axis is graduated in equivalent PBS concentration as described in section 3.4.1.

In the case of PEG used as the diluent molecule (shown in Figure 5.4 c), the hybridization signal was very low at about 0.02. It is 4 times lower than the signal obtained from pure P_2 surface (0.08) and about 8 times lower than the signal obtained from two-component surface of P_2 and

200 μM MCH (0.17). This could be due to the fact that PEG is able to remove more efficiently surface bounded molecules, causing a great loss of P_2 at recognition interface. To demonstrate that, we also used PM-IRRAS to study the pure P_2 surface exchanged with 200 μM PEG (shown in figure 5.5). After exchanging with 200 μM PEG, the bands (1240 and 1550~1750 cm^{-1}) corresponding to DNA disappear, which was similar to the spectra obtained from pure P_2 surface treated with 400 μM MCH. Therefore, the band centered at 1110 cm^{-1} was most probably due to the stretching of C-O-C [215]–[218], instead of the vibration of the PO_4^{3-} group of the DNA phosphodiester backbone. In the literature [128], thiolated diluent molecules of high molar mass are described as being able to produce greater van der Waals forces between them in the layer and to create higher driving force to remove surface bound DNA through Au-S bond. There are only few reports on the use of two-step method to form DNA/PEG surface applied in the measurement of DNA/DNA hybridization, while short thiolated oligo(ethylene glycol) (OEG) of relatively small molar mass are often used. For example, Lee [129] have studied the composition of DNA surfaces after exposure to 50 μM OEG (MW = 347 g/mol) for different time from 0.5 h to 18 h. Their results showed that a 1 h exposure to 50 μM OEG produces a DNA/OEG surface which has the strongest hybridization signal. Longer times (> 1h) of exposure lead to the removal of the DNA probes and reduce the hybridization signal. For molecules with a large molar mass, such as PEG, the concentration and exposure time may need to be decreased to avoid the large loss of probe DNA during the exchange process.

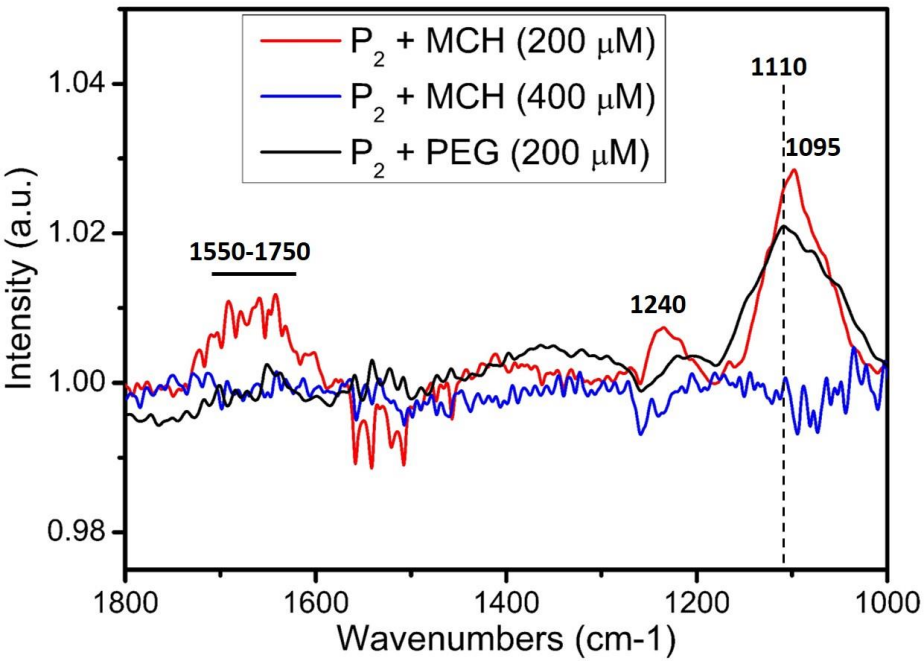

Figure 5.5 PM-IRRAS spectra of two-component surfaces of pure P_2 with 200 μM MCH, 400 μM MCH or 200 μM PEG.

In the cases of diluent-P_2 and oligo-T used as diluent molecules (shown in Figure 5.4 d and e), the hybridization signals slightly decrease from 0.08 (pure P_2 surface) to 0.06 (P_2 + 200 μM diluent P_2) and 0.07 (P_2 + 200 μM oligo-T), respectively, In addition, SPR signals of 0.02 and 0.04 were clearly observed for the negative controls for diluent-P_2 and oligo-T, respectively. This could be due to two reasons. One is that T_2 could be nonspecifically adsorbed on these two-component surfaces of P_1 with diluent-P_2 or oligo-T. The other one is occurrence of cross-contamination in the two-step method, that is, the detached P_2 from area 3 during exchanging process can bound on area 1, resulting in hybridization signal in the negative control experiment. In order to confirm whether nonspecific adsorption occurred, we prepared binary solutions containing P_1 and diluent-P_2 or oligo-T in PBS 10X, then deposited the binary solution on the whole reaction area (1+2+3) of cleaned gold surfaces and incubated overnight (one step method). As in previous SPR measurements, 1 μM of T_2 in PBS 5X was flowed on the treated gold surfaces in SPR biosensor and no signal was observed in the whole reaction area (data not shown). It indicated that T_2 could not adsorb non-specifically on the two-component surfaces of P_1 with diluent-P_2 or oligo-T. As a result, the SPR signals measured for the negative controls in the first experiments may rather result from cross-contamination (Figure 5.4 d and e). The reason why cross contamination did not occur in the cases of alkyl chain (MCH and PEG) could probably be due to the fact that they are neutral molecules. Compared to the negatively charged diluent DNA molecules, they could insert into the negatively charged DNA molecules layer more easily and quickly, preventing the re-absorption of P_2 on the area of contrast experiments.

As a conclusion, with our two-step method, 200 μM MCH in dilution process (2 h) performs best in fabrication of two-component surface to efficiently increase the hybridization signal in SPR measurement without causing great loss of probe nor cross-contamination. Therefore, 200 μM MCH in PBS 10X was used in exchanging process (2 h) to prepare two-component surfaces for all subsequent SPR measurements in this thesis.

5.2.2 Influence of ionic strength on DNA hybridization

In this section, we studied the effect of ionic strength on the P_1T_1 and P_2T_2 hybridizations at 25ºC. The sequences of P_1, T_1, P_2 and T_2 are presented in table 5.1. P_1 is complementary to T_1 and P_2 is complementary to T_2. They have different sequences but same length of 15 base pairs (bp) involved in hybridization. The double strand P_1T_1 has 67% of GC pairs, and the double strand P_2T_2 has 60% of GC pairs. Using the Santalucia's nearest-neighbor model [7], $\Delta G°_{25}$ for two double strands P_1T_1 and P_2T_2 were estimated to be 23.6 and 23.4 kcal/mol. Therefore, the double strands P_1T_1 and P_2T_2 have similar thermodynamic stabilities at 25°C. The ionic strength was varied by using different buffer solution concentrations: PBS 1X, 2X, 5X, 8X and 10X. All

these concentrations of PBS were prepared by dissolving the same amount of NaCl, KCl, Na_2HPO_4 and KH_2PO_4 into different volumes of water. For example, the resultant PBS 1X has a final concentration of 137 mM NaCl, 2.7 mM KCl, 10 mM Na_2HPO_4 and 1.8 mM KH_2PO_4. The ionic strengths of the PBS solutions were estimated by:

$$I = \frac{1}{2}\sum_{i=1}^{n} c_i z_i^2 \qquad \text{Equation 5.1}$$

where c_i is the molar concentration of ion i and Z_i is its charge number. The estimated ionic strengths of five different concentrations of PBS with Equation 5.1 are presented in Table 5.2. Depending on the

ionic strength, the Debye length λ, which is a measure of how far the electrostatic effect can be screened, is given by [219]:

$$\lambda = \sqrt{\frac{\varepsilon_r \varepsilon_0 k_B T}{2 N_A e^2 I}} \qquad \text{Equation 5.2}$$

where I is the buffer ionic strength, ε_r is the relative permittivity of the medium, ε_0 is the vacuum permittivity, k_B is the Boltzmann constant, N_A is Avogadro's number and e is the elementary charge. In the case of electrolyte solution in water and at 25ºC, the Debye length can be expressed as [220], [221]:

$$\lambda = \frac{0.304}{\sqrt{I}} \qquad \text{Equation 5.3}$$

Therefore, the Debye lengths of different concentrations of PBS at 25ºC were estimated by Equation 5.3 and are given in Table 5.2.

	PBS 1X	PBS 2X	PBS 5X	PBS 8X	PBS 10X
Ionic strength (mM)	171.5	343	857.5	1372	1715
Debye length (nm)	0.73	0.52	0.33	0.26	0.23

Table 5.2 Summary of ionic strengths and Debye lengths for different PBS concentrations.

P_1T_1 and P_2T_2 hybridization were conducted at these five different concentrations of PBS at 25°C and the sensorgrams are presented in Figure 5.6. The target solution concentrations are 1 μM in all the cases. When the ionic strength is increased, the hybridization efficiency for both P_1T_1 and P_2T_2 also increases: PBS 1X < 2X < 5X ≈ 8X ≈ 10X. This is in agreement with the work of Okahata [2], in which the hybridization rate and efficiency increase gradually with the increasing concentration of NaCl from 0.1 to 0.5 M. At high ionic strength, the electrostatic

repulsions between probe molecules are effectively screened and higher hybridization rate and efficiency are reached. These results could be supported with the estimated Debye length in PBS shown in Table 5.2. The Debye length decreases as ionic strength increases from 171.5 mM (PBS 1X) to 857.5 mM (PBS 5X), then decreases marginally from 857.5 mM (PBS 5X) to 1715 mM (PBS 10X). Therefore, DNA hybridization is only weakly influenced by salt concentrations above 5X. On the basis of these observations, we decided to conduct subsequent DNA hybridization in PBS 5X of ionic strength at 858 mM.

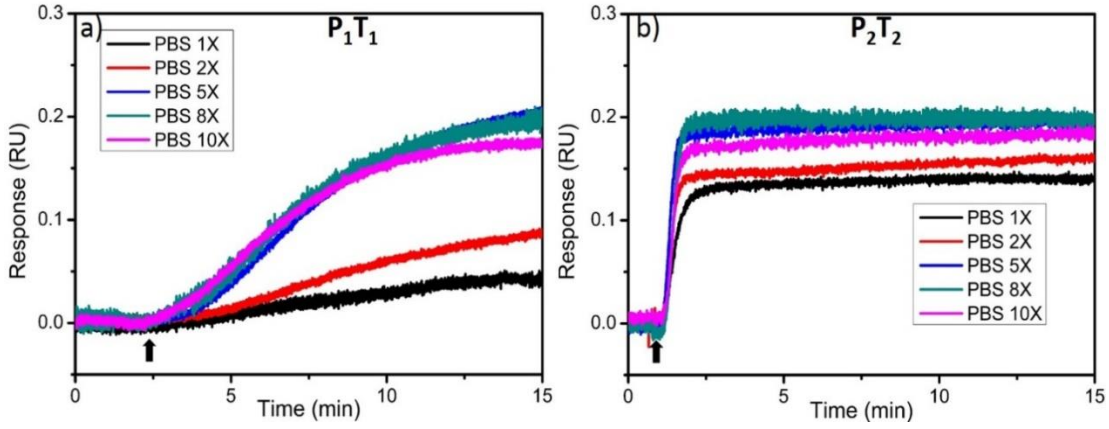

Figure 5.6 P_1T_1 (a) and P_2T_2 (b) hybridization sensorgrams at five different ionic strengths: 171.5 mM (PBS 1X), 343 mM (PBS 2X), 858 mM (PBS 5X), 1372 mM (PBS 8X) and 1715 mM (PBS 10X). The solid arrow (↑) indicates the injection of 1 μM target DNA solutions. The flow rate was fixed at 65 μl/min. All the hybridization reactions were conducted at 25°C.

However, according to the equivalent thermodynamic stability of double strands P_1T_1 and P_2T_2, it was unexpected to observe such a big difference of hybridization kinetics between them at each ionic strength under same experimental condition. Duplex P_1T_1 formed very slowly, especially at low salt concentration below PBS 5X. When the salt concentration is above PBS 5X, the formation of duplex P_1T_1 reached equilibrium after 14 min. However, it is still much slower than the kinetic of P_2T_2 formation, which can reach the equilibrium within 1 min in the same conditions. From the literature [64], the secondary structure of DNA strands, like hairpins, is described to be able to influence the hybridization efficiency and kinetic dramatically. Therefore, the slower hybridization kinetics in the case of P_1T_1 duplex formation is hypothesized to be the result of hairpin configuration of P_1 and T_1, which is investigated in next section.

5.2.3 Influence of secondary structure on DNA hybridization

Figure 5.7 displays the hairpin structures predicted by Mfold [4] under condition of 25°C and PBS 5X for P_1, T_1, P_2 and T_2 sequences. P_1 and T_1 sequences are able to form similar hairpins having 3 CG base pairing to close the loop. These two hairpins of P_1 and T_1 have predicted $\Delta G°_{25}$ and melting temperatures of -3.78 kcal/mol, 68°C and -3.77 kcal/mol, 62°C, respectively. P_2 sequence is able to form the hairpin structure having 2 CG bases paring to close the loop. However, the domain involved in the loop is not part of the sequence involved in the hybridization with T_2 and the structure is less stable. The predicted $\Delta G°_{25}$ value and melting temperature are -1.06 kcal/mol and 41°C. T_2 sequence does not form any hairpin.

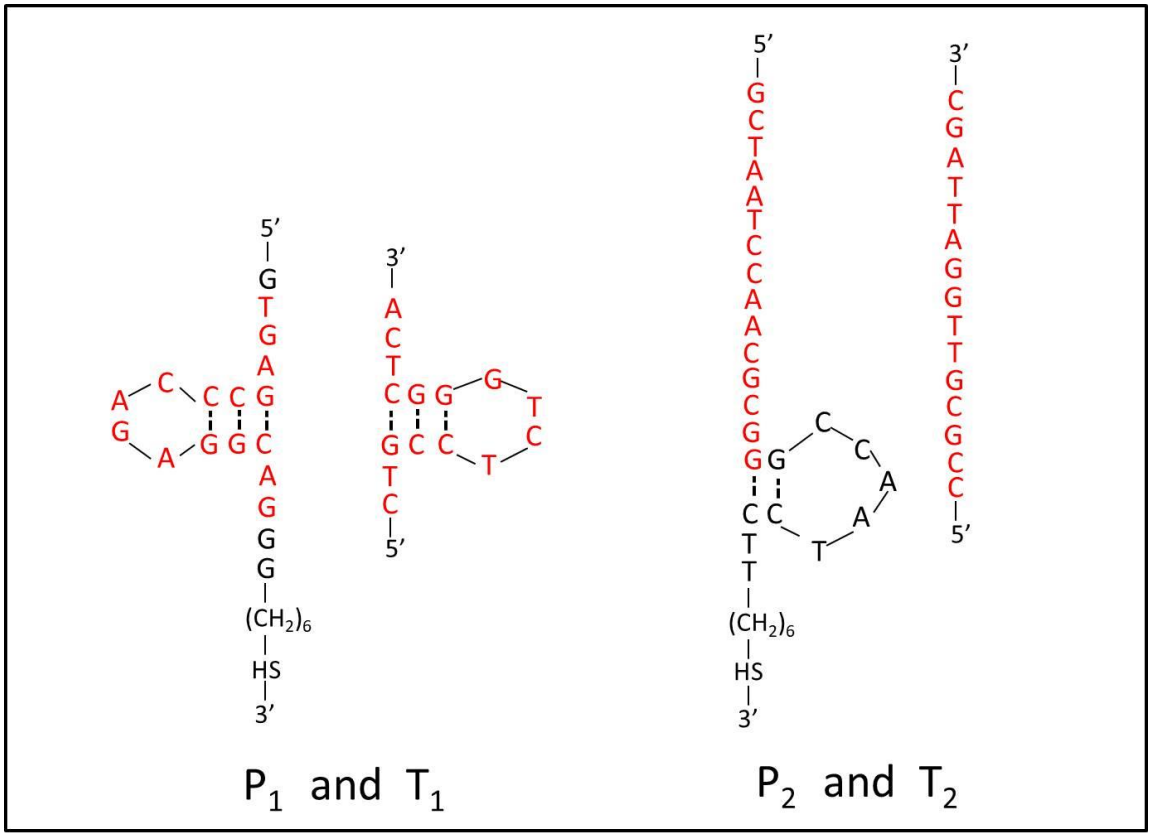

Figure 5.7 Scheme of hairpin structures of DNA sequences (P_1, T_1, P_2 and T_2), predicted by Mfold with conditions of 25°C and PBS 5X. The complementary sequences for hybridization of P_1T_1 and P_2T_2 are in red. P_1 and T_1 are two sequences having similar hairpins with 10 bp in the part of sequences involved in hybridization, while P_2 and T_2 are two sequences without hairpins at hybridization part.

In order to verify that hairpin formations could slow the P_1T_1 hybridization, we have conducted the hybridization of P_1T_1 at different temperatures of 20°C, 45°C and 65ºC. 65ºC corresponds to the melting temperature of the hairpin structure of P_1 and T_1 as estimated by Mfold. The hybridization kinetic data are presented in Figure 5.8. A clear trend in the rate and efficiency of duplex P_1T_1 formation at different temperatures is observed: 65°C>45°C>25°C. The fastest kinetic is obtained at 65°C, reaching equilibrium in less than 1 min and the hybridization efficiency increases by a factor of about 2 from 25°C to 65°C (signal increased from 0.18 to 0.36). This phenomenon was also observed by other groups [64], [222], [223].

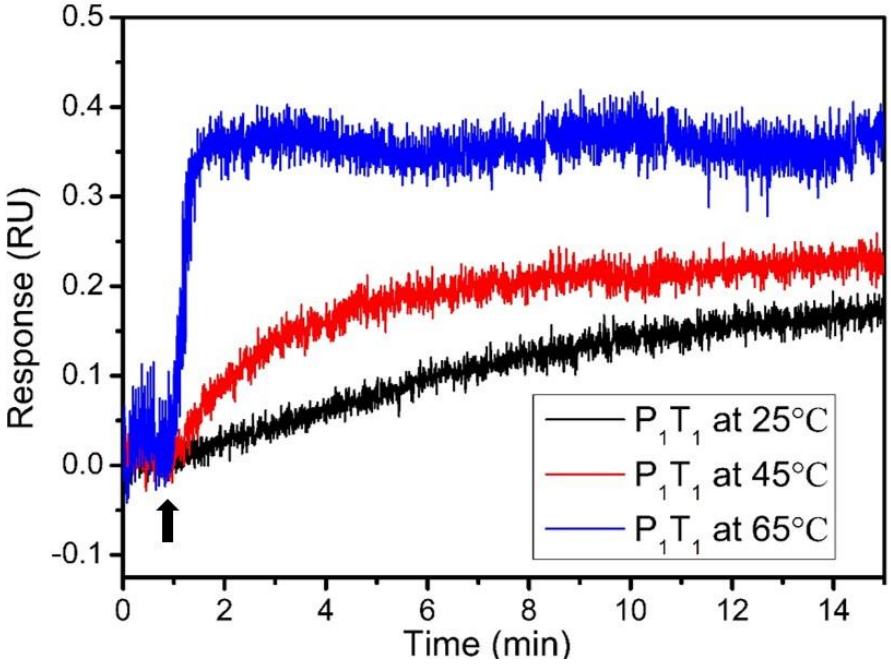

Figure 5.8 Hybridization sensorgrams of P_1T_1 at different temperature. The temperature varies from 25°C to 65°C. The solid arrow (↑) indicates the injection of 1 μM target DNA solutions. All the hybridization reactions were conducted at the flow rate of 65 μl/min and in PBS 5X.

As reported before [224], the DNA hybridization includes two processes: nucleation and zippering. Nucleation is the formation of transient intermediate with a few base pairs, and zippering is when the rest of the bases form fully bound helix. According to these two processes, the slower kinetics and limited efficiency of hybridization between DNA strands having secondary structure at low temperature could be due to two reasons. Firstly, the secondary structure decreases the number of potential nucleation sites, resulting in a longer nucleation time than for linear DNA. Secondly, in zippering, the secondary structure has to be destructed to form a complete duplex, which creates an additional reaction barrier. Indeed, a systematic

analysis on the effect of temperature on DNA hybridization with secondary structure is given in the work of Chen [191]. The apparent activation energy for the hybridization of DNA with secondary structure is proposed. At low temperature, this energy depends on the structure and can be positive. Whereas at high temperature (especially above the melting temperature of structured single stranded DNA), the apparent activation energy decreases to negative value and become structure independent. In addition, Halperin [69] proposed an extended Langmuir model to determine the equilibrium hybridization constant of DNA having hairpins. In this model, the reversible conversion between the formation and melting of hairpins in the solution is taken into account. The target DNA needs firstly to melt its hairpins and is then able to hybridize with the probe on the surface. Accordingly, hairpins reduce the initial concentration of target DNA that are actually involved in the hybridization, thereby reducing the hybridization kinetics and efficiency.

5.2.4 Repeatability test of DNA hybridization

In order to verify the repeatability of DNA hybridization measurement on the same sensorchip, we conducted five times of hybridization on the same DNA sensor chip which is regenerated by 100 mM NaOH. The T_1 - P_1 hybridization system was used in these preliminary experiments. P_1 modified by thiol group is coupled on gold surface by Au-S bond, and T_1 is the target which is complementary with P_1. The sequences are shown in Table 5.3.

P_1	5'-GTG AGC CCA GAG GCA GGG-$(CH_2)_6$-HS
T_1	5'-CTG CCT CTG GGC TCA

Table 5.3 DNA sequences used in this section. The complementary parts are in blue.

The mixed SAMs on the sensor chip used here include P_1 and Mercaptohexanol (MCH). It is fabricated by two-steps method as previously described. Figure 5.9 presents the sensorgrams of P_1T_1 hybridization repetition on the same chip regenerated by 100 mM NaOH. All the hybridizations were performed by injecting 1 µM T_1 in PBS 5X and at 25°C. There is an acceptable repeatability between these measurements. It demonstrates that regeneration step remove all bounded DNA and doesn't change the probe DNA in a way that would influence its strength or affinity towards the targets.

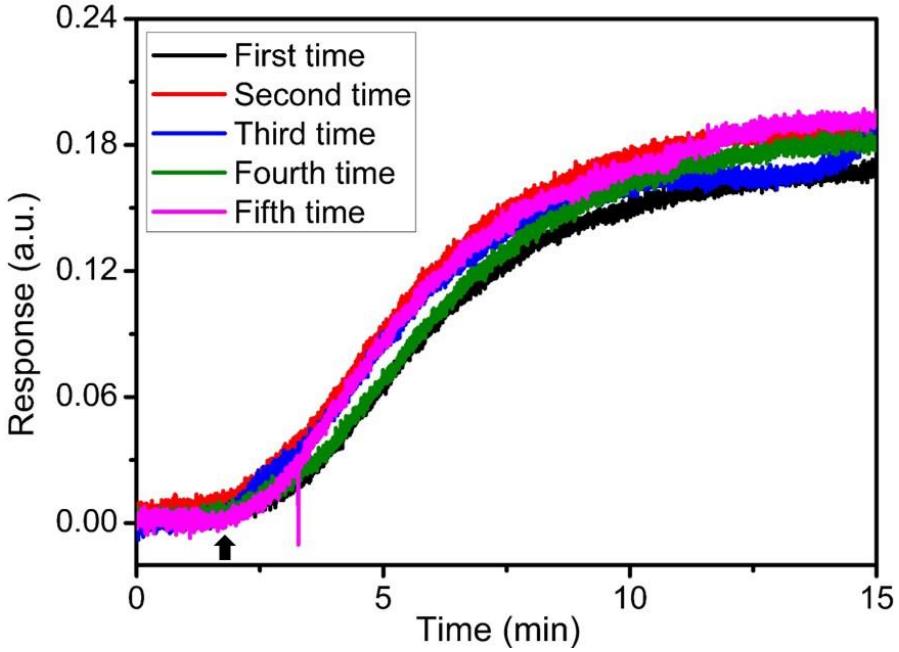

Figure 5.9 Overlay plot of sensorgrams of P_1T_1 hybridization for five times on the same sensor chip regenerated by 100 mM NaOH. The solid arrow (↑) indicates the injection of target DNA (T_1) solutions. All the hybridizations were performed by injecting 1 μM T_1 in PBS 5X and at 25°C.

5.2.5 Conclusions

In this section, we firstly compared four different molecules used as diluent molecules for the fabrication of two-component surfaces applied in our SPR measurement. Using a two-step method, exchanging with 200 μM MCH for 2 h seems to work best to efficiently increase the hybridization signal without causing much loss of probe nor cross-contamination. The resulting surfaces are used in subsequent K_d measurements of DNA hybridization by SPR.

After, the influences of ionic strength and secondary structure on DNA/DNA hybridization on surfaces were sequentially investigated using our SPR biosensor. The results showed that the effect of ionic strength on DNA hybridization becomes negligible when using PBS buffer at a concentration higher than 5X. In the case of DNA strands having secondary structures, raising the temperature can greatly increase the hybridization rate and efficiency, especially when the temperature exceeds the melting temperature of the secondary structures. Since the evanescent field fluorescence biosensor is not equiped with a heating stage, P_2 - T_2 sequences without secondary structure were preferred for K_d measurements in next section. All the hybridization of P_2T_2 are conducted in PBS 5X and at 25ºC.

5.3 Determination of DNA hybridization K_d by three surface based methods

In this section, we measured the dissociation constant K_d of the hybridization of T_2 with P_2 by three surface based methods: surface plasmon resonance biosensor, evanescent field fluorescence biosensor and fluorescent microarray.

5.3.1 Determination of DNA hybridization K_d by surface plasmon resonance

Firstly, the dissociation constant K_d of P_2T_2 hybridization was measured by surface plasmon resonance (SPR) biosensor. Figure 5.10 shows one set of hybridization curves of T_2 with P_2 on the same chip regenerated by 100 mM NaOH. All hybridizations were performed with injections of 1 ml T_2 solution at increased concentrations from 10 nM to 500 nM in PBS 5X at the flow rate of 65 µl/min. Then pure buffer was flowed through the flow cell, thus initiating the dissociation. However, the dissociation was not observed with our SPR system. This is because the DNA hybridization is a very high affinity reaction and the dissociation reaction is very slow. Therefore, it may take a long time to detect the dissociation reaction, which requires the SPR to have high sensitivity and to be stable for a long time. In our case, only the hybridization phase were recorded and analyzed.

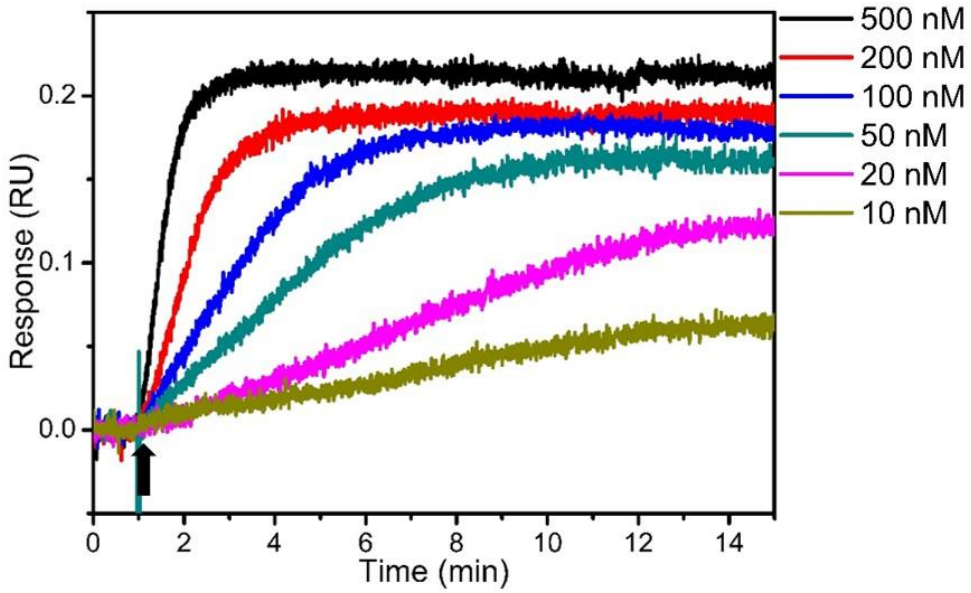

Figure 5.10 SPR sensorgrams of P_2T_2 hybridization on the same DNA chip regenerated by 100 mM NaOH. The solid arrow (↑) at t=1 min indicates the injection of the T_2 solutions at different concentrations for the recording of the hybridization phase kinetics. The target concentrations were 10, 20, 50, 100, 200, and 500 nM. All hybridizations were conducted at 25°C and in PBS 5X. The flow rate was fixed at 65 µl/min.

The real-time data obtained from SPR were interpreted using the one-step model in combination with the pseudo-first-order kinetics (described in section 1.2.2.1):

$$R(c,t) = R_{eq}(c)(1 - e^{-(t-t_0)/\tau}) \qquad \text{Equation 5.4}$$

where R_{eq} is the response at equilibrium for different target concentration c, and τ is the hybridization timescale given by:

$$\tau^{-1} = k_{on}c + k_{off} \qquad \text{Equation 5.5}$$

By fitting each hybridization kinetic phase with the one-step kinetic model (Equation 5.4), both the kinetic (τ^{-1}) and equilibrium (R_{eq}) information can be obtained. However, we could not find a satisfactory fit to the experimental data with a Langmuir model despite there was no experimental evidence of mass transport limitation (experiments run at higher flow rate). Therefore we decided to perform two fitting methods, one focusing on the early time range after the target injection (later called kinetic analysis) and one focusing on the value reached at longer times near equilibrium (later called equilibrium analysis). For the kinetic analysis, we plot the reciprocal of the hybridization timescale τ^{-1} obtained by fitting *vs.* target concentration c (shown in Figure 5.11). The hybridization rate constant k_{on} and the denaturation rate constant k_{off} were then obtained as the slope and intercept of τ^{-1} *vs.* c plot. Then, the dissociation constant K_d was calculated by k_{off}/k_{on}. For equilibrium analysis, we plot the R_{eq} fitted values *vs.* target concentration to obtain the hybridization binding isotherm and the K_d values were calculated thanks to the linear regression with Equation 5.6 (illustrated in section 1.2.2.2).

$$\frac{c}{R_{eq}} = \frac{1}{R_{max}}c + \frac{K_d}{R_{max}} \qquad \text{Equation 5.6}$$

The SPR measurements were repeated three times, and the resulting rate and dissociation constants are displayed in Table 5.4. The mean values are the average of these three independent measurements. By comparing the values of K_d estimated from the kinetic and equilibrium analysis, we observed a good agreement with both values within the error bars. It indicates that such one-step Langmuir kinetic model interpretes well the kinetic of DNA hybridization in our SPR system. In addition, our rate and dissociation constants are in the same order of magnitude as the results reported by other groups who used DNA strand of similar length [1], [225].

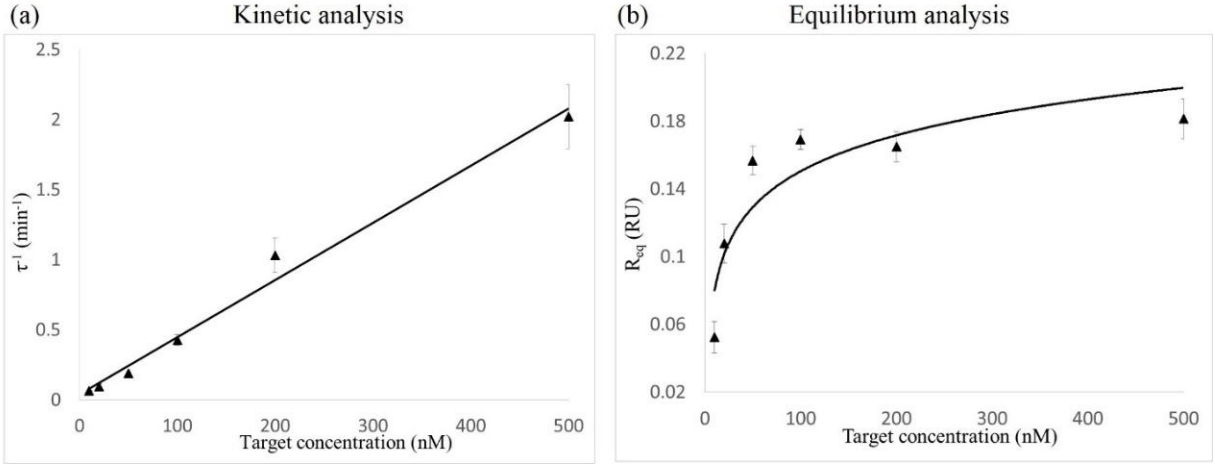

Figure 5.11 (a) Plot of 1/τ, obtained from the hybridization curves (Figure 5.10) with one-step kinetic model, as a function of the target concentration c. (b) Hybridization binding isotherm of equilibrium analysis: R_{eq} fitted values as a function of target concentration. The data points were taken from the mean values of three measurements. The error bars represent the standard deviation of these three measurements.

	k_{on} ($nM^{-1}min^{-1}$)	k_{off} (min^{-1})	K_d-kinetic (nM)[a]	K_d-equilibrium (nM)
First time	$(3.0\pm0.1)*10^{-3}$	0.075±0.029	25	16±5
Second time	$(3.8\pm0.2)*10^{-3}$	0.039±0.026	10	20±7
Third time	$(4.5\pm0.3)*10^{-3}$	0.094±0.05	21	12±2
Mean value	$(3.8\pm0.6)*10^{-3}$	0.072±0.024	19±6	16±3

Table 5.4 Rate constants and dissociation constants for P_2T_2 hybridization obtained from three independent measurements on three samples. Mean value is the average of these three measurements. Typical R^2 values for all the fitting were above 0.95. [a] Calculated from k_{off}/k_{on}.

5.3.2 Determination of DNA hybridization K_d by evanescent field fluorescence biosensor

Next, evanescent field fluorescence biosensor was used to study the kinetic and equilibrium parameters of P_2T_2 hybridization at two different probe densities. The P_2 used in evanescent field fluorescence biosensor was modified by biotin and labeled with cy5, and T_2 was also labeled with Cy5 (shown in Table 5.5).

P_2	5'-Cy5-GCT AAT CCA ACG CGG GCC AAT CCT T-$(CH_2)_6$-biotin
T_2	5'-Cy5-CCG CGT TGG ATT AGC

Table 5.5 DNA sequences used in evanescent field fluorescence biosensor. The complementary parts are in red color.

The immobilization of P_2 on the chip was driven by biotin-streptavidin interaction and monitored by fluorescence measurement. Two surfaces with different P_2 densities were obtained by using different concentrations of P_2 solutions for immobilization. Figure 5.12 shows fluorescence intensity as a function of the concentrations of P_2 solutions poured in the cell (10 and 20 nM). The fluorescence intensity reported in Figure 5.12 were the mean values of fluorescence intensity (FI) of 8 wells in one chip. They deviated by less than 7% for 10 nM and 13% for 20 nM. The fluorescence intensity arising from the solutions (10 nM and 20 nM) was negligible with respect to the one originating from bound probes. Therefore, the measured fluorescence was considered to be related to P_2 surface density.

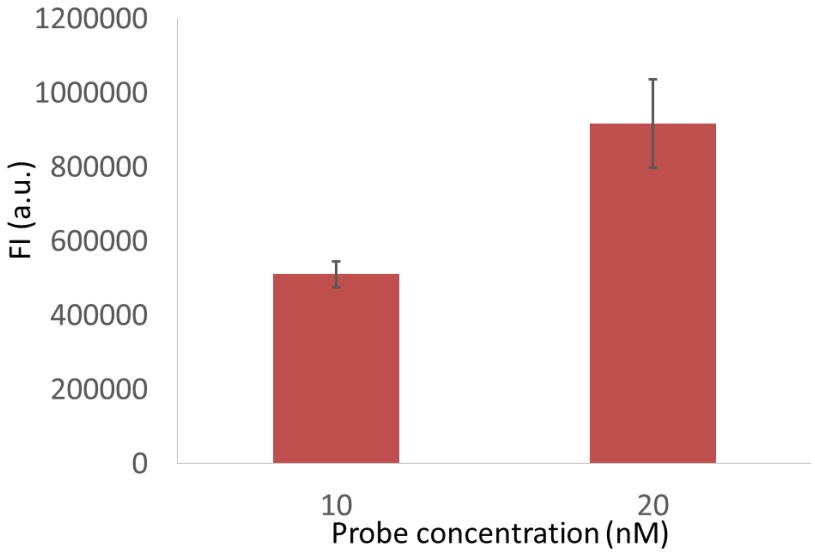

Figure 5.12 Fluorescence intensity recorded using 10 and 20 nM of biotinilated DNA (P_2) in streptavidin modified wells.

The evanescent-field fluorescence biosensor allows detecting the DNA hybridization on surfaces by monitoring the fluorescence intensity in real time. Figure 5.13 shows the sensorgrams of P_2T_2 hybridization on the surfaces deposited with 10 and 20 nM of P_2 solutions. Hybridization experiments were conducted by incubation with 50 µl T_2 solutions at 6 different concentrations: 10, 20, 50, 100, 200, and 500 nM in a static mode (no flow). All hybridizations were carried out at 25°C and in PBS 5X.

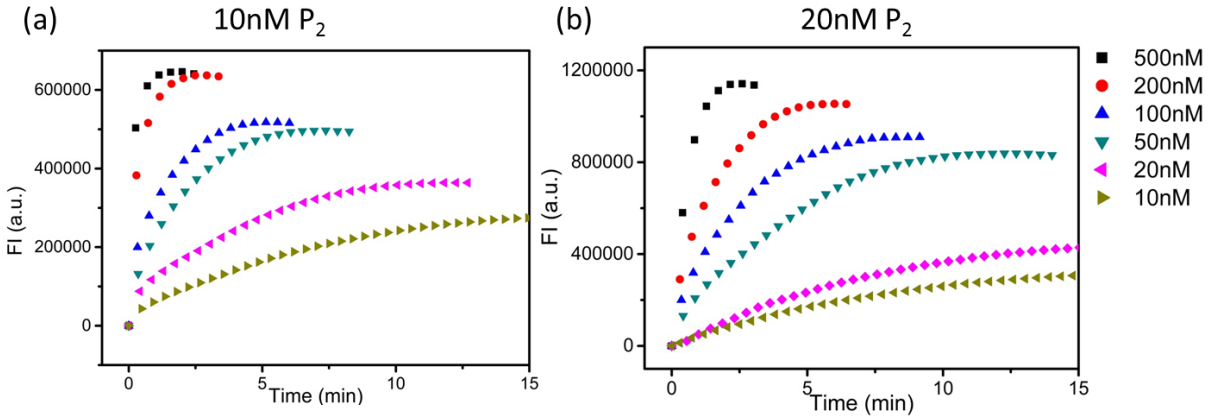

Figure 5.13 Real-time observation of DNA/DNA hybridization at the surfaces deposited with 10 (a) and 20 nM (b) P_2 solutions. The T_2 concentrations were 10, 20, 50, 100, 200, and 500 nM respectively. All hybridization reactions were carried out at 25°C and in PBS 5X.

Similarly to SPR measurements, the real-time hybridization data (Figure 5.13) obtained from the evanescent field fluorescent biosensor were interpreted using one-step model in combination with pseudo-first-order kinetics (Equation 5.4). The kinetic analysis was performed by plotting the mean values of three measurements of $1/\tau$ as a function of target concentration c (presented in Figure 5.14 a). Linear regression was performed for each surface probe density, leading to an estimation of rate constants k_{on} and k_{off}. K_d was deduced by k_{off}/k_{on}. Figure 5.14 b presents the equilibrium analysis of hybridization isotherm obtained by plot the FI_{eq} fitted values from sensorgrams with increased concentration c of target for each probe density, and the K_d values were predicted thanks to linear regression with Equation 5.6.

The real-time fluorescence measurements were repeated three times for each probe density, and the resulting rates and dissociation constants were averaged and summarized in Table 5.6. The dissociation constant K_d obtained from these tests were on the same order of magnitude with the results obtained by SPR. In addition, as the surface probe density increases (from 10 nM to 20 nM), association rate constant k_{on} decreases by a large margin, while dissociation rate constant k_{off} decreases slightly, which leads a slight increase of K_d derived by k_{off}/k_{on}.

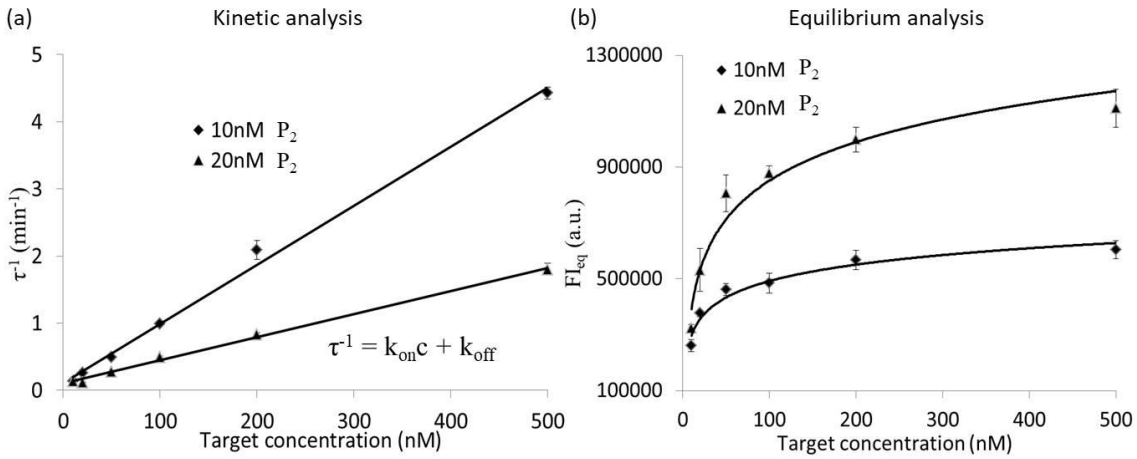

Figure 5.14 (a) Plots of 1/τ, obtained from the hybridization curves (Figure 5.13) with one-step kinetic model, as a function of the target (T_2) concentration for two surfaces deposited with 10 and 20 nM P_2 solutions. (b) Hybridization binding isotherms on two surfaces deposited with 10 and 20 nM P_2 solutions: FI_{eq} fitted values from sensorgrams as a function of target concentration. The data points were taken from the mean values of three independent measurements at three samples. The error bars represent the standard deviation of these replicate measurements.

	k_{on} ($nM^{-1}min^{-1}$)	**k_{off} (min^{-1})**	**K_d-kinetic (nM)**	**K_d-equilibrium (nM)**
10 nM P_2	$(7.2\pm0.3)*10^{-3}$	0.09±0.015	14±5	16±3
20 nM P_2	$(3.9\pm0.3)*10^{-3}$	0.081±0.003	21±1	27±3

Table 5.6 Rate constants and dissociation constants of P_2T_2 hybridization at the surfaces deposited with 10 nM and 20 nM P_2 solutions. The values were averaged from three independent measurements on three samples. For each measurement, typical R^2 value for the fitting was above 0.95.

5.3.3 Determination of DNA hybridization K_d by fluorescent microarray

Finally, we used fluorescent microarray to measure the dissociation constant K_d of P_2T_2 hybridization. The P_2 used in fluorescent microarray was modified by NH_2 and labeled with Cy3, and T_2 was labeled with Cy5 (show in Table 5.7).

P_2	5'-Cy3-GCT AAT CCA ACG CGG GCC AAT CCT T-$(CH_2)_6$-NH_2
T_2	5'-Cy5-CCG CGT TGG ATT AGC

Table 5.7 DNA sequences used in fluorescent microarray. Complementary parts were in red color.

The immobilization of P_2 on the glass was achieved by NHS-ester chemistry, and the resulting probe density was evaluated by fluorescence measurement at 532 nm (FI_{532}). The influence of relative surface densities of DNA probes on the measurement of the dissociation constant value was also investigated. This parameter can be varied by using different concentrations in the spotting solutions [142]. Here, four different concentrations (50, 100, 500, 1000 nM) of P_2 solution were used to fabricate four surfaces with different probe densities. Figure 5.15 shows the fluorescence measurement at 532 nm (FI_{532}) emitted by P_2 bound on surface as a function of concentrations of spotted P_2 solution. The FI_{532} presented in Figure 5.15 were the mean values of 640 spots (32 spots * 20 wells) and deviate by less than 4%, 11%, 8% and 4% for P_2 solution at 50, 100, 500 and 1000 nM, respectively. The FI_{532} value was considered to be related to P_2 surface density.

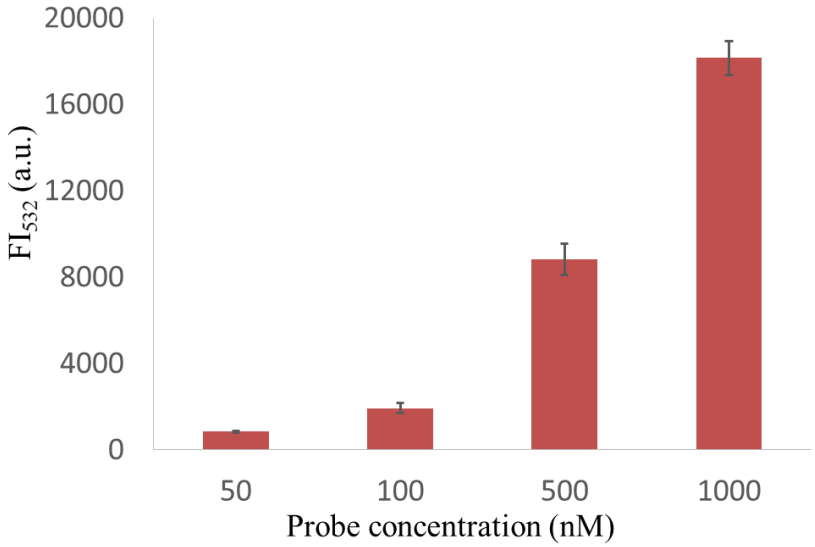

Figure 5.15 Fluorescence intensity at 532 nm (FI_{532}) obtained with the concentration of P_2 spotted at 50, 100, 500 and 1000 nM.

For each P_2 surface density, the hybridization isotherm was obtained by incubation with increasing target (T_2) concentrations from 0.01 to 2000 nM in a static mode (no flow). Figure 5.16 shows the fluorescence intensity at 635 nm (FI_{635}) emitted by T_2 hybridized to P_2 on surfaces as a function of T_2 concentrations used. The FI_{635} reported in Figure 5.16 was the mean value of 32 spots. As with the two other methods, all the DNA hybridizations were conducted at 25°C and in PBS 5X.

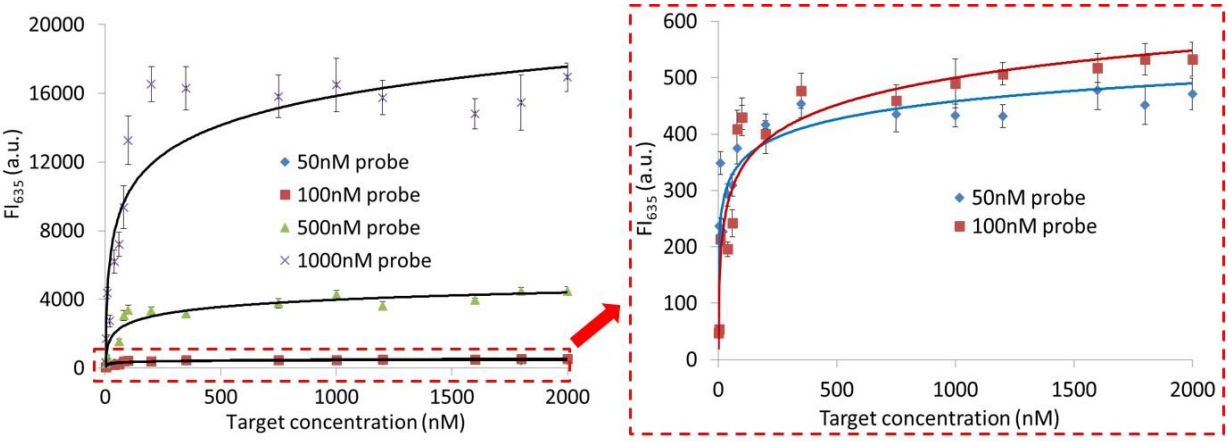

Figure 5.16 (a) Hybridization binding isotherms on four surfaces deposited with 50, 100, 500 and 1000 nM probe DNA (P_2) solutions, (b) Enlargement of area marked by red box in (a)

The dissociation constant K_d for each probe density was calculated thanks to linear regression (Equation 5.6) and presented in Table 5.8. The values obtained by fluorescent microarray were of the same order of magnitude as that obtained by SPR and evanescent field fluorescence biosensor. In addition, we also observed an increase of dissociation constant as the probe density increases. There was no further experiment for the probe concentration beyond 1000 nM. Therefore, we cannot conclude that the dissociation constant reaches a plateau after the probe concentration increased to 500 nM.

	50nM probe	100nM probe	500nM probe	1000nM probe
K_d-equilibrium (nM)	7±2	37±9	54±12	53±11

Table 5.8 Dissociation constants of DNA hybridization, obtained from fluorescence microarray, at the surfaces deposited with 50, 100, 500 and 1000 nM probe (P_2) solutions. The deviation is obtained from linear fitting with Equation 5.6. Typical R^2 values for the fitting were all above 0.99.

There have been lots of reports on the effect of probe density on DNA hybridization, and most of them found the high probe density has a negative influence on the kinetics and efficiency of DNA hybridization. For example, Peterson and co-workers [12] found that as the probe density increases the hybridization efficiency after 30 min varied from 95 to 15% and the hybridization kinetics is slower. The same phenomenon was observed by Su [11], when the surface density increases from $2*10^{12}$ to $6*10^{12}$ molecules/cm^2, the hybridization efficiency decreases from 100% to 50%. Steel *et al* [133] reported that the hybridization efficiency could reach up to 100% when probe density is less than $4*10^{12}$ molecules/cm^2, and fall off sharply when it exceeds $4*10^{12}$ molecules/cm^2. Since K_d is related to the thermodynamic property of hybridization, it can be deduced that high probe density may impose an additional thermodynamic barrier for DNA hybridization compared to lower probe density. This additional thermodynamic barrier at high surface probe density is not yet fully understood but is likely to be due to a combination of effects, including lower degree of freedom of surface bound DNA and high steric hindrance [12].

Indeed, Dugas *et al* [9] has investigated the density of DNA probes immobilized by NHS-ester chemistry on glass, which is the same method as we used. The results showed that 10 μM DNA probe solution can give a surface probe density at around $2*10^{12}$ molecules/cm^2. Considering that the highest concentration of DNA probe solution used in our case is 1 μM, the resulting probe surface density is probably less than $2*10^{12}$ molecules/cm^2, which is less than that reported in the literatures [11] [12] [133]. However, the techniques used to study DNA surface densities in literatures varied with each other, including SPR [12], QCM [11] and electrochemistry [133], while Dugas [9] used radioactivity analysis. Therefore, the probe densities determined by different techniques may vary with a different extent from the actual values. Furthermore, due to the different immobilization methods used, the surface densities of "activated DNA probe" (standing up on surfaces) could be different under the same measured surface probe density. Therefore, the comparison of the present results with literature data is difficult.

It should be noticed that both evanescent field fluorescence biosensor and fluorescent microarray were performed in static flow mode. A potential problem in the data analysis is the depletion of target concentration in the solution during the reactions. Both pseudo-first kinetic model and Langmuir model are based on the assumption that concentration of free target remains constant during the reactions. Therefore, the depletion of target could result in a decrease of the amount of probe-target complex at equilibrium, leading to an overestimated K_d value [226], [227]. However, for most interactions measured under normal conditions (medium

affinity and probe capacity systems) this effect is small [228]. In our case, considering the high binding affinity between DNA strands, this may contribute to the increase of K_d.

5.4 Comparison of three surface based methods

In this section, a comparison of three surface based methods for the measurement of DNA hybridization in terms of operability and the quality of data obtained is given.

For SPR and evanescent field fluorescent, it was possible to compare two different approaches for data mining. The first one is based on the fitting of a set of kinetic curves and the second one on extracting the K_d from Langmuir Isotherms. Both techniques gave similar results.

We also studied the effect of probe surface density for the three techniques on the determination of the dissociation constant. Actually, our data seems to indicate that the main source of variability for K_d determination is the surface probe density. Consequently, comparison of the three techniques is significant only if at least the surface densities are similar.

The DNA hybridization monitored by surface plasmon resonance is easy to carry out and can be done without any labelling. The possibility to easily regenerate and reuse sensor chips with no significant loss in assay performance is a major attraction in the quest for a SPR assay. Furthermore, since the SPR assay is performed in fluidic mode, the target concentration will always be constant, which impede the influence of target depletion on the measurement of K_d based on some simple fitting models, such as: pseudo-first kinetic and Langmuir model. However in our system, the fluidic mode requires relatively more targets than the static mode. In our SPR measurement, 1000 µl DNA target solution at each concentration was used in single measurement, while the evanescent field fluorescence biosensor and fluorescent microarray require 20 µl and 1.5-2 µl of DNA target solution at each concentration, respectively. By now, the combination of SPR imaging and dedicated microfluidic "lab-on-a-chip" allow the measurements of many biomolecular interactions simultaneously, which could effectively reduce the measurement time and sample consumption [10], [229]–[231].

The evanescent field fluorescence biosensor performing on real-time basis could provide kinetic data of DNA hybridization, but require labeling the targets with fluorescent dyes. For the chips used in evanescent field fluorescence biosensor, the immobilization of streptavidin was achieved by physical adsorption which has some potential drawbacks over chemisorption, such as lack of control on the adsorption process, the potential for protein denaturation upon adsorption [94], [95], [232]. This could cause the low reproducibility of subsequent immobilization of biotin-DNA, which is the amount of immobilized biotin-DNA may vary

greatly at the same concentration of biotin-DNA solution used. In my experiments, the DNA surface densities in some wells deviated from the mean values two times (data not shown), and these wells would not be used in the measurement of hybridization K_d.

Fluorescent microarray is a very sensitive method, especially for the detection of small molecules. Since it's not performed on real-time basis, it can only give end-point data. However, the end-point data were obtained after washing process to remove the target solution. The washing process may promote the dissociation and destroy the equilibrium state of reactions, leading to the K_d overestimated. This is particularly evident in some low-affinity reactions. In our case, the K_d given by fluorescent microarray is still comparable with that obtained by the other two methods, this is due to the fact that the DNA hybridization is a very high affinity reaction so that the washing process with only PBS buffer after hybridization doesn't has much effect on the formed DNA duplex. This is also observed in our SPR experiments.

5.5 Conclusions

In this chapter, we aimed at optimizing the experimental conditions for DNA hybridization on gold substrates and at comparing three surface-based techniques for the K_d measurements of DNA duplex formation.

First, the effect of pH on thiolated DNA grafting on gold surface was studied by PM-IRRAS. Our results showed that the acidic environment (pH=5.5) seemed beneficial for thiolated DNA grafting on gold surface.

Next, a two step method consisting of 1) DNA probe grafting followed by 2) an exchange reaction (dilution) with a diluent molecule was performed to form mixed SAMs. The influence on DNA hybridization of parameters including the nature, concentration of diluent molecules and dilution time have been studied. Best results were obtained after dilution with a 200 µM MCH solution for 2 h. The ionic strength of the running buffer employed during DNA duplex formation was also studied. To this aim, PBS solutions at different concentrations were used. The measured hybridization signal increased from PBS 1X to PBS 5X which is probably due to a decrease of the electrostatic repulsion between DNA strands. Higher PBS concentrations did not lead to a significant improvement. In addition, it has been found that secondary structures seriously decrease the DNA hybridization kinetics.

The hybridization K_d of the probe P_2 with the target T_2 was measured by SPR, evanescent field fluorescence and fluorescent microarray. The measured K_ds spanned from 7 to 54 nM. We

found that for a given technique the K_ds varied as a function of probe density. Indeed, higher probe densities led to an increase of DNA hybridization K_d (lower affinity). The reasons for this could relate to higher steric hinderance and/or lower freedom of the immobilized probes.

Conclusions and outlooks

Conclusions and outlooks

In this thesis, we have presented the validation of our homemade SPR system and optimization of gold surfaces to study DNA/DNA hybridization. Furthermore, K_d measurements of DNA/DNA hybridization by three surface-based methods (SPR biosensor, evanescent field fluorescence biosensor and fluorescent microarray) were described and compared with each other.

First of all, we validated the SPR system by monitoring the SPR signal as the concentration of PBS buffer changed. The results showed the measured SPR signal is linearly related to the concentration of PBS buffer which is linearly related to the refractive index in the near vicinity of sensor chips. In addition, we demonstrated that the y-axis Response Unit (RU) in our experiments can be approximatively converted in 'Biacore Response Unit' by multiplying the values by ~1400. After, we investigated the repeatability of DNA hybridization measurement on the same sensorchip regenerated by 100 mM NaOH. An acceptable repeatability was found over five mesurements. This indicates that multiple tests (at least 5 times) can be conducted on the same sensor chip using 100 mM NaOH as regeneration solution which can leave the activity of the DNA probe intact.

Secondly, in order to obtain a clean and unoxidized gold surface for the fabrication of DNA chip used in SPR, two cleaning methods (piranha solution and oxygen plasma) were compared. We optimized the assay conditions of piranha solution cleaning (H_2SO_4/H_2O_2 volume ratio, temperature and time) and found that the optimal cleaning condition are as follows: H_2SO_4/H_2O_2 volume ratio at 3:1, preheating the sulfuric acid to 90°C and cleaning for 5 min. The gold surfaces after optimized piranha solution and oxygen plasma cleaning were compared in the aspects of water wettability, roughness, cleanness, oxidation and thiolated DNA grafting. The results showed that the gold slides cleaned by the oxygen plasma have higher water wettability (0°) than that (~20°) cleaned by the optimized piranha solution. The surface topography was not affected by the surface cleaning in both cases. In addition, for the two methods, a stable gold oxide layer could not be detected by XPS. Therefore, the better water wettability of gold surface after oxygen plasma cleaning is most probably due to an improved surface cleanness. The subsequent thiolated DNA immobilization on the cleaned gold surfaces didn't show significant difference between these two cleaning methods. It indicates these two cleaning methods can be used as alternatives to each other for preconditioning gold surfaces applied in thiolated DNA immobilization.

Thirdly, we optimized the conditions for DNA/DNA hybridization on in-house gold substrates, the influence of parameters including diluent molecules in mixed SAMs, ionic strength and secondary structure were evaluated. The dilution of the probe on the surface of the chip was performed usind a two-step method consisting of 1) DNA probe grafting followed by 2) an exchange reaction with the diluent molecule. The results showed, that exchanging with 200 μM MCH for 2 h seems to work best to efficiently increase the hybridization signal without causing lots loss of probe and cross-contamination. The effect of ionic strength on DNA hybridization was low for PBS buffer higher than 5X. It is attributed to the fact that the Debye length is only weakly affected for higher ionic strengh. In addition, the secondary structure has been found to dramatically decrease the hybridization efficiency and kinetics. Therefore, DNA strands that doesn't have a secondary structure at room temperature were used for the hybridization K_d measurement by SPR biosensor. The measured K_d by SPR biosensor was found to be the same order of magnitude as that obtained by evanescent field fluorescence biosensor and fluorescent microarray. Furthermore, it has been found that high surface probe densities could lead to an increase of DNA hybridization K_d (lower affinity). This may be due to two reasons. One is that a high surface probe density leads to a high steric hindrance and lower degree of freedom of surface bound DNA. The other is that the high surface probe density and binding affinity leads to the consumption of a large number of target DNA molecules which cannot be neglected in static mode operation and thus leads to overestimation of K_d.

Eventually, we compared these three surface based techniques: SPR biosensor, evanescent field fluorescence biosensor and fluorescent microarray for measuring DNA/DNA hybridization. SPR biosensor is a real-time monitoring system and does not require any kind of labeling of the sample. It runs in fluidic mode, so it can eliminate the effect of sample depletion on the K_d measurement by a simple model. But this also means that it needs more samples than static mode in our system. The evanescent field fluorescemce biosensor is also a real-time detection system, while it is performed in static mode and need to label the sample. The first step of probe immobilization is the physical adsorption of streptavidin, which has some potential drawbacks, such as lack of control on the adsorption process, its denaturation. These could lead to lower reproducibility of probe immobilization. Fluorescent microarray is a high sensitive method that requires very small amount of samples. However, it can only provide end-point data. For some low-affinity reactions, the cleaning process to remove the unbound targets may destroy the original equilibrium state, which could affect the measurement of K_d.

Future work will be focused on the following two aspects. (1) The homemade SPR biosensor will be used for measuring the K_d of interaction between lectin LecA from *Pseudomonas*

aeruginosa (PA) and glycoclusters. After, the K_d will be compared with that obtained by DNA directed immobilization (DDI) based glycocluster microarray. (2) The K_d of the lectin-glycocluster interaction at different temperatures will be measured by SPR biosensor and DDI microarrays, and then the thermodynamic analysis of the interaction will be conducted by the van't Hoff equation to obtain the entropy and enthalpy of the interaction.

References

References:

[1] J. B. Fiche, A. Buhot, R. Calemczuk, and T. Livache, "Temperature Effects on DNA Chip Experiments from Surface Plasmon Resonance Imaging: Isotherms and Melting Curves," *Biophys. J.*, vol. 92, no. 3, pp. 935–946, Feb. 2007.

[2] Y. Okahata, M. Kawase, K. Niikura, F. Ohtake, H. Furusawa, and Y. Ebara, "Kinetic Measurements of DNA Hybridization on an Oligonucleotide-Immobilized 27-MHz Quartz Crystal Microbalance," *Anal. Chem.*, vol. 70, no. 7, pp. 1288–1296, Apr. 1998.

[3] J. Zhang, H. P. Lang, G. Yoshikawa, and C. Gerber, "Optimization of DNA Hybridization Efficiency by pH-Driven Nanomechanical Bending," *Langmuir*, vol. 28, no. 15, pp. 6494–6501, Apr. 2012.

[4] M. Zuker, "Mfold web server for nucleic acid folding and hybridization prediction," *Nucleic Acids Res.*, vol. 31, no. 13, pp. 3406–3415, Jul. 2003.

[5] R. Owczarzy *et al.*, "IDT SciTools: a suite for analysis and design of nucleic acid oligomers," *Nucleic Acids Res.*, vol. 36, no. suppl_2, pp. W163–W169, Jul. 2008.

[6] Santalucia John, H. T. Allawi, and P. A. Seneviratne, "Improved Nearest-Neighbor Parameters for Predicting DNA Duplex Stability," *Biochemistry*, vol. 35, no. 11, pp. 3555–3562, Jan. 1996.

[7] J. Santalucia, "A unified view of polymer, dumbbell, and oligonucleotide DNA nearest-neighbor thermodynamics," *Proc. Natl. Acad. Sci.*, vol. 95, no. 4, pp. 1460–1465, Feb. 1998.

[8] N. Peyret, P. A. Seneviratne, H. T. Allawi, and J. Santalucia, "Nearest-Neighbor Thermodynamics and NMR of DNA Sequences with Internal A·A, C·C, G·G, and T·T Mismatches," *Biochemistry*, vol. 38, no. 12, pp. 3468–3477, Mar. 1999.

[9] V. Dugas, G. Depret, Y. Chevalier, X. Nesme, and É. Souteyrand, "Immobilization of single-stranded DNA fragments to solid surfaces and their repeatable specific hybridization: covalent binding or adsorption," *Sens. Actuators B Chem.*, vol. 101, no. 1, pp. 112–121, Jun. 2004.

[10] I. Mannelli, L. Lecerf, M. Guerrouache, M. Goossens, M. C. Millot, and M. Canva, "DNA immobilisation procedures for surface plasmon resonance imaging (SPRI) based microarray systems.," *Biosens. Bioelectron.*, vol. 22, no. 6, pp. 803–809, Jan. 2007.

[11] X. Su, Y.-J. Wu, R. Robelek, and W. Knoll, "Surface Plasmon Resonance Spectroscopy and Quartz Crystal Microbalance Study of Streptavidin Film Structure Effects on Biotinylated DNA Assembly and Target DNA Hybridization," *Langmuir*, vol. 21, no. 1, pp. 348–353, Jan. 2005.

[12] A. W. Peterson, R. J. Heaton, and R. M. Georgiadis, "The effect of surface probe density on DNA hybridization," *Nucleic Acids Res.*, vol. 29, no. 24, pp. 5163–5168, Dec. 2001.

[13] C.-Y. Lee, P. Gong, G. M. Harbers, D. W. Grainger, D. G. Castner, and L. J. Gamble, "Surface coverage and structure of mixed DNA/alkylthiol monolayers on gold: characterization by XPS,

NEXAFS, and fluorescence intensity measurements," *Anal. Chem.*, vol. 78, no. 10, pp. 3316–3325, May 2006.

[14] J. Xu and S. L. Craig, "Thermodynamics of DNA Hybridization on Gold Nanoparticles," *J. Am. Chem. Soc.*, vol. 127, no. 38, pp. 13227–13231, Sep. 2005.

[15] L. M. Demers *et al.*, "A fluorescence-based method for determining the surface coverage and hybridization efficiency of thiol-capped oligonucleotides bound to gold thin films and nanoparticles," *Anal. Chem.*, vol. 72, no. 22, pp. 5535–5541, Nov. 2000.

[16] S. Peeters *et al.*, "Impact of spacers on the hybridization efficiency of mixed self-assembled DNA/alkanethiol films," *Biosens. Bioelectron.*, vol. 24, no. 1, pp. 72–77, Sep. 2008.

[17] M. Fried and D. M. Crothers, "Equilibria and kinetics of lac repressor-operator interactions by polyacrylamide gel electrophoresis," *Nucleic Acids Res.*, vol. 9, no. 23, pp. 6505–6525, Dec. 1981.

[18] M. M. Garner and A. Revzin, "A gel electrophoresis method for quantifying the binding of proteins to specific DNA regions: application to components of the Escherichia coli lactose operon regulatory system," *Nucleic Acids Res.*, vol. 9, no. 13, pp. 3047–3060, Jul. 1981.

[19] R. N. Knibbs, N. Agrwal, J. L. Wang, and I. J. Goldstein, "Carbohydrate-binding protein 35. II. Analysis of the interaction of the recombinant polypeptide with saccharides," *J. Biol. Chem.*, vol. 268, no. 20, pp. 14940–14947, Jul. 1993.

[20] J. Oravcova´, B. Bo¨hs, and W. Lindner, "Drug-protein binding studies new trends in analytical and experimental methodology," *J. Chromatogr. B. Biomed. Sci. App.*, vol. 677, no. 1, pp. 1–28, Feb. 1996.

[21] Q. Deng, I. German, D. Buchanan, and R. T. Kennedy, "Retention and Separation of Adenosine and Analogues by Affinity Chromatography with an Aptamer Stationary Phase," *Anal. Chem.*, vol. 73, no. 22, pp. 5415–5421, Nov. 2001.

[22] J. Hirabayashi *et al.*, "Oligosaccharide specificity of galectins: a search by frontal affinity chromatography," *Biochim. Biophys. Acta BBA - Gen. Subj.*, vol. 1572, no. 2, pp. 232–254, Sep. 2002.

[23] S. D. Mendonsa and M. T. Bowser, "In Vitro Evolution of Functional DNA Using Capillary Electrophoresis," *J. Am. Chem. Soc.*, vol. 126, no. 1, pp. 20–21, Jan. 2004.

[24] F. Banères-Roquet, M. Gualtieri, P. Villain-Guillot, M. Pugnière, and J.-P. Leonetti, "Use of a Surface Plasmon Resonance Method To Investigate Antibiotic and Plasma Protein Interactions," *Antimicrob. Agents Chemother.*, vol. 53, no. 4, pp. 1528–1531, Apr. 2009.

[25] C. Jiang and D. W. Armstrong, "Use of CE for the determination of binding constants," *Electrophoresis*, vol. 31, no. 1, pp. 17–27, Jan. 2010.

[26] M. Jing and M. T. Bowser, "Methods for measuring aptamer-protein equilibria: A review," *Anal. Chim. Acta*, vol. 686, no. 1, pp. 9–18, Feb. 2011.

[27] N. Jonker, J. Kool, H. Irth, and W. M. A. Niessen, "Recent developments in protein-ligand affinity mass spectrometry," *Anal. Bioanal. Chem.*, vol. 399, no. 8, pp. 2669–2681, Mar. 2011.

[28] M. Dvořák, J. Svobodová, M. Beneš, and B. Gaš, "Applicability and limitations of affinity capillary electrophoresis and vacancy affinity capillary electrophoresis methods for determination of complexation constants," *Electrophoresis*, vol. 34, no. 5, pp. 761–767, Mar. 2013.

[29] Y. Takeda *et al.*, "Parallel quantification of lectin–glycan interaction using ultrafiltration," *Carbohydr. Res.*, vol. 375, pp. 112–117, Jun. 2013.

[30] H. Nevídalová, L. Michalcová, and Z. Glatz, "In-depth insight into the methods of plasma protein-drug interaction studies: Comparison of capillary electrophoresis-frontal analysis, isothermal titration calorimetry, circular dichroism and equilibrium dialysis," *Electrophoresis*, vol. 39, no. 4, pp. 581-583, Feb. 2018.

[31] D. S. Smith and S. A. Eremin, "Fluorescence polarization immunoassays and related methods for simple, high-throughput screening of small molecules," *Anal. Bioanal. Chem.*, vol. 391, no. 5, pp. 1499–1507, Jul. 2008.

[32] B. P. Duckworth and C. C. Aldrich, "Development of a high-throughput fluorescence polarization assay for the discovery of phosphopantetheinyl transferase inhibitors," *Anal. Biochem.*, vol. 403, no. 1, pp. 13–19, Aug. 2010.

[33] A. Göhler, C. Büchner, S. André, S. Doose, H. Kaltner, and H.-J. Gabius, "Sensing ligand binding to a clinically relevant lectin by tryptophan fluorescence anisotropy," *Analyst*, vol. 136, no. 24, pp. 5270–5276, Nov. 2011.

[34] A. Göhler, C. Büchner, S. André, Sören Doose, H. Kaltner, and H.-J. Gabius, "Analysis of homodimeric avian and human galectins by two methods based on fluorescence spectroscopy: Different structural alterations upon oxidation and ligand binding," *Biochimie*, vol. 94, no. 12, pp. 2649–2655, Dec. 2012.

[35] A. Göhler, S. André, H. Kaltner, M. Sauer, H.-J. Gabius, and S. Doose, "Hydrodynamic Properties of Human Adhesion/Growth-Regulatory Galectins Studied by Fluorescence Correlation Spectroscopy," *Biophys. J.*, vol. 98, no. 12, pp. 3044–3053, Jun. 2010.

[36] N. L. Thompson, A. M. Lieto, and N. W. Allen, "Recent advances in fluorescence correlation spectroscopy," *Curr. Opin. Struct. Biol.*, vol. 12, no. 5, pp. 634–641, Oct. 2002.

[37] Q. Dai, X. Liu, J. Coutts, L. Austin, and Q. Huo, "A One-Step Highly Sensitive Method for DNA Detection Using Dynamic Light Scattering," *J. Am. Chem. Soc.*, vol. 130, no. 26, pp. 8138–8139, Jul. 2008.

[38] A. D. Hanlon, M. I. Larkin, and R. M. Reddick, "Free-Solution, Label-Free Protein-Protein Interactions Characterized by Dynamic Light Scattering," *Biophys. J.*, vol. 98, no. 2, pp. 297–304, Jan. 2010.

[39] D. Some, "Light-scattering-based analysis of biomolecular interactions," *Biophys. Rev.*, vol. 5, no. 2, pp. 147–158, Mar. 2013.

[40] R. B. Thompson, "Chapter 5 - Fluorescence Lifetime Biosensors," in *Optical Biosensors*, Amsterdam: Elsevier Science, pp. 143–171, 2002.

[41] J. A. Levitt, D. R. Matthews, S. M. Ameer-Beg, and K. Suhling, “Fluorescence lifetime and polarization-resolved imaging in cell biology,” *Curr. Opin. Biotechnol.*, vol. 20, no. 1, pp. 28–36, Feb. 2009.

[42] T. Ha, “Single-Molecule Fluorescence Resonance Energy Transfer,” *Methods*, vol. 25, no. 1, pp. 78–86, Sep. 2001.

[43] I. L. Medintz, E. R. Goldman, M. E. Lassman, and J. M. Mauro, “A Fluorescence Resonance Energy Transfer Sensor Based on Maltose Binding Protein,” *Bioconjug. Chem.*, vol. 14, no. 5, pp. 909–918, Sep. 2003.

[44] B. Belardi, G. P. O’Donoghue, A. W. Smith, J. T. Groves, and C. R. Bertozzi, “Investigating Cell Surface Galectin-Mediated Cross-Linking on Glycoengineered Cells,” *J. Am. Chem. Soc.*, vol. 134, no. 23, pp. 9549–9552, Jun. 2012.

[45] S. Udenfriend, L. Gerber, and N. Nelson, “Scintillation proximity assay: A sensitive and continuous isotopic method for monitoring ligand/receptor and antigen/antibody interactions,” *Anal. Biochem.*, vol. 161, no. 2, pp. 494–500, Mar. 1987.

[46] J. F. Glickman, A. Schmid, and S. Ferrand, “Scintillation Proximity Assays in High-Throughput Screening,” *ASSAY Drug Dev. Technol.*, vol. 6, no. 3, pp. 433–455, Jun. 2008.

[47] M. Harndahl, M. Rasmussen, G. Roder, and S. Buus, “Real-time, high-throughput measurements of peptide–MHC-I dissociation using a scintillation proximity assay,” *J. Immunol. Methods*, vol. 374, no. 1, pp. 5–12, Nov. 2011.

[48] S. M. Pascal *et al.*, “Nuclear magnetic resonance structure of an SH2 domain of phospholipase C-γ1 complexed with a high affinity binding peptide,” *Cell*, vol. 77, no. 3, pp. 461–472, May 1994.

[49] K. Umemoto, H. Leffler, A. Venot, H. Valafar, and J. H. Prestegard, “Conformational Differences in Liganded and Unliganded States of Galectin-3,” *Biochemistry*, vol. 42, no. 13, pp. 3688–3695, Apr. 2003.

[50] J. J. Ziarek, D. Baptista, and G. Wagner, “Recent developments in solution nuclear magnetic resonance (NMR)-based molecular biology,” *J. Mol. Med.*, vol. 96, no. 1, pp. 1–8, Jun. 2017.

[51] Y.-H. Chu, Y. M. Dunayevskiy, D. P. Kirby, P. Vouros, and B. L. Karger, “Affinity Capillary Electrophoresis−Mass Spectrometry for Screening Combinatorial Libraries,” *J. Am. Chem. Soc.*, vol. 118, no. 33, pp. 7827–7835, Jan. 1996.

[52] C. V. Robinson *et al.*, “Probing the Nature of Noncovalent Interactions by Mass Spectrometry. A Study of Protein−CoA Ligand Binding and Assembly,” *J. Am. Chem. Soc.*, vol. 118, no. 36, pp. 8646–8653, Jan. 1996.

[53] C. S. Ho *et al.*, “Electrospray ionisation mass spectrometry: Principles and clinical applications,” *Clin. Biochem. Rev.*, vol. 24, no. 1, pp. 3–12, 2003.

[54] K. P. Murphy, E. Freire, and Y. Paterson, “Configurational effects in antibody–antigen interactions studied by microcalorimetry,” *Proteins Struct. Funct. Bioinforma.*, vol. 21, no. 2, pp. 83–90, Feb. 1995.

[55] J. E. Ladbury and B. Z. Chowdhry, “Sensing the heat: the application of isothermal titration calorimetry to thermodynamic studies of biomolecular interactions,” *Chem. Biol.*, vol. 3, no. 10, pp. 791–801, Oct. 1996.

[56] T. K. Dam, R. Roy, S. K. Das, S. Oscarson, and C. F. Brewer, “Binding of Multivalent Carbohydrates to Concanavalin A andDioclea grandiflora Lectin. Thermodynamic analysis of the 'multivalency effect'," *J. Biol. Chem.*, vol. 275, no. 19, pp. 14223–14230, May 2000.

[57] S. Leavitt and E. Freire, “Direct measurement of protein binding energetics by isothermal titration calorimetry,” *Curr. Opin. Struct. Biol.*, vol. 11, no. 5, pp. 560–566, Sep. 2001.

[58] T. K. Dam, R. Roy, D. Pagé, and C. F. Brewer, “Negative Cooperativity Associated with Binding of Multivalent Carbohydrates to Lectins. Thermodynamic Analysis of the ‘Multivalency Effect,’” *Biochemistry*, vol. 41, no. 4, pp. 1351–1358, Jan. 2002.

[59] B. E. Lang and F. P. Schwarz, “Thermodynamic dependence of DNA/DNA and DNA/RNA hybridization reactions on temperature and ionic strength,” *Biophys. Chem.*, vol. 131, no. 1, pp. 96–104, Dec. 2007.

[60] M. W. Freyer and E. A. Lewis, “Isothermal Titration Calorimetry: Experimental Design, Data Analysis, and Probing Macromolecule/Ligand Binding and Kinetic Interactions,” *Methods Cell Biol.*, vol. 84, 2008, pp. 79–113.

[61] R. J. Falconer, A. Penkova, I. Jelesarov, and B. M. Collins, “Survey of the year 2008: applications of isothermal titration calorimetry,” *J. Mol. Recognit.*, vol. 23, no. 5, pp. 395–413, Sep. 2010.

[62] H. Akiba and K. Tsumoto, “Thermodynamics of antibody–antigen interaction revealed by mutation analysis of antibody variable regions,” *J. Biochem.*, vol. 158, no. 1, pp. 1–13, Jul. 2015.

[63] A. M. Rossi and C. W. Taylor, “Analysis of protein-ligand interactions by fluorescence polarization,” *Nat. Protoc.*, vol. 6, no. 3, p. 365, Mar. 2011.

[64] Y. Gao, L. K. Wolf, and R. M. Georgiadis, “Secondary structure effects on DNA hybridization kinetics: a solution versus surface comparison,” *Nucleic Acids Res.*, vol. 34, no. 11, pp. 3370–7, 2006.

[65] H. Zhao, L. F. Boyd, and P. Schuck, “Measuring Protein Interactions by Optical Biosensors,” *Curr. Protoc. Protein Sci.*, vol 88, no. 1, pp. 20.2.1-20.2.25, Apr. 2017.

[66] J. Svitel, A. Balbo, R. A. Mariuzza, N. R. Gonzales, and P. Schuck, “Combined Affinity and Rate Constant Distributions of Ligand Populations from Experimental Surface Binding Kinetics and Equilibria,” *Biophys. J.*, vol. 84, no. 6, pp. 4062–4077, Jun. 2003.

[67] J. Svitel, H. Boukari, D. Van Ryk, R. C. Willson, and P. Schuck, “Probing the Functional Heterogeneity of Surface Binding Sites by Analysis of Experimental Binding Traces and the Effect of Mass Transport Limitation,” *Biophys. J.*, vol. 92, no. 5, pp. 1742–1758, Mar. 2007.

[68] I. I. Gorshkova, J. Svitel, F. Razjouyan, and P. Schuck, “Bayesian Analysis of Heterogeneity in the Distribution of Binding Properties of Immobilized Surface Sites,” *Langmuir*, vol. 24, no. 20, pp. 11577–11586, Oct. 2008.

[69] A. Halperin, A. Buhot, and E. B. Zhulina, “On the hybridization isotherms of DNA microarrays: the Langmuir model and its extensions,” *J. Phys. Condens. Matter*, vol. 18, no. 18, p. S463, 2006.

[70] Åke Larsson, “Regression analysis of simulated radio-ligand equilibrium experiments using seven different mathematical models,” *J. Immunol. Methods*, vol. 206, no. 1–2, pp. 135–142, 1997.

[71] H. Ravan, S. Kashanian, N. Sanadgol, A. Badoeidalfard, and Z. Karami, “Strategies for optimizing DNA hybridization on surfaces,” *Anal. Biochem.*, vol. 444, no. 1, pp. 41–46, 2014.

[72] A. Tlili, A. Abdelghani, S. Ameur, and N. Jaffrezic-Renault, “Impedance spectroscopy and affinity measurement of specific antibody–antigen interaction,” *Mater. Sci. Eng. C*, vol. 26, no. 2, pp. 546–550, Mar. 2006.

[73] J. J. Lundquist and E. J. Toone, “The cluster glycoside effect,” *Chem. Rev.*, vol. 102, no. 2, pp. 555–578, Feb. 2002.

[74] R. T. Lee and C. L. Yuan, “Affinity enhancement by multivalent lectin–carbohydrate interaction,” *Glycoconj. J.*, vol. 17, no. 7–9, pp. 543–551, 2000.

[75] T. J. Schmitt and T. A. Knotts, “Thermodynamics of DNA hybridization on surfaces,” *J. Chem. Phys.*, vol. 134, no. 20, p. 205105, May 2011.

[76] S. J. Hurst, H. D. Hill, and C. A. Mirkin, “‘Three-Dimensional Hybridization’ with Polyvalent DNA−Gold Nanoparticle Conjugates,” *J. Am. Chem. Soc.*, vol. 130, no. 36, pp. 12192–12200, Sep. 2008.

[77] A. Halperin, A. Buhot, and E. B. Zhulina, “Sensitivity, Specificity, and the Hybridization Isotherms of DNA Chips,” *Biophys. J.*, vol. 86, no. 2, pp. 718–730, Feb. 2004.

[78] S. C. Huang, H. Swerdlow, and K. D. Caldwell, “Binding of Biotinylated DNA to Streptavidin-Coated Polystyrene Latex,” *Anal. Biochem.*, vol. 222, no. 2, pp. 441–449, Nov. 1994.

[79] S.-C. Huang, M. D. Stump, R. Weiss, and K. D. Caldwell, “Binding of Biotinylated DNA to Streptavidin-Coated Polystyrene Latex: Effects of Chain Length and Particle Size,” *Anal. Biochem.*, vol. 237, no. 1, pp. 115–122, May 1996.

[80] J. N. Wilson, Y. Wang, J. J. Lavigne, and U. H. F. Bunz, “A biosensing model system: selective interaction of biotinylated PPEs with streptavidin-coated polystyrene microspheres,” *Chem. Commun.*, no. 14, pp. 1626–1627, 2003.

[81] G. B. Sigal, C. Bamdad, A. Barberis, J. Strominger, and G. M. Whitesides, “A self-assembled monolayer for the binding and study of histidine-tagged proteins by surface plasmon resonance,” *Anal. Chem.*, vol. 68, no. 3, pp. 490–497, Feb. 1996.

[82] L. Nieba *et al.*, “Biacore Analysis of Histidine-Tagged Proteins Using a Chelating NTA Sensor Chip,” *Anal. Biochem.*, vol. 252, no. 2, pp. 217–228, Oct. 1997.

[83] J. F. Hainfeld, W. Liu, C. M. R. Halsey, P. Freimuth, and R. D. Powell, “Ni–NTA–Gold Clusters Target His-Tagged Proteins,” *J. Struct. Biol.*, vol. 127, no. 2, pp. 185–198, Sep. 1999.

[84] G. Agarwal, R. R. Naik, and M. O. Stone, “Immobilization of Histidine-Tagged Proteins on Nickel by Electrochemical Dip Pen Nanolithography,” *J. Am. Chem. Soc.*, vol. 125, no. 24, pp. 7408–7412, Jun. 2003.

[85] G. Tanaka, H. Funabashi, M. Mie, and E. Kobatake, “Fabrication of an antibody microwell array with self-adhering antibody binding protein,” *Anal. Biochem.*, vol. 350, no. 2, pp. 298–303, Mar. 2006.

[86] J. M. Fowler, M. C. Stuart, and D. K. Y. Wong, “Self-Assembled Layer of Thiolated Protein G as an Immunosensor Scaffold,” *Anal. Chem.*, vol. 79, no. 1, pp. 350–354, Jan. 2007.

[87] D. Gao, N. McBean, J. S. Schultz, Y. Yan, A. Mulchandani, and W. Chen, “Fabrication of Antibody Arrays Using Thermally Responsive Elastin Fusion Proteins,” *J. Am. Chem. Soc.*, vol. 128, no. 3, pp. 676–677, Jan. 2006.

[88] T. H. Ha *et al.*, “Oriented Immobilization of Antibodies with GST-Fused Multiple Fc-Specific B-Domains on a Gold Surface,” *Anal. Chem.*, vol. 79, no. 2, pp. 546–556, Jan. 2007.

[89] S. Injae, P. Sungjin, and L. Myung-ryul, “Carbohydrate Microarrays: An Advanced Technology for Functional Studies of Glycans,” *Chem. – Eur. J.*, vol. 11, no. 10, pp. 2894–2901, Jan. 2005.

[90] J. E. Butler *et al.*, “The physical and functional behavior of capture antibodies adsorbed on polystyrene,” *J. Immunol. Methods*, vol. 150, no. 1–2, pp. 77–90, Jun. 1992.

[91] K. M. McLean, S. L. McArthur, R. C. Chatelier, P. Kingshott, and H. J. Griesser, “Hybrid biomaterials: Surface-MALDI mass spectrometry analysis of covalent binding versus physisorption of proteins,” *Colloids Surf. B Biointerfaces*, vol. 17, no. 1, pp. 23–35, Jan. 2000.

[92] D. S. Grubisha, R. J. Lipert, H.-Y. Park, J. Driskell, and M. D. Porter, “Femtomolar Detection of Prostate-Specific Antigen: An Immunoassay Based on Surface-Enhanced Raman Scattering and Immunogold Labels,” *Anal. Chem.*, vol. 75, no. 21, pp. 5936–5943, Nov. 2003.

[93] S. Paulie, P. Perlmann, and H. Perlmann, “Chapter 64 - Enzyme-Linked Immunosorbent Assay,” *Cell Biology (Third Edition)*, vol. 1, pp. 533–538, 2006.

[94] C. D. Heyes, A. Y. Kobitski, E. V. Amirgoulova, and G. U. Nienhaus, “Biocompatible Surfaces for Specific Tethering of Individual Protein Molecules,” *J. Phys. Chem. B*, vol. 108, no. 35, pp. 13387–13394, Sep. 2004.

[95] S. Kwang Lim, S. Perrier, and C. Neto, “Patterned chemisorption of proteins by thin polymer film dewetting,” *Soft Matter*, vol. 9, no. 9, pp. 2598–2602, 2013.

[96] M. Wilchek and E. A. Bayer, “The avidin-biotin complex in bioanalytical applications,” *Anal. Biochem.*, vol. 171, no. 1, pp. 1–32, May 1988.

[97] A. Jain and K. Cheng, “The principles and applications of avidin-based nanoparticles in drug delivery and diagnosis,” *J. Controlled Release*, vol. 245, pp. 27–40, Jan. 2017.

[98] F. Höök, A. Ray, B. Nordén, and B. Kasemo, “Characterization of PNA and DNA Immobilization and Subsequent Hybridization with DNA Using Acoustic-Shear-Wave Attenuation Measurements,” *Langmuir*, vol. 17, no. 26, pp. 8305–8312, Dec. 2001.

[99] W. Knoll *et al.*, “Streptavidin arrays as supramolecular architectures in surface-plasmon optical sensor formats,” *Colloids Surf. Physicochem. Eng. Asp.*, vol. 161, no. 1, pp. 115–137, Jan. 2000.

[100] F. Caruso, E. Rodda, D. N. Furlong, K. Niikura, and Y. Okahata, “Quartz Crystal Microbalance Study of DNA Immobilization and Hybridization for Nucleic Acid Sensor Development,” *Anal. Chem.*, vol. 69, no. 11, pp. 2043–2049, Jun. 1997.

[101] B. S. Bochner *et al.*, “Glycan Array Screening Reveals a Candidate Ligand for Siglec-8,” *J. Biol. Chem.*, vol. 280, no. 6, pp. 4307–4312, Feb. 2005.

[102] M. J. Linman, J. D. Taylor, H. Yu, X. Chen, and Q. Cheng, “Surface Plasmon Resonance Study of Protein−Carbohydrate Interactions Using Biotinylated Sialosides,” *Anal. Chem.*, vol. 80, no. 11, pp. 4007–4013, Jun. 2008.

[103] J. Diao, D. Ren, J. R. Engstrom, and K. H. Lee, “A surface modification strategy on silicon nitride for developing biosensors,” *Anal. Biochem.*, vol. 343, no. 2, pp. 322–328, 2005.

[104] G. Li, N. Xi, and D. H. Wang, “Probing membrane proteins using atomic force microscopy,” *J. Cell. Biochem.*, vol. 97, no. 6, p. 1191, 2006.

[105] H. J. Choi, N. H. Kim, B. H. Chung, and G. H. Seong, “Micropatterning of biomolecules on glass surfaces modified with various functional groups using photoactivatable biotin.,” *Anal. Biochem.*, vol. 347, no. 1, pp. 60–66, 2005.

[106] Y. Wang, T. Prokein, M. Hinz, H. Seliger, and W. A. Goedel, “Immobilization and hybridization of oligonucleotides on maleimido-terminated self-assembled monolayers.,” *Anal. Biochem.*, vol. 344, no. 2, pp. 216–223, 2005.

[107] E. Perez *et al.*, “Influence of the Molecular Design on the Antifouling Performance of Poly(ethylene glycol) Monolayers Grafted on (111) Si,” *Langmuir*, vol. 28, no. 41, pp. 14654–14664, Oct. 2012.

[108] A. Faucheux *et al.*, “Well-Defined Carboxyl-Terminated Alkyl Monolayers Grafted onto H−Si(111): Packing Density from a Combined AFM and Quantitative IR Study,” *Langmuir*, vol. 22, no. 1, pp. 153–162, Jan. 2006.

[109] H. Jin *et al.*, “X-ray Studies of Self-Assembled Organic Monolayers Grown on Hydrogen-Terminated Si(111),” *Langmuir*, vol. 20, no. 15, pp. 6252–6258, Jul. 2004.

[110] B. Baur *et al.*, “Chemical functionalization of GaN and AlN surfaces,” *Appl. Phys. Lett.*, vol. 87, no. 26, p. 841, 2005.

[111] F. Frederix *et al.*, “Enhanced Performance of an Affinity Biosensor Interface Based on Mixed Self-Assembled Monolayers of Thiols on Gold,” *Langmuir*, vol. 19, no. 10, pp. 4351–4357, 2003.

[112] D. E. Khoshtariya, T. D. Dolidze, D. Sarauli, and E. R. Van, “High-pressure probing of a changeover in the charge-transfer mechanism for intact cytochrome c at gold/self-assembled monolayer junctions,” *Angew. Chem.*, vol. 45, no. 2, pp. 277–81, 2005.

[113] T. Wink, S. J. van Zuilen, A. Bult, and W. P. van Bennekom, “Self-assembled Monolayers for Biosensors,” *The Analyst*, vol. 122, no. 4, 1997.

[114] L. H. D. And and R. G. Nuzzo, “Synthesis, Structure, and Properties of Model Organic Surfaces,” *Annu. Rev. Phys. Chem.*, vol. 43, no. 1, pp. 437–463, 1992.

[115] Y. Jun, X. Y. Zhu, and J. W. Hsu, “Formation of alkanethiol and alkanedithiol monolayers on GaAs(001),” *Langmuir*, vol. 22, no. 8, p. 3627, 2006.

[116] T. T. Yu, “Structural comparison of self-assembled monolayers of n-alkanoic acids on the surfaces of silver, copper, and aluminum,” *J. Am. Chem. Soc.*, vol. 115, no. 10, pp. 4350–4358, 1993.

[117] S. Besbes, H. B. Ouada, J. Davenas, L. Ponsonnet, N. Jaffrezic, and P. Alcouffe, “Effect of surface treatment and functionalization on the ITO properties for OLEDs,” *Mater. Sci. Eng. C*, vol. 26, no. 2–3, pp. 505–510, 2006.

[118] K. C. Lin and S. M. Chen, “The electrochemical preparation of FAD/ZnO with hemoglobin film-modified electrodes and their electroanalytical properties.,” *Biosens. Bioelectron.*, vol. 21, no. 9, pp. 1737–45, 2006.

[119] P. Wang, O. Hadjar, P. L. Gassman, and J. Laskin, “Reactive landing of peptide ions on self-assembled monolayer surfaces: an alternative approach for covalent immobilization of peptides on surfaces,” *Phys. Chem. Chem. Phys.*, vol. 10, no. 11, pp. 1512–1522, 2008.

[120] L. Liu *et al.*, “Activity analysis of the carbodiimide-mediated amine coupling reaction on self-assembled monolayers by cyclic voltammetry,” *Electrochim. Acta*, vol. 89, pp. 616–622, Feb. 2013.

[121] V. Dugas, C. Demesma, Y. Chevolot, and E. Souteyrand, “Use of organosilanes in biosensors,” *Nova Science Pub. Inc.* UK, 2010.

[122] A. Ulman, “Formation and Structure of Self-Assembled Monolayers,”*J. Am. Chem. Soc.*, vol. 96, no. 4, pp. 1533–1554, 1996.

[123] H. P. Lesch, M. U. Kaikkonen, J. T. Pikkarainen, and S. Ylä-Herttuala, “Avidin-biotin technology in targeted therapy,” *Expert Opin. Drug Deliv.*, vol. 7, no. 5, pp. 551–564, May 2010.

[124] T. M. Herne. And and M. J. Tarlov, “Characterization of DNA Probes Immobilized on Gold Surfaces,” *J. Am. Chem. Soc.*, vol. 119, no. 38, pp. 8916–8920, 1997.

[125] Y. Xue, X. Li, H. Li, and W. Zhang, “Quantifying thiol–gold interactions towards the efficient strength control,” *Nat. Commun.*, vol. 5, p. 4348, Jul. 2014.

[126] S. Chen, L. Li, C. L. Boozer, and S. Jiang, “Controlled Chemical and Structural Properties of Mixed Self-Assembled Monolayers of Alkanethiols on Au(111),” *Langmuir*, vol. 16, no. 24, pp. 9287–9293, Nov. 2000.

[127] P. Gong, C. Lee, L. J. Gamble, D. G. Castner and D. W. Grainger, “Hybridization Behavior of Mixed DNA/Alkylthiol Monolayers on Gold: Characterization by Surface Plasmon Resonance and 32P Radiometric Assay,” *Anal. Chem.*, vol. 78, no. 10, p. 3326, 2006.

[128] E. L. Wong, E. Chow, and J. J. Gooding, “DNA recognition interfaces: the influence of interfacial design on the efficiency and kinetics of hybridization,” *Langmuir*, vol. 21, no. 15, p. 6957, 2005.

[129] C. Y. Lee, L. J. Gamble, D. W. Grainger, and D. G. Castner, “Mixed DNA/oligo(ethylene glycol) functionalized gold surfaces improve DNA hybridization in complex media,” *Biointerphases*, vol. 1, no. 2, p. 82, 2006.

[130] A. Opdahl, D. Y. Petrovykh, H. Kimura-Suda, M. J. Tarlov and L. J. Whitman, “Independent control of grafting density and conformation of single-stranded DNA brushes,” *Proc. Natl. Acad. Sci.*, vol. 104, no. 1, pp. 9–14, Jan. 2007.

[131] H. Kimura-Suda, D. Y. Petrovykh, M. J. Tarlov, and L. J. Whitman, “Base-Dependent Competitive Adsorption of Single-Stranded DNA on Gold,” *J. Am. Chem. Soc.*, vol. 125, no. 30, pp. 9014–9015, Jul. 2003.

[132] J. T. Woodard, M. L. Walker, C. W. Meuse, D. J. Vanderah, G. E. Poirier and A. L. Plant, “Effect of an Oxidized Gold Substrate on Alkanethiol Self-Assembly,” *Langmuir*, vol. 16, no. 12, pp. 5347–5353, 2000.

[133] A. B. Steel, T. M. Herne, and M. J. Tarlov, “Electrochemical Quantitation of DNA Immobilized on Gold,” *Anal. Chem.*, vol. 70, no. 22, pp. 4670–4677, Nov. 1998.

[134] L. A. Chrisey, G. U. Lee, and C. E. O’Ferrall, “Covalent Attachment of Synthetic DNA to Self-Assembled Monolayer Films,” *Nucleic Acids Res.*, vol. 24, no. 15, pp. 3031–3039, Aug. 1996.

[135] M. J. O’Donnell, K. Tang, H. Köster, C. L. Smith, and C. R. Cantor, “High-Density, Covalent Attachment of DNA to Silicon Wafers for Analysis by MALDI-TOF Mass Spectrometry,” *Anal. Chem.*, vol. 69, no. 13, pp. 2438–2443, Jul. 1997.

[136] Y.-K. Cho *et al.*, “Characterization of DNA immobilization and subsequent hybridization using in situ quartz crystal microbalance, fluorescence spectroscopy, and surface plasmon resonance,” *J. Colloid Interface Sci.*, vol. 278, no. 1, pp. 44–52, Oct. 2004.

[137] M. S. Shchepinov, S. C. Case-Green, and E. M. Southern, “Steric Factors Influencing Hybridisation Of Nucleic Acids To Oligonucleotide Arrays,” *Nucleic Acids Res.*, vol. 25, no. 6, pp. 1155–1161, Mar. 1997.

[138] E. Southern, K. Mir, and M. Shchepinov, “Molecular interactions on microarrays,” *Nat. Genet.*, vol. 21, no. 1s, pp. 5–9, Jan. 1999.

[139] C. Ge, J. Liao, W. Yu, and N. Gu, “Electric potential control of DNA immobilization on gold electrode,” *Biosens. Bioelectron.*, vol. 18, no. 1, pp. 53–58, Jan. 2003.

[140] A. Vainrub and B. M. Pettitt, “Surface electrostatic effects in oligonucleotide microarrays: Control and optimization of binding thermodynamics,” *Biopolymers*, vol. 68, no. 2, pp. 265–270, Feb. 2003.

[141] I. Y. Wong and N. A. Melosh, “Directed Hybridization and Melting of DNA Linkers using Counterion-Screened Electric Fields,” *Nano Lett.*, vol. 9, no. 10, pp. 3521–3526, Oct. 2009.

[142] L. Dupin *et al.*, “Effects of the Surface Densities of Glycoclusters on the Determination of Their IC50 and Kd Value Determination by Using a Microarray,” *ChemBioChem*, vol. 16, no. 16, pp. 2329–2336, Nov. 2015.

[143] M. Phaner-Goutorbe, V. Dugas, Y. Chevolot, and E. Souteyrand, "Silanization of silica and glass slides for DNA microarrays by impregnation and gas phase protocols: A comparative study," *Mater. Sci. Eng. C*, vol. 31, no. 2, pp. 384–390, 2011.

[144] R. W. Wood, "On a Remarkable Case of Uneven Distribution of Light in a Diffraction Grating Spectrum," *Proc. Phys. Soc. Lond.*, vol. 18, no. 1, p. 269, 1902.

[145] E. Kretschmann and H. Raether, "Notizen: Radiative Decay of Non Radiative Surface Plasmons Excited by Light," *Z. Für Naturforschung A*, vol. 23, no. 12, pp. 2135–2136, 2014.

[146] A. Otto, "Excitation of nonradiative surface plasma waves in silver by the method of frustrated total reflection," *Z. Für Phys. Hadrons Nucl.*, vol. 216, no. 4, pp. 398–410, Aug. 1968.

[147] C. Nylander, B. Liedberg, and T. Lind, "Gas detection by means of surface plasmon resonance," *Sens. Actuators*, vol. 3, pp. 79–88, Jan. 1982.

[148] B. Liedberg, C. Nylander, and I. Lunström, "Surface plasmon resonance for gas detection and biosensing," *Sens. Actuators*, vol. 4, pp. 299–304, Jan. 1983.

[149] L. Marton, J. A. Simpson, H. A. Fowler, and N. Swanson, "Plural Scattering of 20-kev Electrons in Aluminum," *Phys. Rev.*, vol. 126, no. 1, pp. 182–192, Apr. 1962.

[150] K. Matsubara, S. Kawata, and S. Minami, "Optical chemical sensor based on surface plasmon measurement," *Appl. Opt.*, vol. 27, no. 6, pp. 1160–1163, Mar. 1988.

[151] L. S. Jung, C. T. Campbell, T. M. Chinowsky, M. N. Mar, and S. S. Yee, "Quantitative Interpretation of the Response of Surface Plasmon Resonance Sensors to Adsorbed Films," *Langmuir*, vol. 14, no. 19, pp. 5636–5648, Sep. 1998.

[152] J. Pollet *et al.*, "Fiber optic SPR biosensing of DNA hybridization and DNA–protein interactions," *Biosens. Bioelectron.*, vol. 25, no. 4, pp. 864–869, Dec. 2009.

[153] S. Zhan, X. Wang, and Y. Liu, "Fast centroid algorithm for determining the surface plasmon resonance angle using the fixed-boundary method," *Meas. Sci. Technol.*, vol. 22, no. 2, pp. 025201, 2011.

[154] Y. Liu, S. Chen, Q. Liu, J.-F. Masson, and W. Peng, "Compact multi-channel surface plasmon resonance sensor for real-time multi-analyte biosensing," *Opt. Express*, vol. 23, no. 16, pp. 20540–20548, Aug. 2015.

[155] E. Gazzola, A. Pozzato, G. Ruffato, E. Sovernigo, and A. Sonato, "High-throughput fabrication and calibration of compact high-sensitivity plasmonic lab-on-chip for biosensing," *Optofluidics Microfluid. Nanofluidics*, vol. 3, no. 1, pp. 13-21, 2016.

[156] V. Silin, H. Weetall, and D. J. Vanderah, "SPR Studies of the Nonspecific Adsorption Kinetics of Human IgG and BSA on Gold Surfaces Modified by Self-Assembled Monolayers (SAMs)," *J. Colloid Interface Sci.*, vol. 185, no. 1, pp. 94–103, Jan. 1997.

[157] J. Geng, E. Zhang, and X. Yu, "A scanning surface plasmon resonance sensor based on the phase shift algorithm," *Meas. Sci. Technol.*, vol. 23, no. 4, pp. 045105, 2012.

[158] D. Jang, G. Chae, and S. Shin, "Analysis of Surface Plasmon Resonance Curves with a Novel Sigmoid-Asymmetric Fitting Algorithm," *Sensors*, vol. 15, no. 10, pp. 25385–25398, Sep. 2015.

[159] L. Diéguez, N. Darwish, M. Mir, E. Martínez, M. Moreno, and J. Samitier, "Effect of the Refractive Index of Buffer Solutions in Evanescent Optical Biosensors," *Sensor lett.*, vol. 7, no. 5, pp. 851-855, Oct. 2009.

[160] H. L. Skriver and N. M. Rosengaard, "Surface energy and work function of elemental metals," *Phys. Rev. B*, vol. 46, no. 11, pp. 7157–7168, Sep. 1992.

[161] T. Smith, "The hydrophilic nature of a clean gold surface," *J. Colloid Interface Sci.*, vol. 75, no. 1, pp. 51–55, May 1980.

[162] G. L. Gaines Jr., "On the water wettability of gold," *J. Colloid Interface Sci.*, vol. 79, p. 295, Jan. 1981.

[163] M. E. Schrader, "Wettability of clean metal surfaces," *J. Colloid Interface Sci.*, vol. 100, no. 2, pp. 372–380, Aug. 1984.

[164] J. Drelich and E. Chibowski, "Superhydrophilic and Superwetting Surfaces: Definition and Mechanisms of Control," *Langmuir*, vol. 26, no. 24, pp. 18621–18623, Dec. 2010.

[165] B. Koslowski *et al.*, "Oxidation of preferentially (111)-oriented Au films in an oxygen plasma investigated by scanning tunneling microscopy and photoelectron spectroscopy," *Surf. Sci.*, vol. 475, no. 1, pp. 1–10, Mar. 2001.

[166] M. L. White, "The Wetting of Gold Surfaces by Water," *J. Phys. Chem.*, vol. 68, no. 10, pp. 3083–3085, Oct. 1964.

[167] M. L. White and J. Drobek, "The Effect of Residual Abrasives on the Wettability of Polished Gold Surfaces," *J. Phys. Chem.*, vol. 70, no. 11, pp. 3432–3436, Nov. 1966.

[168] D. E. King, "Oxidation of gold by ultraviolet light and ozone at 25 °C," *J. Vac. Sci. Technol. Vac. Surf. Films*, vol. 13, no. 3, pp. 1247–1253, May 1995.

[169] S. D. Evans, R. Sharma, and A. Ulman, "Contact angle stability: Reorganization of monolayer surfaces?," *Langmuir*, vol. 7, no. 1, pp. 156–161, Jan. 1991.

[170] L. M. Fischer *et al.*, "Gold cleaning methods for electrochemical detection applications," *Microelectron. Eng.*, vol. 86, no. 4, pp. 1282–1285, Apr. 2009.

[171] H. Min, J.-W. Park, H. K. Shon, D. W. Moon, and T. G. Lee, "ToF-SIMS study on the cleaning methods of Au surface and their effects on the reproducibility of self-assembled monolayers," *Appl. Surf. Sci.*, vol. 255, no. 4, pp. 1025–1028, Dec. 2008.

[172] D. R. Jung, D. E. King, and A. W. Czanderna, "Metal overlayers on organic functional groups of self-organized molecular assemblies. II. X-ray photoelectron spectroscopy of interactions of Cu/CN on 12-mercaptododecanenitrile," *J. Vac. Sci. Technol. Vac. Surf. Films*, vol. 11, no. 4, pp. 2382–2386, Jul. 1993.

[173] P. Fuchs, K. Marti, and S. Russi, “Materials for mass standards: long-term stability of PtIr and Au after hydrogen and oxygen low-pressure plasma cleaning,” *Metrologia*, vol. 49, no. 6, p. 615, 2012.

[174] F. Palazon, “Surface functionalization of heterogeneous gold / silica substrates for the selective anchoring of biomolecules and colloids onto LSPR biosensors,” PhD thesis, Ecole Centrale de Lyon, 2014.

[175] H. Ron and I. Rubinstein, “Alkanethiol Monolayers on Preoxidized Gold. Encapsulation of Gold Oxide under an Organic Monolayer,” *Langmuir*, vol. 10, no. 12, pp. 4566–4573, Dec. 1994.

[176] J. J. Pireaux, M. Liehr, P. A. Thiry, J. P. Delrue, and R. Caudano, “Electron spectroscopic characterization of oxygen adsorption on gold surfaces: II. Production of gold oxide in oxygen DC reactive sputtering,” *Surf. Sci.*, vol. 141, no. 1, pp. 221–232, Jun. 1984.

[177] M.-Y. Tsai and J.-C. Lin, “Preconditioning Gold Substrates Influences Organothiol Self-assembled Monolayer (SAM) Formation,” *J. Colloid Interface Sci.*, vol. 238, no. 2, pp. 259–266, Jun. 2001.

[178] “Handbook for Cleaning for Semiconductor Manufacturing: Fundamentals and Applications,” *Scrivener Publishing LLC.*, USA, 2011.

[179] A. I. Stadnichenko, L. S. Kibis, D. A. Svintsitskiy, S. V. Koshcheev, and A. I. Boronin, “Application of RF discharge in oxygen to create highly oxidized metal layers,” *Surf. Eng.*, vol. 34, no. 1, pp. 1–5, Jan. 2018.

[180] A. I. Stadnichenko, S. V. Koshcheev, and A. I. Boronin, “An XPS and TPD study of gold oxide films obtained by exposure to RF-activated oxygen,” *J. Struct. Chem.*, vol. 56, no. 3, pp. 557–565, Jun. 2015.

[181] J. H. Linn and W. E. Swartz, “An XPS Study of the Effects of CF_4 Plasmas on Gold Surfaces,” *Appl. Spectrosc.*, vol. 39, no. 5, pp. 755–760, Sep. 1985.

[182] A. Krozer and M. Rodahl, “X-ray photoemission spectroscopy study of UV/ozone oxidation of Au under ultrahigh vacuum conditions,” *J. Vac. Sci. Technol. Vac. Surf. Films*, vol. 15, no. 3, pp. 1704–1709, May 1997.

[183] S. H. Brewer, S. J. Anthireya, S. E. Lappi, D. L. Drapcho, and S. Franzen, “Detection of DNA Hybridization on Gold Surfaces by Polarization Modulation Infrared Reflection Absorption Spectroscopy,” *Langmuir*, vol. 18, no. 11, pp. 4460–4464, May 2002.

[184] M. Tsuboi, “Infrared Spectra and Secondary Structure of Deoxyribonucleic Acid,” *Prog. Theor. Phys. Suppl.*, vol. 17, pp. 99–107, Jan. 1961.

[185] J. Liquier, P. Coffinier, M. Firon, and E. Taillandier, “Triple Helical Polynucleotidic Structures: Sugar Conformations Determined by FTIR Spectroscopy,” *J. Biomol. Struct. Dyn.*, vol. 9, no. 3, pp. 437–445, Dec. 1991.

[186] D. Yang *et al.*, “DNA Materials: Bridging Nanotechnology and Biotechnology,” *Acc. Chem. Res.*, vol. 47, no. 6, pp. 1902–1911, Jun. 2014.

[187] Y. Chevolot *et al.*, “DNA directed immobilization glycocluster array: applications and perspectives,” *Curr. Opin. Chem. Biol.*, vol. 18, pp. 46–54, Feb. 2014.

[188] Y. Chevolot *et al.*, "DNA-Based Carbohydrate Biochips: A Platform for Surface Glyco-Engineering," *Angew. Chem. Int. Ed.*, vol. 46, no. 14, pp. 2398–2402, Mar. 2007.

[189] M. E. Craig, D. M. Crothers, and P. Doty, "Relaxation kinetics of dimer formation by self complementary oligonucleotides," *J. Mol. Biol.*, vol. 62, no. 2, pp. 383–401, Dec. 1971.

[190] M. Eigen and D. Pörschke, "Co-operative non-enzymic base recognition: I. Thermodynamics of the helix-coil transition of oligoriboadenylic acids at acidic pH," *J. Mol. Biol.*, vol. 53, no. 1, pp. 123–141, Oct. 1970.

[191] C. Chen, W. Wang, Z. Wang, F. Wei, and X. S. Zhao, "Influence of secondary structure on kinetics and reaction mechanism of DNA hybridization," *Nucleic Acids Res.*, vol. 35, no. 9, pp. 2875–2884, May 2007.

[192] M. M. A. Sekar, W. Bloch, S. John, and P. M, "Comparative study of sequence-dependent hybridization kinetics in solution and on microspheres," *Nucleic Acids Res.*, vol. 33, no. 1, pp. 366–375, Jan. 2005.

[193] I. Y. Wong and N. A. Melosh, "An Electrostatic Model for DNA Surface Hybridization," *Biophys. J.*, vol. 98, no. 12, pp. 2954–2963, Jun. 2010.

[194] E. Huang, M. Satjapipat, S. Han, and F. Zhou, "Surface Structure and Coverage of an Oligonucleotide Probe Tethered onto a Gold Substrate and Its Hybridization Efficiency for a Polynucleotide Target," *Langmuir*, vol. 17, no. 4, pp. 1215–1224, Feb. 2001.

[195] A. Angeli *et al.*, "Design and Synthesis of Galactosylated Bifurcated Ligands with Nanomolar Affinity for Lectin LecA from Pseudomonas aeruginosa," *ChemBioChem*, vol. 18, no. 11, pp. 1036–1047, Jun. 2017.

[196] A. Angeli *et al.*, "Glycoclusters with Additional Functionalities for Binding to the LecA Lectin from Pseudomonas aeruginosa," *ChemistrySelect*, vol. 2, no. 32, pp. 10420–10427, Nov. 2017.

[197] T. Ozawa *et al.*, "A Novel Rabbit Immunospot Array Assay on a Chip Allows for the Rapid Generation of Rabbit Monoclonal Antibodies with High Affinity," *PLoS One*, vol. 7, no. 12, pp. e52383, Dec. 2012.

[198] J.-L. Mergny, "Fluorescence Energy Transfer as a Probe for Tetraplex Formation: The i-Motif," *Biochemistry*, vol. 38, no. 5, pp. 1573–1581, Feb. 1999.

[199] G.-S. Jiao and K. Burgess, "Oligonucleotides with strongly fluorescent groups π-Conjugated to a nucleobase: syntheses, melting temperatures, and conformation," *Bioorg. Med. Chem. Lett.*, vol. 13, no. 16, pp. 2785–2788, Aug. 2003.

[200] J. Mineno, Y. Ishino, T. Ohminami, and I. Kato, "Fluorescent labeling of a DNA sequencing primer," *DNA Seq.*, vol. 4, no. 3, pp. 135–141, Jan. 1993.

[201] S. A. E. Marras, F. R. Kramer, and S. Tyagi, "Efficiencies of fluorescence resonance energy transfer and contact-mediated quenching in oligonucleotide probes," *Nucleic Acids Res.*, vol. 30, no. 21, pp. e122–e122, Nov. 2002.

[202] J.-L. Mergny and J.-C. Maurizot, “Fluorescence Resonance Energy Transfer as a Probe for G-Quartet Formation by a Telomeric Repeat,” *ChemBioChem*, vol. 2, no. 2, pp. 124–132, Feb. 2001.

[203] B. G. Moreira, Y. You, M. A. Behlke, and R. Owczarzy, “Effects of fluorescent dyes, quenchers, and dangling ends on DNA duplex stability,” *Biochem. Biophys. Res. Commun.*, vol. 327, no. 2, pp. 473–484, Feb. 2005.

[204] G. V. Sherbet, M. S. Lakshmi, and F. Cajone, “Isoelectric characteristics and the secondary structure of some nucleic acids,” *Biophys. Struct. Mech.*, vol. 10, no. 3, pp. 121–128, Sep. 1983.

[205] G. Stotzky, “Persistence and Biological Activity in Soil of Insecticidal Proteins from Bacillus thuringiensis and of Bacterial DNA Bound on Clays and Humic Acids,” *J. Environ. Qual.*, vol. 29, no. 3, pp. 691–705, Jan. 2000.

[206] K. Saeki and T. Kunito, “Adsorptions of DNA molecules by soils and variable-charged soil constituents,” *Curr. Res. Technol. Educ. Top. Appl. Microbiol. Microb. Biotechnol.*, vol. 1, pp. 188–195, Jan. 2010.

[207] K. M. Koo, A. A. I. Sina, L. G. Carrascosa, M. J. A. Shiddiky, and M. Trau, “DNA–bare gold affinity interactions: mechanism and applications in biosensing,” *Anal. Methods*, vol. 7, no. 17, pp. 7042–7054, Aug. 2015.

[208] S. Zorn *et al.*, “Stability of hexa(ethylene glycol) SAMs towards the exposure to natural light and repeated reimmersion,” *Appl. Surf. Sci.*, vol. 258, no. 20, pp. 7882–7888, Aug. 2012.

[209] J. Maciel, M. I. Oliveira, R. M. Gonçalves, and M. A. Barbosa, “The effect of adsorbed fibronectin and osteopontin on macrophage adhesion and morphology on hydrophilic and hydrophobic model surfaces,” *Acta Biomater.*, vol. 8, no. 10, pp. 3669–3677, Oct. 2012.

[210] K. L. Prime and G. M. Whitesides, “Self-Assembled Organic Monolayers: Model Systems for Studying Adsorption of Proteins at Surfaces,” *Science*, vol. 252, no. 5009, pp. 1164–1167, May 1991.

[211] M Mrksich and and G. M. Whitesides, “Using Self-Assembled Monolayers to Understand the Interactions of Man-made Surfaces with Proteins and Cells,” *Annu. Rev. Biophys. Biomol. Struct.*, vol. 25, no. 1, pp. 55–78, Apr. 1996.

[212] B. T. Houseman and M. Mrksich, “The microenvironment of immobilized Arg-Gly-Asp peptides is an important determinant of cell adhesion,” *Biomaterials*, vol. 22, no. 9, pp. 943–955, May 2001.

[213] K. A. Peterlinz, R. M. Georgiadis, T. M. Herne, and M. J. Tarlov, “Observation of Hybridization and Dehybridization of Thiol-Tethered DNA Using Two-Color Surface Plasmon Resonance Spectroscopy,” *J. Am. Chem. Soc.*, vol. 119, no. 14, pp. 3401–3402, Apr. 1997.

[214] R. Levicky, T. M. Herne, M. J. Tarlov, and S. K. Satija, “Using Self-Assembly To Control the Structure of DNA Monolayers on Gold: A Neutron Reflectivity Study,” *J. Am. Chem. Soc.*, vol. 120, no. 38, pp. 9787–9792, Sep. 1998.

[215] L. Kankate, U. Werner, A. Turchanin, A. Gölzhäuser, H. Großmann, and R. Tampé, "Protein resistant oligo(ethylene glycol) terminated self-assembled monolayers of thiols on gold by vapor deposition in vacuum," *Biointerphases*, vol. 5, no. 2, pp. 30–36, Jun. 2010.

[216] R. Valiokas *et al.*, "On the quality and structural characteristics of oligo(ethylene glycol) assemblies on gold: An experimental and theoretical study," *J. Electron Spectrosc. Relat. Phenom.*, vol. 172, no. 1, pp. 9–20, May 2009.

[217] P. Harder, M. Grunze, R. Dahint, G. M. Whitesides, and P. E. Laibinis, "Molecular Conformation in Oligo(ethylene glycol)-Terminated Self-Assembled Monolayers on Gold and Silver Surfaces Determines Their Ability To Resist Protein Adsorption," *J. Phys. Chem. B*, vol. 102, no. 2, pp. 426–436, Jan. 1998.

[218] R. Valiokas, S. Svedhem, M. Östblom, S. C. T. Svensson, and B. Liedberg, "Influence of Specific Intermolecular Interactions on the Self-Assembly and Phase Behavior of Oligo(Ethylene Glycol)-Terminated Alkanethiolates on Gold," *J. Phys. Chem. B*, vol. 105, no. 23, pp. 5459–5469, Jun. 2001.

[219] W. B. Russel, W. B. Russel, D. A. Saville, and W. R. Schowalter, *Colloidal Dispersions*. Cambridge University Press, 1989.

[220] G. H. Findenegg, "J. N. Israelachvili: Intermolecular and Surface Forces (With Applications to Colloidal and Biological Systems). Academic Press, London, Orlando, San Diego, New York, Toronto, Montreal, Sydney, Tokyo 1985. 296 Seiten, Preis: $ 65.00.," *Berichte Bunsenges. Für Phys. Chem.*, vol. 90, no. 12, pp. 1241–1242, Dec. 1986.

[221] T. Braschler, S. Wu, F. Wildhaber, S. A. Bencherif, and D. J. Mooney, "Soft nanofluidics governing minority ion exclusion in charged hydrogels," *Soft Matter*, vol. 11, no. 20, pp. 4081–4090, May 2015.

[222] M. Steichen and C. Buess-Herman, "Electrochemical detection of the immobilization and hybridization of unlabeled linear and hairpin DNA on gold," *Electrochem. Commun.*, vol. 7, no. 4, pp. 416–420, Apr. 2005.

[223] F.-C. Chien *et al.*, "An investigation into the influence of secondary structures on DNA hybridization using surface plasmon resonance biosensing," *Chem. Phys. Lett.*, vol. 397, no. 4, pp. 429–434, Oct. 2004.

[224] G. Niranjani and R. Murugan, "Theory on the Mechanism of DNA Renaturation: Stochastic Nucleation and Zipping," *PLoS One*, vol. 11, no. 4, p. e0153172, Apr. 2016.

[225] K. Tawa and W. Knoll, "Mismatching base-pair dependence of the kinetics of DNA–DNA hybridization studied by surface plasmon fluorescence spectroscopy," *Nucleic Acids Res.*, vol. 32, no. 8, pp. 2372–2377, Apr. 2004.

[226] N. J. de Mol, E. Plomp, M. J. E. Fischer, and R. Ruijtenbeek, "Kinetic Analysis of the Mass Transport Limited Interaction between the Tyrosine Kinase lck SH2 Domain and a Phosphorylated Peptide Studied by a New Cuvette-Based Surface Plasmon Resonance Instrument," *Anal. Biochem.*, vol. 279, no. 1, pp. 61–70, Mar. 2000.

[227] N. J. de Mol, M. I. Catalina, F. J. Dekker, M. J. E. Fischer, A. J. R. Heck, and R. M. J. Liskamp, "Protein Flexibility and Ligand Rigidity: A Thermodynamic and Kinetic Study of ITAM-Based Ligand Binding to Syk Tandem SH2," *ChemBioChem*, vol. 6, no. 12, pp. 2261–2270.

[228] P. R. Edwards, C. H. Maule, R. J. Leatherbarrow, and D. J. Winzor, "Second-Order Kinetic Analysis of IAsys Biosensor Data: Its Use and Applicability," *Anal. Biochem.*, vol. 263, no. 1, pp. 1–12, Oct. 1998.

[229] D. Kohlheyer, G. A. J. Besselink, S. Schlautmann, and R. B. M. Schasfoort, "Free-flow zone electrophoresis and isoelectric focusing using a microfabricated glass device with ion permeable membranes," *Lab. Chip*, vol. 6, no. 3, pp. 374–380, 2006.

[230] D. Kohlheyer, J. C. T. Eijkel, S. Schlautmann, A. van den Berg, and R. B. M. Schasfoort, "Microfluidic High-Resolution Free-Flow Isoelectric Focusing," *Anal. Chem.*, vol. 79, no. 21, pp. 8190–8198, Nov. 2007.

[231] V. Kanda, J. K. Kariuki, D. J. Harrison, and M. T. McDermott, "Label-Free Reading of Microarray-Based Immunoassays with Surface Plasmon Resonance Imaging," *Anal. Chem.*, vol. 76, no. 24, pp. 7257–7262, Dec. 2004.

[232] W. Norde and C. E. Giacomelli, "Conformational changes in proteins at interfaces: From solution to the interface, and back," *Macromol. Symp.*, vol. 145, no. 1, pp. 125–136.

Annexes

Annex A Surface characterization tools

A.1 Contact angle goniometry

The contact angle is the angle formed by the intersection of the liquid-solid interface and the liquid-gas interface (see in Figure A.1) of a liquid droplet on a surface. The line where solid (S), liquid (L), and gas (G) co-exist is referred to as the "three-phase contact line". The angle between the liquid-gas interface tangent line over the three-phase contact line and the solid-liquid interface is the contact angle.

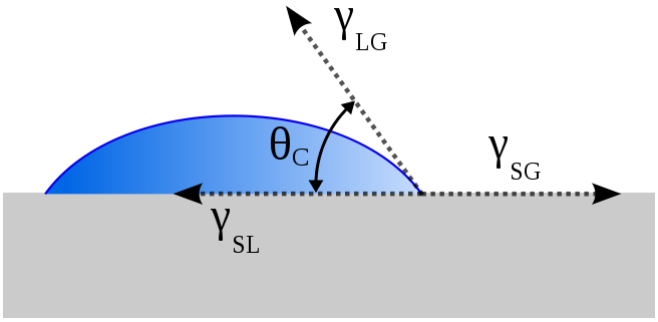

Figure A.1 Contact angle at liquid-gas-solid interface. Adapted from Wikipedia.

The interfacial tension between the three phases should satisfy Young's equation:

$$\gamma_{SG} = \gamma_{SL} + \gamma_{LG} \cos\theta_C \qquad \text{Equation A.1}$$

where γ_{SG} is solid-gas interfacial tension, γ_{SL} is solid-liquid interfacial tension, γ_{LG} is liquid-gas interfacial tension and θ_C is contact angle. Contact angles are generally used as the primary data in wettability studies, which indicate the degree of wetting when a solid and a liquid interact. For example, the smaller the water-solid contact angle is, the higher the hydrophilicity of the solid is. In general, surfaces with a contact angle of less than 90° are referred to as hydrophilic surfaces and the fluid spreads over a large area on the surface; while surfaces with a contact angle greater than 90° are hydrophobic surfaces so the fluid tends to minimize its contact with the surface and to form a compact liquid droplet. The water wettability of a solid surface is determined by its chemical composition and microstructure. The greater the surface free energy of the solid, the more easily it is wetted by water and vice versa. A simple setup for contact angle measurement is composed of a syringe to deposit a droplet of controlled volume onto surfaces and a camera to capture an image of the droplet and calculate the contact angle.

A.2 AFM

Atomic Force Microscopy (AFM) is a high resolution type of scanning probe microscopy that is used to study the surface structure of samples. The key component of the AFM is a microscopic cantilever with a nanoscale tip used to scan sample surfaces. This cantilever is tens to hundreds of micrometers in size, generally made of silicon or silicon nitride, and its tip has a radius of curvature on the order of tens of nanometers. The height of the cantilever is controlled by piezoelectric ceramics and its deflection is monitored by a laser beam and photodiode quadrant (see in Figure A.2).

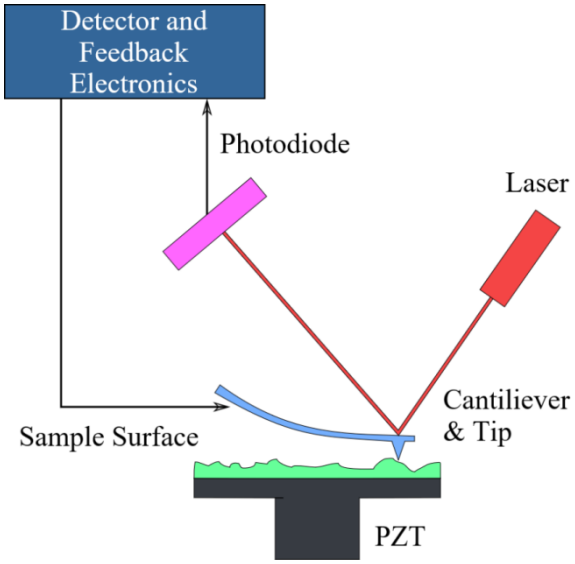

Figure A.2 Schematic view of AFM. Adapted from Wikipedia.

The main working modes of AFM are contact mode and tapping mode. In contact mode, the cantilever contacts the surface of the sample and the topography of the surface is obtained from its deflection when it moves on the surface. In tapping mode, the tip of the cantilever does not contact the surface of the sample, but is rather set to oscillate at a slightly higher frequency than its resonant frequency and with typical amplitudes of oscillations of 100-200 nm. The topography of the surface can be obtained from changes in the amplitude of oscillations when the tip moves over the sample surface. In both cases, instead of measuring directly the deflection or change in amplitude of the oscillations, AFM systems are usually set-up to maintain these parameters constant by a feedback loop, so that it is the signal necessary to maintain them that, indirectly, gives the topography of the surface.

AFM has several advantages over other surface imaging techniques (like Scanning Electron Microscopy for example). AFM does not require any special treatment of the sample, which can cause irreversible damage to the surface, and provides real three-dimensional surface map. Furthermore, AFM imaging can be performed under normal pressure and even in liquid environments, while SEM need to operate under high vacuum.

A.3 XPS

X-ray Photoelectron Spectroscopy (XPS) is a surface-sensitive quantitative spectroscopic technique used to determine the composition, content and chemical state of the elements present on a surface. This technique uses X-rays to irradiate the samples and to excite the core electronic levels of the atom presents on the surface of the sample up to ~10 nm depth. The excited photoelectrons escape the material with different kinetic energies (E_k) depending on there binding energy E_b in the atoms. E_b is independent on the photon energy (E_{photon}) of the X-rays used and only depends on its parent element and atomic energy level. The spectrometer measures E_k and the relations between these energy parameters is given by:

$$E_{photon} = E_b + E_k + W \qquad \text{Equation A.2}$$

where W is the spectrometer work function, E_{photon} is determined by the source (eg: 1486.6 eV of an aluminum source-AlK_α) and E_k is the measured kinetic energy. The XPS analyzer counts the number of photoelectrons at different kinetic energies (E_k). The data are presented as a graph of relative intensity (usually expressed as counts of counts/s) versus binding energy of electron (E_b), which is referred to as XPS spectrum. Three kinds of information can be obtained from XPS spectrum. The first one is the nature of the elements within the 10 nm thickness of the sample (except hydrogen and helium) which is based on binding energy of each peak. The second is the relative percentage of each element, which is obtained by measuring the peak area of the element. The third is the chemical or electronic state of the element, which is obtained by measuring the 'chemical shift' of the peak. This refers to the fact that electrons from the same orbital of the same element have slightly different binding energies depending on the chemical environment or electric state of the given atom. For example, the gold atom in metallic state has a different XPS spectrum ($Au4f_{7/2}$ and $Au4f_{5/2}$ peaks around 84 and 88 ev) than that (85.5 and 89.5 eV) in the oxidation state as Au_2O_3.

A.4 PM-IRRAS

Polarization Modulation-InfraRed Reflection-Adsorption Spectroscopy (PM-IRRAS) is a method developped to improve the sensitivity of infrared spectroscopy of thin layers deposited on metalic surfaces. It takes advantage of the so-called "surface selection rule" upon reflection on metallic surfaces. Because the phase shift of the s component (see Figure A.3) is nearly 180° for all the angles of incidence, the net amplitude of this IR radiation is nearly zero on the surface so this polarization is not sensitive to the substrate surface. In contrast, the phase shift of the p component depends upon the angle of incidence and the net amplitude of the field usually shows a maximum at grazing incidence angle (~88°). PM-IRRAS uses this s component signal as a 'real time' background signal, thus eliminating all signals coming from the gas phase (vapor of water and carbon dioxide) and generating high signal to noise ration spectra. The active vibrations that can be detected on the surface with the p component must have a component of the dynamic dipole polarized in the direction perpendicular to the sample surface.

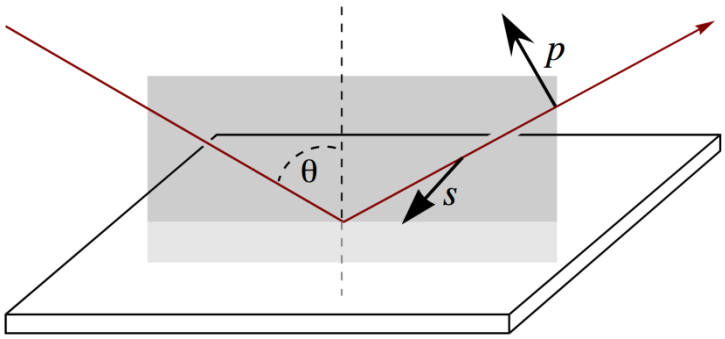

Figure A.3 Schematic illustration of the p and s polarization radiation. Adapted from Wikipedia.

In a typical PM-IRRAS setup, the incident beam is firstly linearly polarized. Then, the beam goes through a ZnSe Photo Elastic Modulator (PEM) which switches the polarization from p to s at high frequency. After that, the beam reflects on the sample surface according to the angle θ of incidence. After the detector and preamplifier, the signal is either high pass filtered and demodulated for polarization modulation by a Lock-in Amplifier (LIA) leading to an output signal corresponding to the difference spectrum (Rp-Rs) or low-pass filtered to eliminate the high frequency PEM component, providing the (Rp+Rs) signal. The final step of data processing is to ratio these spectra to get the 'free from atmospheric contamination' spectrum given by:

$$\frac{\Delta R}{R} = (R_p - R_s)/(R_p + R_s) \qquad \text{Equation A.3}$$

Annex B Evanescent field fluorescence biosensor

The evanescence field fluorescence biosensor (Davos diagnositics) is based on evanescence excitation of fluorophores bound to the sensor chip surface. When a light wave travels from a medium of high refractive index toward a lower refractive index medium, it undergoes a total internal reflection above a certain incidence angle (critical angle). The associated electromagnetic field does not suddenly vanish at the interface between the two different media but has a finite penetration depth into the lower-index medium. This electromagnetic field is called an evanescent field and its strength decreases exponentially with the distance from the interface. In general, the penetration depth of the evanescent field into the low-index medium is only hundreds of nanometers. When used as an excitation source, only fluorophores bound to the substrate are excited, while the majority of free labeled targets is outside of the excitation field range. With this technique, real-time studies of the kinetics of target binding to the surface can be achieved by monitoring the fluorescent intensity with time.

The set up used in our case is composed of two elements. One is a 8-well biosensor chip (shown in Figure B.1), each well with a volume of ca. 80 µl. The chip is produced by injection molding of polystyrene identical to the material used to produce ELISA microplates and has been treated to achieve high binding. The chip has 2 areas: the upper part consists of 8 separated polystyrene wells and the lower part of a prism with surfaces of high optical quality. The wells of the chip are separated by 4.5 mm and are numbered from 1-8 (the 1st well that is located at the outer end of the chip). During a measurement, well 1 is the first well that is measured followed by the other wells sequentially.

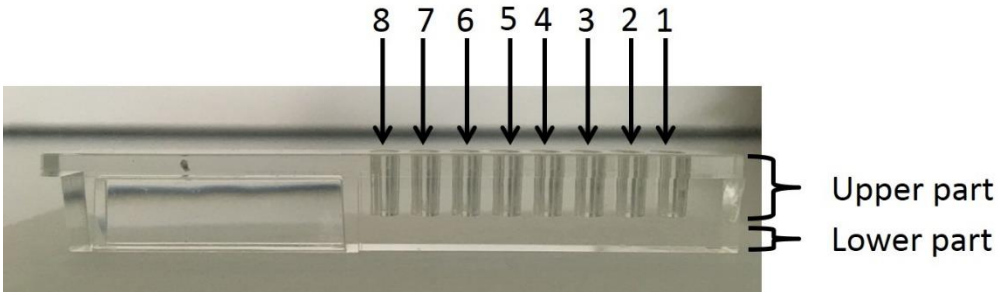

Figure B.1 Numbering of the wells of the chips. The chip has 2 areas: the upper part consists of 8 separated polystyrene wells and the lower part of a prism with surfaces of high optical quality.

The other element composing the system is the reader that measures the light emitted by the exited fluorophores. The principle of the reader is depicted in Figure B.2. A laser diode with a wavelength of 635 nm is directed toward the side wall of the prism, where it is refracted and then reflected at the bottom of the well (total internal reflection).

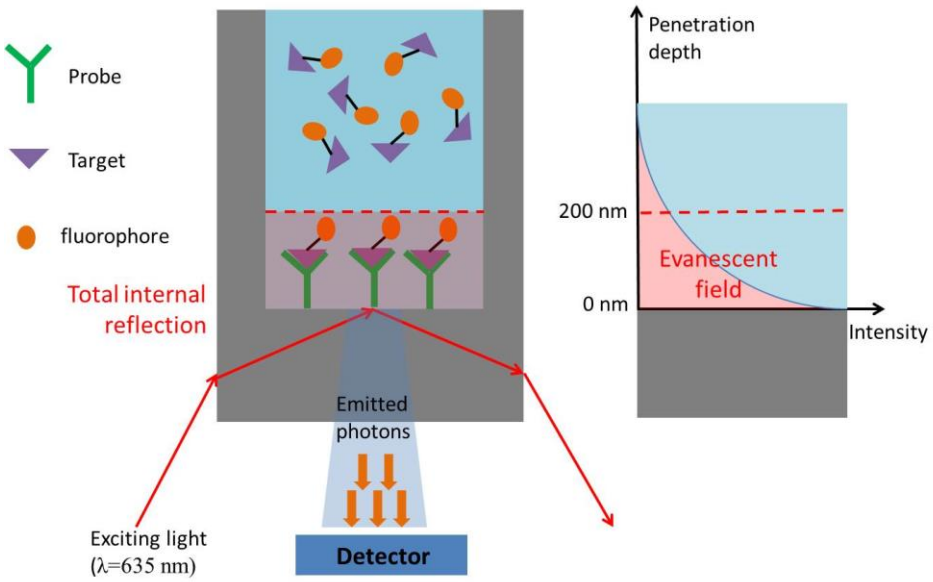

Figure B.2 Schematic representation of biosensor Technology: The exciting light beam is reflected under total internal reflection at the liquid - solid interface at the bottom of a well of a biosensor chip. By this optical phenomenon a 200 nanometer bottom layer of the adjacent liquid is illuminated. Only fluorophors localized in this evanescence field will absorb and emit photons independent of other background molecules present in the liquid (not illuminated above 200 nm).

Photons emitted through the bottom of the prism are collected, filtered and measured by a detector. The measurements have to be done immediately after the addition of the target solutions. The instrument scans one well at a time by moving the chip; consequently, the frequency of acquisition is quite low.

Résumé en français

Résumé en français

Introduction

Les biocapteurs au sens large sont constitués d'une couche de « bio-reconnaissance » et d'un transducteur. La couche de bio-reconnaissance permet la capture spécifique de l'analyte (parfois appelée cible) à détecter. Cette couche est généralement, mais pas uniquement, constituée de biomolécules (ADN, protéines, sucres) immobilisées à la surface du transducteur. Ces molécules immobilisées sont souvent appelées sondes. Le transducteur a pour rôle de transformer cet évènement de capture par la couche de bio-reconnaissance en une grandeur physique mesurable permettant ainsi la détection de l'analyte. Si plusieurs sondes sont organisées en rangées ordonnées à la surface du transducteur, ces dispositifs sont alors appelés biopuces (microarray). Leurs applications (biopuces et biocapteurs) concernent les applications biomédicales, agroalimentaires, environnementales… Ces dispositifs permettent aussi, d'un point de vue plus fondamental, de déterminer des grandeurs thermodynamiques et cinétiques de réactions de bio-reconnaissance tel que les ΔG, K_d, ΔH, k_{on} et k_{off}. Cependant, les réactions de bio-reconnaissance en phase hétérogène aux interfaces peuvent mener à des variations d'un dispositif à l'autre dues à la chimie de greffage, aux différents matériaux constitutifs des transducteurs ou à des phénomènes de transport de masse.

En effet, Buhot *et al* [1] ont démontré qu'il était possible de déterminer grâce à la résonance des plasmons de surface les grandeurs thermodynamiques telles que K_d, ΔG, ΔH correspondant à l'hybridation ADN/ADN sur une surface de 50 nm d'or en s'appuyant sur le loi de Van't Hoff. Cependant, plusieurs revues de la littérature tendent aussi à souligner l'impact de la chimie de surface et des conditions expérimentales sur les résultats des mesure de K_d. Par exemple, ces auteurs indiquent l'effet de la densité de surface des brins d'ADN immobilisés sur leur conformation ou sur l'apparition de gêne stérique [11], [12], [133]. Il est donc possible que des constantes de dissociation déterminées par des techniques de surfaces différentes et donc employant des transducteurs différents donne lieu à des résultats différents.

Ce travail de thèse a donc pour objectif de déterminer par trois techniques différentes les constantes de dissociation. Nous avons choisi comme réaction de bio-reconnaissance modèle l'hybridation ADN/ADN.

Ces trois techniques sont la résonance des plasmons de surface (SPR) réalisée sur des surface d'or, la fluorescence excitée par champ évanescent réalisée sur un matériau polymère et la cartographie de fluorescence « conventionnelle » réalisée sur substrat de verre. Les deux

premières techniques permettent de réaliser des mesures en temps réel. Pour ces deux premiers cas, une onde évanescente est exploitée pour sonder l'interface solide/liquide. En effet, cette onde évanescente qui est générée à l'interface de deux milieux d'indice différent voit son amplitude décroitre exponentiellement avec la distance à l'interface. Ainsi, l'origine du signal est issue majoritairement de l'interface. Pour la cartographie de fluorescence « conventionnelle », les cibles fluorescentes sont détectées après incubation et lavages. Les mesures sont donc réalisées en point final. Les mesures SPR se font avec une circulation/apport en continu de cibles alors que pour les deux autres techniques l'incubation est faite sans flux. Enfin l'instrument SPR utilisé lors de ce travail a été développé à l'INL, les deux autres techniques exploitant des instruments commerciaux.

Le présent manuscrit est donc structuré autour des 4 objectifs suivant:

- Validation de l'instrument SPR développé en interne
- Développement de protocoles robustes pour la préparation de substrat d'or. En effet la littérature semble donner des résultats contradictoires quant aux effets des différents modes de nettoyage de l'or (plasma O_2 et acide de Caro) sur l'état d'oxydation de l'or, et les conséquences de cette préparation sur les étapes de greffage qui suivent.
- Optimisation des conditions de greffage des oligonucléotides sondes et des conditions d'hybridation sur les substrats d'or.
- Comparaison des constantes de dissociations obtenues par les techniques décrites ci-dessus.

La structure du manuscrit est donc :

Le chapitre 1 est dédié aux rappels des principes de base en thermodynamique et notamment ceux couramment utilisés pour décrire les réactions de bio-reconnaissance. Les différentes techniques permettant de déterminer les constantes de dissociation sont ensuite présentées. Un focus particulier est fait sur les techniques en phase hétérogène et en particulier sur les paramètres influençant les mesures de constantes d'affinité aux interfaces. Le travail de thèse est ensuite replacé dans cette perspective.

Le chapitre 2 concerne les matériels et méthodes et correspond donc à une description des protocoles expérimentaux

Le chapitre 3 est dédié à la description et à la validation de notre instrument SPR. Une procédure « qualité » avant chaque mesure SPR a été développée. Cette procédure est aussi présentée.

Le chapitre 4 est relatif au pré-conditionnement de l'or avant les réactions d'immobilisation. Deux méthodes de nettoyage ont été comparées : le plasma O_2 et le traitement avec une solution piranha (acide de Caro). Après optimisation des paramètres expérimentaux relatifs à la solution d'acide de Caro, l'impact de ces deux méthodes de nettoyage a été étudié et discuté notamment en termes de topographie, de composition élémentaire et sur les états d'oxydation des éléments présents (l'or notamment). Les effets du nettoyage sur l'immobilisation d'oligonucléotides modifiés avec des fonctions mercaptans ont ensuite été étudiés.

Le chapitre 5 concerne pour sa part l'optimisation des conditions d'hybridation ADN/ADN sur nos substrats d'or pour les mesures SPR. Enfin, les K_ds d'hybridation de deux oligonucléotides complémentaires sont mesurés par les trois techniques décrites plus haut et comparés.

Enfin le manuscrit se termine avec une discussion et conclusions générales.

Chapitre 1

La thermodynamique est la discipline qui s'intéresse aux flux de chaleur et d'énergies notamment lors de transformations chimiques ou biochimiques. Un système thermodynamique se définit par la nature et les propriétés des échanges qu'il a avec le milieu extérieur. Il peut être ouvert, fermé ou isolé. L'état d'un système est défini par ces variables d'états qui peuvent être extensives ou intensives. Parmi ces variables d'états, l'enthalpie, l'entropie et l'enthalpie libre permettent de décrire les échanges d'énergie et de chaleur ainsi que la spontanéité d'une transformation pour un système fermé et à pression constante. Ces constantes sont liées entre elles par l'équation :

$$\Delta G = \Delta H - T\Delta S \qquad \textit{Equation 1}$$

Ou ΔG et ΔH, sont l'enthalpie libre, l'enthalpie exprimées en Joules. ΔS, l'entropie de la réaction est exprimée en Joules/Kelvin et T la température en Kelvin.

Enfin, la constante d'équilibre K_a d'une transformation est liée à la variation d'enthalpie libre au cours cette réaction par l'équation :

$$\Delta G^{o}_{(T)} = RT \ln(K_{a(T)}) \qquad \text{Equation 2}$$

R est la constante des gaz parfaits, T la température, K_a la constante d'équilibre. La constante de dissociation K_d pour une interaction de reconnaissance de type :

$$P + T \leftrightarrow PT$$

est l'inverse de la constant d'équilibre (K_a). Si bien que toute technique permettant de mesurer le K_d d'une interaction biomoléculaire permet de déterminer ΔG. Si ΔH est aussi mesurée, alors ΔS peut être calculée.

Il existe plusieurs techniques permettant de mesurer les K_d d'interactions. Certaines sont réalisées en solution, d'autres sur des surfaces. Par ailleurs, il est possible de distinguer les méthodes basées sur la caractérisation des états d'équilibre de celles basées sur des mesures cinétiques.

Parmi toutes les techniques en solutions, le titrage calorimétrique isotherme est la «méthode de référence ». Cette technique mesure la chaleur de réaction en fonction d'ajout connu et croissant d'un des réactifs. Elle permet de déterminer l'enthalpie, l'entropie et la stœchiométrie d'une réaction.

Pour ce qui concerne les techniques basée sur des mesures à l'interface liquide/solide, la mesure se fait souvent grâce à l'immobilisation de l'un des partenaires sur un substrat solide. Après capture de la cible (molécule à détecter) par la sonde (molécule immobilisée), cette interaction est transformée en une grandeur mesurable par le transducteur. Il existe des transducteurs optiques (fluorescence, SPR, interféromètre…), des transducteurs mécaniques (microbalance à quartz), électrochimiques… Ces techniques ont comme avantage par rapport aux techniques en solution d'être en général moins consommatrice en molécules et d'être à haut débit. Elles ont comme inconvénient de nécessiter l'immobilisation de l'un des partenaires, ce qui peut influencer le résultat final.

Ces techniques, qu'elles soient réalisées par mesures cinétiques ou par mesures en point final, s'appuient sur des modèles pour extraire les grandeurs thermodynamiques. De manière courante, les modèles sont basés sur une reconnaissance bimoléculaire de type :

$$P + T \leftrightarrow PT$$

Les seuls espèces possibles sont donc P, T et PT. Ce qui signifie que toute autre réaction est exclue. De ce fait, la cible (T) est considérée comme étant uniquement en équilibre avec son complexe (PT). Elle ne peut pas être en équilibre entre différentes conformations ou en équilibre avec sa forme adsorbée non spécifiquement sur le substrat et sa forme en solution. Autrement dit, toutes les cibles non liées avec P doivent être équivalentes. Il en est de même pour les sondes. Les interactions inter-sonde sont donc par exemple exclues.

Sur la base de ce modèle bimoléculaire simplifié, il est alors possible d'écrire que, à l'équilibre, on a:

$$K_d = \frac{[P][T]}{[PT]} \qquad \text{Equation 3}$$

Grâce à la loi de conservation de masse et en considérant que la variation de concentration en cible est négligeable, cette équation peut être transformée en :

$$\frac{X_{eq}}{1-X_{eq}} = \frac{C_T}{K_d} \qquad \text{Equation 4}$$

X_{eq} correspond au rapport du signal mesuré pour une concentration en cible C_T à l'équilibre sur le signal maximal mesurable. Ce signal correspond au nombre de sondes maximales disponibles pour l'interaction. Ainsi, en mesurant le signal obtenu pour plusieurs concentration en cible (C_T), il est possible d'extraire la constante de dissociation.

Il est aussi possible d'écrire que pour une concentration c instantanée de T, on a à tout instant t:

$$S_a(c,t) = S_{eq}(c)(1 - e^{-(t-t_0)/\tau}) \qquad \text{Equation 5}$$

S_a correspond au signal mesuré au temps t lors de la phase d'association c'est-à-dire du temps initial t_0 au moment de l'injection jusqu'à l'obtention de l'équilibre. S_{eq} est le signal mesuré lorsque l'équilibre est atteint. τ est la constante de temps de la réaction qui est une fonction de la constante cinétique d'association et de dissociation.

Lors de la phase de dissociation :

$$s_d\,(c,t) = s_a\,(c,t_c)e^{-k_{off}(t-t_c)} \qquad \text{Equation 6}$$

Où S_d est le signal mesuré lors de la phase de dissociation.

En mesurant les cinétiques d'association et de dissociation pour différentes concentrations initiales en cible et en ajustant l'ensemble des courbes simultanément, il est possible de

déterminer les paramètres cinétiques d'association (k_{on}) et de dissociation (k_{off}) et donc de déterminer K_d.

Parmi les paramètres expérimentaux qui peuvent influencer la mesure, il faut noter :

- La pureté de la solution de cible. En effet la présence de molécules tierces peut engendrer de l'adsorption non-spécifique ou des réactions croisées et donc un signal. La variation du signal n'est, dans ce cas, pas exclusivement liée à la capture de la cible par la sonde et un K_d apparent est alors mesuré. Pour en tenir compte il est nécessaire de réaliser des contrôles idoines.
- La variation de la concentration de la cible pendant la réaction. En effet, dans le modèle de Langmuir, la variation de concentration en cible due à l'interaction est considérée comme négligeable par rapport à la concentration initiale. Pour certaines interactions très affines, il faut s'assurer que cette assomption est vraie surtout aux faibles concentrations en cible.
- La propension de la cible à exister sous plusieurs états : conformations, adsorbée ou non… Par exemple, un oligonucléotide de faible poids moléculaire possède statistiquement moins de repliements possibles que son équivalent génomique.
- La disparité de la sonde : la disparité de la sonde étant définie ici comme les différents états dans lesquels la sonde existe à la surface du transducteur : repliement, orientation…En général, les modèles considèrent une seule population de sondes.
- La chimie de surface : celles- ci peut donner lieu à une disparité plus ou moins élevées des sondes.
- La densité de surface des sondes. C'est un paramètre important car il peut influencer la disparité des sondes mais aussi engendrer soit de la gêne stérique soit au contraire exacerber l'interaction sonde/cible comme c'est le cas par exemple avec les interactions sucre /protéines (effet cluster de surface).
- La courbure et la rugosité de la surface.
- La proximité de la surface : la surface peut être perçue comme un mur impénétrable qui réduit le nombre de conformations possibles pour la cible et la sonde ainsi que le nombre de degrés de liberté. Selon Halperin *et al*, [69] ces paramètres ont peu d'influence. En revanche, Schmidt [75] ainsi que Hurst [76] indiquent que la proximité de la surface stabilise la formation du duplex ADN/ADN. De plus l'interface correspondant à un microenvironnement dont les paramètres sont différents de ceux observés dans la

solution : c'est par exemple le cas de la concentration en ions (double couche de diffusion).

- Les interactions non spécifiques. Nous avons déjà mentionné plus haut l'adsorption non-spécifique qui correspond à une force attractive exercée par la surface sur la cible. Cependant, il est possible aussi d'imaginer l'inverse c'est-à-dire l'existence de force répulsives. Par exemple, l'influence du potentiel zéta à l'interface solide/liquide sur l'attraction ou la répulsion d'une cible d'ADN.
- Les conditions expérimentales comme la température, le pH, la force ionique…. qui peuvent influencer les interactions entre la cible et la sonde mais aussi les interactions sonde/sonde, sonde/surface, cible/cible et cible/surface.

Bien qu'il existe des modèles qui permettent de tenir compte de certaines de ces déviations par rapport au modèle standard de Langmuir, il n'en reste pas moins que la comparaison de plusieurs techniques peut se révéler difficile du fait de ces variations expérimentales et ce d'autant plus que pour chaque transducteur les stratégies de couplage de la sonde sur le support sont variables et mènent donc à des populations de sondes qui peuvent être très différentes d'un substrat à un autre. En effet, il existe plusieurs stratégies de greffage basées soient sur des interactions faibles (physisorption), des interactions biomoléculaires (streptavidine/biotine ou protéine G/anticorps) ou la formation de liaisons covalentes. Dans ce dernier cas, différentes réactions chimiques existent en fonction du substrat considéré et de la biomolécule à immobiliser (Tableau 1 and Figure 1).

Substrat	Verre/ SiO_x, SiN_x	Si	Nitrure du groupe (GaN, AlN)	Metaux (Au, Cu, Ag, Pt)	GaAs	Oxydes métalliques (Ag, Au, Al)	Oxides: ITO, TiO_2, ZnO
Réaction	Silane	Hydrosilylation	Silane	Thiol	Thiol	Acides carboxyliques	Acides phosphoniques
Ref.	[9], [103]–[106]	[107]	[110]	[111]–[114]	[115]	[116]	[117], [118]

Tableau 1.exemple de réactions de greffage de molécules sur différents substrats.

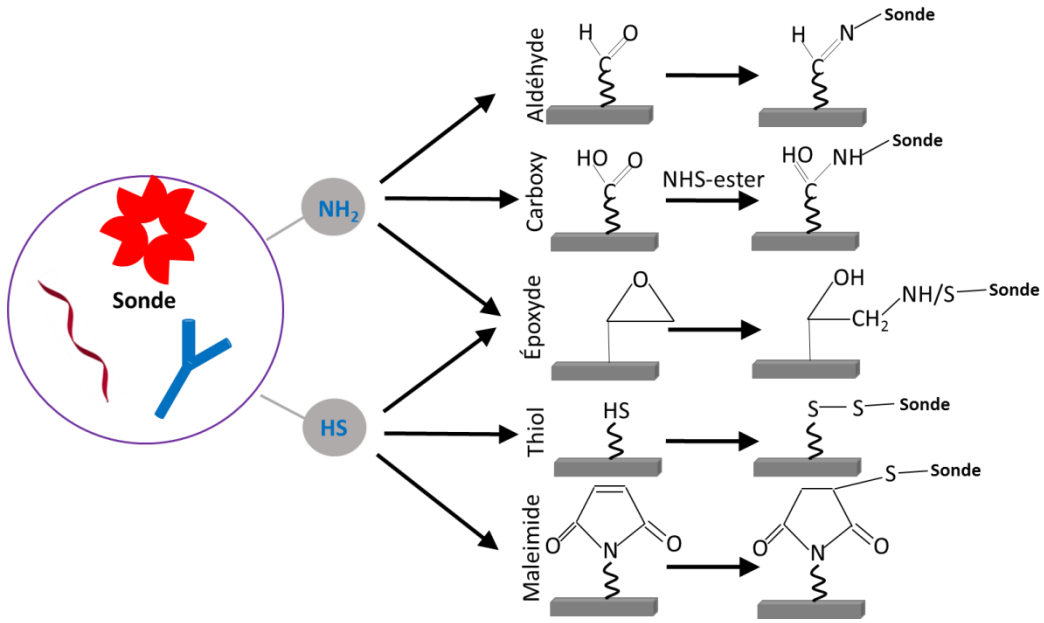

Figure 1 Schéma des principales réactions décrites dans la littérature pour le greffage de biomolécules sur des substrats fonctionnalisés.

Pour ce qui concerne le greffage de biomolécules sur un substrat d'or, une des réactions les plus décrites concerne la réaction des mercaptans avec l'or. Cette réaction permet notamment de greffer directement une sonde oligonucléotidique modifiée avec un groupement fonctionnel thiol.

Dans ce présent travail de thèse, nous avons utilisé trois techniques pour déterminer les constantes de dissociation pour l'hybridation de deux brins oligonucléotidiques (ODN). Ces trois techniques font appel soit à un substrat d'or de 50 nm, soit à un substrat polymérique (polystyrène), soit à un substrat en verre. Les brins d'ADN ont donc été immobilisés soit

directement sur l'or en utilisant des ODN modifiés avec une fonction thiol, soit en exploitant l'interaction streptavidine/biotine sur le substrat polymérique, soit la chimie des esters activés sur le verre. Dans le cas du substrat polymérique, après physisorption de la streptavidine sur le support, un ODN modifié avec de la biotine est immobilisé. Dans le cas du verre, une première étape a consisté à introduire des fonctions carboxyliques à la surface du verre grâce à une réaction de silanisation suivi d'une réaction de couplage avec un ODN modifié portant une amine primaire.

Comme précédemment indiqué, les rendements d'hybridation de deux oligonucléotides complémentaires dont l'un des partenaires est immobilisé, dépendent de la densité de surface, de la proximité de la surface, de l'orientation des brins, de leurs conformations et des paramètres expérimentaux.

Dans le cadre de cette thèse, nous avons tout d'abord entrepris de déterminer les conditions expérimentales permettant de maximiser le signal SPR d'hybridation sur notre instrument. Ensuite, les K_d mesurés sur cet appareil ont été comparés à ceux obtenus par deux autres techniques de surfaces à savoir, la fluorescence excitée par champ évanescent et la cartographie de fluorescence par scanner de fluorescence.

Chapitre 2

Dans ce chapitre, le lecteur trouvera une description des réactifs, substrats et des appareils utilisés. Les instruments de caractérisation utilisés sont la mesure d'angle de contact, la spectrométrie photo-électronique (XPS), la spectroscopie infrarouge de réflexion-absorption à modulation de phase (PM-IRRAS), la microscopie de force atomique (AFM). Les conditions opératoires d'utilisation de ces instruments sont décrites.

De plus, les modes opératoires pour la préparation de surface d'or, de verre et de polymères sont décrits.

Enfin, les protocoles de greffage d'oligonucléotides modifiés thiol, biotine ou amine sur les trois substrats sont décrits. Enfin les conditions utilisées pour réaliser l'hybridation de ces brins immobilisés avec leurs oligonucléotides complémentaires et les mesures de K_d sont décrites.

Chapitre 3

La résonance des plasmons de surface mesure la variation d'indice de réfraction à l'interface métal/diélectrique. C'est aujourd'hui une des techniques les plus utilisée pour la réalisation de mesures d'affinité entre un ligand et un récepteur.

Les plasmons de surface sont une excitation collective d'électrons libres confinée à la surface métallique. Cette oscillation crée un champ électromagnétique (tel que représenté sur la Figure 2) qui décroît exponentiellement dans les deux milieux avec des longueurs de décroissance typiques de quelques dizaines de nanomètres dans le métal et jusqu'à plusieurs centaines de nanomètres dans le diélectrique.

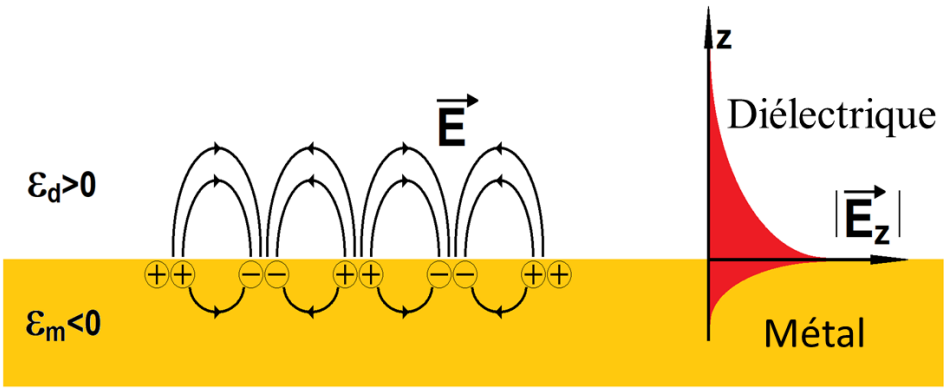

Figure 2 Oscillation collective des électrons à l'interface métal/diélectrique

Pour pouvoir exciter les plasmons avec une lumière incidente, il faut que le nombre d'onde de la lumière coïncide avec celui des plasmons. Pour ce faire, il est nécessaire de ralentir la lumière grâce à un prisme. Dans ces conditions il est possible de trouver pour une longueur d'onde donnée un angle pour lequel la lumière entre en résonance avec les plasmons engendrant ainsi une perte de l'intensité de la lumière réfléchie. Il en découle que toute variation d'indice de réfraction engendre une variation des conditions de couplage. Celle-ci peut être suivie en angle, en longueur d'onde ou en intensité (cf Figure 3).

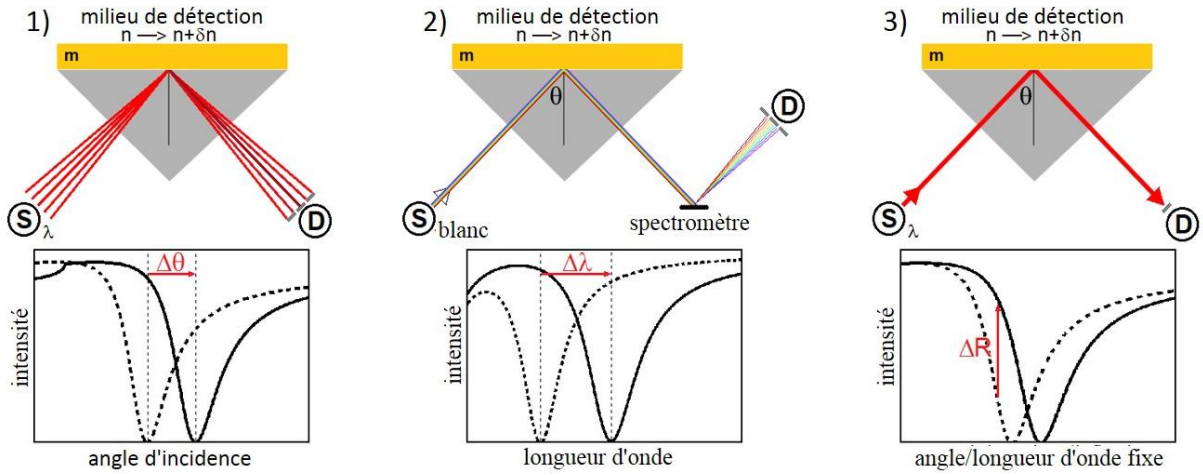

Figure 3 Les conditions de couplage entre la lumière incidente et les plasmons peut être suivi en angle (1), longueur d'onde (2) ou intensité (3). S : source. D : Détecteur

Ainsi, pour une surface d'or sur laquelle sont immobilisées des sondes comme par exemple de l'ADN, l'interaction de la sonde avec la cible engendre une variation d'indice qui peut être suivie en temps réel en déterminant à chaque instant les conditions de couplage (longueur d'onde de couplage, angle de couplage ou intensité).

Historiquement, il existe deux configurations d'instrument proposées par Kretschmann [145] et Otto [146] (Figure 4)

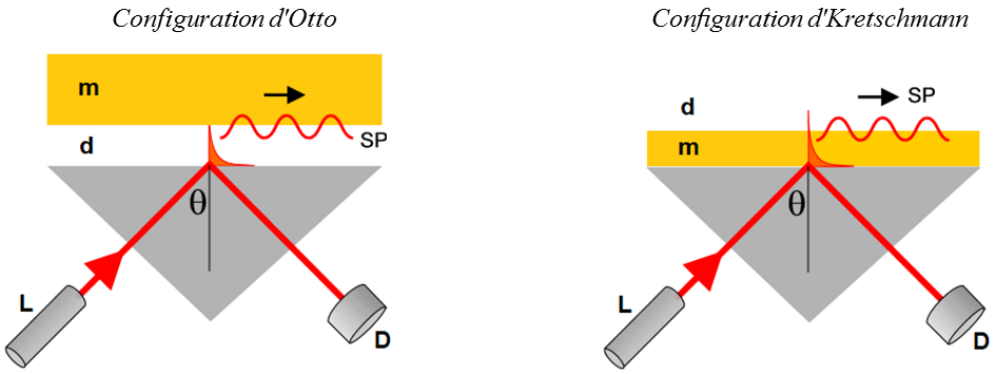

Figure 4: Présentation de la configuration d'Otto et de Kretschmann.

Dans le cas de l'instrument développé à l'INL, il possède une configuration de Kretschmann avec un suivi des conditions de couplage en angle en utilisant un faisceau en éventail (wedge-shaped beam system) qui permet de sonder les conditions de couplage angulaire sur plusieurs angles simultanément. En effet comme illustré sur la figure 5, la ligne focale symbolisée en rouge sur la figure du haut correspond à plusieurs conditions de couplage angulaire où chaque

pixel de la ligne correspond à un angle de couplage différent. Autrement dit en mesurant pour chaque pixel de la ligne l'intensité de la lumière réfléchie, une courbe de type de celle schématisée dans la figure 3 (1) est obtenue.

Le système développé est adapté à l'utilisation de lame de microscope de verre en BK7, avec 3 nm de chrome et 50 nm d'or.

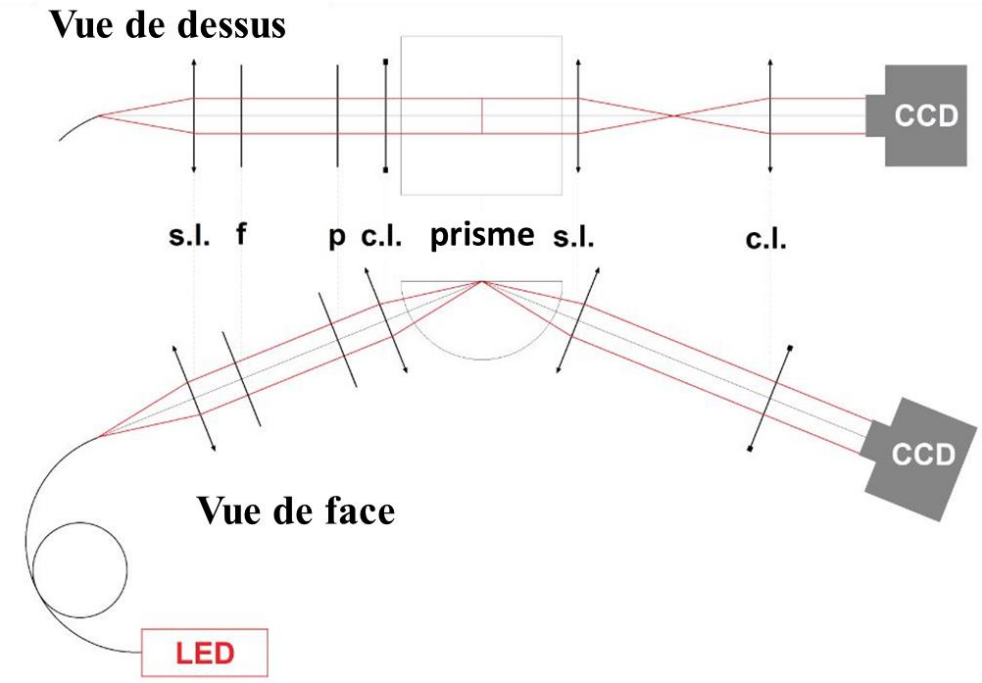

Figure 5 : présentation schématique de l'optique de l'instrument. s.l.: lentille sphérique; c.l.: lentille cylindrique; f: filtre passe-bas; p: polariseur.

Les courbes ainsi obtenues sont ajustées en temps réel par un polynôme de degré 3 ce qui permet de déterminer en temps réel la position du dip (l'angle pour lequel la condition de résonance est vérifiée) et d'obtenir une courbe du type de celle présentée à la figure 6 qui donne la variation de l'angle de résonance en fonction du temps.

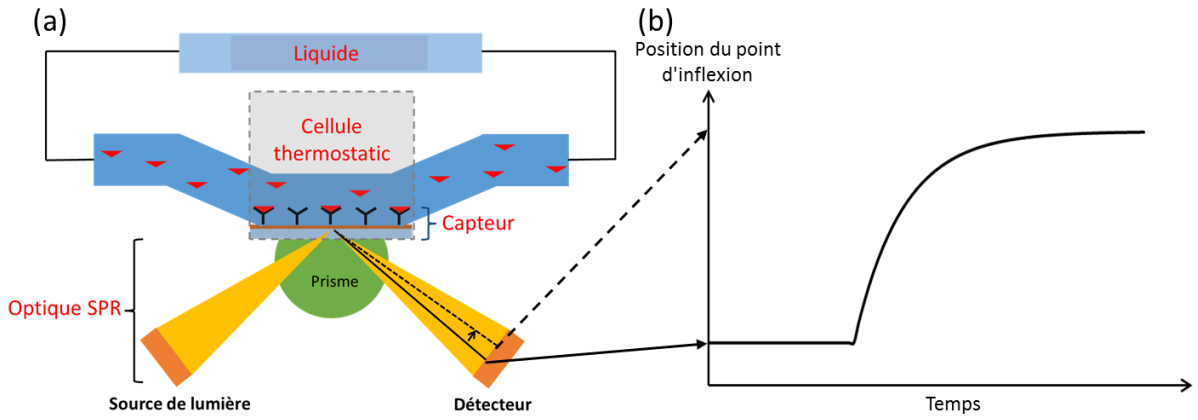

Figure 6 : présentation schématique de la mesure d'une cinétique.

De manière à pourvoir réaliser des cinétique de réaction en solution, nous avons développé une cellule fluidique (Figure 7) d'un volume de 15 µL et contrôlée en température puisque l'indice de réfraction pour un milieu donné est une fonction de la température. La température est stabilisée à ± 0.1°C. La circulation des fluides est assurée par une pompe à double piston de type pompe HPLC et une valve de séparation de flux permettant d'ajuster le flux de 10 à 100 µL/min. Enfin, une boucle d'injection de HPLC de 1 ml complète le système fluidique.

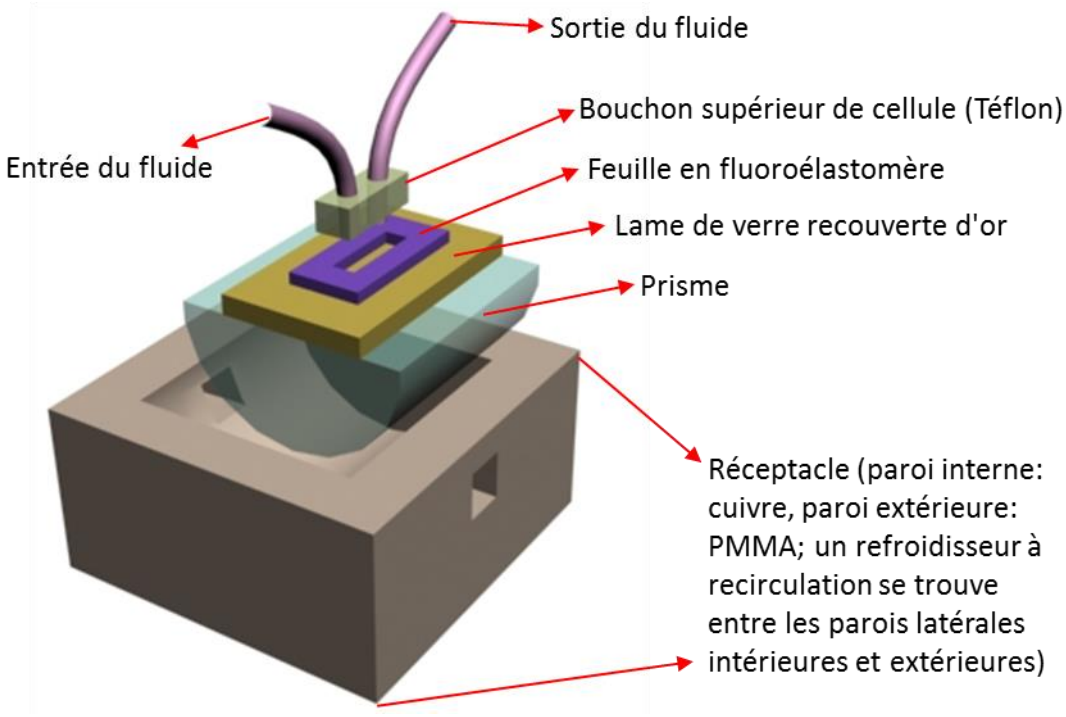

Figure 7 Schéma de la cellule fluidique.

Nous avons ensuite cherché à qualifier notre instrument en réalisant des sauts d'indice. Pour se faire nous avons opté pour des solutions de tampon phosphate (PBS) de concentrations variables qui sont couramment employées dans la littérature. Il est ainsi plus aisé de comparer notre instrument avec ceux de la littérature. Nos résultats montrent une linéarité sur l'ensemble de la gamme étudiée avec une sensibilité de 64.67 pixel par saut de concentration de PBS (cf Figure 8).

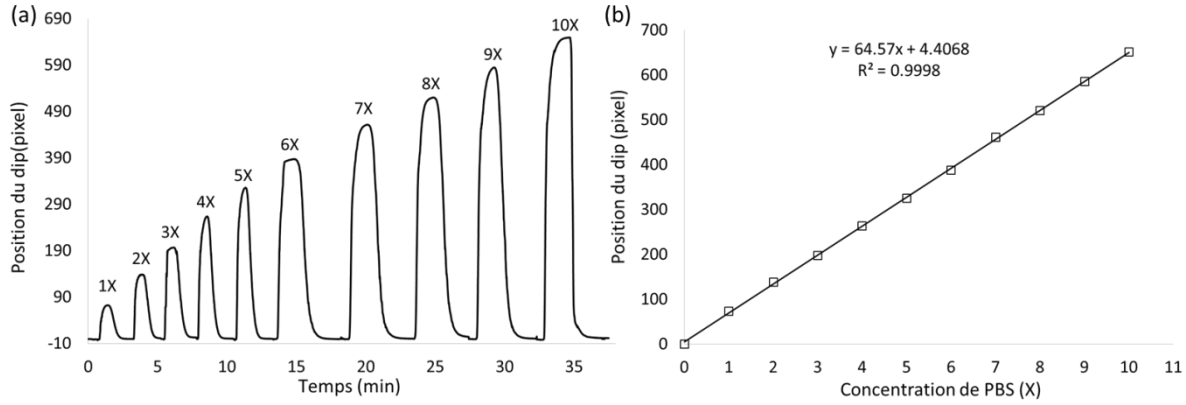

Figure 8 Calibration de l'instrument SPR avec des sauts d'indice provoqués par l'injection de solutions de PBS de concentrations varies.

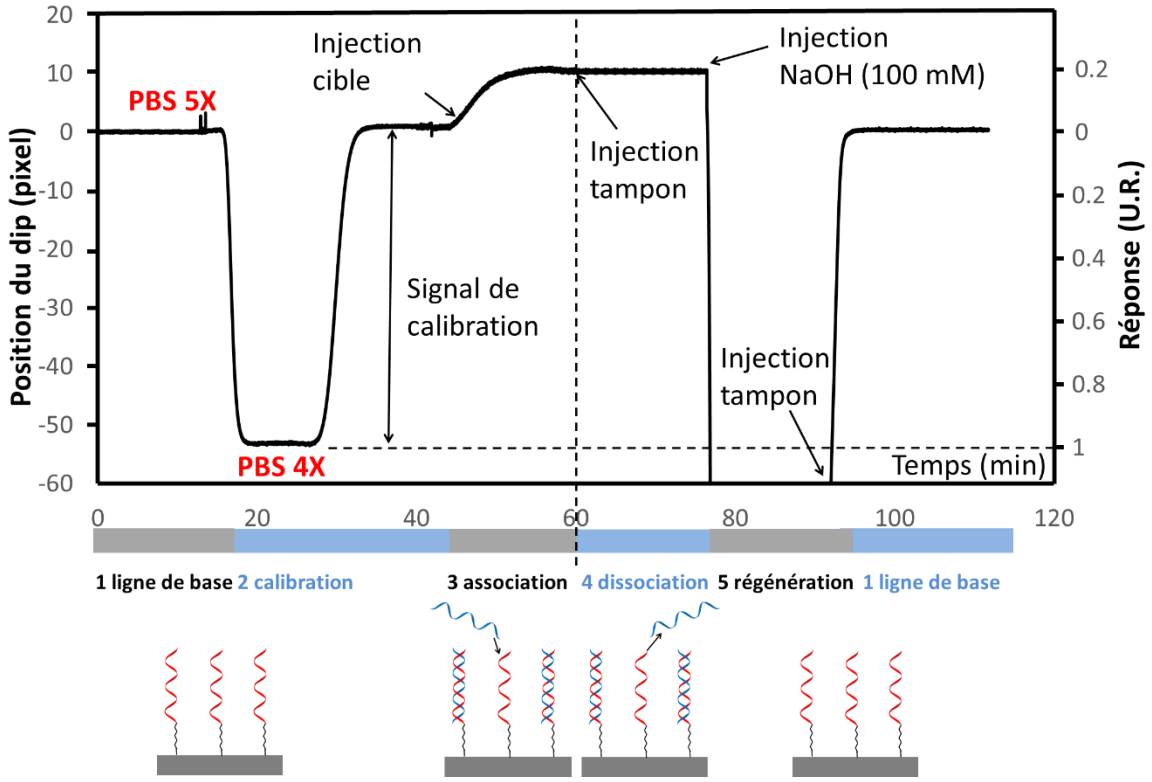

Figure 9 : Exemple de la procédure utilisée avant chaque mesure.

Chapitre 4

La première étape lors d'une fonctionnalisation chimique consiste à nettoyer le substrat de manière à permettre l'accès des molécules aux sites de réaction sur le support. Cette étape sert aussi parfois à activer ces sites.

L'énergie de surface de l'or propre est élevée ce qui entraîne la pollution rapide de sa surface par les contaminants de l'air. Un traitement oxydant de type acide de Caro (solution piranha, UV/ozone ou plasma oxygène) est donc nécessaire. Cependant dans la littérature, l'angle de contact de l'or propre avec l'eau reste matière à débat. Selon certains auteurs [161]–[163], cet angle est de 0° pour de l'or propre, alors que pour d'autres auteurs [165]–[167], cet angle de zéro degré est dû à la présence d'un oxyde suite aux étapes de nettoyage. La présence de cet oxyde engendrerait des problèmes lors de la réaction de couplage avec les thiols notamment cela engendrerait une inhomogénéité.

Dans un premier temps nous avons donc suivi la variation de l'angle de contact d'une goutte d'eau sur une surface d'or fraîchement déposée en fonction du temps (Figure 10).

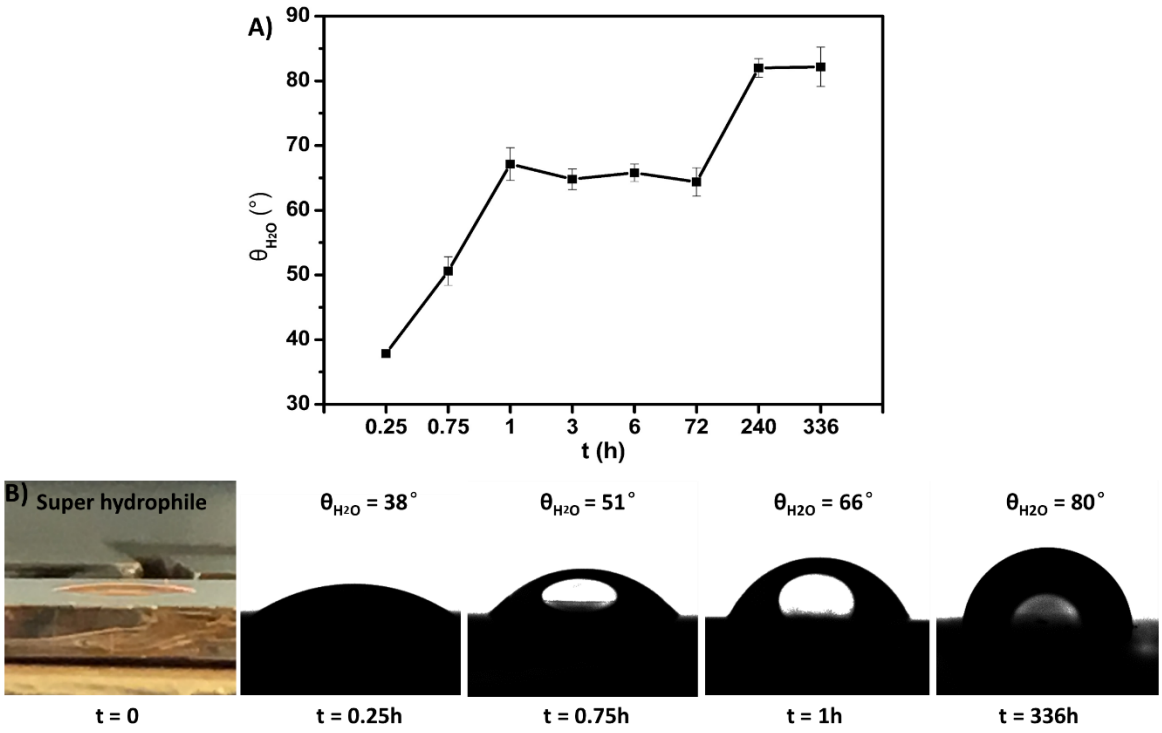

Figure 10 Variation de l'angle de contact mesuré d'une goutte d'eau sur une surface d'or fraîchement déposée en fonction du temps.

A t= 0 s, c'est-à-dire juste au moment de la sortie du substrat du bâti d'évaporation, nous avons trouvé un angle de contact avec l'eau inférieur à environ 10°. Après 15 minutes, cet angle est déjà de 35° et de 70° après une heure. Ce point est important car certains auteurs préconisent d'attendre 24h après nettoyage de façon à permettre la disparition de l'oxyde d'or formé lors du nettoyage avant de réaliser la réaction de couplage.

Nous avons donc comparé deux méthodes de nettoyage afin de déterminer 1) l'efficacité de nettoyage et 2) si ces nettoyages engendraient la formation d'oxyde. Leur efficacité a été évaluée par la mesure de l'angle de contact avec l'eau en faisant l'hypothèse que plus l'angle de contact serait faible plus la surface serait propre. Cependant dans le cadre de cette hypothèse il a fallu étudier la formation d'un oxyde et la rugosité de surface. Ces deux paramètres pouvant aussi engendrer une diminution de l'angle de contact. Les deux méthodes de nettoyage étudiées sont l'acide de Caro et le plasma oxygène.

Sur cette base nous avons tout d'abord cherché à optimiser le nettoyage par une solution de piranha puisque la littérature ne dégage pas un consensus sur les conditions optimales [169]. Les paramètres étudiés sont le rapport H_2O_2/H_2SO_4, la température et le temps de réaction. Les résultats sont présentés dans la Figure 11.

Rapport volumique H_2SO_4/H_2O_2	**Angle de contact θ_{H2O} (°)**
1:1	56 ± 12
2:1	52 ± 19
3:1	32 ± 4
4:1	33 ± 3
5:1	43 ± 11

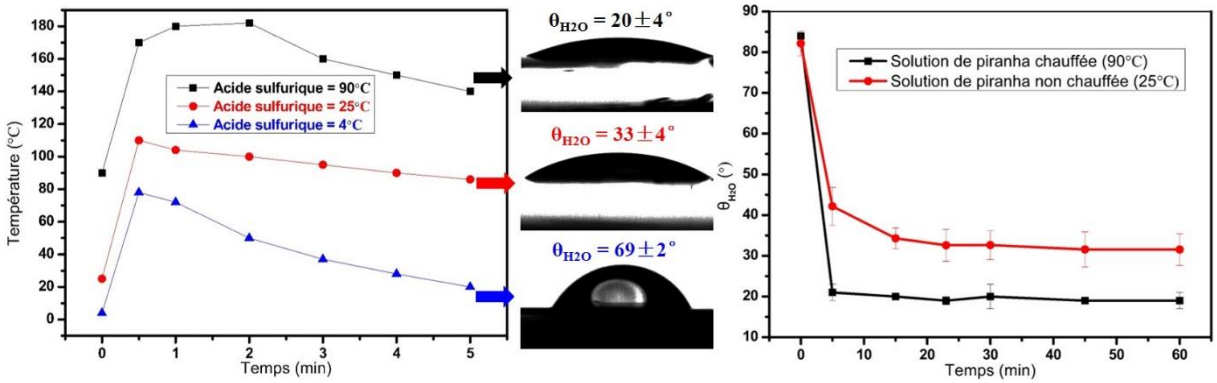

Figure 11 Variation de l'angle de contact d'une goutte d'eau mesuré sur une surface d'or fraîchement nettoyée en fonction du rapport H_2O_2/H_2SO_4 (tableau du haut), en fonction de la température (en bas à gauche) et en fonction du temps (en bas à droite). Pour ces deux dernières courbe un rapport H_2O_2/H_2SO_4 de 1/3 en volume a été utilisé.

Nous avons donc trouvé que les conditions optimales semblaient être un nettoyage avec un rapport H_2O_2/H_2SO_4 de 1/3 pendant 5 minutes avec un préchauffage de l'acide sulfurique à 90°C. Ces conditions conduisent à un angle de contact avec l'eau de 20°.

Ce nettoyage a ensuite été comparé avec un nettoyage par plasma inductif O_2 de 5 minutes. Ce nettoyage conduit à un angle de contact avec l'eau de 0°. La question était donc cette différence d'environ 20° observée entre le nettoyage au plasma O_2 et le piranha, est-elle due à l'efficacité du nettoyage, à la présence d'un oxyde ou à une différence de rugosité.

Pour ce faire, des substrats d'or de 50 nm d'épaisseur ont donc été nettoyés par un mélange piranha ou par plasma O_2 et caractérisés par XPS et AFM afin d'étudier leurs rugosité, et le degré d'oxydation de l'or. Les résultats sont présentés Figures 12 et 13.

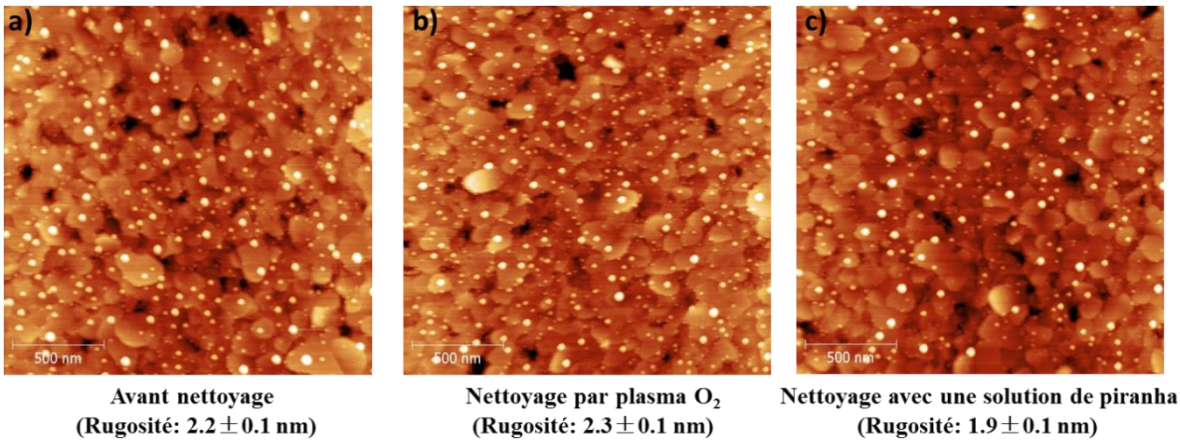

Figure 12 Images réalisées en microscopie de force atomique (AFM) de substrats d'or 50 nm d'épaisseur avant et après nettoyage par plasma O_2 (5 min) ou par traitement avec une solution de piranha (1/3, 90° 5 min).

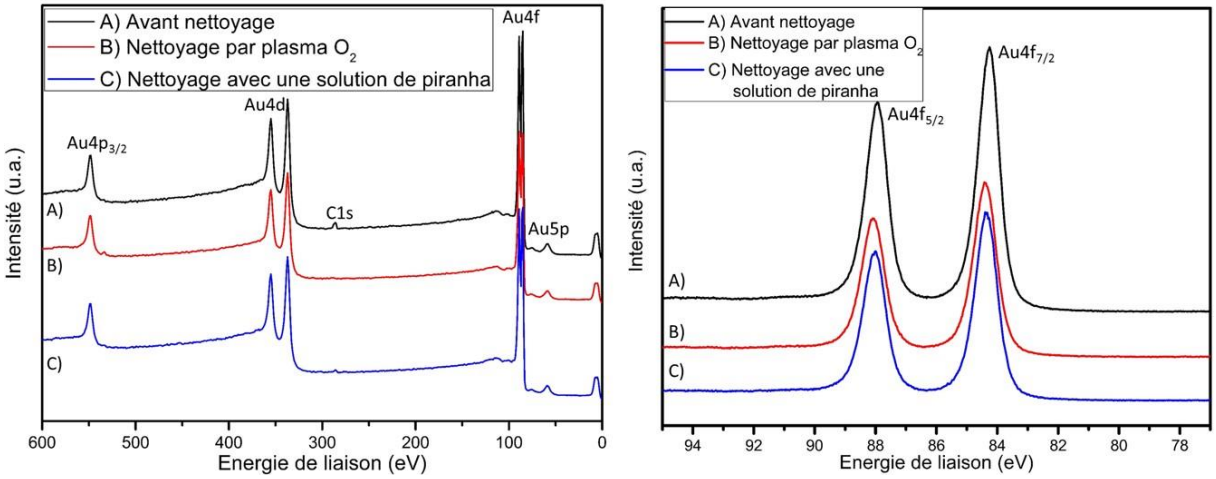

Figure 13 Spectres XPS de substrats d'or 50 nm d'épaisseur avant et après nettoyage par plasma O_2 (5min) ou par traitement avec une solution de piranha (1/3, 90° 5 min).

L'observation AFM de substrat d'or de 50 nm d'épaisseur avant et après nettoyage par plasma O_2 ou par traitement avec une solution de piranha montre une rugosité arithmétique de 2.3, 2.2 et 1.9 nm, respectivement. La différence de mouillabilité n'est donc pas imputable à une variation de la rugosité de surface.

Le spectre général XPS ne permet pas de mettre en évidence la présence d'oxygène quel que soit la méthode de nettoyage choisie. Le spectre du pic 4f de l'or confirme l'absence d'oxyde. Ceci est en contradiction avec les résultats précédents de Palazon *et al* [174] qui avait observé la présence d'un oxyde après plasma oxygène. Cependant, les conditions de plasma utilisées par ces auteurs étaient différentes, notamment la puissance était environ 10 fois supérieure à celle employée dans cette étude. Selon Linn *et al* [181], le temps d'exposition plasma détermine l'épaisseur de l'oxyde. Dans nos conditions, il est donc possible que le faible temps d'exposition et la faible puissance du plasma n'engendre qu'une couche d'oxyde très fine et très éphémère. Par ailleurs, après le traitement piranha, aucun oxyde n'a pu être mesuré par XPS. Cela est peut-être dû au fait que l'oxyde est détruit lors du rinçage dans l'eau [182].

Enfin, nous avons étudié l'impact du nettoyage sur le greffage d'oligonucléotides modifiés avec une fonction thiol. La caractérisation a été réalisée par spectroscopie infrarouge de réflexion-absorption à modulation de phase (PM-IRRAS, figure 14). L'épaisseur des substrats d'or était alors de 200 nm.

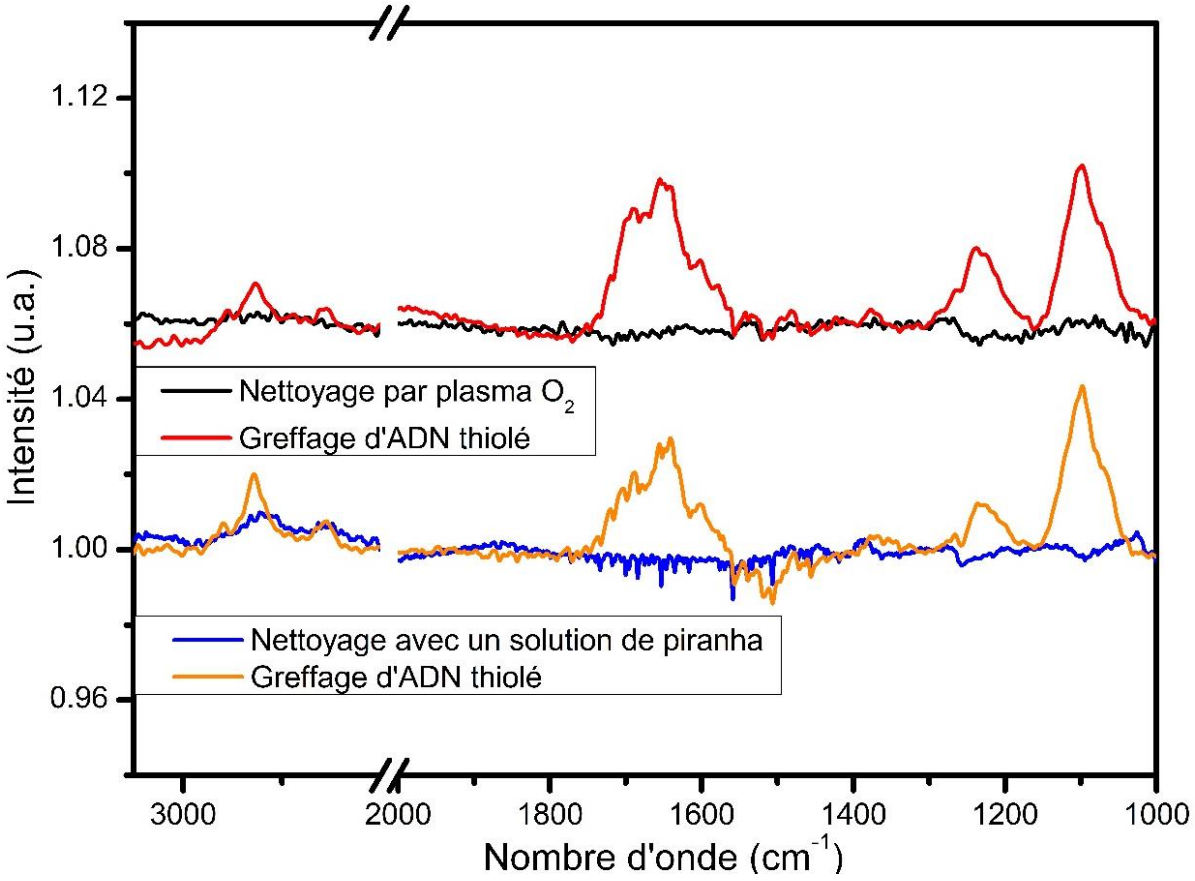

Figure 14 Spectres PM-IRRAS de substrats d'or nettoyés par plasma O_2 de 5 minutes (noir), nettoyé avec un solution de piranha (1/3, 90° 5 min) (bleu), nettoyés par plasma O_2 de 5 minutes suivi d'un réaction de greffage d'oligonucléotide modifié avec un fonction thiol (rouge), nettoyé avec un solution de piranha (1/3, 90° 5 min) suivi d'un réaction de greffage d'oligonucléotide modifié avec un fonction thiol (orange).

D'après les spectres PM-IRRAS obtenus, les greffages d'oligonucléotide ne montrent pas de différences significatives.

Chapitre 5

Dans ce chapitre l'objectif était de 1) optimiser les conditions d'hybridation notamment sur surface d'or de manière à optimiser le signal SPR et 2) de comparer les constantes de dissociation obtenues par SPR avec celles obtenues par les techniques de fluorescence par champ évanescent et cartographie de fluorescence. Pour la SPR et la fluorescence par champ évanescent, il est possible de suivre la réaction de reconnaissance en temps réel et donc d'obtenir les K_d soit par mesure en point final soit par ajustement des paramètres cinétiques.

Comme modèle, nous avons choisi de mesurer les constantes d'équilibre de l'hybridation d'oligonucléotides (ODN). Les sondes et cibles utilisées sont décrites dans le Tableau 2.

Sonde:	**P_1**: 5'-GTG AGC CCA GAG GCA GGG-$(CH_2)_6$-HS
	P_2: 5'-GCT AAT CCA ACG CGG GCC AAT CCT T-$(CH_2)_6$-HS
Cible:	**T_1:** 5'-CTG CCT CTG GGC TCA
	T_2: 5'-CCG CGT TGG ATT AGC
Molécules Diluantes:	**MCH (6-mercapto-1-hexanol)**: HS-$(CH_2)_6$-OH (MW = 134 g/mol)
	PEG-thiol (Polyethylene glycol methyl ether thiol): HS-CH_2CH_2-$(OCH_2CH_2)_n$-OCH_3 (MW = 2000 g/mol, n≈43)
	Oligo-T: 5'-TTT TTT TTT T-$(CH_2)_6$-HS (MW = 2872 g/mol)
	Diluant-P_2: 5'-GCC AAT CCT T-$(CH_2)_6$-HS (MW = 3159 g/mol)

Tableau 2 Description des oligonucléotides utilisés pour l'hybridation sur or.

Le premier paramètre que nous avons optimisé fut le pH de la solution d'immobilisation des ODN modifiés avec une fonction thiol. Le tampon employé fut un tampon phosphate (PBS 10x) de concentration 1.37 M de NaCl,, 27 mM de KCl et 100 mM de phosphate. Les pH testés s'étendaient de 5.5 à 10. Après immobilisation, les substrats d'or de 200 nm d'épaisseur ont été observés par PM-IRRAS. Les spectres obtenus sont présentés Figures 15.

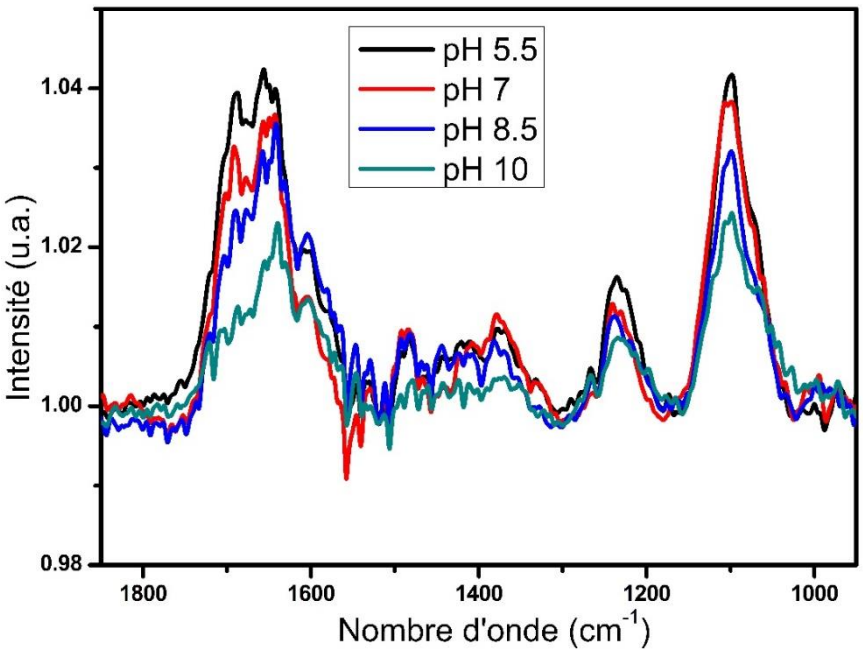

Figure 15 Spectres PM-IRRAS de substrats d'or 200 nm modifiés avec un ADN modifié portant une fonction thiol. La réaction de greffage est réalisée à différents pH dans du PBS 10X à 25°C et une concentration en ODN de 20 µM.

Ces spectres semblent indiqués que plus le pH est bas plus l'immobilisation est efficace. D'après la littérature, ceci pourrait être dû à une réduction de la répulsion électrostatique du fait d'une plus grande protonation des fonctions phosphate des brins d'ODN [3], [207]. Cependant, cela reste surprenant car le tampon d'immobilisation possède une force ionique élevée.

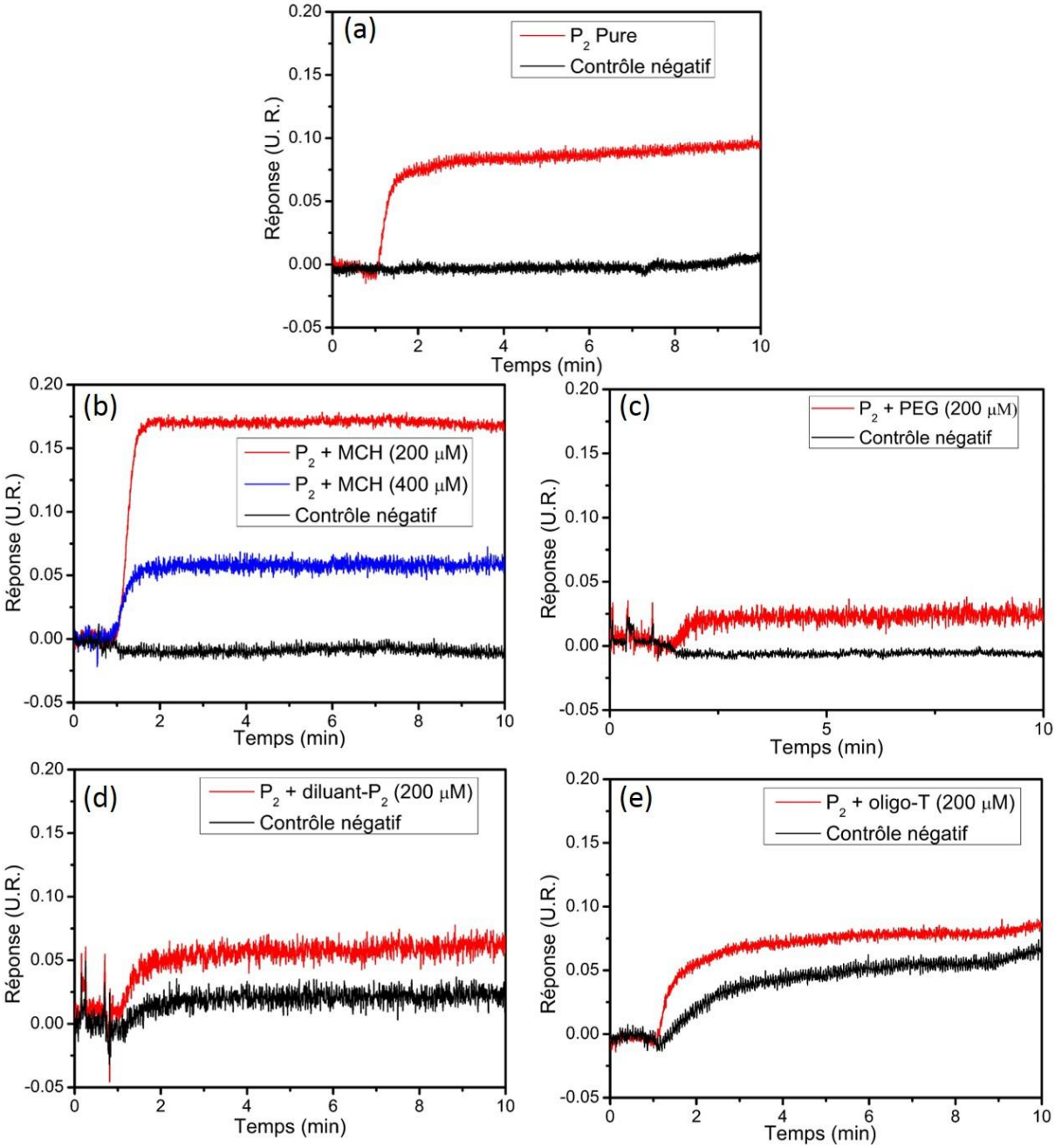

Figure 16 Sensogrammes obtenus lors de l'hybridation de la sonde P2 avec T2 pour différentes molécules diluantes.

Les couches d'ODN selon la littérature doivent être diluées avec une molécule dite diluante de manière à limiter la gêne stérique. Notre protocole est basé sur une réaction d'échange, c'est-à-dire que les sondes ODN sont tout d'abord immobilisées sur le substrat d'or formant une couche constituée à 100% d'ODN. Les substrats sont ensuite incubés dans une solution de molécules diluantes ce qui permet de les remplacer partiellement par celle-ci. 4 molécules diluantes ont été testées et sont décrites tableau 2. Les sensorgrammes obtenus sont présentés Figure 16.

Ce que l'on peut noter sur les sensorgrammes, c'est l'effet bénéfique du diluant MCH sur le signal. Les diluants basés sur des séquences courtes d'ADN engendrent sur le témoin négatif un signal de 50 à 80 % du signal observé pour les brins complémentaires. Et lorsque nous employons un PEG modifié avec une fonction thiol, une perte de signal est observée. Les spectres PM-IRRAS semblent indiquer que le PEG modifié thiol dans nos conditions de remplacement déplace totalement les ODN (Figure 17).

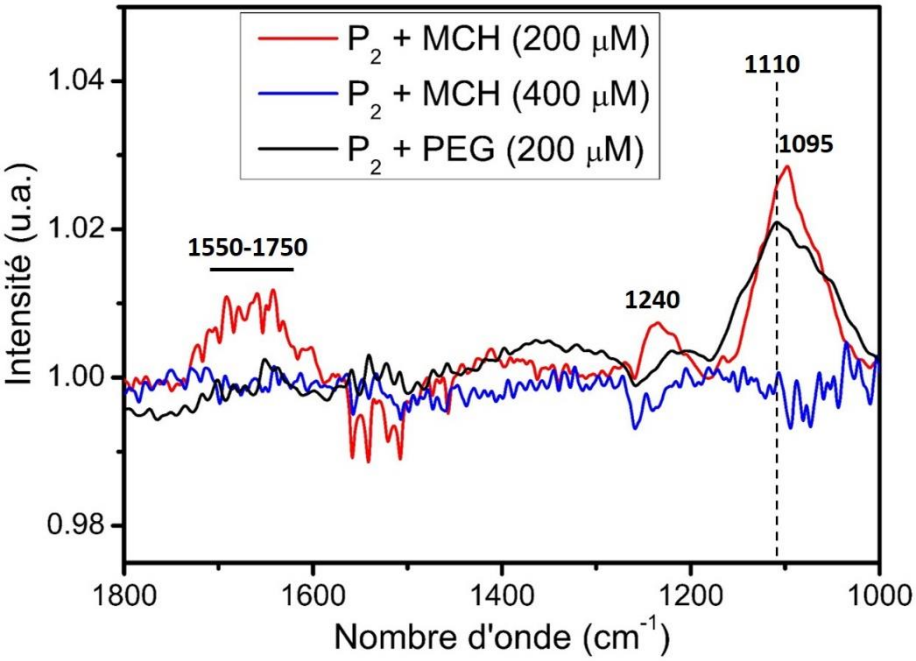

Figure 17 Spectres PM-IRRAS de substrats d'or 200 nm d'épaisseur modifiés avec des ODN-SH puis incubés en présence de MCH ou de PEG-SH.

Ensuite nous avons comparé les résultats obtenus pour deux couples de sonde/ cible (P_1/T_1 et P_2/T_2, voir tableau 2). Les résultats sont présentés Figure 18.

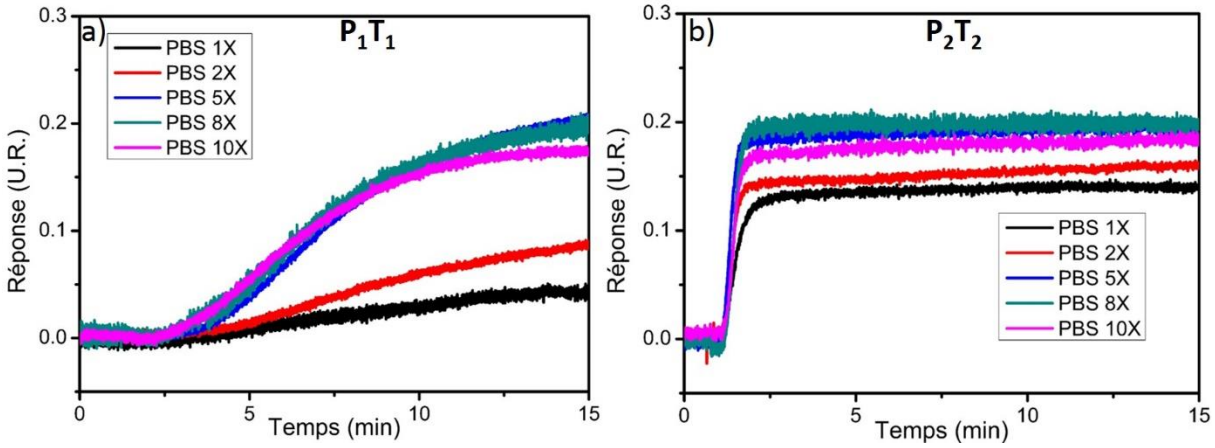

Figure 18 Sensorgrammes d'hybridations des couples P_1/T_1 et P_2/T_2.

La cinétique d'hybridation telle que mesurée sur P_1/T_1 est plus lente que celle observée pour P_2T_2. La modélisation sur DINAmelt (http://unafold.rna.albany.edu/?q=DINAMelt) indique la présence de structures secondaires pour P_1 et T_1 alors que T_2 ne fait pas de structure secondaire (Figure 19).

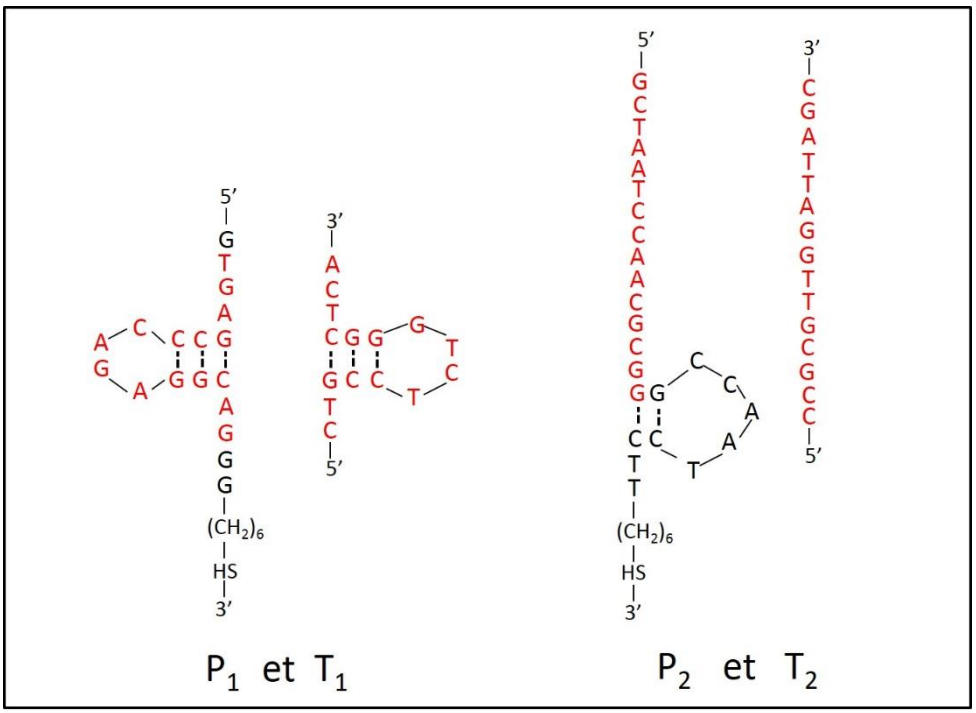

Figure 19 Structures secondaires pour P1, T1, P2 et T2 calculée sur DINAmelt

En revanche si l'hybridation est réalisée à 65°C, les structures secondaires sont détruites et nous retrouvons pour le couple P_1/T_1, une cinétique d'hybridation dont le comportement est proche de celle observée pour P_2/T_2. (Figure 20)

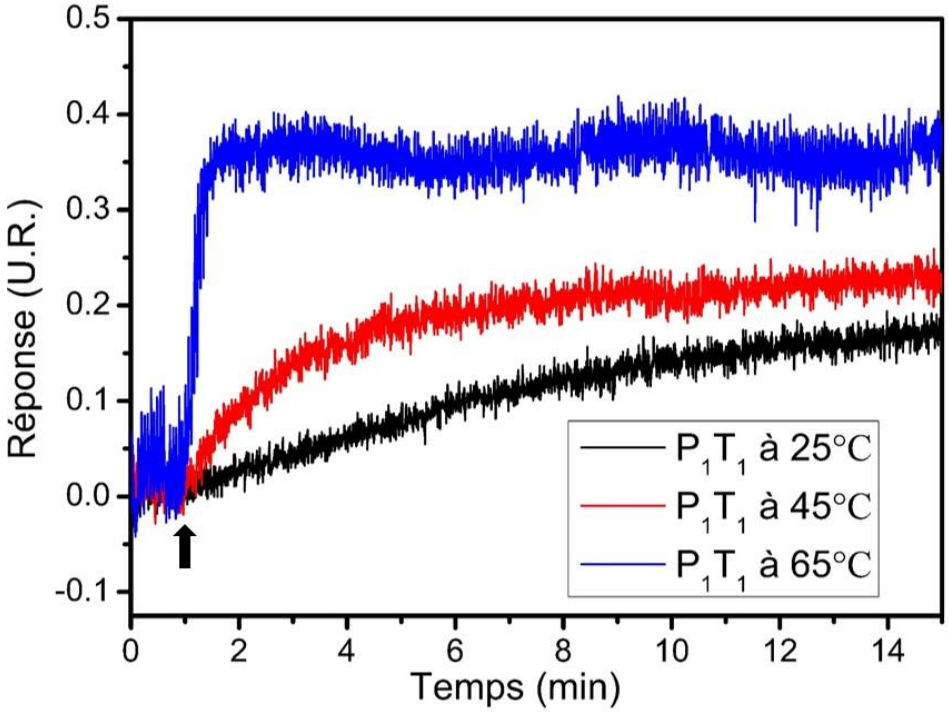

Figure 20 Sensorgramme observés pour P1T1 à 25, 45 et 65 °C.

Cependant l'appareil de fluorescence par champ évanescent ne permet pas de chauffer à 65° C. Nous avons donc choisi de travailler avec le couple P_2/T_2 et de garder les conditions d'hybridation des 25°C en PBS 5X.

Pour la comparaison des trois techniques, les sondes et cible utilisées sont décrites Tableau 3.

Technique	Sonde/Cible	Concentrations
SPR Diluent MCH	5'-Cy5-GCT AAT CCA ACG CGG GCC AAT CCT T-$(CH_2)_6$-SH	20 µM
	5'-Cy5-CCG CGT TGG ATT AGC	
Fluorescence par champ évanescent	Sonde: 5'-Cy5-GCT AAT CCA ACG CGG GCC AAT CCT T-$(CH_2)_6$-biotin	10 et 20 nM
	Cible: 5'-Cy5-CCG CGT TGG ATT AGC	
Cartographie de fluorescence	Sonde : 5'-Cy5-GCT AAT CCA ACG CGG GCC AAT CCT T-$(CH_2)_6$-NH_2	50, 100, 500, 1000 nM
	Cible : 5'-Cy5-CCG CGT TGG ATT AGC	

Tableau 3 Sondes utilisées pour les mesures de K_d par SPR, fluorescence par champ évanescent et cartographie de fluorescence.

La Figure 21 présente les sensorgrammes obtenus par résonance des plasmons de surface pour le couple de séquences P_2/T_2 en fonction de la concentration en T_2 (cible). La figure 22 présente les ajustements opérés soit pour l'analyse des courbes de vitesse soit l'isotherme de Langmuir. Les résultats sont résumés Tableau 4.

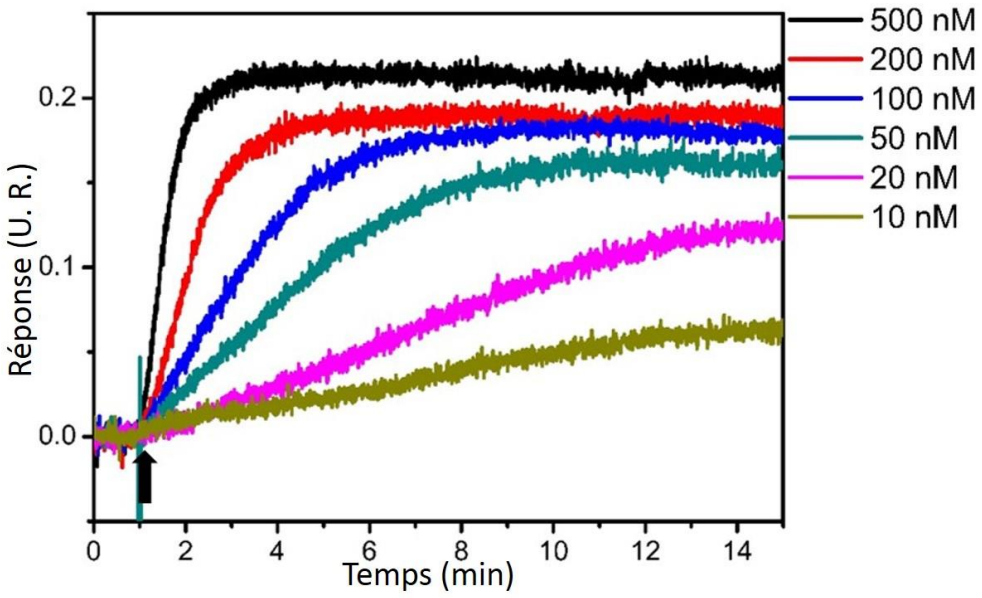

Figure 21: Sensorgrammes obtenus par résonance des plasmons de surface pour le couple de séquences P_2/T_2 en fonction de la concentration en T_2 (cible). Les conditions sont PBS 5x, 25°C.

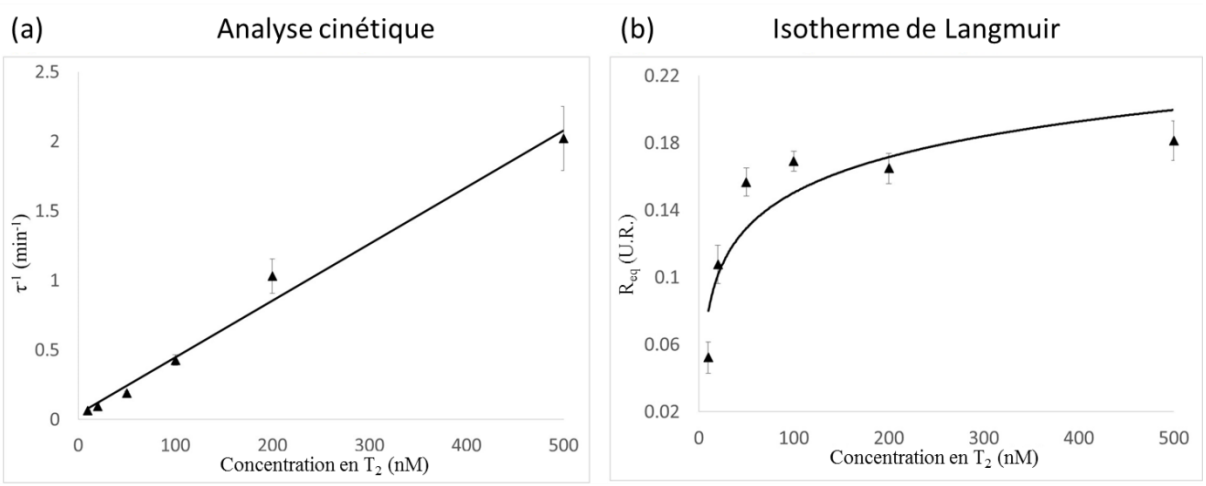

Figure 22 Ajustements opérés soit pour l'analyse des courbes de vitesse soit l'isotherme de Langmuir.

	K_d- (nM)[a] Ajustement cinétique	K_d- (nM) Isotherme de Langmuir
Valeur moyenne	19±6	16±3

Tableau 4 K_d mesurés pour l'hybridation P2/T2 à 25 °C dans du PBS 5x par SPR selon deux modalités d'analyse. [a] calculé par k_{off}/k_{on}.

La Figure 23 présente les courbes cinétiques de reconnaissance obtenues par fluorescence par champ évanescent pour le couple de séquences P_2/T_2 en fonction de la concentration en T_2 (cible). La figure 24 présente les ajustements opérés soit pour l'analyse des courbes de vitesse soit l'isotherme de Langmuir. Le Tableau 5 résume les résultats obtenus pour deux concentrations en sondes (10 et 20 nM) dans la solution d'immobilisation.

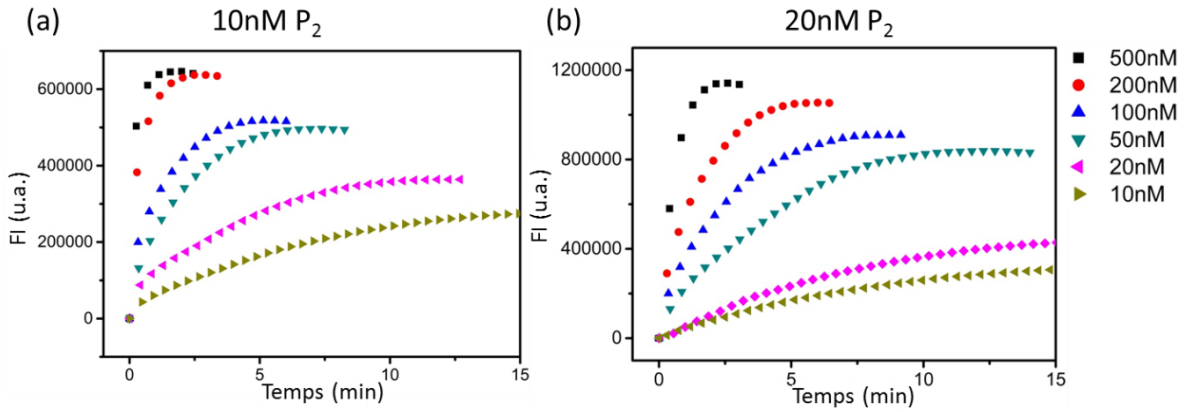

Figure 23 : Courbes cinétiques de reconnaissance obtenues par fluorescence par champ évanescent pour le couple de séquences P2/T2 en fonction de la concentration en T2 (cible). Les conditions sont PBS 5x, 25°C.

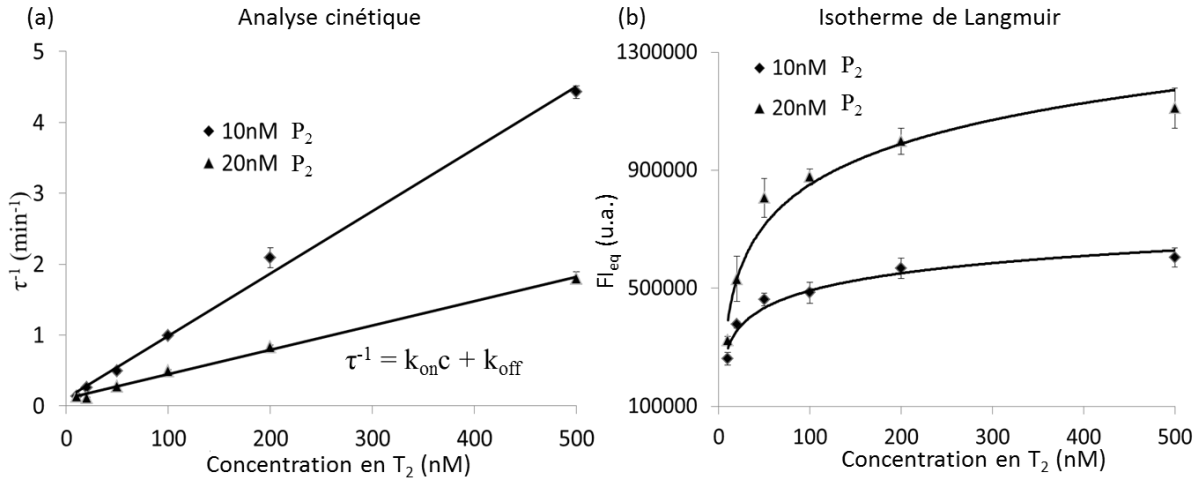

Figure 24 : Ajustements opérés soit pour l'analyse des courbes de vitesse soit l'isotherme de Langmuir

	K_d- (nM) Ajustement cinétique	**K_d- (nM) Isotherme de Langmuir**
10 nM P_2	14±5	16±3
20 nM P_2	21±1	27±3

Tableau 5: K_d mesurés pour l'hybridation P2/T2 à 25 °C dans du PBS 5x par fluorescence par champ évanescent selon deux modalités d'analyse et pour deux concentrations en sondes dans la solution d'immobilisation (10 et 20 nM)

La Figure 25 présente l'isotherme obtenue par cartographie de fluorescence pour les quatres concentrations en sonde dans la solution d'immobilisation. Le Tableau 6 résume les résultats obtenus pour ces 4 concentrations.

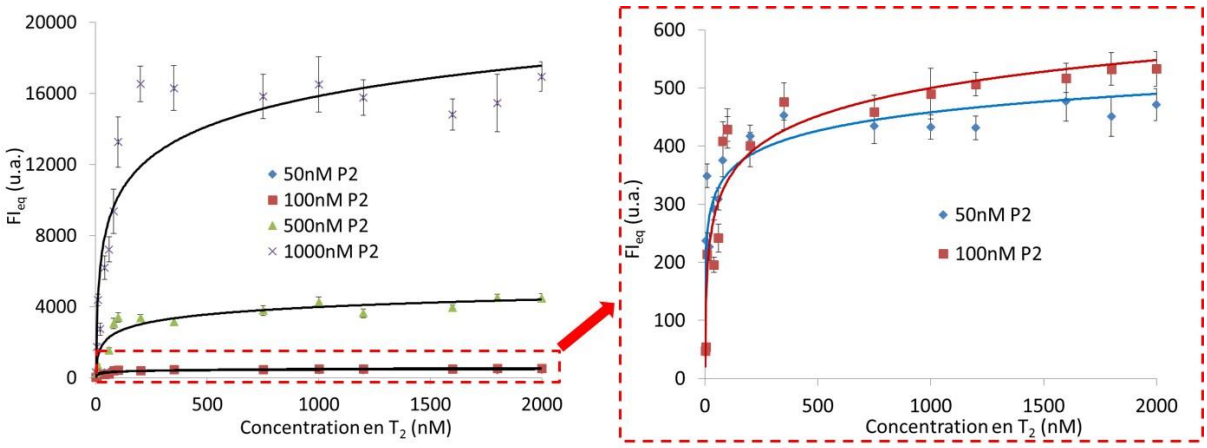

Figure 25 Isotherme obtenue par cartographie de fluorescence.

	[sonde]= 50 nM	[sonde]= 100 nM	[sonde]= 500 nM	[sonde]= 1000 nM
K_d (nM)	7±2	37±9	54±12	53±11

Tableau 6 Constante de dissociation obtenues pour l'hybridation de l'ADN par cartographie de fluorescence pour des densités de sondes spottées de 50, 100, 500 et 1000 nM.

Pour ces trois techniques, nous avons comparé les K_d obtenus. Pour la SPR et pour la fluorescence par champ évanescent, il est possible de traiter les données soit par une approche cinétique, c'est-à-dire par extractions de k_{on} et k_{off}. Pour les trois techniques, il est possible de construire un isotherme Langmuir et de le linéariser par une courbe de Scatchard. De cette courbe, il est possible d'extraire la constante de dissociation qui correspond à l'intersection de la droite avec l'axe des ordonnées. Le traitement des données selon l'une ou l'autre des approches ne semble pas indiquer de différence significative. En revanche, la densité de sonde est un paramètre qui d'après nos résultats donne, y compris pour une même technique, une variabilité importante sur la détermination du K_d. Ceci implique que pour pouvoir les comparer, il faudrait pouvoir s'assurer que les densités de surface sont similaires. Or pour chaque technique, la densité de surface en sondes est estimée par des modalités différentes, donnant une densité relative mais pas absolue. Il faudrait donc pouvoir étalonner chacune des mesures de densité en sonde afin de remonter à leur densité absolue en sonde.

Conclusions et perspectives

Lors de ce travail de thèse nous souhaitions obtenir par trois techniques différentes basées sur une reconnaissance aux interfaces solide/liquide, les constantes de dissociation pour l'hybridation de deux oligonucléotides. Ces trois techniques étaient la résonance des plasmons de surface, la fluorescence par champ évanescent et la cartographie de fluorescence. Le deux premières techniques permettent un suivi en temps réels de la reconnaissance et permettent donc de suivre la cinétique de réaction. Nous avons donc pour ces deux techniques comparées deux approches pour le traitement des données. Une approche dite cinétique qui extrait pour une série de courbes obtenues à différentes concentrations les paramètres cinétiques. Ces paramètres permettant ensuite de déterminer la constante de dissociation. Pour les trois techniques, nous avons aussi utilisé l'approche qui est basée sur la construction d'un isotherme de Langmuir, à partir duquel il est possible de déterminer la constante de dissociation.

Dans un premier temps nous avons optimisé les paramètres expérimentaux relatifs à la mise en œuvre des mesures par SPR sur l'instrument développé à l'INL.

Cette optimisation accomplie, la comparaison des trois techniques a permis de montrer que le paramètre qui induit le plus de variabilité dans la détermination de K_d est la densité de sondes en surface. Il faudra donc pour réaliser une comparaison qui fait sens s'assurer que la densité en sonde est similaire pour les trois techniques.

Curriculum vitae

Muchen LI

Email: muchenli2@gmail.com

Education:

2015.10-2018.10 **PhD** student at INL, Ecole Centrale de Lyon, France

2012.09-2015.06 **M.S**. of materials chemistry, University of Science and Technology Beijing, China

2008.09-2012.06 **B.S.** of materials, Yantai University, China

Research experience:

2015.10-2018.10 **PhD Dissertation of** "Development of a system for probing DNA/DNA hybridization using surface plasmon resonance: in comparison with fluorescent microarray and evanescent field fluorescence biosensor"

Competences: Glycan microarray, SPR, evanescent field fluorescence biosensor, surface chemistry, kinetic modeling.

Ecole Centrale de Lyon, Ecully, France

2012.11-2015.06 **2 years joint training postgraduate study, master thesis of** "Study on wettability of ordered honeycomb structural responsive polymer films under photoelectric stimulus"

Competences: Structural effect on wettabilities of natural materials; bio-inspired and smart interfacial materials; Mastering the material characterization and testing methods: including AFM, SEM, XPS, XRD, IR, UV

Institute of Chemistry Chinese Academy of Science, Beijing, China

Publications:

1. A. Angeli**, M. Li**, L. Dupin, G. Vergoten, M. Noel, M. Madaoui, S. Wang, A. Meyer, T. Gehin, S. Vidal, J.-J. Vasseur, Y. Chevolot, F. Morvan. Design and synthesis of galactosylated bifurcated ligands with Nanomolar affinity for Lectin LecA from Pseudomonas aeruginosa. *ChemBioChem*, 2017, 18: 1036-1047.

2. A. Angeli, L. Dupin, M. Madaoui, **M. Li**, G. Vergoten, S. Wang, A. Meyer, T. Gehin, S. Vidal, J.-Ja. Vasseur, Y. Chevolot, F. Morvan. Glycoclusters with additional functionalities for binding to the lectin from pseudomonas aeruginosa. *ChemistySelect*, 2017, 2: 10420-10427.
3. T. Guo, **M. Li (co-first author)**, L. Heng, L. Jiang. Special adhesion of natural honeycomb wall and their application. *Phys. Chem. Chem. Phys.*, 2015, 17: 6242-6247.
4. T. Guo, **M. Li**, L. Heng, L. Jiang. Design of honeycomb structure surfaces with controllable oil adhesion underwater. *RSC Advances*, 2015. 5: 62078-62083.
5. **M. Li**, B. Wang, L. Heng, L. Jiang. Surface-independent reversible transition of oil adhesion under water induced by lewis acid-base interactions. *Adv. Mater. Interfaces*, 2014, 1: 1400298.
6. L. Heng, J. Li, **M. Li**, D. Tian, L. Fan, L. Jiang, B. Tang. Ordered honeycomb structure surface generated by breath figures for liquid reprography. *Adv. Funct. Mater.*, 2014, 24: 7241-7248.
7. L. Heng, R. Hu, S. Chen, **M. Li**, L. Jiang, B. Tang. Ordered Honeycomb structural interfaces for anticancer cells growth. *Langmuir*, 2013, 29: 14947-14953.
8. L. Heng, B. Wang, **M. Li**, Y. Zhang, L. Jiang, Advances in fabrication materials of honeycomb structure films by breath-figure method. *Materials*, 2013, 6: 460-482.

Scientific communications:

Oral presentation：

1. M. Li, T. Géhin, C. Yeromonahos, J.-P. Cloarec, J. Zhang, Y. Chevolot, Cleaning and DNA functionalization of gold surface for biosensor application. INL PhD Days, Lyon, France, 26-27 October 2017.

Poster presentations:

2. M. Li, L. Dupin, A. Angeli, F. Casoni, M. Noël, G. Vergoten, S. Wang, A. Meyer, S. Vidal, T. Géhin, J.-J. Vasseur, F. Morvan, Y. Chevolot. Screening of glycoclusters targeting the lectin PA-IL *Pseudomonas aeruginosa* using glycocluster microarray technology. V^{ème} Journée Rhône-Alpes des Biomolécules, Lyon, France, 7 Juin 2016.

3. M. Li, L. Dupin, A. Angeli, F. Casoni, M. Noël, G. Vergoten, S. Wang, A. Meyer, S. Vidal, T. Géhin, J.-J. Vasseur, F. Morvan, Y. Chevolot. Screening of glycoclusters targeting the lectin PA-IL *Pseudomonas aeruginosa* using glycocluster microarray technology. INL PhD Days, Lyon, France, 20-21 October 2017

4. **M. Li**, T. Géhin, J.-P. Cloarec, J. Zhang, Y. Chevolot, Cleaning and DNA functionalization of gold surface for biosensor application. 4ème Journée thématique du GDR B2i, Paris, France, 6 Avril 2018
5. **M. Li**, T. Géhin, J.-P. Cloarec, J. Zhang, Y. Chevolot, Cleaning and DNA functionalization of gold surface for biosensor application. 23ème Colloque de Recherche Inter Écoles Centrales, Marseille, France, 29 May – 02 Juin 2017
6. **M. Li**, T. Géhin, J.-P. Cloarec, J. Zhang, Y. Chevolot, Cleaning and DNA functionalization of gold surface for biosensor application. 2nd Journées Plénières GDR B2I, Bordeaux, France, 28-29 Juin 2017.

Languages:

Chinese (Native), English (Fluent, Ielts: 6.5), French (Beginner)

Other activities:

Volunteer Service in Beijing Children's Hope Family (14/07/2014-27/07/2014):

I worked as a translator for American volunteers in Beijing Children's Hope Family. My main job is to do the translations work and look after the children in special needs.

dernière page de la thèse

AUTORISATION DE SOUTENANCE

Vu les dispositions de l'arrêté du 25 mai 2016,

Vu la demande du directeur de thèse

Monsieur Y. CHEVOLOT

et les rapports de

M. Y. ROUPIOZ
Directeur de Recherche CNRS - UMR 5819 Systèmes Moléculaires et nano Matériaux pour l'Energie et la Santé (SyMMES) - Commissariat à l'Energie Atomique et aux Energies Alternatives - 17 rue des Martyrs - 38054 Grenoble cedex 9

et de

Mme A-C. GOUGET-LAEMMEL
Chargée de Recherche CNRS HDR - UMR 7643 - Laboratoire de Physique de la Matière Condensée (LPMC) - Ecole Polytechnique - Route de Saclay - 91128 Palaiseau cedex

Monsieur LI Muchen

est autorisé à soutenir une thèse pour l'obtention du grade de **DOCTEUR**

Ecole doctorale ELECTRONIQUE, ELECTROTECHNIQUE, AUTOMATIQUE

Fait à Ecully, le 11 octobre 2018

P/Le directeur de l'E.C.L.
La directrice des Etudes

ECOLE CENTRALE DE LYON
Service Scolarité
ECULLY

M-A. GALLAND

Abstract: Biosensors are powerful detection and analysis tools that have been widely applied in pharmaceuticals, healthcare, biomedical research, and environmental monitoring. However different biosensors use different transducers and therefore different substrates and surface chemistries. All of these parameters may have an effect on the biomolecular reactions at the interface and lead to a deviation in dissociation constant K_d measurements. In this context, this PhD work aimed at comparing three different techniques: fluorescent microarray, evanescent field fluorescence biosensor and surface plasmon resonance (SPR) biosensor, to determine DNA hybridization K_d. For the classical fluorescence microarray, the substrate is a glass slide and the detection is performed at the end of the experiment. In the case of evanescent field fluorescence biosensor, polystyrene is the substrate and it permits a real-time detection. SPR is performed on thin gold film. It is a real-time and a label-free technique. The two fluorescent based techniques require to label the targets with fluorescent dyes prior to the measurements. One important factor determining the performance of the analysis is the surface chemistry of the sensor chip. Herein, we have optimized gold surface chemistry for thiol modified DNA grafting. We studied two cleaning methods: piranha solution and oxygen plasma, aiming at obtaining a clean gold surface without oxidation of the gold. Then, we optimized SPR assay parameters such as interfacial structure of sensor chip, ionic strength... After, these three techniques were used to measure the DNA hybridization K_d. The results showed that the K_ds measured are similar for the three techniques. In addition, increasing surface probe density resulted in an increase of K_d of DNA hybridization.

Keywords: DNA hybridization; Dissociation constant; Surface plasmon resonance, Fluorescent microarray, Evasnescent field fluorescence, Surface chemistry

Résumé: Les biocapteurs sont des outils de détection et d'analyse puissants qui ont été largement utilisés dans les domaines de la santé, de la recherche biomédicale et de l'environnement. Cependant, différents biocapteurs utilisent différents transducteurs qui varient par la nature des substrats utilisés et par la chimie de surface. Tous ces paramètres peuvent avoir un effet sur les réactions biomoléculaires aux interfaces et conduire à des variations de la mesure de la constante de dissociation K_d. Dans ce contexte, ce travail de thèse visait à comparer trois techniques différentes: biopuce avec une détection par fluorescence, biocapteur à fluorescence par champ évanescent et biocapteur par résonance de plasmon de surface (SPR). Ces trois techniques ont été comparées pour la détermination de la constant de dissociation de l'hybridation de l'ADN. Pour la biopuce à fluorescence classique, le substrat est une lame de verre et la mesure est effectuée à la fin de l'expérience. Dans le cas du biocapteur à fluorescence à champ évanescent, le polystyrène est le substrat et une détection en temps réel est réalisée. La SPR est réalisée sur un film d'or mince. C'est une technique en temps réel et sans marquage. Les deux techniques basées sur la fluorescence nécessitent de marquer les cibles avec un fluorophore avant la mesure. Un facteur important déterminant la performance de l'analyse est la chimie de surface du capteur. Ici, nous avons optimisé la chimie de la surface de l'or pour le greffage d'ADN modifié thiol. Nous avons étudié deux méthodes de nettoyage: la solution de piranha et le plasma d'oxygène, dans le but d'obtenir une surface d'or propre sans oxydation de l'or. Ensuite, nous avons optimisé les paramètres lors de la mesure SPR comme par exemple la structure interfaciale du capteur, la force ionique .... Enfin, ces trois techniques ont été utilisées pour mesurer la constante de formation du duplex ADN/ADN. Les résultats ont montré que les K_d sont du même ordre de grandeur pour les trois techniques. De plus, pour les trois techniques, une augmentation de la densité de sonde de surface a entraîné une baisse d'affinité telle que mesurée.

Mots clés: Hybridation d'ADN; Constante de dissociation; Résonance de plasmon de surface, Biopuce, fluorescence, Fluorescence par champ évanescent, Chimie de surface